Design and Preparation of Electrocatalysts Based on Ordered Mesoporous Carbons for Oxygen Reduction Reaction

Jae Yeong Cheon

School of Molecular Sciences
(Chemistry)

Graduate School of UNIST

Design and Preparation of Electrocatalysts Based on Ordered Mesoporous Carbons for Oxygen Reduction Reaction

A dissertation
submitted to the Graduate School of UNIST
in partial fulfillment of the
requirements for the degree of
Doctor of Philosophy

Jae Yeong Cheon

12. 11. 2015 of submission
Approved by

Advisor
Sang Hoon Joo

Design and Preparation of Electrocatalysts Based on Ordered Mesoporous Carbons for Oxygen Reduction Reaction

Jae Yeong Cheon

This certifies that the dissertation of Jae Yeong Cheon is approved.

12. 11. 2015 of submission

Advisor: Sang Hoon Joo

Youngsik Kim

Hoi Ri Moon

Kwangjin An

Gu-Gon Park

Abstract

The research presented in this dissertation is aimed at the development of electrocatalysts for the oxygen reduction reaction (ORR) based on ordered mesoporous carbons (OMCs). The ORR is a key reaction in electrochemical energy devices such as fuel cells and metal-air batteries. Because of its sluggish kinetics compared to its counterpart reaction (*i.e.*, hydrogen oxidation reaction in fuel cells), ORR needs to be catalyzed by a precious metal such as platinum, to achieve favorable reaction kinetics. However, the high cost and scarcity of Pt limit the large-scale application of these systems. Therefore, tremendous efforts have been devoted to developing highly active, cost-effective electrocatalysts for the ORR. In this regard, this thesis presents multiple approaches to develop efficient electrocatalysts based on OMCs, from supported Pt catalysts to heteroatom-doped, non-precious metal catalysts.

The first part of this thesis presents OMC-supported platinum catalysts for the ORR. We investigated the effect of different framework structures of OMCs on the activity and durability for the ORR by comparing the electrochemical behaviors of Pt nanoparticle catalysts supported on these different OMC supports. For this purpose, three representative OMCs were used as support materials: CMK-3, CMK-3G, and CMK-5. These OMCs with the same hexagonal mesostructure have different carbon frameworks and graphiticities, which can affect their surface areas and microporosities. Pt/CMK-3G exhibited the highest electrochemically active surface area, kinetic current density, mass activity, and half-wave potential, whereas Pt/CMK-3 showed the lowest values. Pt/CMK-3G also showed the highest ORR activity after an accelerated durability test, with a minimal shift in half-wave potential. The higher ORR activity of Pt/CMK-3G is attributed to the formation of highly crystalline Pt particles as well as its highly graphitic, crystalline carbon structure, which causes the weak adsorption of surface oxides and a strong interaction between the Pt particles and the support.

In addition to investigation of the effect of different framework structures of OMCs on the performance in the ORR, we developed highly conductive and durable OMC-based nanocomposites. Ordered mesoporous carbon-carbon nanotube (OMC-CNT) nanocomposites, were synthesized via a nanocasting method that used ordered mesoporous silica (OMS) as a template and Ni-phthalocyanine as a carbon source. For comparison, two OMCs with varying degrees of conductivity, OMC(Suc) and OMC(Pc), were also prepared using sucrose and phthalocyanine, respectively. Among the three Pt/OMC catalysts, the Pt/OMC-CNT catalyst showed activity that was superior to those of the Pt/OMC(Suc) and Pt/OMC(Pc) catalysts. This trend was even more pronounced after accelerated durability tests (ADTs), which were performed to test the durability of the catalysts. In single-cell tests that are more relevant with respect to the practical applications, the Pt/OMC-CNT catalyst showed a current density that was higher than those of the other two catalysts after high-voltage degradation tests. The half-cell and single-cell tests using the Pt/OMC catalysts indicated that the rigidly interconnected

structure and the highly conductive frameworks of the OMC-CNT nanocomposites were concomitantly responsible for their enhanced durability and single cell performance.

The second part describes our approach to develop metal-free electrocatalysts for the ORR. A recent study showed that nanostructured carbon materials doped with a variety of heteroatoms have promising ORR activity, yet understanding of the underlying working principles of these materials has been limited to theoretical prediction. In this regard, we prepared a series of heteroatom-doped OMCs for a systematic study on the dopant effects in the ORR. The triple-doped N,S,O-OMC exhibited superior catalytic activity and reaction kinetics in the ORR in an alkaline medium when compared with the dual-doped (N,O-OMC and S,O-OMC) and the mono-doped (O-OMC) OMC catalysts. We found a systematic variation in the work functions, measured by surface-sensitive Kelvin probe force microscopy, depending on the type of dopant used. Significantly, the work functions of these heteroatom-doped OMCs displayed a strong correlation with the activity and reaction kinetics for the ORR.

The last part addresses the transition metal and nitrogen-doped OMCs as high-performance catalysts for fuel cell and metal-air battery applications. We developed a new type of non-precious metal catalyst based on ordered mesoporous porphyrinic carbons (M-OMPC, M = Fe and/or Co) with high surface areas and tunable pore structures, which were prepared by nanocasting OMS templates with metalloporphyrin precursors. The FeCo-OMPC catalyst exhibited excellent ORR activity in an acidic medium, higher than those of other non-precious metal catalysts. It showed a higher kinetic current at 0.9 V than Pt/C catalysts, as well as superior long-term durability and MeOH-tolerance. Density functional theory calculations in combination with extended X-ray absorption fine structure analysis revealed a weakening of the interaction between oxygen atoms and FeCo-OMPC compared to Pt/C. This effect and the high surface area of FeCo-OMPC appear to be responsible for its significantly high ORR activity.

We extended our approach to develop a new type of non-precious metal electrocatalyst using macrocyclic compounds as precursors. Nanocasting of OMS by the use of Ni- and Fe- phthalocyanine precursors yielded graphitic nanoshell-embedded mesoporous carbon (GNS/MC) nanohybrids. The GNS/MC exhibited very high activity and durability for the oxygen evolution reaction (OER) and ORR in an alkaline medium. The oxygen electrode activity of the GNS/MC was as low as 0.72 V, which represents one of the best performances among non-precious metal bifunctional oxygen electrocatalysts. The GNS/MC also exhibited very high long-term durability for the OER and ORR. The high electrocatalytic performance of the GNS/MC can be ascribed to the contributions of residual transition metal (Ni and Fe) entities, nitrogen-doped defect-rich graphitic nanoshells, and the high surface area of the mesoporous structure. Significantly, in aqueous Na-air battery tests, the GNS/MC-based cell exhibited superior performance to Ir/C- and Pt/C-based cells and demonstrated the first example of a rechargeable aqueous Na-air battery.

Portions of this thesis have been published in the following articles co-written by the author and have been reprinted and/or adapted with permission from their respective publishers.

Chapter 2. adapted from *Carbon* **2014**, *72*, 354. with permission from Elsevier.

Copyright Clearance Center RightsLink®

Home | Account Info | Help

Title: Impact of framework structure of ordered mesoporous carbons on the performance of supported Pt catalysts for oxygen reduction reaction

Author: Nam-In Kim,Jae Yeong Cheon,Jae Hyung Kim,Jinhae Seong,Jun-Young Park,Sang Hoon Joo,Kyungjung Kwon

Publication: Carbon

Publisher: Elsevier

Date: June 2014

Copyright © 2014 Elsevier Ltd. All rights reserved.

Logged in as:
Jae Yeong Cheon
Account #:
3000602328

LOGOUT

Order Completed

Thank you very much for your order.

This is a License Agreement between Jae Yeong Cheon ("You") and Elsevier ("Elsevier"). The license consists of your order details, the terms and conditions provided by Elsevier, and the payment terms and conditions.

Get the printable license.

License Number	3756880531125
License date	Nov 27, 2015
Licensed content publisher	Elsevier
Licensed content publication	Carbon
Licensed content title	Impact of framework structure of ordered mesoporous carbons on the performance of supported Pt catalysts for oxygen reduction reaction
Licensed content author	Nam-In Kim,Jae Yeong Cheon,Jae Hyung Kim,Jinhae Seong,Jun-Young Park,Sang Hoon Joo,Kyungjung Kwon
Licensed content date	June 2014
Licensed content volume number	72
Licensed content issue number	n/a
Number of pages	11
Type of Use	reuse in a thesis/dissertation
Portion	full article
Format	both print and electronic
Are you the author of this Elsevier article?	Yes
Will you be translating?	No
Title of your thesis/dissertation	Design and Preparation of Electrocatalysts Based on Ordered Mesoporous Carbons for Oxygen Reduction Reaction
Expected completion date	Feb 2016
Estimated size (number of pages)	150
Elsevier VAT number	GB 494 6272 12
Permissions price	0.00 USD
VAT/Local Sales Tax	0.00 USD / 0.00 GBP
Total	0.00 USD

ORDER MORE... CLOSE WINDOW

Copyright © 2015 Copyright Clearance Center, Inc. All Rights Reserved. Privacy statement. Terms and Conditions.
Comments? We would like to hear from you. E-mail us at customercare@copyright.com

Chapter 3. adapted from *J. Mater. Chem. A*, **2013**, *1*, 1270. with permission from RSC.

Ordered mesoporous carbon–carbon nanotube nanocomposites as highly conductive and durable cathode catalyst supports for polymer electrolyte fuel cells

J. Y. Cheon, C. Ahn, D. J. You, C. Pak, S. H. Hur, J. Kim and S. H. Joo, *J. Mater. Chem. A*, 2013, **1**, 1270
DOI: 10.1039/C2TA00076H

If you are not the author of this article and you wish to reproduce material from it in a third party non-RSC publication you must formally request permission using RightsLink. Go to our Instructions for using RightsLink page for details.

Authors contributing to RSC publications (journal articles, books or book chapters) do not need to formally request permission to reproduce material contained in this article provided that the correct acknowledgement is given with the reproduced material.

Reproduced material should be attributed as follows:

- For reproduction of material from NJC:
  Reproduced from Ref. XX with permission from the Centre National de la Recherche Scientifique (CNRS) and The Royal Society of Chemistry.
- For reproduction of material from PCCP:
  Reproduced from Ref. XX with permission from the PCCP Owner Societies.
- For reproduction of material from PPS:
  Reproduced from Ref. XX with permission from the European Society for Photobiology, the European Photochemistry Association, and The Royal Society of Chemistry.

Chapter 4. adapted from *J. Am. Chem. Soc.* **2014**, *136*, 8875. with permission from ACS.

Chapter 5. adapted from *Sci. Rep.* **2013**, *3*, 2715. with permission from NPG.

Contents

List of Tables

List of Figures

1. General Introduction

1.1. Fuel Cells

With ever-increasing energy demands and depletion of fossil fuel, the development of renewable and sustainable energy sources is of vital importance in the coming decade. Fuel cells are among the most promising candidates for the reliable and efficient conversion of hydrogen into electricity in automotive, distributed power generation, and portable applications.[1-4]

1.1.1. Overview of fuel cells

Fuel cells are electrochemical devices that convert chemical energy into electrical energy via the oxidation of a fuel (at the anode) and the corresponding reduction of an oxidant (at the cathode). Fuel cell performance is indicated by its polarization curve, a plot of cell voltage versus current density. Figure 1.1 shows a typical polarization curve for a fuel cell with three distinct voltage loss regimes: kinetic loss due to the sluggish ORR kinetics, ohmic loss by resistance of the cell components and interconnections, and mass transport loss at high current densities due to depletion of reactants within the catalyst layer. Kinetic losses are the most challenging because an order-of-magnitude improvement in ORR activity would lead to a gain of only 60–70 mV, and research in catalyst development so far has achieved only modest cell voltage gains of tens of millivolts. Reducing mass transport overpotentials and ohmic overpotentials by the same amount is less difficult.

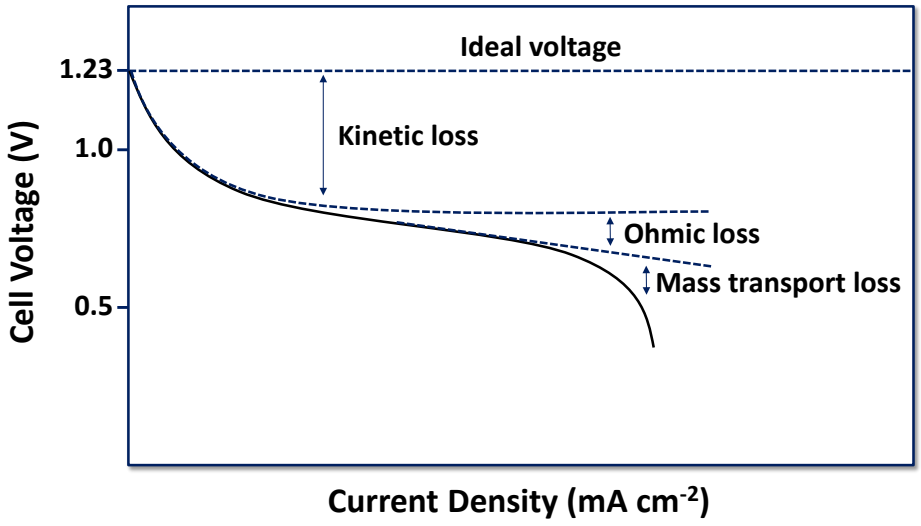

Figure 1.1. Fuel cell polarization curve.

There are five major types of fuel cells as shown in Figure 1.2, differentiated from one another on the basis of their electrolytes. These include polymer electrolyte membrane fuel cells (PEMFCs), alkaline fuel cells (AFCs), phosphoric acid fuel cells (PAFCs), molten carbonate fuel cells

(MCFCs), and solid oxide fuel cells (SOFCs), with each configuration possessing specific advantages and disadvantages.

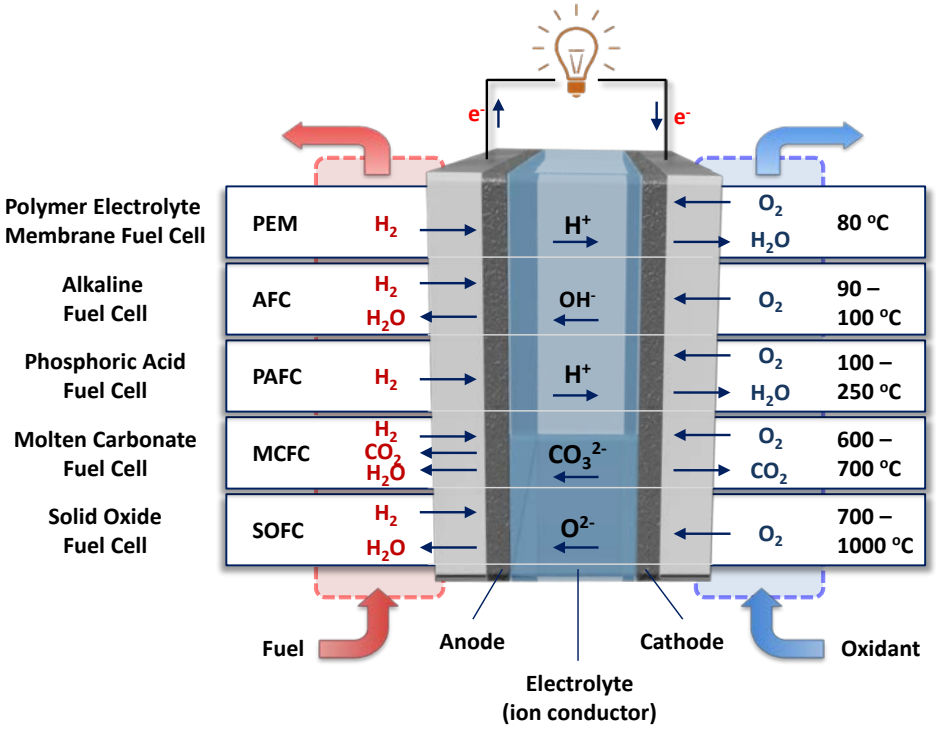

Figure 1.2. Overview of fuel cell types.

For example, SOFCs operate within the 700–1000 °C temperature range, which provides both challenges and advantages. High temperatures make the task of matching materials requirements, mechanical issues, reliability concerns, and thermal expansion more difficult. Advantages include fuel flexibility, high efficiency, and the ability to employ co-generation schemes using the high-quality waste heat that is generated. Similarly, MCFCs also operate at a relatively high temperature of between 600 and 700 °C, which can also improve overall kinetics. However, the performance and applicability of both SOFCs and MCFCs are inhibited by limitations associated with (i) their respective electrolytes, *i.e.*, the use of molten carbonate salt as a liquid electrolyte in MCFCs and ceramic compounds as a solid electrolyte in SOFCs, (ii) the need for CO_2 to be injected into the cathode, and (iii) issues associated with heat corrosion. As a result, both fuel cell types are more suitable for stationary as opposed to mobile applications.

PAFCs are one of the most mature cell types and the first to be used commercially. This type of fuel cell is typically used for stationary power generation, but some PAFCs have been used to power large vehicles such as city buses. PAFCs are less powerful than other fuel cells, given the same weight and volume. As a result, these fuel cells are typically large and heavy. PAFCs are also expensive. They require much higher loadings of expensive platinum catalysts than other types of fuel cells do, which raises the cost.

AFCs were one of the first fuel cell technologies developed, and they were the first type widely used in the U.S. space program to produce electrical energy and water on-board spacecraft. These fuel cells use a solution of potassium hydroxide in water as the electrolyte and can use a variety of non-precious metals as the catalyst at the anode and cathode. The disadvantage of this fuel cell type is that it is easily poisoned by carbon dioxide. In fact, even the small amount of CO_2 in the air can affect this cell's operation, making it necessary to purify both the hydrogen and oxygen used in the cell. This purification process is costly. Susceptibility to poisoning also affects the cell's lifetime (the amount of time before it must be replaced), further adding to cost.

Polymer electrolyte membrane fuel cells (PEMFCs)–also called proton exchange membrane fuel cells–deliver high power density and offer the advantages of low weight and volume compared to other fuel cells. PEMFCs operate at relatively low temperatures, around 80 °C. Low-temperature operation allows them to start quickly (less warm-up time) and results in less wear on system components, resulting in better durability. Owing to these advantages, the largest practical use of PEMFCs has been associated with commercial fuel cell vehicles as potential replacements for internal combustion vehicles. However, it requires the use of a noble-metal catalyst (typically platinum) to separate the hydrogen's electrons and protons, adding to system the cost. The platinum catalyst is also extremely sensitive to carbon monoxide poisoning, making it necessary to employ an additional reactor to reduce carbon monoxide in the fuel gas if the hydrogen is derived from a hydrocarbon fuel.

1.1.2. Acidic and alkaline hydrogen polymer electrolyte membrane fuel cells

PEMFCs can be operated under both acidic and alkaline conditions. In different types of electrolytes, the electrochemical reactions, thermodynamics, kinetics, and mechanisms for catalytic oxygen reduction and fuel oxidation differ.

Figure 1.3 shows schematics of acidic and alkaline PEMFCs. The differences between the PEMFC types are found in the half-fuel cell reactions and the diffusing ion species through the electrolyte. In an acidic PEMFC, the hydrogen used as fuel is oxidized to protons on the anode side and the oxygen is reduced to water on the cathode side. The membrane serves as a separator of both half-cell reactions and proton conductor. In contrast to the acidic PEMFCs, where H^+ ions diffuse from the anode to cathode, OH^- ions are moved from the cathode to anode in alkaline PEMFCs. Therefore, on the cathode side, the oxygen is reduced to hydroxide ions, which diffuse through the anion-conductive membrane to the anode side and react with hydrogen to form water. Although ORR activity is higher in alkaline media compared to that in acid, the sluggish kinetics of the ORR still make it the rate-limiting reaction in the overall fuel cell (Figure 1.4). An additional advantage of alkaline PEMFCs is the possibility of using non-noble metal catalysts such as metal oxides and heteroatom-doped carbons to replace the costly platinum-based catalysts.

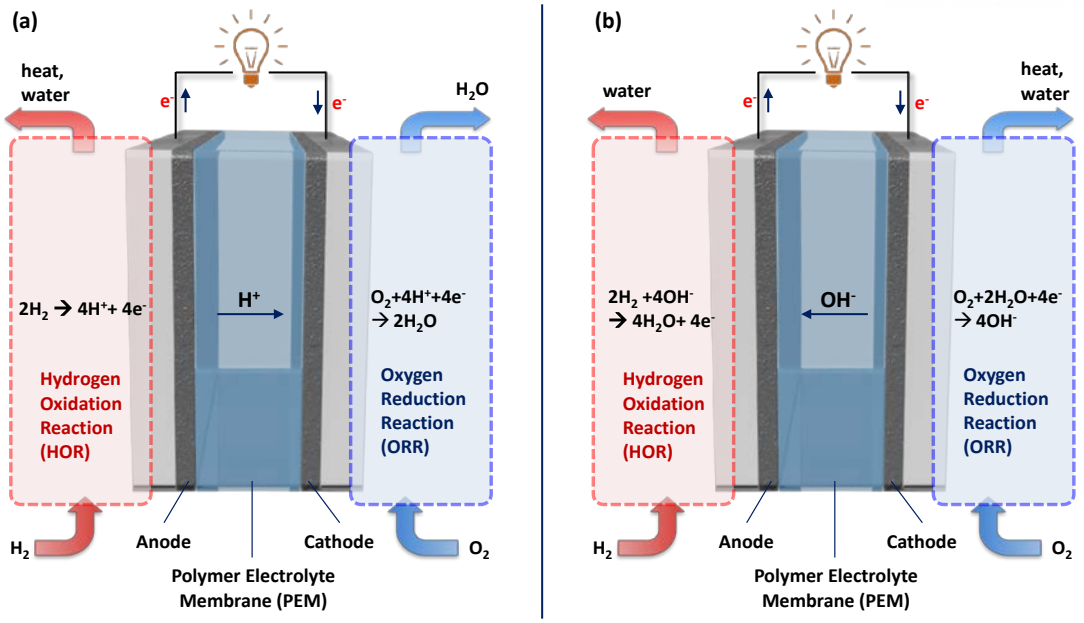

Figure 1.3. Schematic diagrams of (a) acidic and (b) alkaline PEMFCs and the corresponding half-cell reactions.

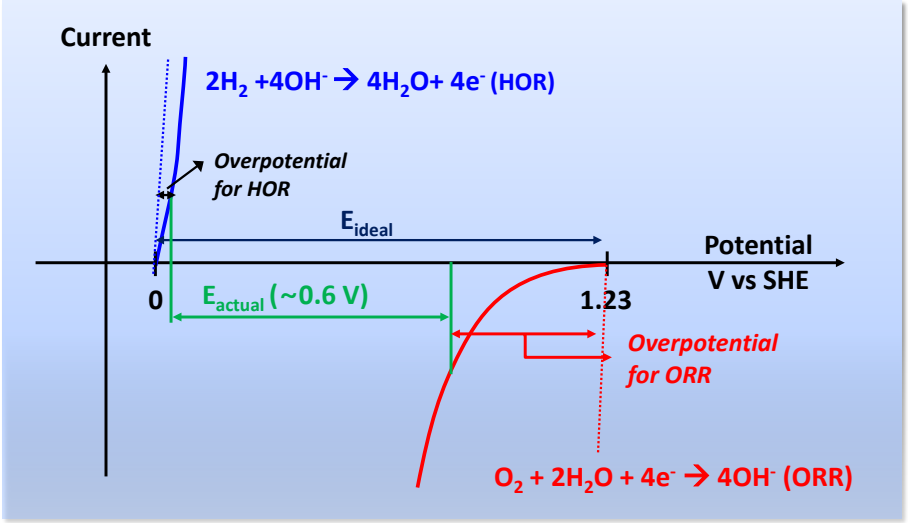

Figure 1.4. Polarization curves for the fuel cell electrochemical reactions in alkaline media and their reaction equations. The lines are not drawn to scale.

1.2. Electrocatalysts for oxygen reduction reaction (ORR)

1.2.1. Class of ORR catalysts

The ORR is generally catalyzed by precious metals such as platinum, to achieve favorable reaction kinetics for practical applications. However, the high cost and scarcity of platinum limit their large-scale applications in relevant energy technologies, such as fuels and metal-air batteries. To circumvent this situation, multi-dimensional efforts have been made over the last decade to develop catalysts for PEMFCs that are more active and stable than the currently most prevalent carbon black-supported platinum (Pt/C) catalysts.[5-12] Figure 1.5 shows the development of ORR catalysts, which

includes non-precious metal catalysts, Pt-M (M = transition metal, such as Co, Ni, Cr, and Fe, to name a few) alloy catalysts, and nanostructured Pt-based catalysts.

One prominent direction of research has been the development of Pt-M alloys and nanoparticles with a core/shell structure for use as catalysts.[13-16] These catalysts generally show enhanced catalytic activity and stability while requiring lower amounts of platinum.[2-5,8,11,12]

Another important approach has been to use novel nanostructured carbon supports, which have a synergistic effect on the activity and durability of Pt catalysts. These types of nanocarbons have included carbon nanofibers[17], carbon nanotubes (CNTs),[9,18,19] OMCs,[20,21] macroporous carbons,[22] and graphene.[23,24]

One can also consider the use of a significantly larger amount of a much cheaper catalyst, instead of a strictly minimized amount of an expensive catalyst such as Pt. In this regard, a great deal of research has been devoted to developing non-precious metal-based[25-28] or metal-free[29-32] catalysts as potential replacements for the Pt-based catalysts.

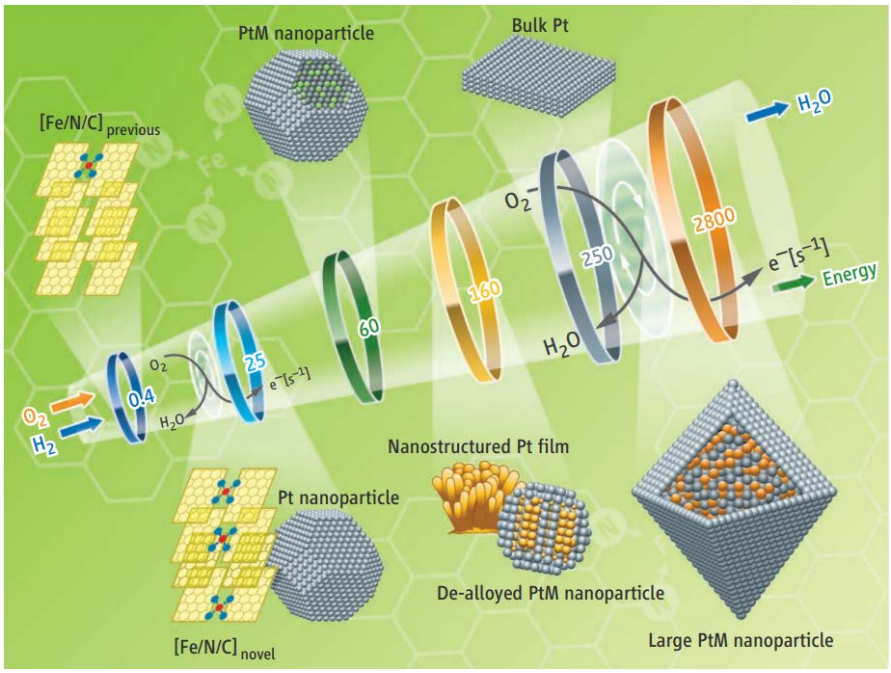

Figure 1.5. Development of different ORR catalysts.[27]

1.2.2. Supported platinum catalysts

To improve the catalytic activity, stability, and utilization of platinum nanoparticles, high surface area carbon black particles have been considered to be the best choice for the electrocatalyst support owing to their large specific surface area favoring the dispersion of an active component, good electric conductivity, and low cost. The surface physicochemical properties and the structure of carbon materials play an important role in the activity and stability of the resultant carbon-supported Pt catalysts because interaction between carbon and Pt can modify the physicochemical and electronic structure of Pt, which in turn influences the catalytic activity and durability. In fact, the durability of

electrocatalysts is one of most critical factors preventing the practical application of fuel cell systems.

The degradation of fuel cell catalysts occurs via several pathways.[33] These include the dissolution of the Pt particles, Ostwald ripening of the Pt particles, corrosion of the carbon support, and detachment and agglomeration of the Pt particles, as shown in Figure 1.6. The corrosion of the carbon support occurs because of the oxidation of carbon to carbon dioxide under the typical fuel cell operation conditions. This carbon corrosion can potentially result in the weakening of the interaction between the carbon support and the Pt particles, thereby leading to the detachment and agglomeration of the Pt particles. Therefore, considerable efforts have been made to develop novel nanostructured carbon supports, which have a synergistic effect on the activity and durability of Pt catalysts. To this end, several types of nanocarbons, including carbon nanofibers, CNTs, OMCs, macroporous carbons, and graphene have been utilized as fuel cell catalyst supports.

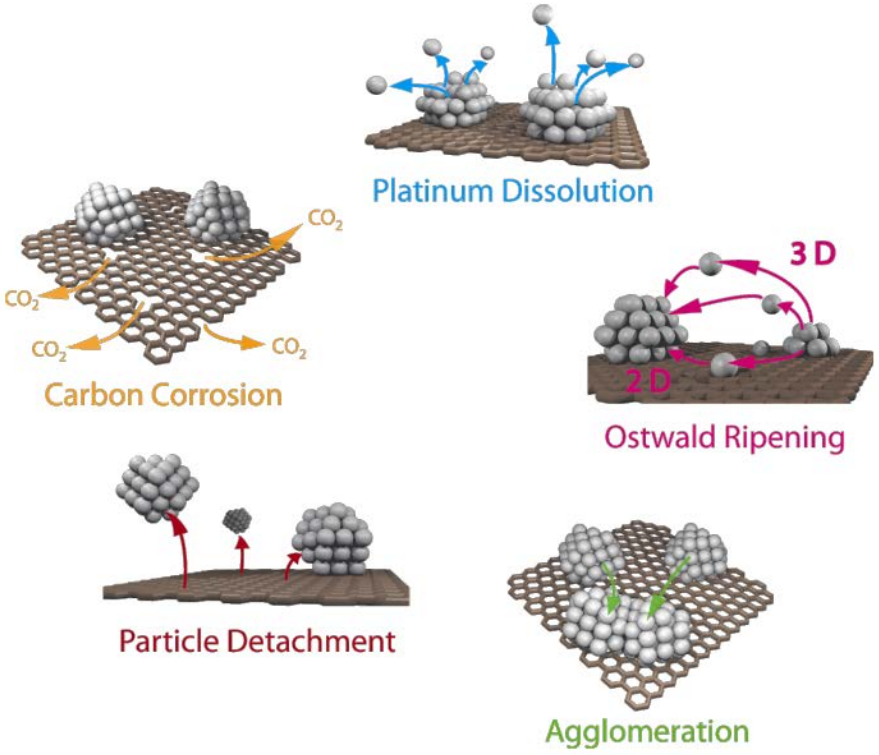

Figure 1.6. Schematic diagrams of suggested degradation mechanism for supported platinum particles in fuel cells.[33]

1.2.3. Heteroatom-doped carbons

Heteroatom-doped carbons with non-metallic elements, including boron, fluorine, nitrogen, phosphorus, and sulfur, are of emerging importance in electrocatalysis.[28-32] Owing to their low cost, these materials are considered as potential replacements for costly catalysts in some vital reactions, for example, as substitutes for platinum for the ORR in fuel cells and metal-air batteries. Nitrogen-doped carbons (NCs) have been more extensively investigated as heteroatom-doped carbon catalysts

for the ORR than have other elements, such as boron, fluorine, phosphorus, and sulfur. NC catalysts essentially contain nitrogen incorporated into the carbon structure, either at the edge or within the core structure of the carbon materials, by replacing one of the sp^2-hybridized carbon atoms in the graphitic structure. Figure 1.7 shows the various forms of NC structures that are considered to be relevant for the ORR. Recent studies have demonstrated that doping of heteroatoms into nanostructured carbon can give rise to enhanced performance in the ORR in terms of both activity and reaction kinetics, when compared with their undoped analogues. However, there are contradicting theories about the structures of the active sites and the role of heteroatoms in NC catalysts.

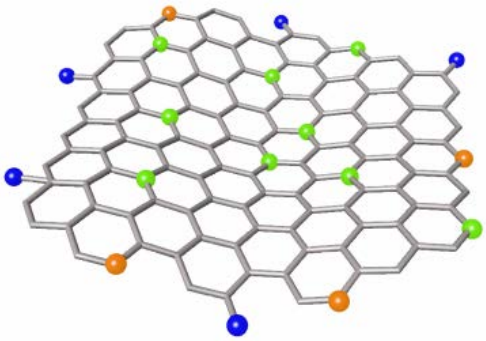

Figure 1.7. Schematic illustration of the functionalized heteroatom in sp^2-hybridized carbon matrices.

Some authors claim that the graphitic species plays the dominant role,[34,35] while others insist that the pyridinic species is more active and dominant.[36,37] Some reports propose the involvement of both pyridinic and graphitic species, as well as pyrrolic species, as active sites.[34]

To understand the intrinsic activity of the different forms of nitrogen-functionalized carbon, it would be desirable to achieve the tailored synthesis of specific forms of the nitrogen-modified carbon.[34] This, however, turns out to be a very challenging task. Many syntheses invariably yield 2–3 types of nitrogen functionalization, so that the product contains a mixture of graphitic, pyridinic, and pyrrolic species as shown in Figure 1.8. In addition, improvement of the ORR performance by multiple dopants is the subject of controversy owing to its complexity.

In efforts to elucidate the promotional effects of dopants in the ORR, it was suggested that changes in the charge and spin densities of the carbon lattice are major factors for the enhanced performance observed with doped nanocarbons[32]; however, these suggestions are based entirely on theoretical calculations. Experimental studies that can systemically correlate the impact of heteroatom doping in nanocarbons with enhanced ORR activity are rare.

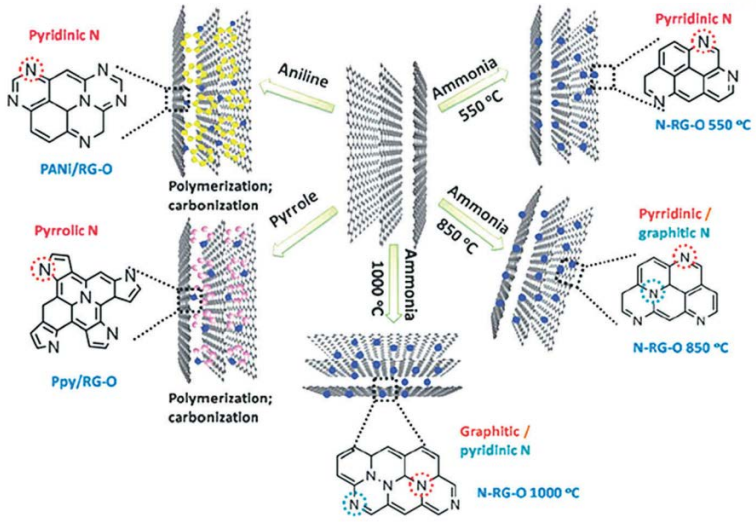

Figure 1.8. Preparation of nitrogen-doped graphene to give different forms of nitrogen-functionalized carbon.[34]

1.2.4. Transition metal-nitrogen-carbon (M-N_x/C)

Transition metal-nitrogen-carbon (M-N_x/C) catalysts are considered the most promising ORR catalysts among the non-precious metal catalysts because they have demonstrated some ORR activity close to that of Pt/C catalysts. Figure 1.9 summarizes the development of ORR catalysts based on M-N_x/C materials. In 1964, Jasinski reported that a Co-phthalocyanine could be used as a catalyst for the ORR in alkaline media.[38] Since then, many macrocyclic transition-metal compounds, such as phthalocyanines and porphyrins, have been extensively investigated as non-Pt ORR catalysts. The basic structure of these complexes is that transition metal atom is coordinated by four nitrogen atoms.

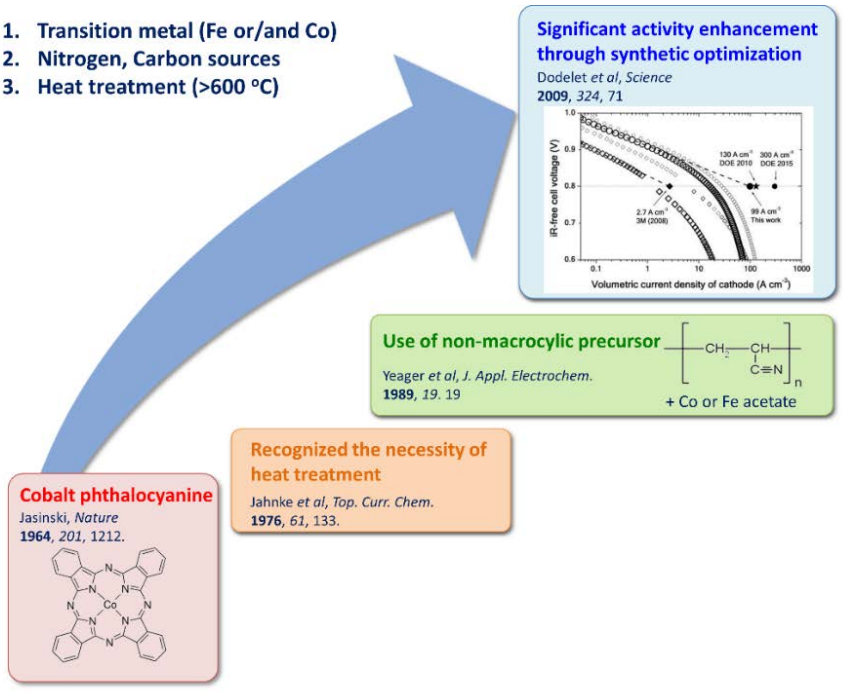

Figure 1.9. Development of M-N_x/C catalysts for ORR

The charge transfer from the electron-rich metal center to the O_2 π^* orbital was believed to lead to an overall weakening of the O-O bond and consequent reduction of O_2.[39] However, the stability of these macrocyclic compounds in acidic solutions was not high enough for them to be used as fuel cell catalysts. Jahnke et al. and other research groups found that high-temperature (>600 °C) heat treatment of such compounds could result in improved the ORR activity and stability. Compared to Pt-based catalysts, ORR activity of these materials is usually quite low, and tremendous efforts have been devoted to enhanceing the ORR activity to potentially replace Pt-based catalysts. The general direction was clear; the transition metal (Fe or/and Co) species, nitrogen, and carbon must be present simultaneously during heat treatment for these materials.

In 1989, Yeager et al. reported that heat-treated polyacrylonitrile (PAN), mixed with Co^{II} or Fe^{II} salts and supported on carbon black, has been found to yield very promising catalysts for the ORR.[40] The nitrile nitrogens on PAN are converted to pyridyl groups during the heat treatment, providing binding sites for the transition metal ions, which then act as catalytic sites for oxygen reduction. This method reveals that for the preparation of M-N_x/C catalysts, transition metal, nitrogen, and carbon do not necessarily exist as a macrocyclic complex. Numerous studies followed using other N-containing precursors and reaction conditions.

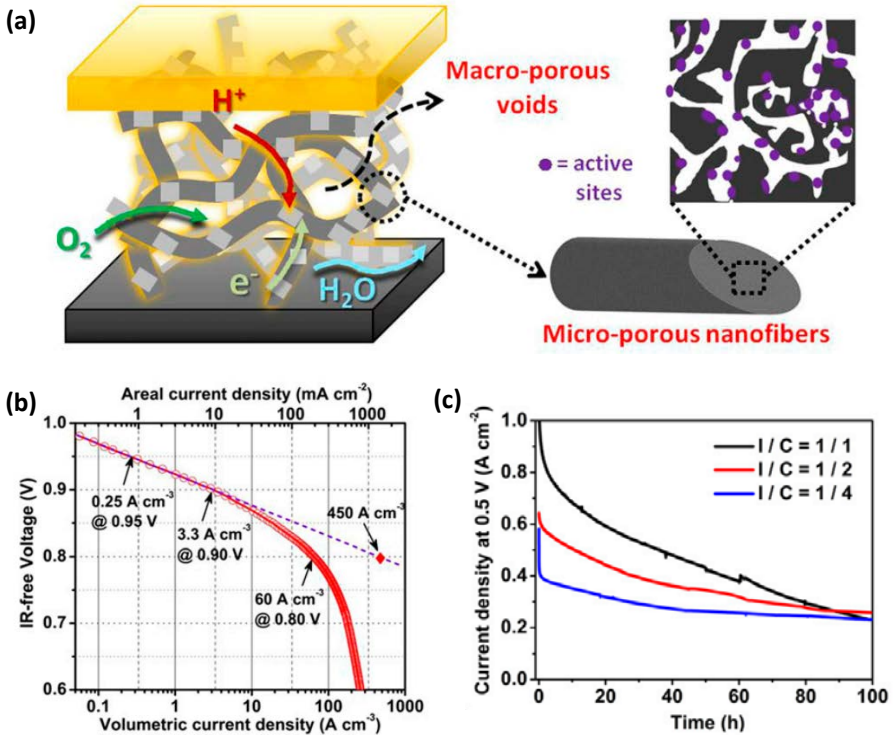

Figure 1.10. (a) Schematic representation of macropore-micropore morphology and charge/mass transfer in the nanofibrous network catalyst, Fe/N/CF. (b) Volumetric current density of Fe/N/CF from a single-cell test. (c) Single-cell current densities as the function of time under a constant voltage hold of 0.5 V with Fe/N/CF cathodes of different I/C ratios: 1/1, 1/2, and 1/4.[42]

Despite these synthetic optimizations by heat treatment, the performance of these M-N_x/C catalysts for the ORR was also low. One of the main reasons was the limited density of active sites. A breakthrough was achieved in 2009 when Dodelet et al. reported the preparation of microporous carbon-supported iron-based catalysts by using iron chloride and 1,10-phenanthroline (Phen) as the metal precursor and nitrogen and carbon precursor, respectively.[25] This catalyst exhibited a volumetric current density of 99 A cm^{-3}, which is two orders of magnitude higher than previously reported activities. Unfortunately, the stability of this catalyst was not high enough for long-term operation; the initially very active catalyst was rapidly deactivated, losing roughly 38% of its initial activity during 100 h of testing with H_2/air at 0.40 V.

The U.S. Department of Energy (DOE) set its 2020 technical target for automotive applications for non-precious metal catalysts at 300 A cm^{-3} (at 0.8 V iR-free cell voltage, 80 °C and total O_2 and H_2 pressure of 150 kPa). The most astonishing result was reported in 2011 by the Dodelet group.[41] By using a metal-organic framework consisting of zeolitic Zn^{II} imidazolate (ZIF-8) as the host for Fe and N precursors [iron(II) acetate and Phen], they prepared an Fe/Phen/ZIF-8 catalyst with a volumetric activity of 230 A cm^{-3} at 0.8 $V_{iR\text{-}free}$, the highest reported at that time for non-Pt-based ORR catalysts in PEMFCs. More recently, Liu et al. reported nanofibrous M-N_x/C catalysts (Fe/N/CF), which exhibited the highest volumetric current density of 450 A cm^{-3} extrapolated from 0.8 $V_{iR\text{-}free}$ (Figure 1.10).[42] This unprecedented high activity was achieved via macroporous nanofiber frameworks which enhance mass transport properties in fuel cells. However, the fuel cell performance was also rapidly decreased by 100 h of testing with H_2/O_2 at 0.5 V (Figure 1.10c).

Since Jasinski first reported a new class of ORR catalysts, efforts to develop efficient non-platinum ORR catalysts have provided encouraging results. Recently reported M-N_x/C catalysts exhibited comparable ORR activity to Pt-based catalysts with improved volumetric current densities in fuel cells. However, previous approaches to obtain high ORR activity relied on multiple pyrolysis steps or toxic ammonia during heat treatment. Furthermore, the challenges of addressing the long-term stability in practical fuel cells and revealing the nature of the catalytic active site remain. A better (*in situ*) characterization and understanding of the reaction mechanism and a knowledge-based synthesis of new catalysts are the prerequisites for further development.

1.3. Outline of This Thesis

Since the first demonstration of a fuel cell by Sir William Grove in 1839, tremendous efforts have been made to develop efficient fuel cell systems for large-scale applications. The bottleneck, particularly at low temperatures is actually the development of materials for the catalysis of the ORR owing to its sluggish kinetics. Therefore, the goal of this thesis was to develop efficient ORR catalysts for fuel cell applications.

This thesis begins with a general introduction of fuel cells and an overview of catalysts for the ORR in chapter 1. The five types of fuel cell are introduced with their respective advantages and disadvantages. Recent developments of electrocatalysts for the ORR are described for each class of catalyst: (i) supported platinum catalysts, (ii) metal-free carbon-based catalysts, (iii) transition metal and nitrogen-doped carbon-based catalysts.

Chapter 2 presents the impact of the framework structures of OMCs on the activity and durability for the ORR. Three representative OMCs were prepared as support materials: CMK-3, CMK-3G, and CMK-5. These OMCs were prepared from the same SBA-15 mesoporous silica template, which has a hexagonal mesostructure, and yet each OMC had a distinguishable framework structure. Hence, these carbons can be used as excellent model systems for a comparative investigation of catalytic activity and durability.

Chapter 3 introduces a new type of OMC-based support, OMC-CNT nanocomposites. The OMC-CNT nanocomposites were used as highly conductive and durable fuel cell catalyst supports for fuel cell applications. For comparison, two OMCs with varying degrees of conductivity, OMC(Suc) and OMC(Pc), were also prepared using sucrose and phthalocyanine, respectively. The ORR activities and kinetics of the Pt/OMC catalysts were investigated in both half-cell and single-cell configurations.

Chapter 4 introduces an approach for the preparation of metal-free electrocatalysts for the ORR. A series of catalysts based on OMCs were prepared with selective doping of N, S, and O. Using surface-sensitive Kelvin probe force microscopy measurements, the work functions of heteoatom-doped OMCs were investigated along with their correlation with enhanced ORR activity.

A new family of non-precious metal catalysts is reported in chapter 5. Self-supported, transition metal-doped ordered mesoporous porphyrinic carbons (M-OMPCs) were prepared by nanocasting ordered mesoporous silica templates with metalloporphyrin precursors. Among the family of M-OMPC catalysts, the Fe and Co co-doped OMPC (FeCo- OMPC) showed extremely high electrocatalytic activity for the ORR in acidic media; this activity is one of the best among those of the non-precious metal catalysts reported in the literature, and even higher than that of the state-of-the-art Pt/C catalyst. The unprecedented high ORR activity of FeCo-OMPC was investigated through density functional theory calculations coupled with extended X-ray absorption fine structure (EXAFS) analysis.

Chapter 6 addresses the design of highly integrated, bifunctional oxygen electrocatalysts based on graphitic nanoshell/mesoporous carbon (GNS/MC) nanohybrids. The GNS/MC catalyst exhibited very high activity and durability for the OER and ORR in an alkaline medium. *In situ* X-ray absorption spectroscopy and Raman spectroscopy data provided critical insights into the structures of catalytic entities in the GNS/MC catalyst for the OER and ORR. Significantly, the first example of a rechargeable aqueous Na-air battery was demonstrated using GNS/MC as an air cathode.

1.4. References

(1) Steele, B. C. H.; Heinzel, A. *Nature* **2001**, *414*, 345.

(2) Gasteiger, H. A.; Kocha, S.S.; Sompalli, B.; Wagner, F. T. *Appl. Catal. B* **2005**, *56*, 9.

(3) Rabis, A.; Rodriguez, P.; Schmidt, T. J. *ACS Catal.* **2012**, *2*, 864.

(4) Debe, M. K. *Nature* **2012**, *486*, 43.

(5) Chan, K. Y.; Ding, J.; Ren, J. W.; Cheng, S. A.; Tsang, K. Y. *J. Mater. Chem.* **2004**, *14*, 505.

(6) Antolini, E. *Appl. Catal. B-Environ.* **2009**, *88*, 1.

(7) Shao, Y. Y.; Liu, J.; Wang, Y.; Lin, Y. H. *J. Mater. Chem.* **2009**, *19*, 46.

(8) Mazumder, V.; Lee, Y.; Sun, S. H. *Adv. Funct. Mater.* **2010**, *20*, 1224.

(9) Zhang, W. M.; Sherrell, P.; Minett, A. I.; Razal, J. M.; Chen, J. *Energ. Environ. Sci.* **2010**, *3*, 1286.

(10) Shrestha, S.; Liu, Y.; Mustain, W. E. *Catal. Rev.* **2011**, *53*, 256.

(11) Qiao, Y.; Li, C. M. *J. Mater. Chem.* **2011**, *21*, 4027.

(12) Wang, C.; Marković, N. M.; Stamenkovic, V. R. *ACS Catal.* **2012**, *2*, 891.

(13) Stamenkovic, V. R.; Fowler, B. ; Mun, B. S.; Wang, G.; Ross, P. N.; Lucas, C. A.; Markovic, N. M. *Science* **2007**, *315*, 493.

(14) Zhang, J.; Sasaki, K.; Sutter, E.; Adzic, R. R. *Science* **2007**, *315*, 220.

(15) Lim, B.; Jiang, M.; Camargo, P. H. C.; Cho, E. C.; Tao, J. ; Lu, X.; Zhu, Y.; Xia, Y. *Science* **2009**, *324*, 1302.

(16) Koh, S.; Strasser, P. *J. Am. Chem. Soc.* **2007**, *129*, 12624.

(17) Bessel, C. A.; Laubernds, K.; Rodriguez, N. M.; Baker, R. T. K. *J. Phys. Chem. B* **2001**, *105*, 1115.

(18) Che, G. L.; Lakshmi, B. B.; Fisher, E. R.; Martin, C. R. *Nature* **1998**, *393*, 346.

(19) Li, W.; Liang, C.; Zhou, W.; Qiu, J.; Zhou, Z.; Sun, G.; Xin, Q. *J. Phys. Chem. B* **2003**, *107*, 6292.

(20) Chang, H.; Joo, S. H.; Pak, C. *J. Mater. Chem.* **2007**, *17*, 3078.

(21) Joo, S. H.; Choi, S. J.; Oh, I. ; Kwak, J. ; Liu, Z.; Terasaki, O.; Ryoo, R. *Nature* **2001**, *414*, 470.

(22) Yu, J. S.; Kang, S.; Yoon, S. B.; Chai, G. *J. Am. Chem. Soc.* **2002**, *124*, 9382.

(23) Yoo, E.; Okata, T.; Akita, T.; Kohyama, M.; Nakamura, J.; Honma, I. *Nano Lett.* **2009**, *9*, 2255.

(24) Kamat, P. V. *J. Phys. Chem. Lett.* **2011**, *2*, 242.

(25) Lefevre, M.; Proietti, E.; Jaouen, F.; Dodelet, J. -P. *Science* **2009**, *324*, 71.

(26) Gasteiger, H. A.; Markovic, N. M. Science **2009**, *324*, 48.

(27) Wu, G.; More, K. L.; Johnston, C. M.; Zelenay, P. *Science* **2011**, *332*, 443.

(28) Cheon, J. Y.; Kim, T.; Choi, Y.; Jeong, H. Y.; Kim, M. G.; Sa, Y. J.; Kim, J.; Lee, Z.; Yang, T. H.; Kwon, K.; Terasaki, O.; Park, G. G.; Adzic, R. R.; Joo, S. H. *Sci. Rep.* **2013**, *3*, 2715.

(29) Zheng, Y.; Jiao, Y.; Jaroniec, M.; Jin, Y.; Qiao, S. Z. *Small* **2012**, *8*, 3550.

(30) Dai, L. *Acc. Chem. Res.* **2013**, *46*, 31.

(31) Paraknowitsch, J. P.; Thomas, A. *Energy Environ. Sci.* **2013**, *6*, 2839.

(32) Wang, D.-W.; Su, D. *Energy Environ. Sci.* **2014**, *7*, 576.

(33) Meier, J. C.; Galeano, C.; Katsounaros, I.; Witte, J.; Bongard, H. J.; Topalov, A. A,; Baldizzone, C.; Mezzavilla, S.; Schuth, F.; Mayrhofer, J. J. *Beilstein J. Nanotechnol.* **2014**, *5*, 44.

(34) Lai, L.; Potts, J. R.; Zhan, D.; Wang, L.; Poh, C. K.; Tang, C.; Gong, H.; Shen, Z.; Lin, J.; Ruoff, R. S. *Energy Environ. Sci.* **2012**, *5*, 7936.

(35) Sidik, R. A.; Anderson, A. B.; Subramanian, N. P.; Kumaraguru, S. P.; Popov, B. N. *J. Phys. Chem. B* **2006**, *110*, 1787.

(36) Rao, C. V.; Cabrera, C. R.; Ishikawa, Y. *J. Phys. Chem. Lett.* **2010**, *1*, 2622.

(37) Xing, T.; Zheng, Y.; Li, L. H.; Cowie, B. C. C.; Gunzelmann, D.; Qiao, S. Z.; Huang, S.; Chen, Y. *ACS Nano* **2014**, *8*, 6856.

(38) Jasinski, R. *Nature* **1964**, *201*, 1212.

(39) Tanaka, A. A.; Fierro, C.; Scherson, D.; Yeager, E. B. *J. Phys. Chem.* **1987**, *91*, 3799.

(40) Gupta, S.; Tryk, D.; Bae, I.; Aldred, W.; Yeager, E. *J. Appl. Electrochem.* **1989**, *19*, 19.

(41) Proietti, E.; Jaouen, F.; Lefèvre, M.; Larouche, N.; Tian, J.; Herranz, J.; Dodelet, J.-P. *Nat. Commun.* **2011**, *2*, 416.

(42) Shui, J.; Chen, C.; Grabstanowicz, L. Zhao, D.; Liu, D.-J. *Proc. Natl. Acad. Sci. U. S. A.* **2015**, *112*, 10629.

2. Impact of Framework Structure of Ordered Mesoporous Carbons on the Performance of Supported Platinum Catalyst for Oxygen Reduction Reaction

2.1. Introduction

Low temperature fuel cells based on fuel (hydrogen and alcohols such as methanol) oxidation and oxygen reduction are representative of environmentally benign energy conversion technologies, and they have been of considerable interest as a promising solution to the replacement of fossil fuel-based energy conversion systems.[1-4] Platinum and platinum alloys are used as catalysts for fuel oxidation and oxygen reduction reactions, and the usage of expensive Pt-based catalysts in fuel cells can be minimized by supporting them on high surface area carbon. In addition to high surface area, which can be obtained through high porosity, a carbon support should have sufficient electrical conductivity to provide an electron path.[5-8]

To fully utilize the high surface area, carbon supports should have a high percentage of mesopores, which can provide a highly accessible surface area to the catalyst. Therefore, it is natural for ordered mesoporous carbons (OMCs) to emerge as a new class of fuel cell catalyst support materials.[9,10] OMCs have unique properties, such as a large surface area of up to 2000 $m^2 g^{-1}$, uniform pore diameters of 2–20 nm, and controllable pore interconnectivity, in addition to high chemical, thermal, and mechanical stability.[11,12] Since the application of OMCs as a Pt catalyst support was first reported,[9] there have been numerous studies on the activities of OMC-supported Pt (Pt/OMC) catalysts for fuel oxidation and oxygen reduction.[13-45] Previous works related to Pt/OMC-based catalysts have focused on enhancing their electrocatalytic activity for fuel oxidation or oxygen reduction reactions by tailoring the structural factors of the OMC supports, which include control of the framework graphiticity,[13,16,21,27,30,38,42] pore connectivity,[18,19,22,23,32,41,44] particle size,[25] doping of heteroelements,[26,33,35-37] and surface functionalization.[15,40,45]

Although the durability of Pt catalysts supported on carbon is of tremendous importance for the commercialization of fuel cells, along with their catalytic activity for fuel oxidation and oxygen reduction, there have been only a few reports on the durability of Pt/OMCs, especially in terms of their use in oxygen reduction reaction (ORR).[30,33,37,38,42] Moreover, there have been no reports, to our knowledge, in which the oxygen reduction activity and durability of Pt catalysts supported on different kinds of OMCs are systematically analyzed and compared.

In the present work, we investigated the effect of different framework structures of OMCs on the activity and durability for the ORR by comparing the electrochemical behaviors of Pt nanoparticle catalysts supported on these different OMC supports. For this purpose, three representative OMCs were used as support materials: CMK-3, CMK-3G, and CMK-5. These OMCs were prepared from the

same SBA-15 mesoporous silica template, which has a hexagonal mesostructure, and yet each OMC had a distinguishable framework structure. Hence, these carbons can be used as excellent model systems for a comparative investigation of catalytic activity and durability. We also examined the activity and durability of a Pt catalyst on activated carbon (Ketjen black®) to further investigate the effect of different carbon pore textures.

2.2. Experimental Section

2.2.1. Synthesis of ordered mesoporous silica SBA-15

Hexagonally ordered mesoporous silica SBA-15 was synthesized following the previously described method, except the modification of hydrothermal temperature.[46] 8.0 g of Pluronic P123 (M_w = 5800, Aldrich), 251.4 g of deionized (DI) water, and 48.6 g of 35 % HCl (35 wt%, Samchun) were added to 500 mL polypropylene bottle, and the mixture was stirred at 35 °C. After the P123 had been completely dissolved, 17.0 g of tetraethyl orthosilicate (98 %, Aldrich) was added to the solution, and the solution was stirred again for 5 min and aged at 35 °C without stirring for 24 h. The reaction mixture was then transferred to a Teflon-lined autoclave and heated at 150 °C for 24 h. The resulting white-colored precipitates were filtered and washed with DI water twice, and then dried in an oven at 60 °C for 1 d. Finally, the dried sample was calcined at 550 °C for 5 h in air.

2.2.2. Synthesis of ordered mesoporous carbons

CMK-3 mesoporous carbon, with uniform carbon nanorods arranged in a hexagonal structure, was synthesized using sucrose as a carbon source and SBA-15 mesoporous silica as a template, respectively.[47] CMK-5, constructed with hexagonal arrays of uniform carbon nanopipes, was prepared using furfuryl alcohol as a carbon source and SBA-15 as a template, respectively.[9] CMK-3G, which has a mesostructure similar to that of CMK-3 but with a more graphitic framework structure, was synthesized as follows.[48,49] 1.51 g of aromatic mesophase pitch (Mitsubishi Gas Chemical Company) and 10 mL of tetrahydrofuran (OCI) were put together in a polypropylene bottle, and this precursor solution was sonicated for 1 h. After the addition of 1.0 g of SBA-15 to the precursor solution, the mixture was stirred at room temperature for 1 h. The mixture was transferred to a crucible and dried at 333 K overnight. The dried mixture was moved to a quartz tube furnace and heated at a rate of 1.4 ^{o}C min^{-1} to 623 K, which exceeds the softening point of the aromatic mesophase pitch (593 K). After maintaining the mixture at 623 K for 4 h, it was heated to 1173 K at a rate of 2.6 K min^{-1} and kept at this temperature for 2 h. The resulting CMK-3G was recovered by removal of the SBA-15 template with a hydrofluoric acid solution.

2.2.3. Preparation of supported platinum catalysts on ordered mesoporous carbons

Pt catalysts supported on the aforementioned OMCs were prepared via incipient-wetness

impregnation of the Pt precursor, followed by hydrogen reduction.[45] 0.5 g of the carbon support was mixed with 1.5 mL of acetone containing the Pt precursor, hexachloroplatinic acid ($H_2PtCl_6 \cdot 6H_2O$, Aldrich). The amount of $H_2PtCl_6 \cdot 6H_2O$ in the solution was adjusted to obtain 10 wt% Pt loading. After being dried in an oven at 60 ^oC overnight, the $H_2PtCl_6 \cdot 6H_2O$-impregnated OMC was heated in H_2 flow to 200 ^oC at a ramping rate of 0.6 ^oC min^{-1} and kept for 2 h at this temperature to reduce $H_2PtCl_6 \cdot 6H_2O$ to Pt metal particles. Hydrogen adsorbed on the Pt particles was removed by heating the sample to 350 ^oC and keeping it at this temperature for 2 h under N_2 flow. For comparison, 10 wt% Pt on a Ketjenblack® (KB) support was also prepared by the same procedure.

2.2.4. Characterization methods

X-ray diffraction (XRD) patterns of the samples were obtained with an X-ray diffractometer (Rigaku D/Max 2500V/PC) equipped with a Cu Kα source at 40 kV and 200 mA. The internal pore structure of the samples was observed by a transmission electron microscope (TEM) (JEM-2100, JEOL) at an accelerating voltage of 200 kV. The porous structure of the samples was analyzed by a nitrogen adsorption experiment at -196 ^oC using a BEL BELSORP-Max system. The surface area and pore size distribution of the samples were calculated by using the Brunauer-Emmett-Teller (BET) equation and the Barrett-Joyner-Halenda (BJH) method, respectively. The micropore size distribution and micropore volume were obtained by using the Horvath-Kawazoe (HK) equation and αs method, respectively.

2.2.5. Electrochemical measurements

Electrochemical properties such as the electrochemically active surface area (ECSA) and the ORR activity of the Pt/OMC catalysts were investigated by rotating ring-disk electrode (RRDE) measurements. To simulate the acidic environment of proton exchange membrane fuel cells, 0.1 M perchloric acid ($HClO_4$) was used as an electrolyte. A Pt wire and a hydrogen reference electrode (Hydroflex®, Gaskatel) were used as the counter and reference electrodes, respectively. The catalyst ink was prepared by mixing 10 mg of the Pt/OMC (or Pt/KB) catalyst, 0.1 mL of deionized (DI) water, 1.07 mL of ethanol, and 0.025 mL of 5 wt% Nafion® (in isopropanol, Aldrich) and dispersed homogenously by sonicating the mixture for 30 min. 3.0 μL of the ink was dropped and dried to form a thin film on a glassy carbon disk electrode with a 0.126 cm^2 geometric surface area. Before the measurement, electrochemical cleaning was performed by sweeping potentials between 0.05 and 1.2 V at a scan rate of 100 mV s^{-1} for 50 cycles in N_2-saturated 0.1 M $HClO_4$. Cyclic voltammetry (CV) was performed in the potential range from 0.05 to 1.2 V at a scan rate of 20 mV s^{-1} in N_2-saturated 0.1 M $HClO_4$. The ORR activity evaluation was carried out by linear sweep voltammetry (LSV) in the anodic direction from 0.2 to 1.1 V with rotating speeds of (100, 400, 900, 1600, and 2500 rpm) at a scan rate of 5 mV s^{-1} in O_2-saturated 0.1 M $HClO_4$. The accelerated durability test (ADT) of the

catalysts was performed to investigate the electrochemical durability of the catalysts. The potential was cycled in N_2-saturated 0.1 M $HClO_4$ between 0.6 and 1.2 V at a scan rate of 50 mV s^{-1} for 2000 cycles.

2.3. Results and Discussion

2.3.1. Synthesis and characterization of OMC supports

The three types of OMCs (CMK-3, CMK-5, and CMK-3G) were prepared via a nanocasting method using SBA-15 as a hard template, as illustrated in Figure 2.1. CMK-3 was synthesized by complete filling of the SBA-15 template with the carbon precursor, whereas CMK-5 was synthesized by the surface templating method, in which the SBA-15 template was functionalized with aluminum acid sites. CMK-3G, which was a graphitized version of CMK-3, was synthesized by using aromatic mesophase pitch as a carbon precursor and a subsequent heat treatment. Therefore, these three carbons all had hexagonal mesostructures but different carbon framework structures and graphiticity, which could affect their surface area, microporosity, and electrical conductivity. We examined how these differences in the structural properties of the OMC supports affected the catalytic activity and durability in the ORR by the Pt/OMC catalysts.

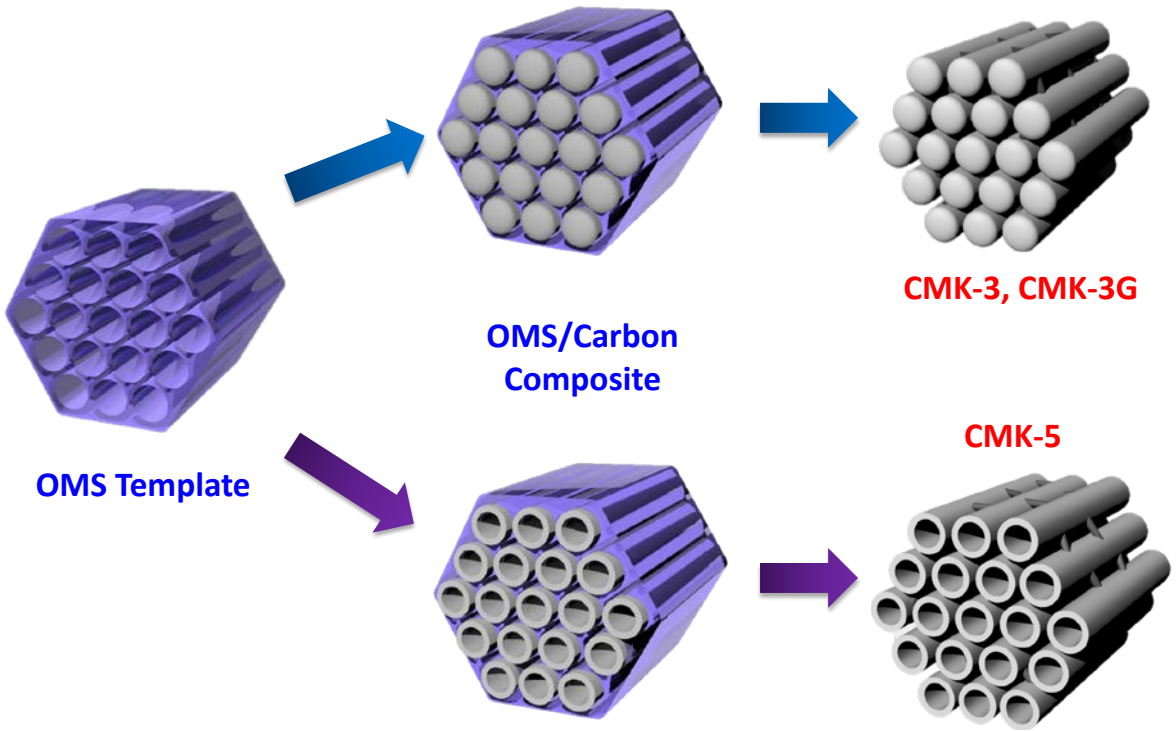

Figure 2.1. Schematic illustration of the nanocasting processes for the three OMCs (CMK-3, CMK-3G, and CMK-5) from the SBA-15 template.

The TEM image of the SBA-15 template (Figure 2.2a), taken along the pores, shows a hexagonal array of uniform mesopores 12 nm in diameter. The TEM images of CMK-3 and CMK-3G (Figure 2.2b and c) clearly show a hexagonal array of uniform carbon nanorods, indicating that the

pores and silica walls of the SBA-15 template were faithfully replicated into the carbon nanorods and mesopores of the OMCs, respectively. The TEM image of CMK-5 (Figure 2.2d) shows hexagonally ordered arrays of circles that can be interpreted as a projection of the CMK-5 structure (Figure 2.1) in the direction parallel to the pore channels. As reported earlier, CMK-5 had two different types of mesopores, one from the porous interior of the nanopipes (white circles) and the other originating from the space between the adjacent nanopipes.[9] A magnified TEM image of CMK-3G parallel to the pore direction (Figure 2.2c, inset) shows the parallel ordering of graphene layers that are orthogonal to the surface of the template.[47] This microstructure of the CMK-3G framework is clearly different from that of CMK-3 and CMK-5, both of which have a rather amorphous-carbon-like framework.

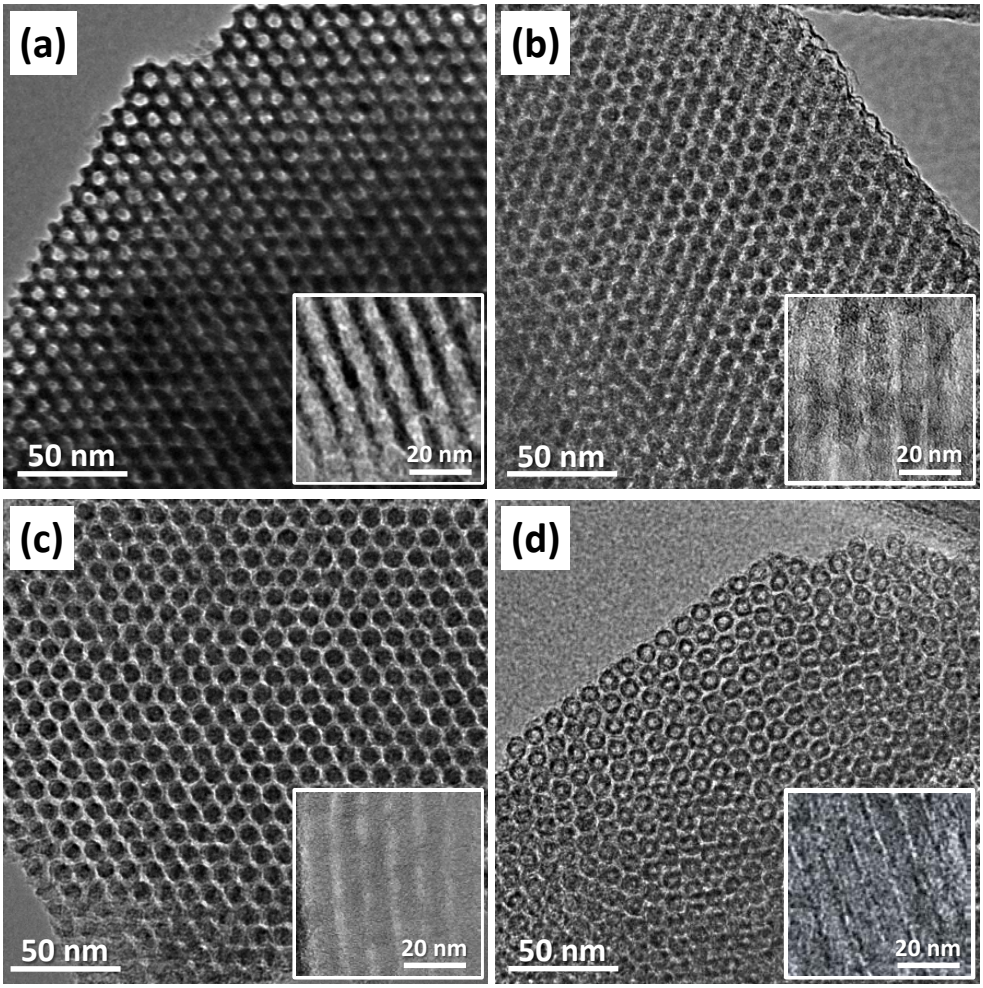

Figure 2.2. TEM images of SBA-15 template and OMCs: (a) SBA-15, (b) CMK-3, (c) CMK-3G, and (d) CMK-5. The inset Figures show high-magnification TEM images of SBA-15 and OMCs parallel to the pore direction.

The ordered mesostructure and framework microstructure of the three OMCs and KB carbon were investigated by small- and wide-angle XRD patterns, respectively (Figure 2.3). The small-angle XRD patterns of the SBA-15 template, CMK-3, and CMK-3G show three distinct diffraction lines

below 2°, which correspond to the (100), (110), and (200) diffractions for the two-dimensional (2D) hexagonal *p6mm* space group.[47,48] The XRD pattern for CMK-5 shows three peaks at similar positions, yet it exhibits a significant difference in diffraction intensity as compared to CMK-3 and CMK-3G.[9] The highly pronounced (100) peak observed in the XRD pattern of CMK-3 dramatically decreases in CMK-5, and the (110) peak was found to be the most intense peak for CMK-5. The weak intensity of the (100) reflection in comparison to that of the (110) reflection is attributed to the diffraction interference between the nanopipe walls and the spacers interconnecting adjacent pipes. The microstructure of the carbon framework was further confirmed by the wide-angle XRD patterns shown in Figure 2.3b. The wide-angle XRD patterns show two major peaks at around 2θ = 26° and 45°, which correspond to the (002) and (101) diffractions of the graphitic frameworks, respectively. The wide-angle XRD patterns of CMK-3 and CMK-5 show very broad peaks, indicative of the amorphous nature of the framework microstructures. In contrast, CMK-3G and KB carbon exhibit much sharper diffraction peaks than CMK-3 or CMK-5, indicating their highly graphitic framework. These wide-angle XRD results are consistent with the TEM images presented in the insets of Figure 2.2.

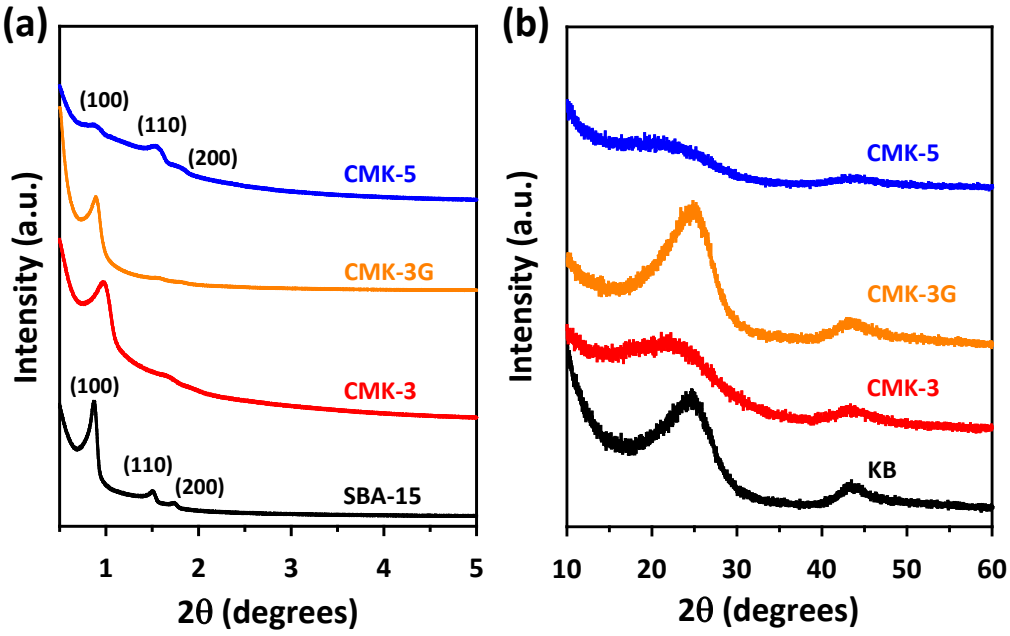

Figure 2.3. (a) Small-angle and (b) wide-angle XRD patterns of SBA-15, OMCs, and KB carbon.

The textural properties of the OMCs and KB carbon were determined from nitrogen physisorption analysis (Figure 2.4 and Table 2.1). The nitrogen adsorption-desorption isotherms for the three OMCs exhibit pronounced hysteresis loops at a relative pressure range of 0.4-0.7, which can be attributed to capillary condensation-evaporation from the mesopores, whereas KB carbon shows a less pronounced hysteresis loop at that same relative pressure range. These results were further

confirmed by the pore size distribution curves, which are shown in Figure 2.4b. The three OMCs show a sharp peak at approximately 5 nm, which corresponds to primary mesopores. In contrast, KB carbon exhibits a featureless peak in the mesoporous regime, indicating its microporous nature. The BET surface areas and total pore volumes of the carbons were 1180 m^2 g^{-1} and 1.33 cm^3 g^{-1} for CMK-3, 400 m^2 g^{-1} and 0.75 cm^3 g^{-1} for CMK-3G, 1730 m^2 g^{-1} and 2.63 cm^3 g^{-1} for CMK-5, and 744 m^2 g^{-1} and 0.76 cm^3 g^{-1} for KB carbon, respectively. It is interesting to note that CMK-3G had a much smaller specific surface area than CMK-3, despite the structural similarity between them. This can be attributed to the fact that the carbon precursor of CMK-3G, aromatic mesophase pitch, contained a considerable amount of large polyaromatic compounds, which endowed CMK-3G with very low microporosity after carbonization. On the other hand, CMK-3, synthesized from sucrose, showed a large number of micropores contained in the mesopore walls, which contributed to its large specific surface area.[47] These characteristics were clearly demonstrated by the micropore analysis (Figure 2.4b and Table 2.1). Figure 2.4b displays the micropore size distribution curves obtained by using the HK algorithm. All the carbons exhibited irregular micropore size distributions at 0.6-1.0 nm. The micropore volumes of the carbons analyzed by the α_s method were 0.22 cm^3 g^{-1}, 0.01 cm^3 g^{-1}, 0.05 cm^3 g^{-1}, and 0.11 cm^3 g^{-1} for CMK-3, CMK-3G, CMK-5, and KB carbon, respectively. CMK-3G exhibited the lowest micropore volume, which can be attributed to its highly graphitized carbon framework, which is consistent with the TEM results and the wide-angle XRD analyses. It should be noted that CMK-3 had a higher micropore volume than CMK-5, which can be ascribed to the thickness of the mesopore walls of CMK-3. The carbon rods of CMK-3 were approximately 8 nm thick, whereas the carbon walls in the nanopipes of CMK-5 were only 2-3 nm thick.

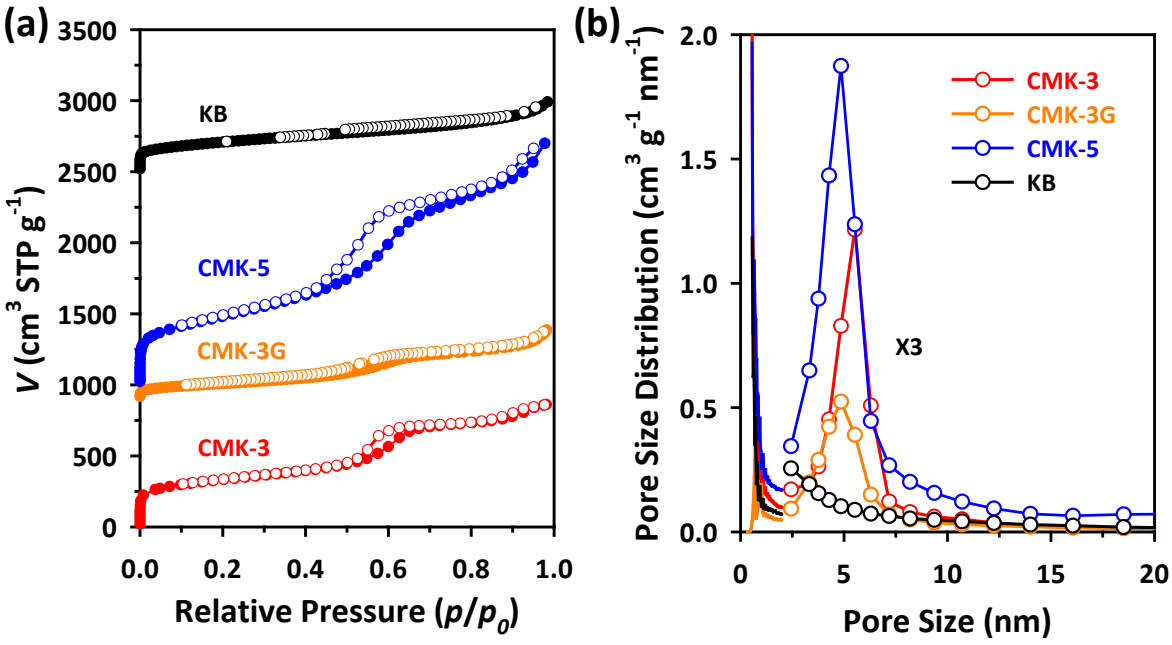

Figure 2.4. (a) N_2 adsorption-desorption isotherms and (b) the corresponding micro- (below 2 nm) and mesopore- (above 2 nm) size distribution curves.

Table 2.1. Textural parameters of OMCs and KB carbon.

Sample	BET surface area (m^2 g^{-1})[a]	Total pore volume (cm^3 g^{-1})[b]	Mesopore volume (cm^3 g^{-1})[c]	Micropore volume (cm^3 g^{-1})[d]	Mesopore size (nm)[e]	Micropore size (nm)[f]
CMK-3	1180	1.33	1.13	0.22	5.5	0.66
CMK-3G	400	0.75	0.76	0.01	4.8	0.71
CMK-5	1730	2.63	2.43	0.05	4.8	0.66
KB	744	0.76	0.58	0.11	-	0.64

[a]BET specific surface area calculated in the range of p/p_0 = 0.05 - 0.2.
[b]Total pore volumes calculated from the amount of N_2 adsorbed at a relative pressure of 0.98.
[c]Mesopore volume obtained by the BJH method.
[d]Micropore volume estimated from α_s plot.
[e]Primary mesopore size calculated by the BJH method from the adsorption branches.
[f]Micropore size determined by the HK method.

2.3.2. Preparation and characterization of Pt/OMC and Pt/KB catalysts

The three OMCs and KB carbon were used as catalyst supports for Pt nanoparticles. The Pt/OMC (or Pt/KB) catalysts were prepared via the impregnation of the Pt precursor followed by hydrogen reduction. The Pt content was controlled to be low enough to circumvent the particle size effect on the ORR activity and durability of Pt/OMCs. Because the amount of Pt loading on a carbon support is subject to the surface area of the carbon support, a study in which the catalytic activity of Pt nanoparticles on different kinds of carbon supports are compared would be flawed if the Pt particle size was not identical. It was confirmed that the ORR activity of a Pt/OMC catalyst depends significantly on the Pt particle size.[28] In addition, it is well known that the long intercrystalline distance of Pt particles is preferable for the correct evaluation of ORR activity.[50] In this sense, the Pt loading was adjusted to 10 wt%, and the TEM images of the Pt/OMCs and Pt/KB (Figure 2.5) indeed show that very small Pt nanoparticles of a similar size were uniformly dispersed, regardless of the type of carbon support. The average size of the Pt nanoparticles was approximately 1 nm; the actual values were 1.0, 0.9, 0.9, and 1.1 nm for CMK-3, CMK-3G, CMK-5, and KB carbon, respectively. The XRD patterns of the Pt/OMCs and Pt/KB are shown in Figure 2.6. All catalysts exhibit only one very broad peak at approximately 40° due to the fact that the size of the Pt nanoparticles was as small as 1 nm, which is consistent with the TEM images and the particle-size distributions presented in Figure 2.5.

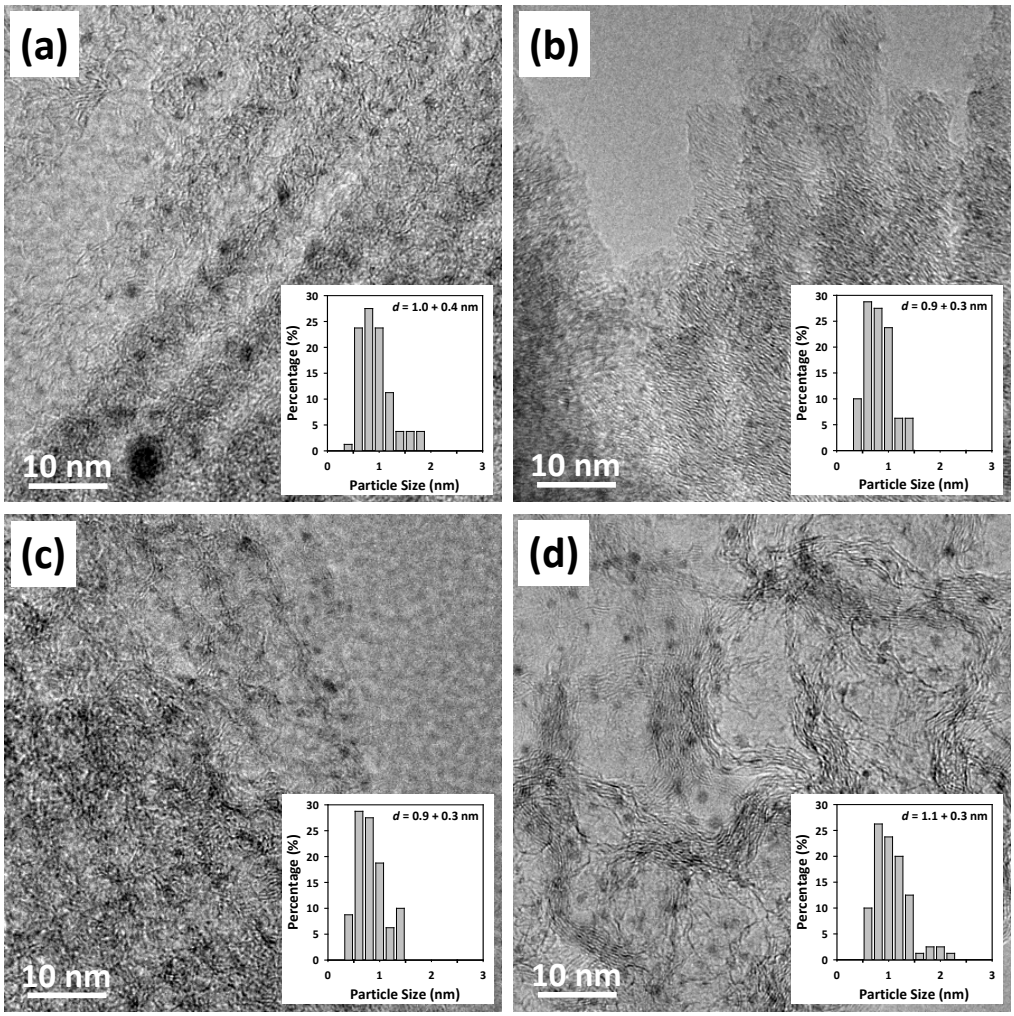

Figure 2.5. TEM images of (a) Pt/CMK-3, (b) Pt/CMK-3G, (c) Pt/CMK-5, and (d) Pt/KB, and their corresponding Pt particle size distribution plots (inset).

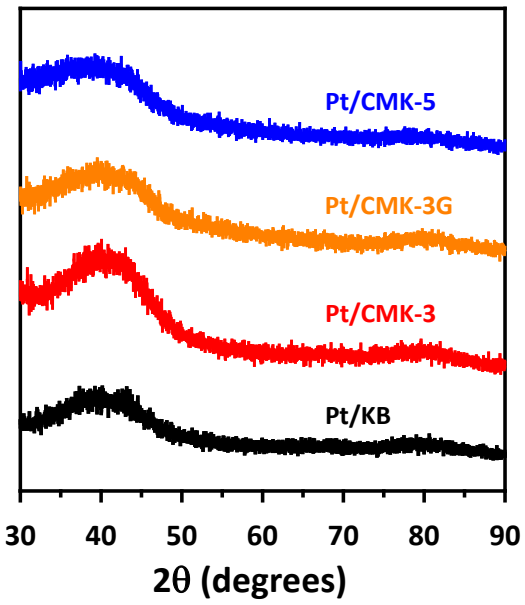

Figure 2.6. XRD patterns of Pt/OMCs and Pt/KB.

2.3.3. Electrochemical activity and durability of Pt/OMC and Pt/KB catalysts

The electrochemical properties of the Pt/OMC and Pt/KB catalysts were investigated by CV and LSV techniques, which were carried out before and after the ADTs. The CVs of the catalysts were measured using a N_2-saturated 0.1 M $HClO_4$ electrolyte in the potential range from 0.05 to 1.2 V at a scan rate of 20 mV s^{-1} (Figure 2.7). The catalysts showed slightly different voltammograms, with typical Pt oxidation and reduction peaks. One distinctive difference was the magnitude of the double layer charging current density, which is generally proportional to the surface area of the carbon supports, as shown in Table 2.1. The oxidation peak originating from the desorption of the adsorbed hydrogen, which is usually observed between 0.05 and 0.4 V, can be resolved into two peaks depending on the degree of exposure of the Pt crystalline facets.[51] Pt/CMK-3, Pt/CMK-5, and Pt/KB showed a broad featureless peak, indicating that the Pt nanoparticles in these catalysts had a polycrystalline Pt surface due to their spherical shape. In contrast, Pt/CMK-3G exhibited two resolved peaks corresponding to hydrogen adsorption and desorption, which is related to the fact that the Pt particles supported on CMK-3G had a better-developed crystalline Pt surface as compared to the other catalysts. The formation of well-faceted surfaces in Pt/CMK-3G may originate from the epitaxial growth of Pt nanoparticles on the graphitic layers in CMK-3G.[52] This difference in crystallinity would affect the catalytic activity, as was revealed from a study of single crystal surfaces, in which the ORR activity of the Pt-based catalysts was found to be highly sensitive to the crystal structure of the Pt surface.[53] In the cathodic scan, the CV shows a peak at approximately 0.55-0.6 V, which corresponds to the reduction of the surface oxide on the Pt nanoparticles.[2] The peak position of the reduction of the surface oxide shifted to a more negative potential as compared to the results of previous reports on high-loading (60 wt%) Pt/OMCs,[25,28] which can be attributed to the smaller Pt nanoparticle size (ca. 1 nm) in this study than in the previous reports (ca. 3-4 nm). It is noteworthy that the peak position corresponding to the reduction of surface oxide is slightly different depending on the kind of carbon support, in spite of the fact that the Pt nanoparticles are of similar size regardless of the type of carbon support. For example, the peaks for Pt/CMK-3G and Pt/KB were positively shifted by ca. 50 mV in comparison to that for Pt/CMK-3 and Pt/CMK-5. This shift possibly indicates that the adsorption strength of OH_{ads} species on Pt/CMK-3G and Pt/KB is weaker than that on Pt/CMK-3 and Pt/CMK-5. The strong adsorption of reactive intermediates such as OH_{ads} on Pt surfaces is known to have an adverse effect on the ORR activity by decreasing the number of adsorption sites for incoming oxygen molecules.[54-56] Thus, one might expect that this effect is associated with the catalytic activity of the catalysts under investigation.

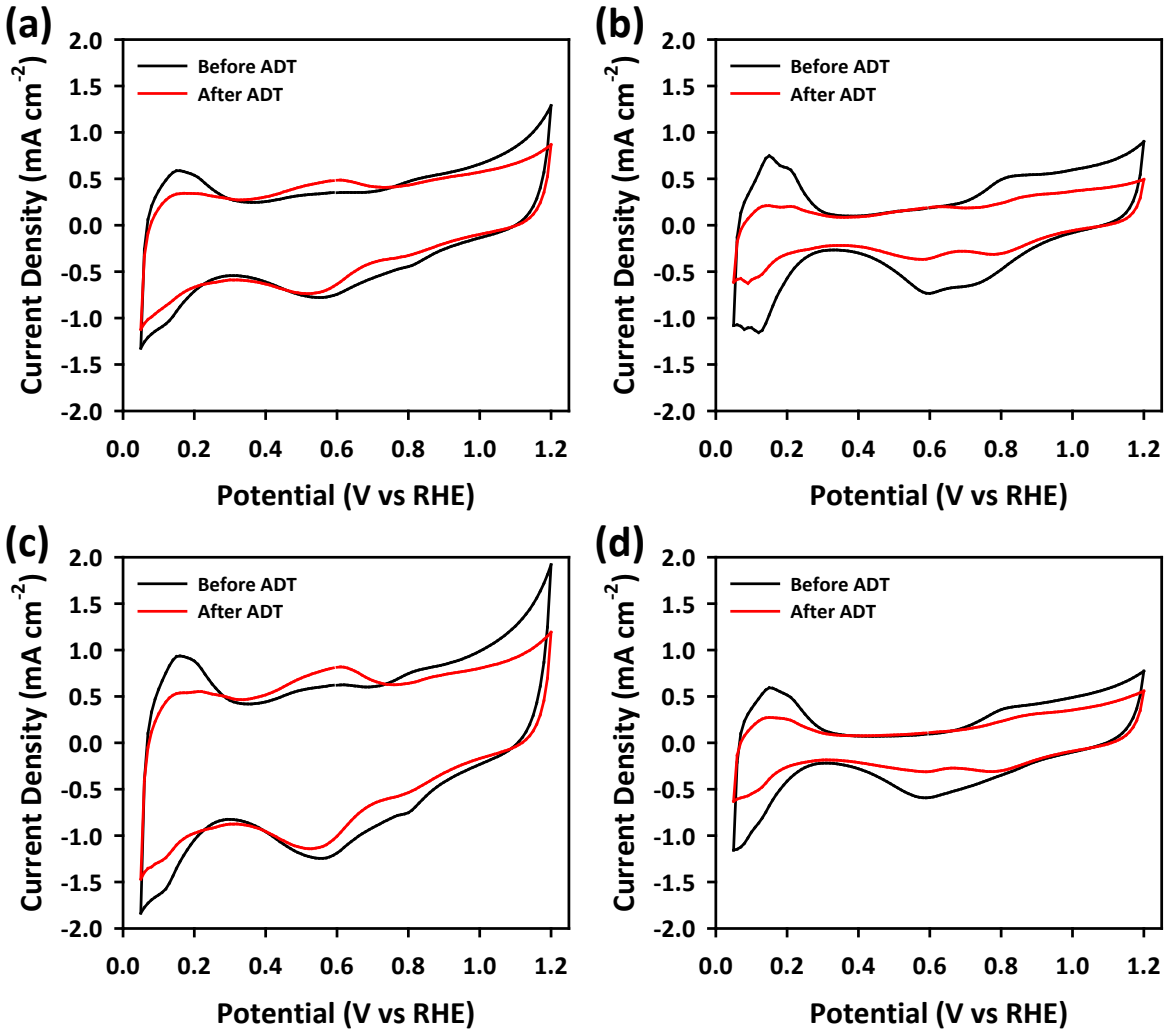

Figure 2.7. Cyclic voltammograms of Pt/OMCs and Pt/KB catalysts before (black) and after (red) ADTs: (a) Pt/CMK-3, (b) Pt/CMK-3G, (c) Pt/CMK-5, and (d) Pt/KB.

The ECSAs of the Pt nanoparticles were calculated from the area of the anodic peak corresponding to the hydrogen desorption (between 0.05 and 0.4 V) after correcting for the double layer charging current by using the following equation:

$$\mathrm{ECSA} = \frac{Q_{\mathrm{H}}}{L \times q_{\mathrm{H}}}$$

where Q_{H} is the charge for the hydrogen desorption (μC cm^{-2}), L is the mass of Pt loaded on the working electrode (g m^{-2}), and q_{H} is the charge required to oxidize a monolayer of hydrogen on Pt (210 μC cm^{-2}). The ECSAs of the Pt/OMC and Pt/KB catalysts are summarized in Table 2.2. The ECSA of the Pt/CMK-3G catalyst was the highest (107 m^2 g^{-1}), whereas that of Pt/CMK-3 was the lowest (55 m^2 g^{-1}) among the catalysts. These results indicate that the ECSA values, which can be directly correlated with the Pt nanoparticle utilization, depend on the pore structure (the number of mesopores and micropores) of the carbon supports. The micropore volume in particular is closely

related to the Pt utilization because Pt nanoparticles embedded within micropores are hardly accessible to a liquid electrolyte.[57,58] That is, a carbon framework such as CMK-3, which contains a large number of micropores, can encapsulate a significant number of Pt nanoparticles, such that they become inaccessible to incoming protons, thereby decreasing the ECSA value of the corresponding catalyst. On the other hand, CMK-3G, with the fewest number of micropores, showed the largest ECSA among the four kinds of Pt/C catalysts, despite its relatively small surface area.

Table 2.2. Comparison of ECSA and ORR activities of the catalysts before and after ADTs.

Sample	ECSA ($m^2 g_{Pt}^{-1}$)	i_k@0.9 V ($mA\ cm^{-2}$)[a]	$i_{k,f} / i_{k,i} * 100$[b]	MA @ 0.9 V ($A\ mg_{Pt}^{-1}$)[c]	$E_{1/2}$ (V)[d]	$\Delta E_{1/2}$ (mV)[e]
Pt/CMK-3	55	0.57		0.029	0.842	
Pt/CMK-3 after ADT	11	0.50	87.8 %	0.026	0.822	20
Pt/CMK-3G	107	1.92		0.098	0.862	
Pt/CMK-3G after ADT	22	1.51	78.6 %	0.077	0.852	10
Pt/CMK-5	81	1.35		0.069	0.858	
Pt/CMK-5 after ADT	13	1.10	81.5 %	0.056	0.845	13
Pt/KB	94	1.29		0.066	0.855	
Pt/KB after ADT	35	0.77	59.7%	0.039	0.833	22

[a]Kinetic current density at 0.9 V calculated with mass-transport correction.
[b]Ratio of kinetic current densities measured after and before the ADT.
[c]MA (mass activity) estimated from kinetic current at 0.9 V normalized to the Pt loading of the disk electrode.
[d]Half-wave potential obtained at which the measured current is equal to one half of diffusion-limited current value.
[e]Difference between half-wave potential values measured before and after the ADT.

The electrocatalytic activities of the Pt/OMC and Pt/KB catalysts for the ORR were investigated by using a RRDE method. Figure 2.8 shows the LSVs of the Pt/OMC and Pt/KB catalysts before and after the ADTs in the potential range from 0.2 to 1.1 V at a scan rate of 5 mV s^{-1} at 1600 rpm. The four catalysts exhibited a similar ORR on-set potential at 0.95 V and a well-defined plateau corresponding to the diffusion-limiting current between 5.6 and 6.0 mA cm^{-2}. The detailed electrochemical properties and ORR activities of the Pt/OMC and Pt/KB catalysts, such as the kinetic current density, mass activity, and half-wave potential, are summarized in Table 2.2. The mass

transport-corrected kinetic current densities at 0.9 V of the catalysts were 0.57, 1.92, 1.35, and 1.29 mA cm^{-2} for Pt/CMK-3, Pt/CMK-3G, Pt/CMK-5, and Pt/KB, respectively. Thus, the Pt/CMK-3G catalyst exhibited the highest kinetic current density at 0.9 V, followed by Pt/CMK-5, Pt/KB, and Pt/CMK-3. The mass activity and half-wave potential of the catalysts exhibited exactly the same trend. Taking into account the similar sizes of the Pt nanoparticles of the four catalysts, the higher catalytic activity of Pt/CMK-3G can be attributed to its distinctive differences from the other catalysts. First, as discussed earlier, the Pt nanoparticles in the Pt/CMK-3G catalyst were more crystalline than the other catalysts. Jaramillo and co-workers reported that spherical Pt nanoparticles have a significant radius of curvature that leads to a large fraction of undercoordinated sites on the surface of the nanoparticles,[59] on which reactive intermediates such as O_{ads} and OH_{ads} make a much stronger bond. Accordingly, these intermediates are known to have a negative impact on the ORR activity.[54-56] The Pt/CMK-3G catalyst, with its much more pronounced crystalline surfaces, had a lower adsorption strength of surface oxide as compared to the other catalysts, which was confirmed by the CV measurements. Another possible reason for the high catalytic activity of the Pt/CMK-3G catalyst is its graphitic carbon framework. This microstructure could facilitate electron transfer between the Pt nanoparticles and the carbon support during the ORR process, which would result in the higher ORR activity of the catalyst.

To gain insight into the durability of the four Pt/C catalysts, we performed cycling tests in the potential range from 0.6 to 1.2 V at a scan rate of 50 mV s^{-1} for 2000 cycles. The electrochemical behaviors of the four catalysts after the ADTs are shown with red lines or dashed lines in Figures 2.7 and 2.8. After the ADTs, all four catalysts exhibited a marked reduction in the areas of hydrogen desorption peaks ranging from 0.05 to 0.4 V (Figure 2.7). Considering the fact that the recycling condition of the ADT was highly demanding (up to 1.2 V), the carbon supports may corrode during the ADT, which concomitantly accelerates the agglomeration and Ostwald ripening of Pt nanoparticles.[60,61] It should be noted that after the ADT, there was a clear distinction in the cyclic voltammograms of the four catalysts during the positive sweep from 0.3 to 0.7 V; Pt/CMK-3 and Pt/CMK-5 had a newly developed peak in this potential range, whereas Pt/CMK-3G and Pt/KB exhibited CV shapes virtually identical to those measured before the ADTs. The generation of the new peak could be associated with the oxidation of the carbon frameworks, as reported earlier.[33,62] Hence, these results could be correlated with the microstructure of the carbon framework, indicating that highly graphitized carbons such as CMK-3G or KB carbons are more resistant to the formation of surface oxygen functional groups during the potential cycling as compared to CMK-3 and CMK-5, which have amorphous-carbon-like frameworks.

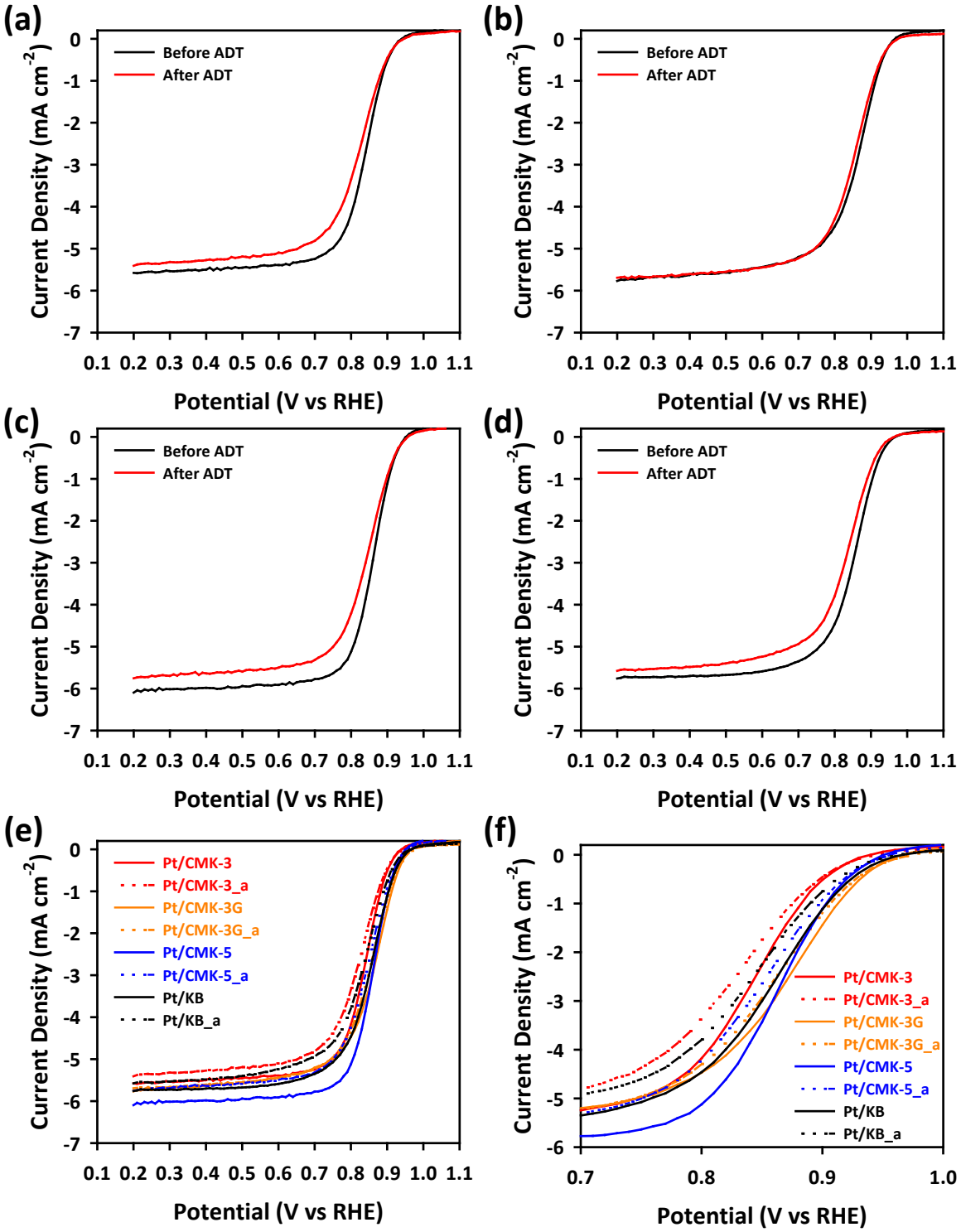

Figure 2.8. ORR polarization curves of Pt/OMCs and Pt/KB catalysts before (black) and after (red) ADTs: (a) Pt/CMK-3, (b) Pt/CMK-3G, (c) Pt/CMK-5, and (d) Pt/KB; (e) merged polarization curves for all catalysts; (f) enlarged polarization curves around 0.9 V.

The changes in ORR catalytic activity after the ADTs were compared for each type of catalyst in Figure 2.8 and Table 2.2. As compared to the other catalysts, the Pt/CMK-3G catalyst showed the highest ORR activity after the ADT, with a minimal 10 mV shift in half-wave potential.

The trends of kinetic current density and mass activity among the catalysts after the ADTs generally followed those measured before the ADTs. Particularly noteworthy is that the OMC-supported catalysts underwent a less significant decrease in current density (or mass activity) than the KB-supported catalyst after the ADTs, indicating the stable nature of the mesoporous architecture of the OMCs during the ADTs. This feature was confirmed again in the comparison of changes in half-wave potentials (Figure 2.9), which revealed that Pt/CMK-3G had a minimal change in half-wave potential, whereas Pt/KB showed the largest decrease. The higher durability of Pt/CMK-3G can be attributed to its graphitic carbon framework, which improves the chemical and electrochemical stability due to a decrease in the number of defect sites of the carbon structure where carbon oxidation begins.[61] In addition, the graphitization results in the increasing strength of π electron sites on the support, which act as anchoring centers for Pt, thus strengthening the metal-support interaction and the resistance of Pt to sintering.[52]

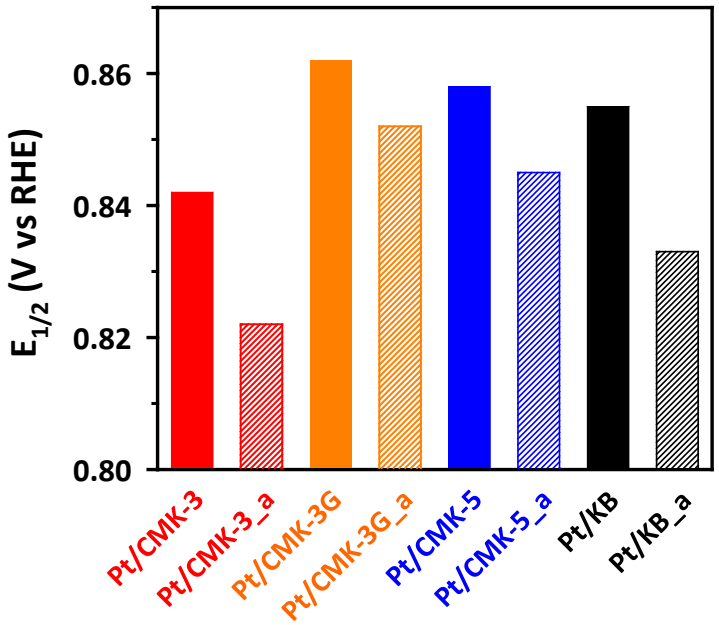

Figure 2.9. Half-wave potentials of Pt/OMCs and Pt/KB before and after ADTs.

Finally, we also note that the micropore volume of each type of carbon can be correlated with its catalytic activity and durability. Figure 2.10 shows the correlation between the mass activity (at 0.9 V) of the four catalysts and the micropore volume of the carbon supports. This relationship clearly establishes that the mass activity of the catalysts is nearly inversely proportional to the micropore volume of carbon supports.

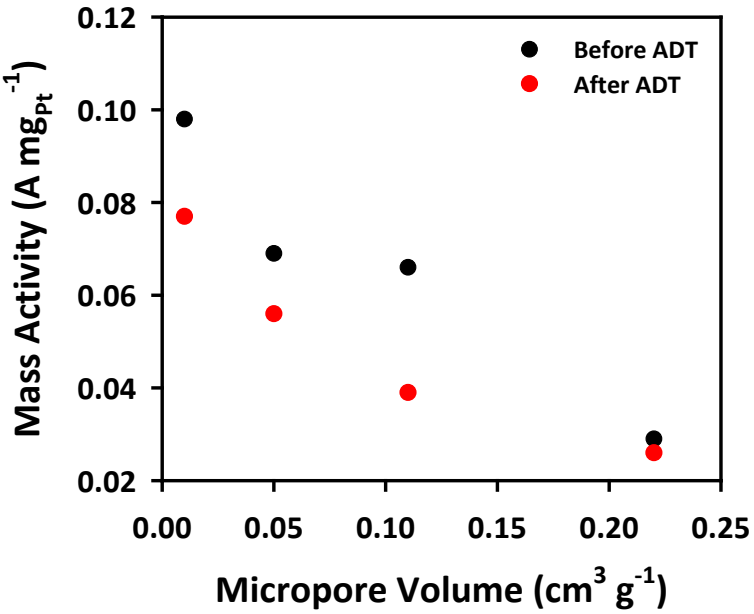

Figure 2.10. Mass activity vs. micropore volume of Pt/OMCs and Pt/KB before (black) and after (red) ADTs.

2.4. Conclusions

A systematic investigation into the impact of the framework structure of OMCs on the activity and durability of Pt/OMC catalysts for the ORR was carried out. For this purpose, three OMCs with a varying degrees of graphiticity, surface area, and microporosity (CMK-3, CMK-3G, and CMK-5) were prepared from the same SBA-15 mesoporous silica template. Pt particles with an average size of 1 nm were uniformly dispersed on these OMCs and on KB carbon. Pt/CMK-3G exhibited the highest kinetic current density at 0.9 V, followed by Pt/CMK-5, Pt/KB, and Pt/CMK-3. The mass activity and half-wave potential of the catalysts exhibited the same trend. Furthermore, Pt/CMK-3G showed the highest ORR activity after an ADT, with a minimal 10 mV shift in half-wave potential. The higher ORR activity of Pt/CMK-3G could be attributed to the formation of highly crystalline Pt particles as well as the highly graphitic, crystalline framework structure, which caused the weak adsorption of surface oxide and strong interaction between the Pt particles and the supports. Moreover, the micropore volume of each type of carbon could be correlated with its catalytic activity and durability, which established that the mass activity of the catalysts was nearly inversely proportional to the micropore volume of the carbon supports.

2.5. References

(1) Steele, B. C. H.; Heinzel, A. *Nature* **2001**, *414*, 345.

(2) Gasteiger, H. A.; Kocha, S.S.; Sompalli, B.; Wagner, F. T. *Appl. Catal. B* **2005**, *56*, 9.

(3) Rabis, A.; Rodriguez, P.; Schmidt, T. J. *ACS Catal.* **2012**, *2*, 864.

(4) Debe, M. K. *Nature* **2012**, *486*, 43.

(5) Yu, X.; Ye, S. *J, Power Sources* **2007**, *172*, 133.

(6) Antolini, E. *Appl. Catal. B Environ.* **2009**, *88*, 1.

(7) Shao, Y.; Liu, J.; Wang, Y.; Lin, Y. *J. Mater. Chem.* **2009**, *19*, 46.

(8) Shrestha, S.; Liu, Y.; Mustain, W. E. *Catal. Rev.* **2011**, *53*, 256.

(9) Joo, S. H.; Choi, S. J.; Oh, I.; Kwak, J.; Liu, Z.; Terasaki, O.; Ryoo, R. *Nature* **2001**, *412*, 169.

(10) Chang, H.; Joo, S. H.; Pak, C. *J. Mater. Chem.* **2007**, *17*, 3078.

(11) Ryoo, R.; Joo, S. H; Kruk, M.; Jaroniec, M. *Adv. Mater.* **2001**, *13*, 677.

(12) Lee, J.; Kim, J.; Hyeon, T. *Adv. Mater.* **2006**, *18*, 2073.

(13) Su, F.; Zeng, J.; Bao, X.; Yu, Y.; Lee, J. Y; Zhao, X. S. *Chem. Mater.* **2005**, *17*, 3960.

(14) Choi, W. C.; Woo, S. I.; Jeon, M. K.; Sohn, J. M.; Kim, M. R.; Jeon, H. J. *Adv. Mater.* **2005**, *17*, 446.

(15) Choi, Y.S; Joo, S. H.; Lee, S. A.; You, D. J.; Kim, H.; Pak, C.; Chang, H.; Seung, D. *Macromolecules* **2006**, *39*, 3275.

(16) Joo, S. H.; Pak, C.; You, D. J.; Lee, S. A.; Lee, H. I.; Kim, J. M.; Chang, H.; Seung, D. *Electrochim. Acta* **2006**, *52*, 1618.

(17) Liu, S. H.; Lu, R. F.; Huang, S. J.; Lo, A. Y.; Chien, S. H.; Liu, S. B. *Chem. Commun.* **2006**, 3435.

(18) Ren, J.; Ding, J.; Chan, K. Y.; Wang, H. *Chem. Mater.* **2007**, *19*, 2786.

(19) Zhao, G.; He, J.; Zhang, C.; Zhou, J.; Chen, X.; Wang, T. *J. Phys. Chem. C* **2008**, *112*, 1028.

(20) Kim, H. T.; You, D. J.; Yoon, H. K.; Joo, S. H.; Pak, C.; Chang, H.; Song, I.-S. *J. Power Sources* **2008**, *180*, 724.

(21) Shanahan, P. V.; Xu, L.; Liang, C.; Waje, M.; Dai, S.; Yan, Y. S. *J. Power Sources* **2008**, *185*, 423.

(22) Lei, Z.; Bai, S.; Xiao, Y.; Dang, L.; An, L.; Zhang, G.; Xu, Q. *J. Phys. Chem. C* **2008**, *112*, 722.

(23) Lin, M. L.; Huang, C. C.; Lo, M. Y.; Mou, C. Y. *J. Phys. Chem. C* **2008**, *112*, 867.

(24) Liu, S. H.; Yu, W. Y.; Chen, C. H.; Lo, A. Y.; Hwang, B.-J.; Chien, S.-H.; Liu, S.-B. *Chem. Mater.* **2008**, *20*, 1622.

(25) Joo, S. H.; Lee, H. I.; You, D. J.; Kwon, K.; Kim, J. H.; Choi, Y. S.; Kang, M.; Kim, J. M.; Pak, C.; Chang, H.; Seung, D. *Carbon* **2008**, *46*, 2034.

(26) Lee, H. I.; Joo, S. H.; Kim, J. H.; You, D. J.; Kim, J. M.; Park, J.-N.; Chang, H.; Pak, C. *J. Mater. Chem.* **2009**, *19*, 5934.

(27) Gupta, G.; Slanac, D. A.; Kumar, P.; Wiggins-Camacho, J. D.; Wang, X.; Swinnea, S.; More, K. L.; Stevenson, K. J.; Johnston, K. P. *Chem. Mater.* **2009**, *21*, 4515.

(28) Joo, S. H.; Kwon, K.; You, D. J.; Pak, C.; Chang, H.; Kim, J. M. *Electrochim. Acta* **2009**, *54*, 5746.

(29) Liu, S. H.; Chiang, C. C.; Wua, M. T.; Liu, S. B. *Int. J. Hydrogen Energy* **2010**, *35*, 8149.

(30) Gupta, G.; Slanac, D. A.; Kumar, P.; Wiggins-Camacho, J. D.; Kim, J. Ryoo, R.; Stevenson, K. J.; Johnston, K. P. *J. Phys. Chem. C* **2010**, *114*, 10796.

(31) Chen, M.-H.; Jiang, Y.-X.; Chen, S.-R.; Huang, R.; Lin, J.-L, Chen, S.-P.; Sun, S.-G. *J. Phys. Chem. C* **2010**, *114*, 19055.

(32) Song, S.; Liang, Y.; Li, Z.; Wang, Y.; Fu, R.; Wu, D.; Tsiakaras, P. *Appl. Catal. B* **2010**, *98*, 132.

(33) Kwon, K.; Jin, S. A.; Pak, C.; Chang, H.; Joo, S. H.; Lee, H. I.; Kim, J. H.; Kim, J. M. *Catal. Today* **2011**, *164*, 186.

(34) Calvillo, L.; Celorrio, V.; Moliner, R.; Lazaro, M. J. *Mater. Chem. Phys.* **2011**, *127*, 335.

(35) Guo, Y.; He, J.; Wang, T.; Xue, H.; Hu, Y.; Li, G.; Tang, J.; Sun, X. *J. Power Sources* **2011**, *196*, 9299.

(36) Liu, S.-H.; Chen, S.-C.; Sie, W.-H. *Int. J. Hydrogen Energy* **2011**, *36*, 15060.

(37) Liu, S.-H.; Wu, M.-T.; Lai, Y.-H.; Chiang, C.-C.; Yu, N.; Liu, S.-B. *J. Mater. Chem.* **2011**, *21*, 12489.

(38) Wu, Z.; Li, W.; Xia, Y.; Webley, P.; Zhao, D. *J. Mater. Chem.* **2012**, *22*, 8835.

(39) Liu, C.; Chen, M.; Du, C.; Zhang, J.; Yin, G.; Shi, P.; Sun, Y. *Int. J. Electrochem. Sci.* **2012**, *7*, 10592.

(40) Sun, X.; He, J.; Tang, J.; Wang, T.; Guo, Y.; Xue, H.; Li, G.; Ma, Y. *J. Mater. Chem.* **2012**, *22*, 10900.

(41) Maiyalagan, T.; Alaje, T. O.; Scott, K. *J. Phys. Chem. C* **2012**, *116*, 2630.

(42) Wu, Z.; Lv, Y.; Xia, Y.; Webley, P.; Zhao, D. *J. Am. Chem. Soc.* **2012**, *134*, 2236.

(43) Xiang, D.; Yin, L. *J. Mater. Chem.* **2012**, *22*, 9584.

(44) Zeng, J.; Francia, C.; Dumitrescu, M. A.; Monteverde Videla, A. H. A.; Ijeri, V. S.; Specchia, S.; Spinelli, P. *Ind. Eng. Chem. Res.* **2012**, *51*, 7500.

(45) Cheon, J. Y.; Ahn, C.; You, D. J.; Pak, C.; Hur, S. H.; Kim, J.; Joo, S. H. *J. Mater. Chem. A* **2013**, *1*, 1270.

(46) Kruk, M.; Jaroniec, M.; Ko, C. H.; Ryoo, R. *Chem. Mater.* **2000**, *12*, 1961.

(47) Jun, S.; Joo, S. H.; Ryoo, R.; Kruk, M.; Jaroniec, M.; Liu, Z.; Ohsuna, T.; Terasaki, O. *J. Am. Chem. Soc.* **2000**, *122*, 10712.

(48) Kim, T. W.; Park, I. S.; Ryoo, R. *Angew. Chem. Int. Ed.* **2003**, *42*, 4375.

(49) Yang, H.; Yan, Y.; Liu, Y.; Zhang, F.; Zhang, R.; Meng, Y.; Li, M.; Xie, S.; Tu, B.; Zhao, D. *J. Phys. Chem. B* **2004**, *108*, 17320.

(50) Watanabe, M.; Sei, H.; Stonehart, P. *J. Electroanal. Chem.* **1989**, *261*, 375.

(51) Vidal-Iglesias, F. J.; Aran-Ais R. M.; Solla-Gullon, J.; Herrero, E.; Feliu, J. M. *ACS Catal.* **2012**, *2*, 901.

(52) Coloma, F.; Sepulvedaescribano, A.; Rodriguezreinoso, F. *J. Catal.* **1995**, *154*, 299.

(53) Stamenkovic, V. R.; Fowler, B.; Mun, B. S.; Wang, G. F.; Ross, P. N.; Lucas, C. A.; Marković, N. M. *Science* **2007**, *315*, 493.

(54) Greeley, J.; Rossmeisl, J.; Hellman, A.; Norskov, J. K. *Z. Phys. Chem.* **2007**, *221*, 1209.

(55) Marković, N. M.; Ross, P. N. *Surf. Sci. Rep.* **2002**, *45*, 121.

(56) Tritsaris, G. A.; Greeley, J.; Rossmeisl, J.; Norskov, J. K. *Catal. Lett.* **2011**, *141*, 909.

(57) Uchida, M.; Fukuoka, Y.; Sugawara, Y.; Eda, N.; Ohta, A. *J. Electrochem. Soc.* **1996**, *143*, 2245.

(58) Gan, L.; Du, H.-D.; Li, B.-H.; Kang, F.-Y. *New Carbon Mater.* **2010**, *25*, 53.

(59) Kibsgaard, J. Gorlin, Y. Chen, Z. Jaramillo, T. F. *J. Am. Chem. Soc.* **2012**, *134*, 7758.

(60) Merzougui, B.; Swathirajan, S. *J. Electrochem. Soc.* **2006**, *153*, A2220.

(61) Shao, Y.; Yin, G.; Gao, Y. *J. Power Sources* **2007**, *171*, 558.

(62) Oh, H. S.; Kim, K.; Ko, Y. J.; Kim, H. *Int. J. Hydrogen Energy* **2010**, *35*, 701.

3. Ordered Mesoporous Carbon-Carbon Nanotube Nanocomposites as Highly Conductive and Durable Cathode Catalyst Supports for Polymer Electrolyte Fuel Cells

3.1. Introduction

Polymer electrolyte fuel cells (PEFCs), including polymer electrolyte membrane fuel cells (PEMFCs) and direct methanol fuel cells (DMFCs), are considered as promising power sources of alternative energy, due to their cleanliness and high efficiency, the reusability of exhaust heat, and the versatility for mobile, transportation, and stationary applications.[1-4] However, the widespread use of PEFCs is critically impeded since they require expensive platinum-based catalysts. Furthermore, these catalysts exhibit sluggish kinetics for oxygen reduction reaction (ORR) and low long-term stability. To circumvent this situation, multi-dimensional efforts have been made over the last decade to develop cathode electrocatalysts for PEFCs that are more active and stable, than the currently most prevalent carbon black-supported platinum (Pt/C) catalysts.[5-12] One prominent direction of research has been the development of Pt-M (M = transition metals, such as Co, Ni, Cr, and Fe, to name a few) alloy and nanoparticles with a core/shell structure for use as catalysts.[13-16] These catalysts generally show enhanced catalytic activity and stability while requiring lesser amounts of platinum.[2-5,8,11,12] Another important approach has been to use novel nanostructured carbon supports,[5-7,9-11] which have a synergistic effect on the activity and durability of Pt catalysts. These nanocarbons have included carbon nanofibers,[17] carbon nanotubes (CNTs),[9,18,19] ordered mesoporous carbons (OMCs),[20,21] macroporous carbons,[22] and graphene.[23,24]

Among the above-mentioned nanostructured carbons, OMCs that are synthesized by “hard” nanocasting[25,26] or by using micelles as templates[27] have emerged as ubiquitous materials for energy conversion and storage devices, including fuel cells,[20,21] solar cells,[28] and batteries.[29] For fuel cell applications, in particular, the OMCs have a range of advantageous characteristics: their large surface area enables high dispersion of supported metal nanoparticles while their highly interconnected, uniform mesopores allow for the efficient transports of fuels and by-products. Since Ryoo and co-workers first realized the promise of these OMCs showed as fuel cell catalyst supports,[21] number of research groups including ours have made a great deal of progress in this area.[23,24,30-72] Significant efforts have been made to maximize the catalytic activities of the OMC-based catalysts, and these efforts have included attempts to control the graphitic nature, pore sizes, and particle sizes of the OMCs as well as to modify functional groups present on their surfaces.

The use of OMCs as fuel cell catalysts, however, still poses a major challenge since these OMCs exhibit low durability.[55] In fact, the durability of electrocatalysts, along with their low activity, is one of most critical factors preventing the practical application of fuel cell systems. The degradation

of fuel cell catalysts occurs via several pathways. These include the dissolution of the Pt particles, the Ostwald ripening of the Pt particles, the corrosion of the carbon support, and the detachment and agglomeration of the Pt particles.[71] The corrosion of the carbon support occurs because of the oxidation of carbon to carbon dioxide under the typical PEFC operation conditions. This carbon corrosion can potentially result in the weakening of the interaction between the carbon support and the Pt particles, thereby leading to the detachment and agglomeration of the Pt particles. Yet, in spite of the obvious importance of OMC-based catalysts, few studies have been investigated the long-term durability of these catalysts, particularly in the single cell configuration.[57,60]

The framework of most OMC has an amorphous structure with relatively low electrical conductivity and poor mechanical strength, resulting in much inferior durability compared to graphitic carbon framework.[72] Chemical vapor deposition (CVD) methods are successful in synthesizing graphitic carbon frameworks; however, CVD method is limited by the use of specialized devices with relatively low carbon yield (less than about 5 wt%, for example, when ferrocene is used as a carbon precursor).[72] Herein, we introduce a new type of porous carbon materials, OMC-CNT nanocomposites, in which the primary particle of the OMC are highly interconnected via CNTs. The structure of the OMC-CNT nanocomposites is such that it combines the advantages of both the carbon entities and should make them particularly attractive for use in high-performance fuel cell catalysts: the OMCs can provide a large surface area, mesoporosity and interconnected porous structure, whereas the CNTs can function as electrical connectors between adjacent OMC particles, thereby lowering the interfacial resistance. Furthermore, highly graphitic nature of CNTs in OMC-CNT nanocomposites can provide superior mechanical strength compared to OMC itself.

In the present work, we report the use of OMC-CNT nanocomposites as a highly conductive and durable fuel cell catalyst supports for the first time. The OMC-CNT nanocomposites were synthesized via a nanocasting method that used ordered mesoporous silica (OMS) particles as a template and Ni-phthalocyanine as a carbon source. For comparison, two OMCs with varying degrees of conductivity, OMC(Suc) and OMC(Pc), were also prepared using sucrose and phthalocyanine, respectively. All three carbons exhibited high surface areas, high pore volumes, and uniform mesopores. The conductivity measurements revealed that the OMC-CNT nanocomposites showed the highest conductivity, followed by the OMC(Pc) and the OMC(Suc). The three carbons were used as fuel cell catalyst supports, and they could readily support Pt nanoparticles with high dispersion (ca. ~ 1.5 nm in size) that were generated via a simple impregnation-reduction method. The ORR activities and kinetics of the Pt/OMC catalysts were measured by the rotating ring-disk electrode (RRDE) technique. The Koutecky-Levich analysis as well as the H_2O_2 yield calculation of the catalysts indicated that the ORR over the Pt/OMC catalysts followed a four-electron pathway. Among the three Pt/OMC catalysts, the Pt/OMC-CNT catalyst showed activity that was superior to those of the Pt/OMC(Suc) and Pt/OMC(Pc) catalysts. This trend was even more pronounced after accelerated

durability tests (ADTs), which were performed to test the durabilities of the catalysts. In single cell tests that are more relevant with respect to the practical applications, the Pt/OMC-CNT catalyst showed a current density that was higher than those of the other two catalysts after high-voltage degradation test. The half-cell and single cell tests using the Pt/OMC catalysts indicated that the rigidly interconnected structure as well as highly conductive frameworks of the OMC-CNT nanocomposites was concomitantly responsible for their enhanced durability and single cell performance. We believe that this work provides unprecedented insights into the durability of the OMC-based catalysts under realistic, single cell operation condition. In turn, these insights may help in establishing the guidelines for the design of high-performance PEFC electrocatalysts based on OMC supports.

3.2. Experimental Section

3.2.1. Synthesis of ordered mesoporous carbon - carbon nanotube nanocomposites

The OMC-CNT nanocomposites were synthesized by a solid-state nanocasting method that used SBA-15 as the template and Ni-phthalocyanine (NiPc, Aldrich) as a precursor, respectively. 1.0 g of the calcined SBA-15 was mixed with 1 g of NiPc, and the mixture was ground for 10 min in a mortar and transferred to an alumina crucible. The mixture was then heated to 900 °C with a ramping rate of 2.5 °C min-1 and remained at this temperature for 3 h under an Ar flow. The resulting carbon-silica composite was then washed twice with hydrofluoric acid (J.T.Baker) at room temperature for 1 h to remove the SBA-15 template. The CMK-3(Pc) was synthesized by the same solid-state method that was used for the OMC-CNT nanocomposites, except using phthalocyanine (Pc, TCI) as the carbon precursors. while the CMK-3(Suc) was prepared by using a previously reported method. The CMK-3(Suc) was synthesized by using a previously reported method by using sucrose (Daejung) as the carbon precursors.[73]

3.2.2. Preparation of supported platinum catalysts on nanocomposite

The OMC-supported Pt catalysts were prepared via an incipient-wetness method. A half gram of the carbon support was mixed with 1.5 mL of acetone containing the Pt precursor, hexachloroplatinic acid (H_2PtCl_6•$6H_2O$, Aldrich).[36] The amount of H_2PtCl_6•$6H_2O$ in the solution was adjusted to obtain 20 wt % Pt loading. After being dried in an oven at 60 °C overnight, the H_2PtCl_6•$6H_2O$ -impregnated OMC was heated in a H_2 flow to 200 °C with a ramping rate of 0.6 °C min^{-1} and kept for 2 h at this temperature to reduce H_2PtCl_6•$6H_2O$ to Pt metal particles. The hydrogen adsorbed on the Pt particles was removed by heating the sample to 350 °C and keeping it at this temperature for 2 h under an Ar flow

3.2.3. Characterization methods

X-ray diffraction (XRD) patterns of the samples were obtained with an X-ray diffractometer (Rigaku D/Max 2500V/PC) equipped with a Cu Kα source at 40 kV and 200 mA. The morphologies of the samples were determined using a scanning electron microscope (SEM) (Quanta 200, FEI) operating at 18 kV. The internal pore structures of the samples were observed by transmission electron microscope (TEM) (JEM-2100F, JEOL) at an accelerating voltage of 200 kV. The porous structures of the samples were analyzed by nitrogen adsorption experiment at -196 °C using a BEL BELSORP-Max system. The surface areas and pore size distributions of the samples were calculated by using the Brunauer-Emmett-Teller (BET) equation and the Barrett-Joyner-Halenda (BJH) method, respectively. The electrical resistivities and thicknesses of the carbons were measured using a powder resistivity measurement system (MCP-PD51, Mitsubishi chemical analytech Co. LTD.) at progressively increasing pressure in the range from 2 to 20 kN. The electrical conductivities of the carbons were calculated using their electrical resistivities and thicknesses.

3.2.4. Electrochemical measurements

The electrochemical characterization of the catalysts was performed using an IviumStat electrochemical analyzer. The characterization experiments were performed at room temperature (25 °C) using a three-compartment electrochemical cell. A Pt-wire counter electrode and a Ag/AgCl reference electrode were used. All potentials reported in this study are with respect to the reversible hydrogen electrode (RHE). A glassy carbon rotating disk electrode was used as the working electrode. This electrode was polished with a 1.0 μm alumina suspension and then with a 0.3 μm suspension in order to give it a mirror finish. 15 mg of the Pt/OMC catalyst was mixed with 0.1 mL of DI water, 1.048 mL of ethanol, and 0.038 mL of 5 wt% Nafion (in isopropanol, Aldrich). The resulting slurry was ultra-sonicated for 30 min to generate a catalyst ink. A total of 3.0 μL of the ink was pipetted onto the glassy carbon electrode and dried in an oven at 70 °C for 5 min. Before the electrochemical measurements, the catalyst was cleaned by cycling the potential between 0 and 1.2 V at 100 mV s^{-1} for 50 cycles using a nitrogen-saturated 0.1 M $HClO_4$ solution as the electrolyte. Cyclic voltammetry (CV) was performed over voltages ranging from 0 to 1.2 V at a scan rate of 20 mV s^{-1} using the nitrogen-saturated 0.1 M $HClO_4$ electrolyte. The RRDE measurements were used to determine the ORR activity in an oxygen-saturated 0.1 M $HClO_4$ electrolyte with linear scanning voltammetry (LSV) performed for voltages ranging from 0.2 to 1.1 V at a scan rate of 5 mV s^{-1}. The accelerated durability test (ADT) was performed on the catalysts by cycling the electrode potential between 0.6 and 1.2 V at 50 mV s^{-1} for 2000 cycles.

3.3. Results and Discussion

3.3.1. Synthesis and characterization of OMC supports

OMC-CNT nanocomposites and two hexagonally ordered CMK-3-type OMCs with varying

degrees of conductivity were synthesized and used as supports for PEFC cathode catalysts, and their catalytic activities and durabilities in half cell and single cell configurations were evaluated. The OMC(Suc) carbon was synthesized via the liquid-phase impregnation of sucrose while the OMC(Pc) carbon and the OMC-CNT nanocomposites were prepared by a solid-state method using Pc and NiPc, respectively.

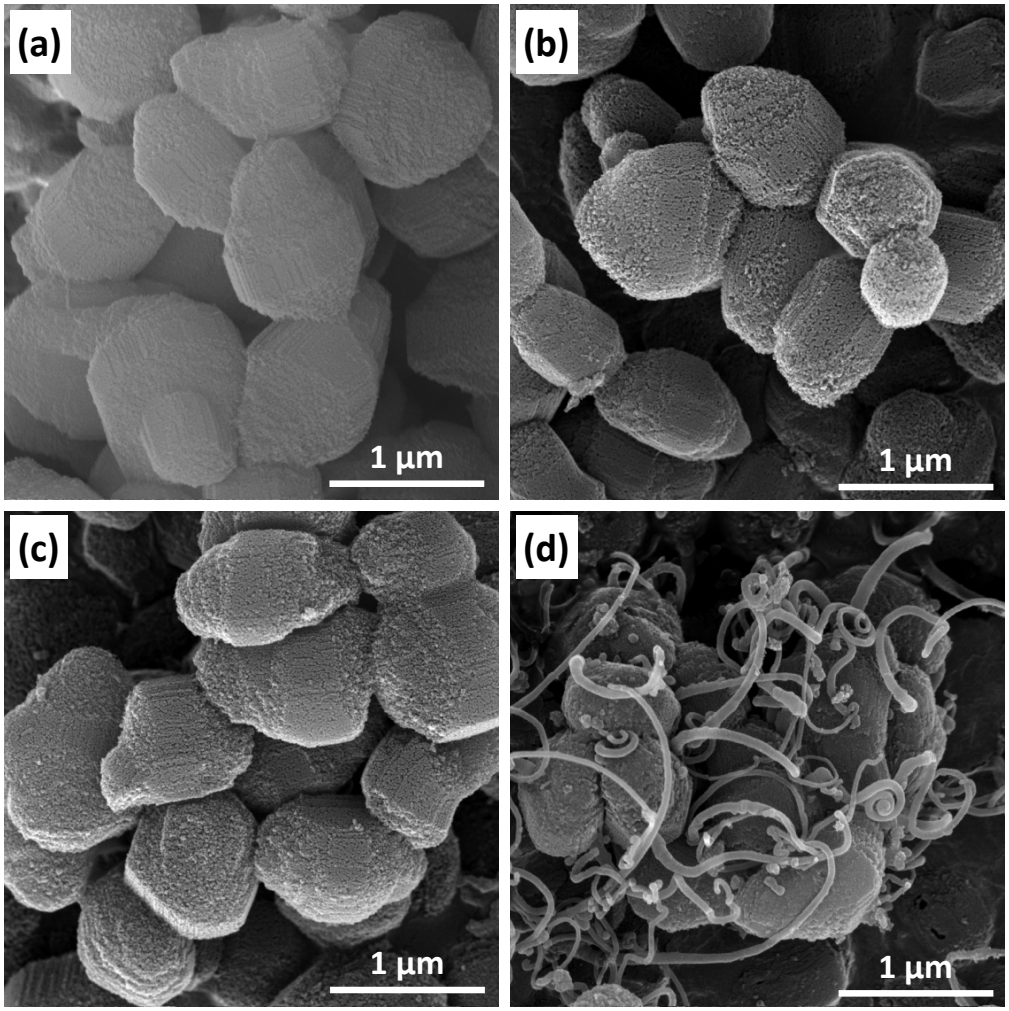

Figure 3.1. SEM images of the (a) SBA-15 template, (b) OMC(Suc), (c) OMC(Pc), and (d) OMC-CNT nanocomposites.

The morphology and porous structure of the SBA-15 template as well as those of the OMC-CNT nanocomposites and the two OMCs were determined from their SEM and TEM images (Figure 3.1 and 3.2). The SEM image of the SBA-15 template (Figure 3.1a) shows spherical particles, with their diameter around 1 μm. It is noted that the obtained SBA-15 particles were spherical when the reaction mixture used to prepare SBA-15 was aged without being stirred at a low temperature (35 °C) was, whereas continuous stirring at 35 °C yielded elongate, fiber-like SBA-15 particles that were a few tens of micrometers in length.[74] A TEM image of the SBA-15 particles (Figure 3.2a) taken along the pores shows uniform mesopores with a diameter of 11 nm in a hexagonal arrangement. The SEM

images of the OMC(Suc) and OMC(Pc) (Figure 3.1b and c) show that the original shapes of the SBA-15 templates, which were spherical, were preserved after the replication process. The TEM images of these two carbons (Figure 3.2b and c) clearly show a hexagonal array of uniform carbon nanorods, indicating that the pores and silica walls of the SBA-15 template were faithfully replicated into the carbon frameworks and pores of the OMCs. In the case of the OMC-CNT nanocomposites, the use of NiPc as a carbon source led to the generation of the spherical OMC particles as well as the CNTs, as demonstrated previously (Figure 3.1d and 3.2d-f).[29] The TEM image of the OMC-CNT nanocomposites (Figure 3.2d) also reveals that the CNTs connected adjacent OMC particles. A closer observation of the interface between the OMC particles and the CNTs (Figure 3.2e and f) showed that the terminal parts of the CNTs were embedded within the OMC frameworks. The formation of CNTs in the OMC-CNT nanocomposites can be attributed to the *in situ* generation of Ni particles during the high-temperature pyrolysis step. The TEM image of the carbon/SBA-15 composite formed using a NiPc precursor (Figure 3.3) shows the formation of Ni particles, which were subsequently etched away during the removal of the SBA-15 template by HF.

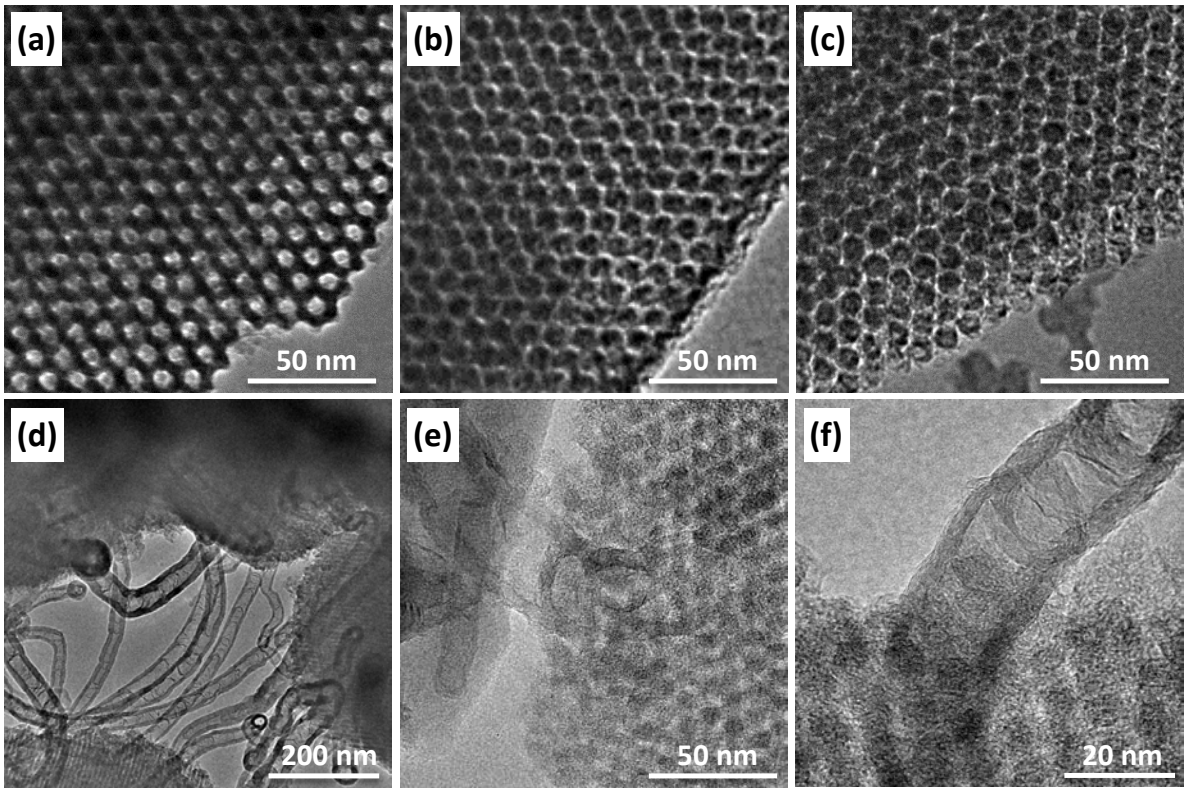

Figure 3.2. TEM images of the (a) SBA-15 template, (b) OMC(Suc), (c) OMC(Pc) and (d-f) OMC-CNT nanocomposites

Therefore, it is likely that the Ni particles served as catalysts for the formation of the multi-walled CNTs, as reported previously.[75] The unique structure of the OMC-CNT nanocomposites would

result in the lowering of the interfacial resistance, which, in turn, would lead to the efficient transport of electrons across the OMC particles.

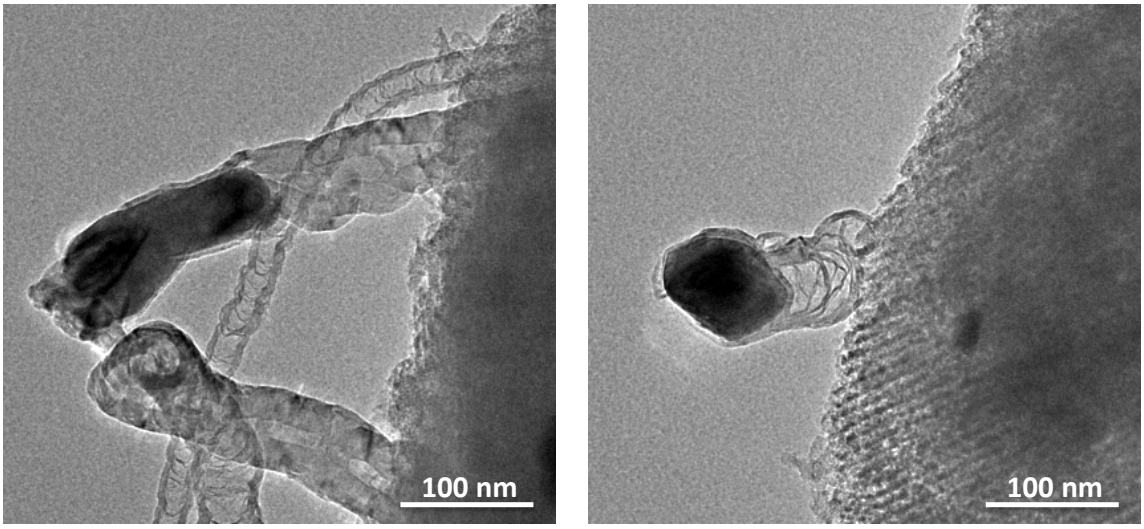

Figure 3.3. TEM images of the carbon/SBA-15 composite during the preparation of OMC-CNT nanocomposites.

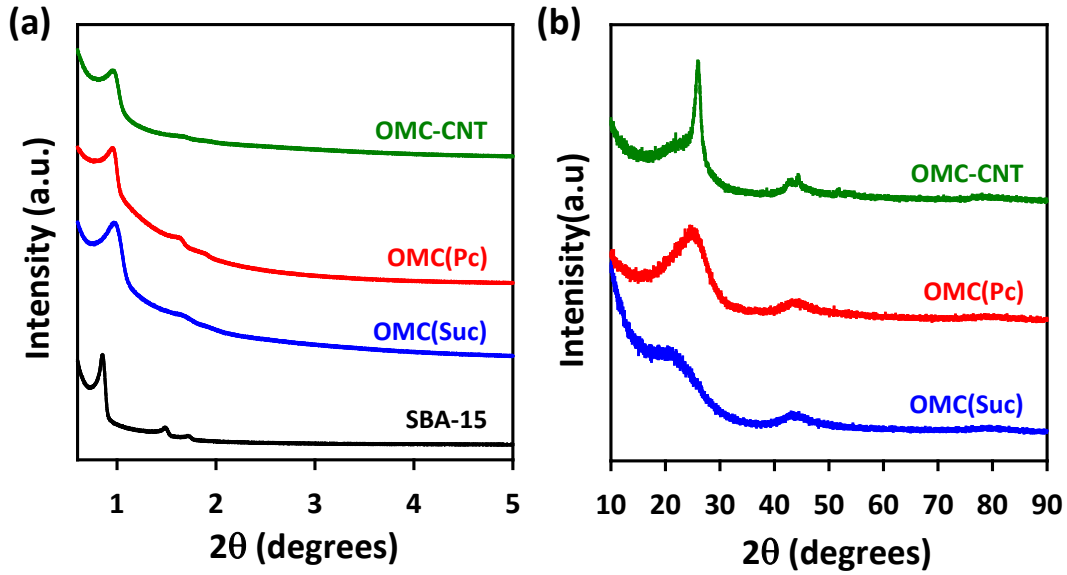

Figure 3.4. (a) Small-angle and (b) wide-angle XRD patterns of the SBA-15 template and the OMCs

The structural integrities and framework microstructures of the OMC-CNT nanocompoistes and the two OMCs were determined by small- and wide-angle XRD patterns, respectively (Figure 3.4). The small-angle XRD patterns of the three carbons show three diffraction lines below 2°. These correspond to the (100), (110), and (200) diffraction planes of hexagonal *p6mm* mesostructure. Among the three carbons, the OMC(Suc) had the smallest unit cell size (see Table 3.1). This was because the sucrose precursor underwent the highest degree of lattice contraction. The wide-angle

XRD patterns of the three carbons were distinctively different, as revealed by the sharpness of the peak appearing between 20° and 30°, which manifested the degree of graphiticity. The sharpness of this peak increased gradually, and the peak for OMC(Suc) was the least sharp and that for the OMC-CNT nanocomposites the sharpest. The use of the aromatic precursors, Pc and NiPc, resulted in the carbon frameworks of the OMC(Pc) and OMC-CNT nanocomposites being more graphitic than that of the OMC(Suc), which used sucrose as the precursor. This was consistent with the results of a previous study.[36] The fact that the peak for the OMC-CNT nanocomposites was the sharpest could be due to the highly graphitic walls of CNTs as well as graphitic framework of the OMC in the nanocomposites. In order to determine graphitic nature, the conductivities of the three carbons were measured using a four-probe method. The changes in the conductivities of the three carbons as a function of pressure are shown in Figure 3.5, and the values of their conductivities at 20 kN are listed in Table 3.1. The results revealed that the OMC-CNT nanocomposites exhibited the highest conductivity (26.1 S cm^{-1}), followed by the OMC(Pc) (18.3 S cm^{-1}), and the OMC(Suc) (12.0 S cm^{-1}). These results were consistent with those obtained from the wide-angle XRD patterns. The conductivities of the carbons would be affected by the resistance of their carbon frameworks as well as that of the interfaces between the OMC particles. The conductivity of the OMC(Pc) being higher than that of the OMC(Suc) is most likely due to the former being graphitic in nature, as revealed by their respective wide-angle XRD patterns.[76] In the case of the OMC-CNT nanocomposites, it is likely that their interfacial resistance was lower than that of the two OMCs because the CNTs could interconnect the separated OMC particles, which would further increase the conductivity.

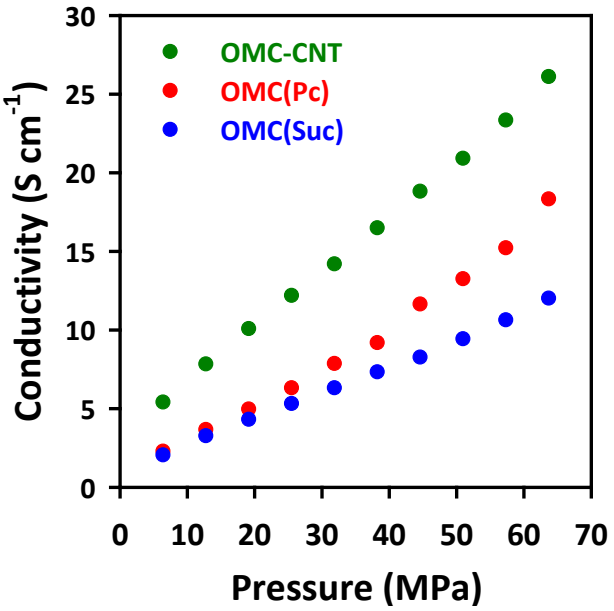

Figure 3.5. Electrical conductivities of the three OMCs under different applied pressures.

The porous structures of the carbons were determined from their nitrogen adsorption isotherms (Figure 3.6 and Table 3.1). The three carbons had similar type IV isotherms, as reported previously (Figure 3.6a).[71] It is interesting to note that the isotherm of the OMC-CNT nanocomposites was similar to those of the OMCs as this indicated that the mesostructure of the OMCs in the nanocomposites was not significantly affected by the intrusion of the CNTs. The pore sizes of the carbons, determined from the adsorption branches of the isotherms, were similar and ranged from 4.9 to 5.5 nm. The BET surface areas and pore volumes of the carbons were 1264 m^2 g^{-1} and 1.246 cm^3 g^{-1}, respectively, for the OMC(Suc), 658 m^2 g^{-1} and 1.193 cm^3 g^{-1}, respectively, for OMC(Pc), and 954 m^2 g^{-1} and 1.056 cm^3 g^{-1}, respectively, for OMC-CNT nanocomposites.

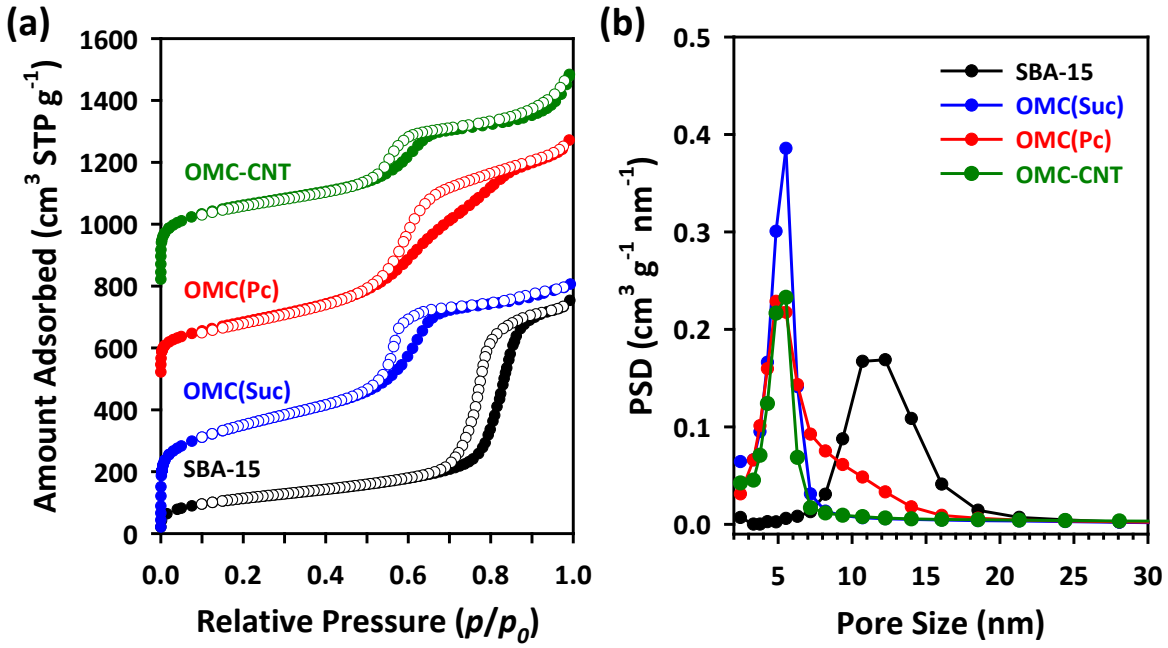

Figure 3.6. (a) Nitrogen adsorption-desorption isotherms of the SBA-15 template and the three OMCs. (b) Pore size distributions of the SBA-15 template and the three carbons, as determined by the BJH method.

Previously, alternative approaches towards composite structures composed of OMC and CNTs were reported.[77,78] Pak and co-workers employed a physical mixture of OMS and CNT as a template to prepare OMC-CNT composites.[77] Zhao and co-workers used a multi-step, sequential process to prepare OMC-CNT composites, which consists of (i) preparation of carbon/OMS composite, (ii) deposition of a metal catalyst on the external surface of the carbon/OMS composite, (iii) growth of CNTs catalyzed by the metal catalyst, and (iv) the removal of the OMS template and catalyst to generate OMC-CNT composites. Compared to these previous works, our method for the OMC-CNT nanocomposites is simple in that the carbon/OMS and CNT structures could be generated simultaneously from a single precursor, NiPc. Furthermore, the CNTs in our OMC-CNT nanocomposistes are rigidly embedded within the OMC frameworks and interconnect adjacent OMC

particles, as confirmed by their SEM and TEM images. These structural features make the OMC-CNT nanocomposites as rigidly interconnected and highly conductive scaffolds, which should be advantageous for energy conversion and storage applications.

Table 3.1. Structural parameters and electrical conductivity for OMS template, OMC, and Pt/OMC catalysts

	a (nm)[a]	S_{BET} (m^2 g^{-1})[b]	V_{tot} (cm^{-3} g^{-1})[c]	V_{micro} (cm^{-3} g^{-1})[d]	d (nm)[e]	σ (S cm^{-1})[f]
SBA-15	11.96	413	1.165	0.005	12.24	-
OMC(Suc)	10.65	1264	1.246	0.05	5.52	12.0
OMC(Pc)	10.70	658	1.193	0.01	4.85	18.3
OMC-CNT	10.70	954	1.056	0.01	5.52	26.1
Pt/OMC(Suc)	10.62	994	1.02	0.02	5.52	-
Pt/OMC(Pc)	11.00	554	0.917	0.005	4.85	-
Pt/OMC-CNT	10.96	716	0.964	0.005	5.52	-

[a]Lattice parameters calculated from XRD patterns ($a = 2\ d100/\sqrt{3}$).
[b]BET surface areas calculated in the range of p/p_0 = 0.05-0.2.
[c]Total pore volumes calculated as the amount of N_2 adsorbed at a relative pressure of 0.99.
[d]Micropore volume obtained from αs plot.
[e]Pore diameters calculated by the BJH method using the adsorption branches.
[f]Electrical conductivity measured at 20 kN.

3.3.2. Preparation and characterization of Pt/OMC catalysts

The three carbons, the OMC(Suc), the (OMC(Pc), and the OMC-CNT nanocomposites, were used as catalyst supports for Pt nanoparticles. The Pt/OMC catalysts were prepared via an impregnation of a Pt precursor, which was followed by hydrogen reduction. The nominal content of Pt was controlled to be 20 wt%. Figure 3.7 shows TEM images of the Pt/OMC catalysts and the particle size distributions of the Pt nanoparticles in these catalysts. The TEM images clearly revealed that the Pt nanoparticles were homogeneously distributed on the carbon nanorods in all three Pt/OMC samples. In the case of the Pt/OMC-CNT catalyst, the Pt nanoparticles were also formed on the CNTs, but the density of particles was rather low owing to the inert nature of the surfaces of the CNTs with respect to the anchoring Pt nanoparticles. The average sizes of the Pt nanoparticles, calculated using approximately 200 particles were, 1.3, 1.5, and 1.2 nm for the OMC(Suc), the OMC(Pc), and the OMC-CNT nanocomposoites, respectively. The wide-angle XRD patterns of the Pt/OMC catalysts are displayed in Figure 3.8. Each catalyst showed three broad peaks, around 40°, 66°, and 81°, respectively, which could be indexed to the (111), (200), and (222) planes of the face-centered-cubic structure of Pt. However, it was impossible to estimate the size of Pt nanocrystals because the peaks were too broad. It should be noted that Pt nanoparticles smaller than 2 nm in size could be generated via a simple incipient wetness-H_2 reduction method. The extremely high dispersion achieved in the case of our catalysts could be ascribed to the large surface area of the OMCs as this provided numerous surface nucleation sites for the growth of the Pt nanoparticles.

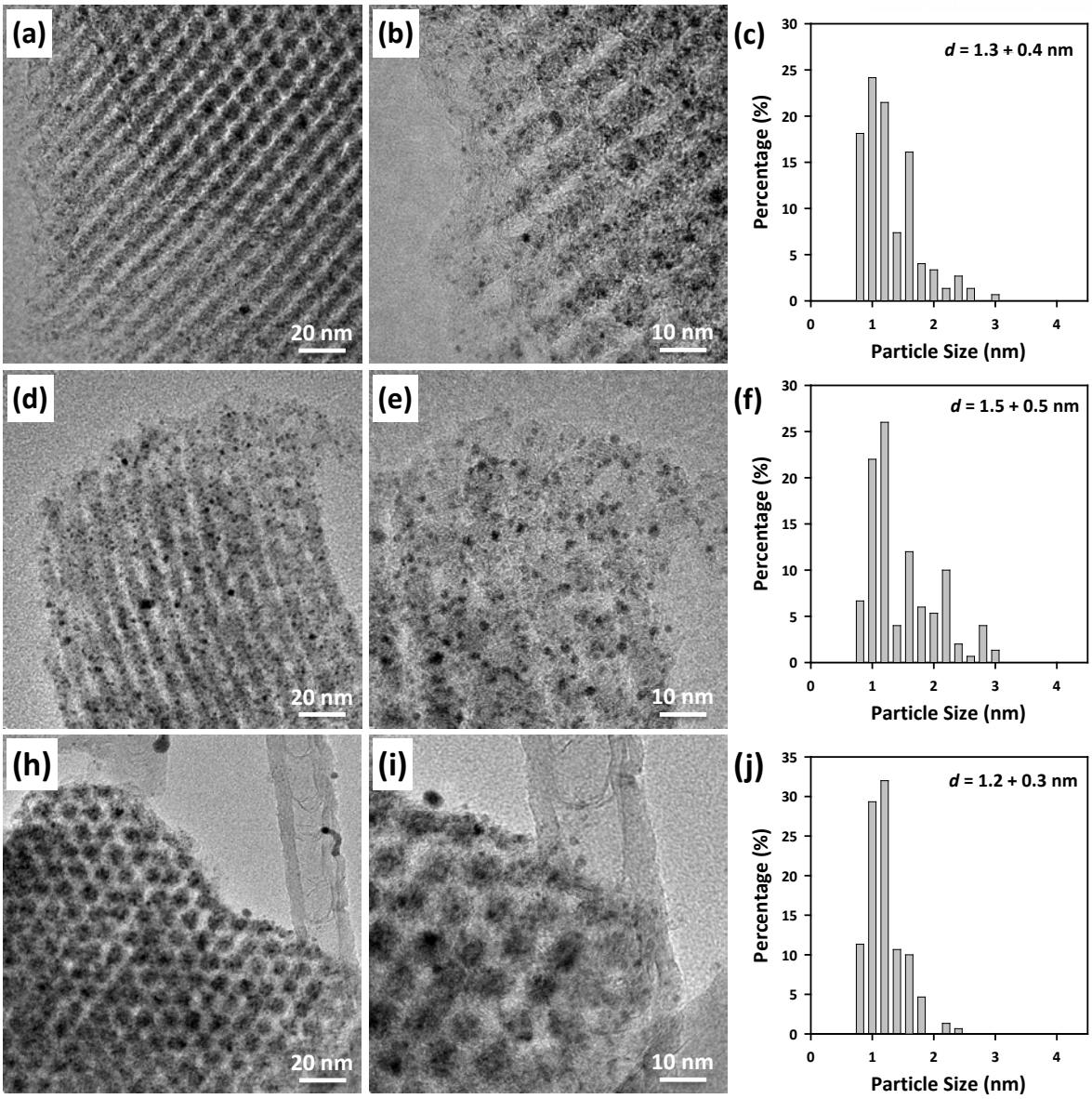

Figure 3.7. TEM images of (a and b) Pt/OMC(Suc), (d and e) Pt/OMC(Pc), and (h and i) Pt/OMC-CNT, and particle size distributions of Pt in (c) Pt/OMC(Suc), (f) Pt/OMC(Pc), and (j) Pt/OMC-CNT.

We had previously demonstrated that Pt nanoparticles 3 nm in size could be supported on the OMC supports, even when the Pt loading was as high as 60 wt%.[36,49] The structural integrities and porosities of the Pt/OMC catalysts were determined from their small-angle XRD patterns and nitrogen-adsorption isotherms. The nitrogen-adsorption isotherms of the Pt/OMC catalysts were type IV isotherms and similar to those of the original OMCs (Figure 3.8). The main difference in the isotherms of the Pt/OMC catalysts and those of the supports was the decrease in the amount of nitrogen adsorbed as a result of the Pt loading. The surface areas and pore volumes of the Pt/OMC catalysts ranged from 554 to 994 $m^2 g^{-1}$ and 0.96 to 1.02 $cm^3 g^{-1}$, respectively.

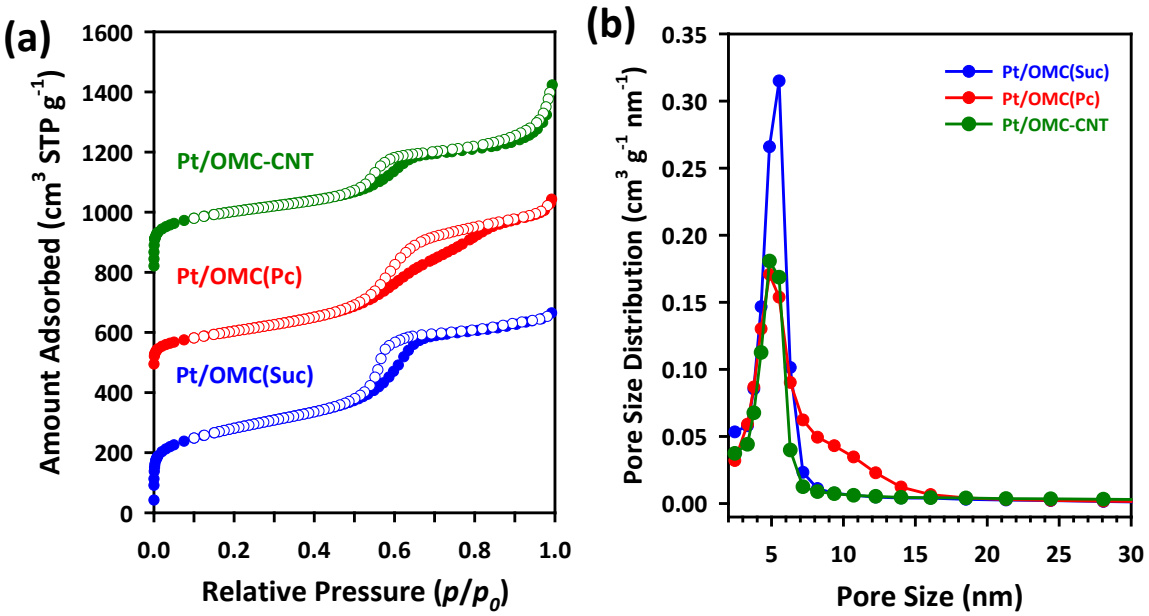

Figure 3.8. (a) Nitrogen adsorption-desorption isotherms and (b) corresponding pore size distribution of Pt/OMC catalysts determined by the BJH method.

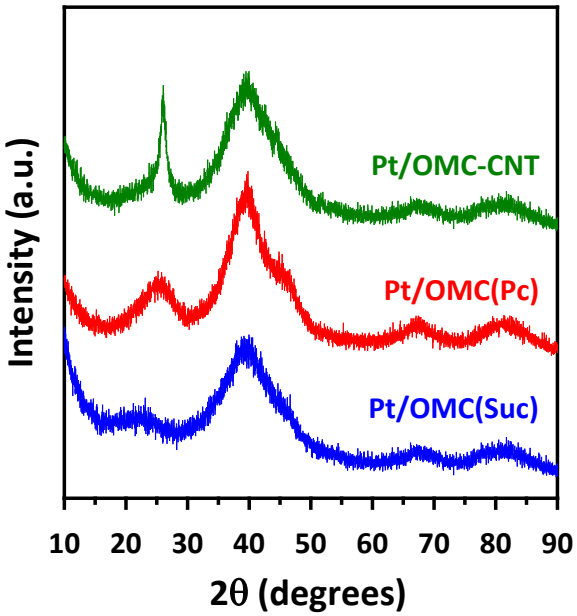

Figure 3.9. Wide-angle XRD patterns of the Pt/OMC catalysts.

Therefore, the Pt/OMC catalysts could be prepared using three carbons with different degrees of graphitic ordering. It should be noted that the sizes of the supported Pt nanoparticle in all three Pt/OMC samples was similar and around 1.5 nm. This should enable one to study effects of the carbon supports exclusively without the effects of the other structural factors.

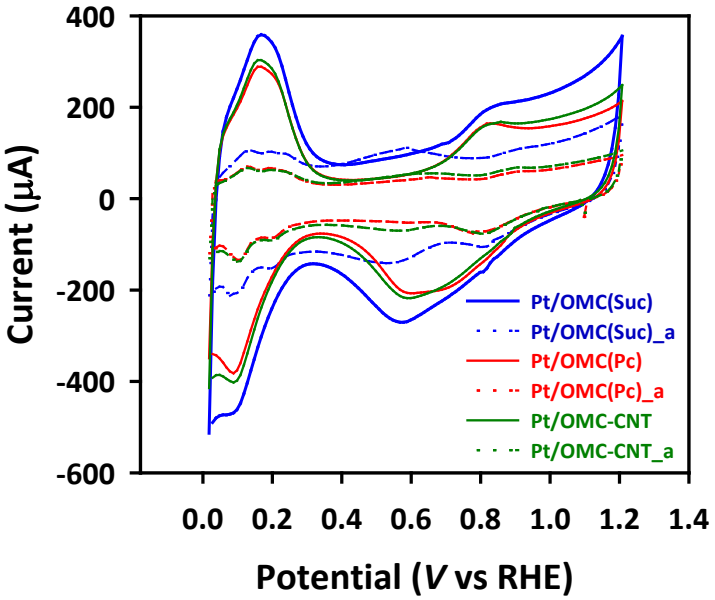

Figure 3.10. Cyclic voltammograms of the Pt/OMC catalysts in a N_2 saturated 0.1 M $HClO_4$ solution at a scan rate of 20 mV s^{-1}.

3.3.3. Electrochemical activities of Pt/OMC catalysts before and after the ADTs

The electrochemical properties of the Pt/OMC catalysts were investigated by CV and linear sweep voltammetry (LSV) for the ORR (Figure 3.10 and 3.11). The CV and LSV measurements were made before and after the ADTs. The CV measurements of the Pt/OMC catalysts were made using N_2-purged 0.1 M $HClO_4$ solution over a scan range of 0.05 to 1.2 V (Figure 3.10). The three Pt/OMC catalysts exhibited similar oxidation and reduction peaks, with the shapes of the peaks being slightly different. One distinctive difference was that the current in the Pt/OMC(Suc) catalyst in the double layer region was higher than those in the case of other two catalysts. This was due to its large BET surface area (see Table 3.1). Two hydrogen oxidation peaks, indicating the oxidative desorption of the adsorbed hydrogen, were observed between 0.05 and 0.4 V. In the reduction scan, the CV measurements showed a peak around 0.55-0.6 V. This peak corresponded to a reduction of surface oxide on Pt nanoparticles. It should be noted that the position of the peak representing the reduction of surface oxide was observed at a potential lower than that previously reported for supported Pt catalysts (between 0.6 and 0.7).[2] This shift in the peak may be attributed to the fact that the Pt particles (ca. 1.5 nm in size) in our Pt/OMC catalysts were smaller than those in the other catalysts (ca. 3-4 nm), and oxygen species are more strongly adsorbed to smaller Pt particles.

The electrochemically active surface areas (ECSAs) of Pt nanoparticles were estimated from the area of the anodic peak corresponding to the H desorption (between 0.04 and 0.4 V) after correcting for the double layer current by using the following equation:

$$\text{ECSA} = Q_H / L \times q_H \qquad (1)$$

where Q_H is the charge for the hydrogen desorption, L is the mass of Pt loaded on the electrode (μg

cm^{-2}), and q_H is the charge required to oxidize a monolayer of H_2 on Pt (0.210 μC cm^{-2}). The ECSAs of Pt/OMC(Suc), Pt/OMC(Pc), and Pt/OMC-CNT catalysts were 110, 124, and 138 m^2 g^{-1}, respectively (see Table 3.2). In addition, the geometric surface areas (GSA) of the Pt nanoparticles were calculated using their particle sizes, which were determined from their TEM images, and the following equation:

$$GSA = 6000 / \rho d \quad (2)$$

where ρ is the density of platinum metal (21.4 x 10^6 g m^{-3}) and d is the average diameter of the Pt nanoparticles (in nm) as determined from the TEM images. The GSAs of the Pt nanoparticles of the Pt/OMC(Suc), Pt/OMC(Pc), and Pt/OMC-CNT catalysts were found to be 216, 187, and 234 m^2 g^{-1}, respectively. A comparison of the ECSA and GSA values reveals that the ECSAs are lower than the GSAs. This can be attributed to the inability of protons to the buried regions of the interfaces between the carbon supports and the Pt nanoparticles. In addition, the blocking or anchoring of Nafion on the surfaces of the Pt nanoparticles may also limit the ability of protons to access these regions. On comparing the three OMC-supported catalysts, it was found that the Pt/OMC-CNT catalyst had the highest ECSA. It was followed by the Pt/OMC(Pc) catalyst and finally the Pt/OMC(Suc) catalyst. It is worth noting that the Pt/OMC(Pc) catalyst had a higher ESCA value than the Pt/OMC(Suc) catalyst, whereas the Pt/OMC(Pc) catalyst showed a lower GSA than the Pt/OMC(Suc) catalyst. This opposite trend may be correlated to the higher micropore volume of the Pt/OMC(Suc) catalyst (see Table 3.1). More Pt nanoparticles will be buried in the micropores as the micropore volume increases.

The electrocatalytic activities of the Pt/OMC catalysts for the ORR were investigated by using an RRDE method. Figure 3.11a shows LSV polarization plots of the Pt/OMC catalysts for the ORR, which were measured in an O_2-saturated 0.1 M $HClO_4$ solution at a rotating speed of 1600 rpm at room temperature. The three Pt/OMC catalysts showed similar polarization curves; they exhibited the on-set potential at 0.96 V and a well-defined plateau corresponding to the diffusion-limiting current between 5.9 and 6.5 mA cm^{-2}. The corresponding Tafel plots based on the kinetic current densities are shown in Figure 3.10b. The specific and mass activities of the Pt/OMC catalysts were calculated by normalizing the kinetic currents with the ECSAs and masses of the Pt nanoparticles, respectively (Figure 3.11c and 3.11d and Table 3.2). Among the three Pt/OMC catalysts, the Pt/OMC-CNT catalyst showed higher ORR activity than the two other catalysts in terms of both specific and mass activity. At 0.85 V (versus the RHE), the specific activity of the Pt/OMC-CNT catalyst was 168 μA cm_{Pt}^{-2}, whereas those of the Pt/OMC(Suc) and Pt/OMC(Pc) catalysts were 124 and 115 μA cm_{Pt}^{-2}, respectively. Thus, the Pt/OMC-CNT catalyst exhibited specific activity that was 26 to 31 % higher than those of the two other catalysts. The mass activity of the Pt/OMC catalysts showed a similar trend as well. The Pt/OMC-CNT catalyst exhibited the highest mass activity (232 mA mg_{Pt}^{-1}). It was followed by the Pt/OMC(Pc) (142 mA mg_{Pt}^{-1}) and finally the Pt/OMC(Suc) catalyst (137 mA mg_{Pt}^{-1}). Taking into account of the similarity of the sizes of the Pt particles of the three Pt/OMC catalysts, the

higher catalytic activity of the Pt/OMC-CNT catalyst can be attributed to its higher conductivity than other two catalysts. This would facilitate the electron transfer in the Pt/OMC-CNT catalyst.

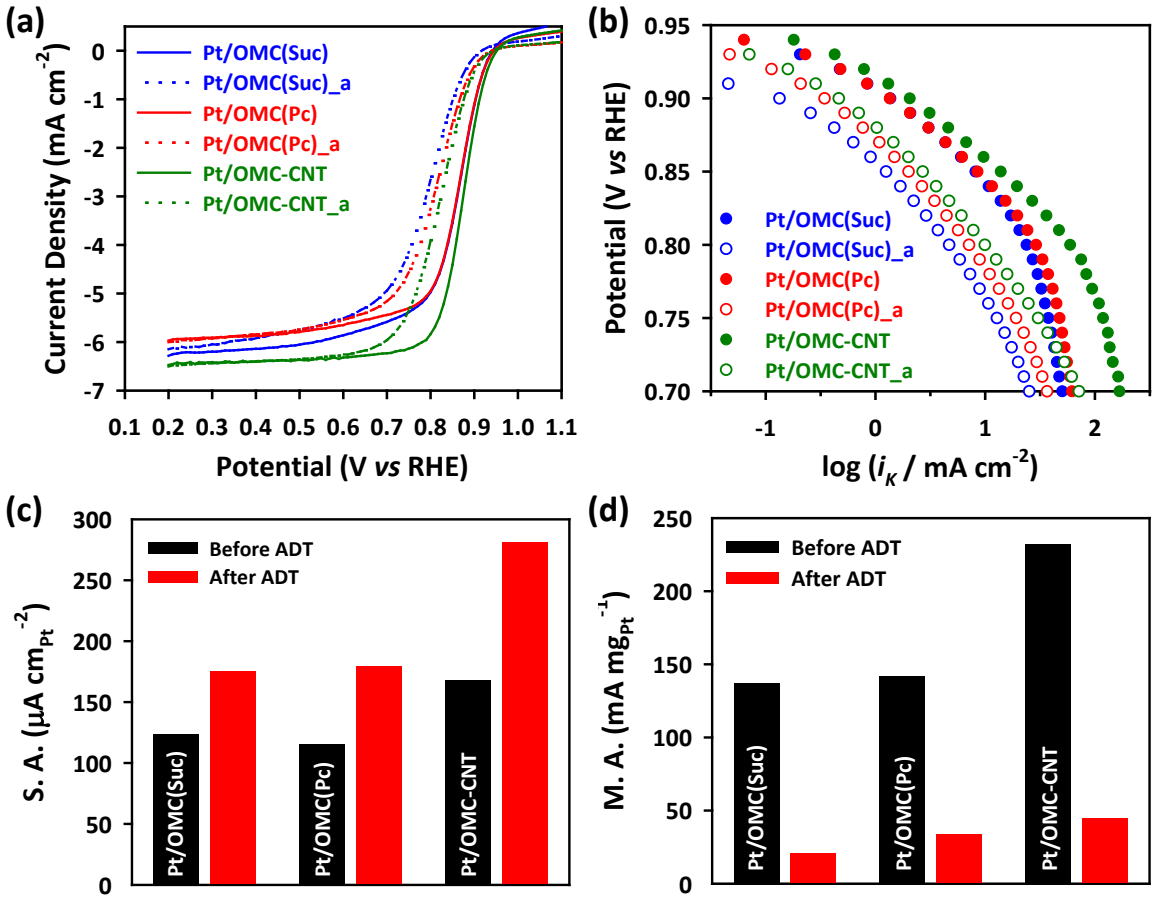

Figure 3.11 (a) Oxygen reduction current densities of the Pt/OMC catalysts supported on glassy-carbon RRDE in an O_2-saturated 0.1 M $HClO_4$ at a rotating speed of 1600 rpm and at a scan rate of 5 mV s^{-1} and (b) the corresponding Tafel plots. Comparison of (c) specific activity and (d) mass activity of Pt/OMC catalysts.

To further explore the kinetic aspects of the Pt/OMC catalysts for the ORR, their respective Koutecky-Levich plots were obtained from the electrode current densities at different rotating speeds. The Koutecky-Levich equation (Eq. 3) relates the inverse current densities with the inverse square root of the rotating speed as follows.

$$\frac{1}{i} = \frac{1}{i_k} + \frac{1}{i_d} = \frac{1}{i_k} + \frac{1}{B\omega^{1/2}} \qquad (3)$$

$$\mathrm{B} = \frac{0.62nFAC_{O_2}D_{O_2}^{2/3}}{\eta^{1/6}} \qquad (4)$$

where i is the experimentally determined current; i_k the kinetic current; i_d the diffusion-limited current; n the number of electrons transferred; F the Faraday constant (96485 C mol^{-1}); A the geometric area of the electrode (0.126 cm^2); C_{O2} the O_2 concentration in the electrolyte (1.26×10^{-3} mol L^{-1}); D_{O2} the diffusion coefficient of O_2 in the $HClO_4$ solution (1.93×10^{-5} cm^2 s^{-1}); and η the viscosity of the

electrolyte (1.01×10^{-2} cm^2 s^{-1}). Figure 3.12a shows the ORR activity of the Pt/OMC-CNT catalyst for rotating speeds varying from 400 to 2500 rpm. The diffusion-limiting current densities increased proportionally with the rotating speed. At a rotating speed of 1600 rpm, the current density for the ORR was 6.5 mA cm^{-2}, which is similar with the previous results obtained on Pt/C supported catalyst using a 0.1M $HClO_4$ solution as the electrolyte at room temperature.[2] This indicated that the diffusion resistance of the thin-film electrodes made of the Pt/OMC-CNT catalyst was negligible.

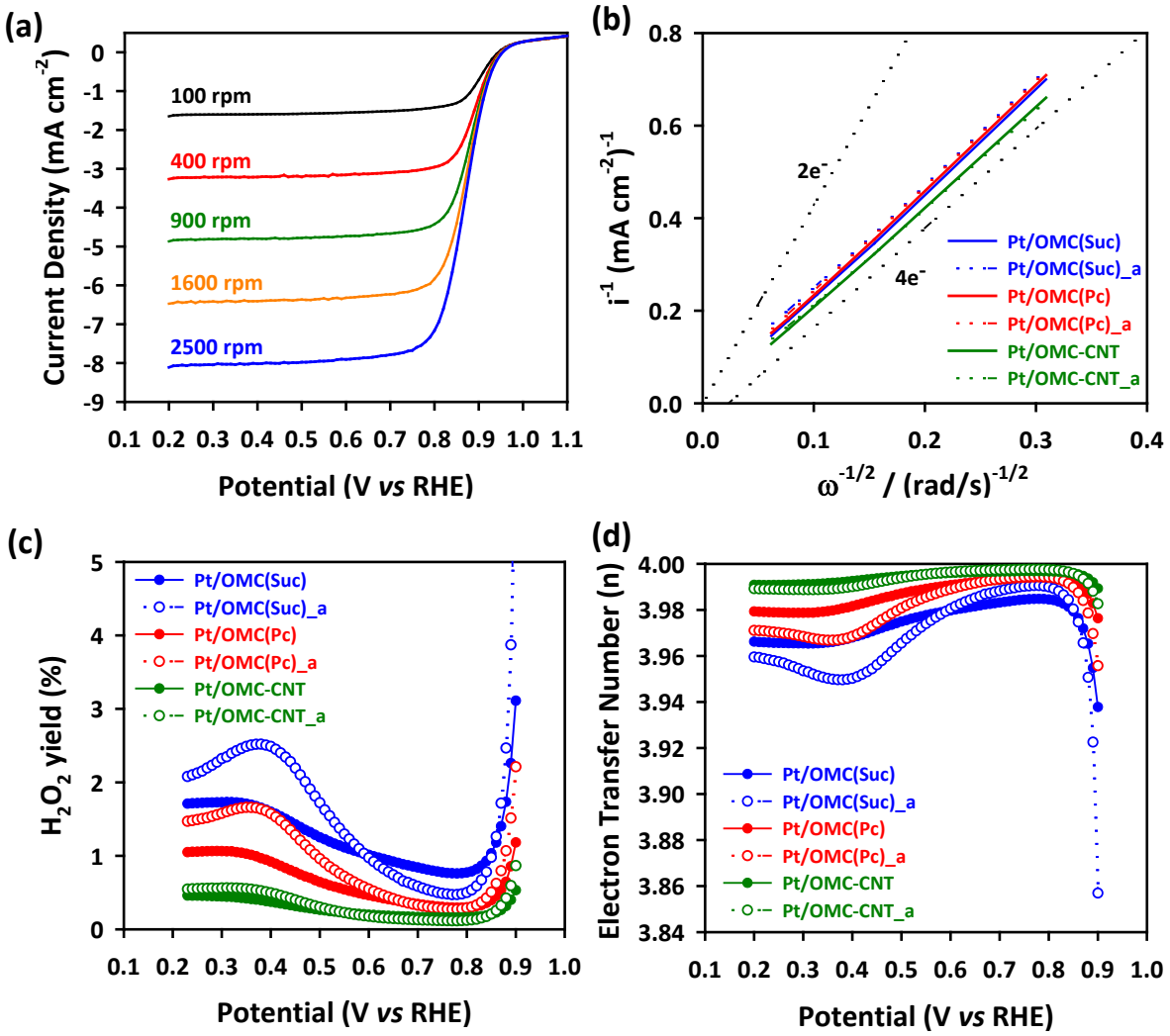

Figure 3.12. (a) Oxygen reduction current densities of the Pt/OMC-CNT catalyst for different rotating speeds. (b) Koutecky-Levich plots of the Pt/OMC catalysts at 0.7 V (versus RHE). (c) H_2O_2 yields and (d) number of electrons transferred for the Pt/OMC catalysts, as determined from the ring currents during the ORR.

The Pt/OMC(Suc) and Pt/OMC(Pc) catalysts also exhibited similar changes in their current densities with the rotating speed. Figure 3.12b shows the Koutecky-Levich plots of the three Pt/OMC catalysts at 0.7 V. The plots clearly show linear lines that are parallel to the theoretical line based on the four-electron transfer. The number of transferred electrons as calculated from the slopes of catalysts are 3.82, 3.81, and 3.98 for Pt/OMC(Suc), Pt/OMC(Pc), and Pt/OMC-CNT catalysts,

respectively, implying that the ORRs by all three catalysts followed a direct four-electron transfer mechanism.

The ORR kinetics of the catalysts was also investigated by measuring the ring-disk currents (Figure 3.12c and 3.12d). The H_2O_2 yields during the ORRs were calculated from the measured ring currents, and the number of electrons transferred could be calculated from the following equation as well.

$$n = \frac{4}{1+\frac{I_R}{NI_D}} \qquad (5)$$

Here, I_D and I_R are the disk and ring currents, respectively, and N is the ring collection efficiency. The H_2O_2 yields of all three catalysts were very low (below 2 %), with the yield of the OMC-CNT catalyst being the lowest. Almost four electrons were transferred in the case of each catalyst. This result corroborated the results of the Koutecky-Levich analysis.

The durabilities of the Pt/OMC catalysts were explored by measuring of the same electrochemical parameters (i.e., those determined by the CVs and the LSV for the ORR) after the ADTs. The ADTs of the catalysts were performed by cycling the electrode potential between 0.6 and 1.2 V at 50 mV s^{-1} for 2000 cycles. The repeated cycling at the voltage of up to 1.2 V should have significantly degraded the thin-film catalysts via several pathways. The values of electrochemical parameters of the three catalysts after the ADTs are shown with dotted lines and open circles in the Figure 3.10 - 3.12. The catalysts are denoted as Pt/OMC(suc)_a, Pt/OMC(Pc)_a, and Pt/OMC-CNT_a. The CVs of all three Pt/OMC catalysts after the ADT (Figure 3.10) showed a significant decrease in the current density, including the areas corresponding to the hydrogen desorption. The ECSAs of the Pt/OMC(suc), Pt/OMC(Pc), and Pt/OMC-CNT catalysts after the ADTs were 12, 19, and 16 m^2 g^{-1}, respectively (Table 3.2). This drastic decrease in the ECSA value could be due to a number of factors, including the Ostwald ripening of the Pt nanoparticles and the loss of the Pt nanoparticles owing to their detachment from the OMC supports. The LSV measurements of the ORR activity after the ADT (Figure 3.11) showed a shift of the half-wave potential to a lower voltage as well as a decrease in the ORR activity. On comparing the results of the measurements of the three catalysts, the differences in voltages corresponding to the half-wave potential before and after the ADTs were 70 mV for the Pt/OMC(Suc), 54 mV for the Pt/OMC(Pc), and 53 mV for the Pt/OMC-CNT. These results indicated that the durability of the Pt/OMC-CNT and Pt/OMC(Pc) catalysts was greater than that of the Pt/OMC(Suc) catalyst. The differences in the specific and mass activities of the Pt/OMC catalysts became even more pronounced after the ADTs (Figure 3.11c and 3.11d and Table 3.2). The Koutecky-Levich plots along with H_2O_2 yield calculations (Figure 3.12) indicated that even after the ADTs of the Pt/OMC catalysts, the ORR still proceeded via a four-electron transfer mechanism.

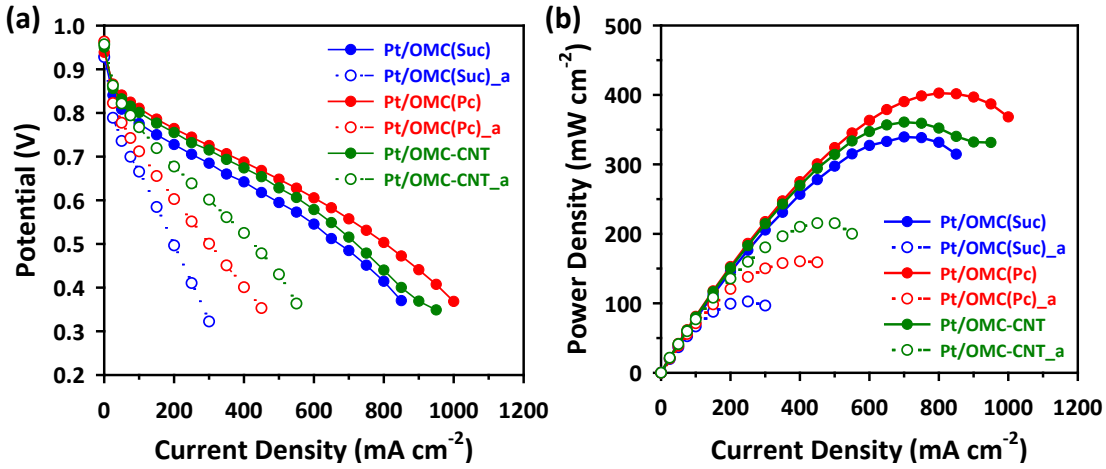

Figure 3.13. (a) H_2-air PEMFC polarization plots of the Pt/OMC cathodes measured at 70 °C with a Pt loading of 0.4 mg cm^{-2}. (b) Corresponding power density plots. The anode catalyst was 40 wt% Pt/C (HiSPEC 4000, Johnson Matthey)

Table 3.2. Electrochemical characterization of Pt/OMC catalysts before and after durability test.

	ECSA (m^2 g_{Pt}^{-1})[a]	S.A[b] (μA cm_{Pt}^{-2})[a]	M.A (mA mg_{Pt}^{-1})[b]	I (mA cm^{-2})[c]	P_{max} (mW cm^{-2})[c]	R_s (Ω cm^2)[d]	R_{ct} (Ω cm^2)[d]
Pt/OMC(Suc)	110	124	137	490	340	0.02	0.09
Pt/OMC(Suc)_a[e]	12	175	21	140	100	0.04	0.27
Pt/OMC(Pc)	124	115	142	610	400	0.02	0.05
Pt/OMC(Pc)_a[e]	19	179	34	200	160	0.05	0.27
Pt/OMC-CNT	138	168	232	560	360	0.02	0.07
Pt/OMC-CNT_a[e]	16	281	45	300	220	0.03	0.13

[a]Electrochemical active surface area (ECSA) calculated from eq. 1.
[b]Mass activity (M.A) and specific activity (S.A) derived from I_k at 0.85 V vs RHE in rotating disk electrode (RDE) test -O_2 saturated 0.1M $HClO_4$ at 1600 rpm and 5 mV s^{-1}.
[c]Current density (I) at 0.6 V and maximum power density (P_{max}) measured in single cell test.
[d]Ohmic resistance (R_s) and charge transfer resistance (R_{ct}) obtained from electrochemical impedance spectra (EIS) before and after high voltage (1.4 V) durability test for 3 h in single cell tests.
[e]Obtained after the durability test.

3.3.4. PEMFC single cell test and EIS characterization of catalysts

The activities and durabilities of Pt/OMC catalysts were investigated further in a single cell configuration, as this configuration can provide deeper insights into the practical applicability of the Pt/OMC catalysts. MEAs using the Pt/OMCs as cathode catalysts were fabricated for this purpose. Since the same commercial Pt/C catalyst was used as the anode in all the MEAs used, any differences in PEMFC performances could be attributed solely to the ORR activity at the cathode. The polarization curves for the PEMFC in the single cell configuration were determined at 70 °C using H_2 and air as the fuel and oxidant, respectively (Figure 3.13 and Table 3.2). The open circuit voltages of the single cell were similar for all three Pt/OMC catalysts and was around 0.9 V. This was consistent with the results of the ORR activity measurements using a half cell configuration. The three MEAs

showed similar current and power densities, with the Pt/OMC(Pc)-based MEA showing the highest values, followed by the Pt/OMC-CNT-based MEA and the Pt/OMC(Suc)-based MEA. The current density at 0.6 V and maximum power density in the case of the Pt/OMC(Pc) catalyst were 610 mA cm^{-2} and 400 mW cm^{-2}, 560 mA cm^{-2} and 360 mW cm^{-2} for the Pt/OMC-CNT catalyst, and 490 mA cm^{-2} and 340 mW cm^{-2} for the Pt/OMC(Suc) catalyst.

The durabilities of the Pt/OMC catalyst-based PEMFCs were investigated by determining the single cell polarization curves after the application of a high voltage (1.4 V) for 3 h in order to degrade the catalysts. After the high-voltage degradation tests, a clear difference in the polarization curves of the MEAs could be observed (dashed lines in Figure 3.13). The Pt/OMC-CNT-based MEA exhibited a current density that was greater than those of the Pt/OMC(Pc)- and Pt/OMC(Suc)-based MEA by 50 to 115 %. The current densities at 0.6 V and maximum power densities of the MEAs after the high-voltage degradation tests were 300 mA cm^{-2} and 220 mW cm^{-2} in the case of the Pt/ OMC-CNT catalyst, 200 mA cm^{-2} and 160 mW cm^{-2} for the Pt/ OMC(Pc) catalyst, and 140 mA cm^{-2} and 100 mW cm^{-2} for the Pt/OMC(Suc) catalyst. It is likely that the markedly superior single cell current density of the Pt/OMC-CNT-based MEA was due to the unique structure of the OMC-CNT supports. In the OMC-CNT nanocomposites, the CNTs can function as rigid electrical connectors that could maintain the interconnectedness of the OMC-CNT nanocomposites under the harsh conditions of the high-voltage degradation test. Furthermore, the CNTs can lower the interfacial resistance between the OMC particles.

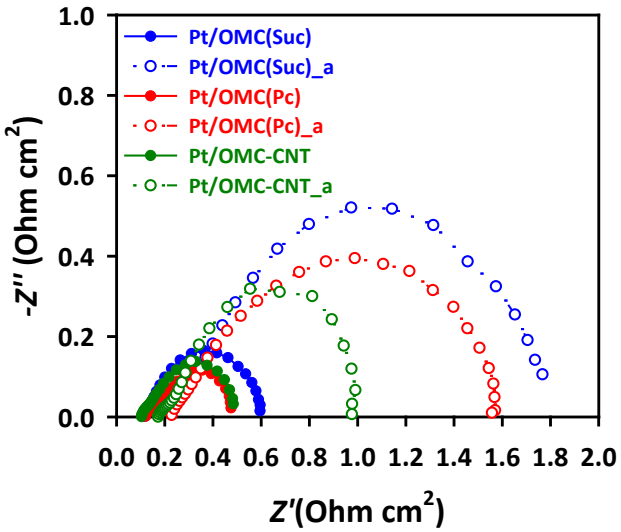

Figure 3.14. Nyquist plots for the Pt/OMC cathodes obtained by electrochemical impedance spectroscopy.

To further explore the origin of distinctively different single cell polarizations, electrochemical impedance spectra of the cells were obtained before and after the high-voltage

degradation test. The Nyquist plots for the PEMFCs with the Pt/OMC cathodes are shown in Figure 3.14, and their ohmic (R_s) and charge-transfer (R_{ct}) resistance values are Tlisted in Table 3.2. The ohmic and charge-transfer resistances of the three Pt/OMC cathodes before the durability tests were similar. This is indicated by the fact that the sizes of the circles in the Nyquist plots are similar. After the high-voltage degradation tests, the Nyquist plots of the PEMFC showed a clear differences, with the plot of the Pt/OMC-CNT-based PEMFC having the smallest circle. The charge-transfer resistance of the Pt/OMC-CNT-based PEMFC was lower than those of the PEMFCs based on the Pt/OMC(Pc) and Pt/OMC(Suc) catalysts by a factor of 2. This difference can be directly correlated to the differences in the respective current densities of the catalysts as determined from their polarization curves. From these results, it is clearly shown that the conductivity of the carbon support system, including the conductivity of frameworks of carbon support as well as interfacial conductivity between the primary particles of carbon support, can significantly affect single cell performance of MEAs based on the carbon-supported catalysts.

3.4. Conclusions

In the present study, we systematically investigated the use of three OMC-based supports that exhibited varying degrees of conductivities (namely, OMC(Suc), OMC(Pc), and OMC-CNT nanocomposites) for applications in PEMFC. In particular, we explored the use of OMC-CNT nanocomposites as a fuel cell catalyst support for the first time. The three OMC-based supports were prepared via a nanocasting strategy and showed large surface areas and pore volumes as well as well-developed mesoporosities. Among the three carbons, the OMC-CNT nanocomposites showed the highest conductivity, followed by the OMC(Pc) and the OMC(Suc). The three carbons could support highly dispersed Pt nanoparticles (1.5 nm). The ORR activities and kinetics of the Pt/OMC catalysts measured by the RRDE method revealed that the ORR activity of the Pt/OMC-CNT catalyst was higher than those of the Pt/OMC(Suc) and Pt/OMC(Pc) catalysts. This trend was even more pronounced after the ADTs. In single cell tests, the Pt/OMC-CNT catalyst also showed markedly superior current density to other two catalysts after the high-voltage degradation tests. We suppose that the rigidly interconnected structure and the highly conductive frameworks of the OMC-CNT nanocomposites are concomitantly responsible for its enhanced conductivity, activity, and durability. We believe that the results of this study provide unprecedented insights into the durability of the OMC-based catalysts under realistic, single cell operation condition. These insights may, in turn, be used to establish the guidelines for the design of high performance PEFC electrocatalysts based on OMC supports.

It is worth noting that the hybridization of two different carbon-based building blocks has emerged recently as a novel strategy for enhancing the activity and durability of fuel cell catalysts. For instance, Huang and co-workers recently reported that the durability of a graphene oxide-

supported Pt catalyst can be significantly improved through its hybridization with carbon black particles.[80] Our OMC-CNT nanocomposites synergistically combine the advantages of the OMCs and CNTs, thereby showing enhanced activity and durability over the OMC-only supports. We believe that when considered with the results of our previous study,[29] wherein we reported the use of OMC-CNT nanocomposites for high performance counter electrode for DSSC, the results of this study demonstrate the versatility of OMC-CNT nanocomposites as general platform materials for energy conversion and storage devices. Hence, the use of OMC-CNT nanocomposites in a wider range of applications is envisaged.

3.5. References

(1) Steele, B. C. H.; Heinzel, A. *Nature* **2001**, *414*, 345.

(2) Gasteiger, H. A.; Kocha, S. S.; Sompalli, B.; Wagner, F. T. *Appl. Catal. B-Environ.* **2005**, *56*, 9.

(3) Rabis, A.; Rodriguez, P.; Schmidt, T. J. *ACS Catal.* **2012**, ***2***, 864.

(4) Debe, M. K. *Nature* **2012**, *486*, 43.

(5) Chan, K. Y.; Ding, J.; Ren, J. W.; Cheng, S. A.; Tsang, K. Y. *J. Mater. Chem.* **2004**, *14*, 505.

(6) Antolini, E. *Appl. Catal. B-Environ.* **2009**, *88*, 1.

(7) Shao, Y. Y.; Liu, J.; Wang, Y.; Lin, Y. H. *J. Mater. Chem.* **2009**, *19*, 46.

(8) Mazumder, V.; Lee, Y.; Sun, S. H. *Adv. Funct. Mater.* **2010**, *20*, 1224.

(9) Zhang, W. M.; Sherrell, P.; Minett, A. I.; Razal, J. M.; Chen, J. *Energ. Environ. Sci.* **2010**, *3*, 1286.

(10) Shrestha, S.; Liu, Y.; Mustain, W. E. *Catal. Rev.* **2011**, *53*, 256.

(11) Qiao, Y.; Li, C. M. *J. Mater. Chem.* **2011**, *21*, 4027.

(12) Wang, C.; Marković, N. M.; Stamenkovic, V. R. *ACS Catal.* **2012**, *2*, 891.

(13) Stamenkovic, V. R.; Fowler, B. ; Mun, B. S.; Wang, G.; Ross, P. N.; Lucas, C. A.; Markovic, N. M. *Science* **2007**, *315*, 493.

(14) Zhang, J.; Sasaki, K.; Sutter, E.; Adzic, R. R. *Science* **2007**, *315*, 220.

(15) Lim, B.; Jiang, M.; Camargo, P. H. C.; Cho, E. C.; Tao, J. ; Lu, X.; Zhu, Y.; Xia, Y. *Science* **2009**, *324*, 1302.

(16) Koh, S.; Strasser, P. *J. Am. Chem. Soc.* **2007**, *129*, 12624.

(17) Bessel, C. A.; Laubernds, K.; Rodriguez, N. M.; Baker, R. T. K. *J. Phys. Chem. B* **2001**, *105*, 1115.

(18) Che, G. L.; Lakshmi, B. B.; Fisher, E. R.; Martin, C. R. *Nature* **1998**, *393*, 346.

(19) Li, W.; Liang, C.; Zhou, W.; Qiu, J.; Zhou, Z.; Sun, G.; Xin, Q. *J. Phys. Chem. B* **2003**, *107*, 6292.

(20) Chang, H.; Joo, S. H.; Pak, C. *J. Mater. Chem.* **2007**, *17*, 3078.

(21) Joo, S. H.; Choi, S. J.; Oh, I. ; Kwak, J. ; Liu, Z.; Terasaki, O.; Ryoo, R. *Nature* **2001**, *414*, 470.

(22) Yu, J. S.; Kang, S.; Yoon, S. B.; Chai, G. *J. Am. Chem. Soc.* **2002**, *124*, 9382.

(23) Yoo, E.; Okata, T.; Akita, T.; Kohyama, M.; Nakamura, J.; Honma, I. *Nano Lett.* **2009**, ***9***, 2255.

(24) Kamat, P. V. *J. Phys. Chem. Lett.* **2011**, *2*, 242.

(25) Ryoo, R.; Joo, S. H.; Kruk M.; Jaroniec, M. *Adv. Mater.* **2001**, *13*, 677.

(26) Lee, J.; Kim, J.; Hyeon, T. *Adv. Mater.* **2006**, *18*, 2073.

(27) Wan, Y.; Zhao, D. *Chem. Rev.* **2007**, *107*, 2821.

(28) Ramasamy, E.; Lee, J. *Chem. Commun.* **2010**, *46*, 2136.

(29) Zhou, H.; Zhu, S.; Hibino, M.; Honma, I.; Ichihara, M. *Adv. Mater.* **2003**, *15*, 2107.

(30) Nam, J.-H.; Jang, Y.-Y.; Kwon, Y.-U.; Nam, J.-D. *Electrochem. Commun.* **2004**, *6*, 737.

(31) Ding, J.; Chan, K.-Y.; Ren, J.; Xiao, F.-S. *Electrochim. Acta* **2005**, *50*, 3131.

(32) Su, F.; Zeng, J.; Bao, X.; Yu, Y.; Lee, J. Y.; Zhao, X. S. *Chem. Mater.* **2005**, *17*, 3960.

(33) Choi, W. C.; Woo, S. I.; Jeon, M. K.; Sohn, J. M.; Kim, M. R.; Jeon, H. J. *Adv. Mater.* **2005**, *17*, 446.

(34) Choi, Y. S.; Joo, S. H.; Lee, S. A.; You, D. J.; Kim, H.; Pak, C.; Chang, H.; Seung, D. *Macromolecules* **2006**, *39*, 3275.

(35) Joo, S. H.; Pak, C.; You, D. J.; Lee, S. A.; Lee, H. I.; Kim, J. M.; Chang, H.; Seung, D. *Electrochim. Acta* **2006**, *52*, 1618.

(36) Liu, S.-H.; Lu, R.-F.; Huang, S.-J.; Lo, A.-Y.; Chien, S.-H.; Liu, S.-B. *Chem. Commun.* **2006**, 3435.

(37) Zhou, J.; He, J.; Dang, W.; Zhao, G.; Zhang, C.; Mei, T. *Electrochem. Solid St.* **2007**, *10*, B191.

(38) Zhou, J.-H.; He, J.-P.; Ji, Y.-J.; Dang, W.-J.; Liu, X.-L.; Zhao, G.-W.; Zhang, C.-X.; Zhao, J.-S.; Fu, Q.-B.; Hu, H.-P. *Electrochim. Acta* **2007**, *52*, 4691.

(39) Calvillo, L.; Lazaro, M. J.; Garcia-Bordeje, E.; Moliner, R.; Cabot, P. L.; Esparbe, I.; Pastor, E.; Quintana, J. J. *J. Power Sources* **2007**, *169*, 59.

(40) Ren, J.; Ding, J.; Chan, K.-Y.; Wang, H. *Chem. Mater.* **2007**, *19*, 2786.

(41) Zhao, G.; He, J.; Zhang, C.; Zhou, J.; Chen, X.; Wang, T. *J. Phys. Chem. C* **2008**, *112*, 1028.

(42) Joo, S. H.; Lee, H. I.; You, D. J.; Kwon, K.; Kim, J. H.; Choi, Y. S.; Kang, M.; Kim, J. M.; Pak, C.; Chang, H.; Seung, D. *Carbon* **2008**, *46*, 2034.

(43) Shanahan, P. V.; Xu, L.; Liang, C.; Waje, M.; Dai, S.; Yan, Y. S. *J. Power Sources* **2008**, *185*, 423.

(44) Fang, B.; Kim, J. H.; Lee, C.; Yu, J. S. *J. Phys. Chem. C* **2008**, *112*, 639.

(45) Lei, Z.; Bai, S.; Xiao, Y.; Dang, L.; An, L.; Zhang, G.; Xu, Q. *J. Phys. Chem. C* **2008**, *112*, 722.

(46) Lin, M.-L.; Huang, C.-C.; Lo, M.-Y.; Mou, C.-Y. *J. Phys. Chem. C* **2008**, *112*, 867.

(47) Liu, S.-H.; Yu, W.-Y.; Chen, C.-H.; Lo, A.-Y.; Hwang, B.-J.; Chien, S.-H.; Liu, S.-B. *Chem. Mater.* **2008**, *20*, 1622.

(48) Joo, S. H.; Kwon, K.; You, D. J.; Pak, C.; Chang, H.; Kim, J. M. *Electrochim. Acta* **2009**, *54*, 5746.

(49) Lee, H. I.; Joo, S. H.; Kim, J. H.; You, D. J.; Kim, J. M.; Park, J. N.; Chang, H.; Pak, C. *J. Mater. Chem.* **2009**, *19*, 5934.

(50) Gupta, G.; Slanac, D. A.; Kumar, P.; Wiggins-Camacho, J. D.; Wang, X.; Swinnea, S.; More, K. L.; Dai, S.; Stevenson, K. J.; Johnston, K. P. *Chem. Mater.* **2009**, *21*, 4515.

(51) Gupta, G.; Slanac, D. A.; Kumar, P.; Wiggins-Camacho, J. D.; Kim, J.; Ryoo, R.; Stevenson, K. J.; Johnston, K. P. *J. Phys. Chem. C* **2010**, *114*, 10796.

(52) Su, F.; Poh, C. K.; Tian, Z.; Xu, G.; Koh, G.; Wang, Z.; Liu, Z.; Lin, J. *Energy & Fuels* **2010**, *24*, 3727.

(53) Liu, S.-H.; Chiang, C.-C.; Wu, M.-T.; Liu, S.-B. *Int. J. Hydrogen Energy* **2010**, *35*, 8149.

(54) Song, S.; Liang, Y.; Li, Z.; Wang, Y.; Fu, R.; Wu, D.; Tsiakaras, P. *Appl. Catal. B-Environ.* **2010**, *98*, 132.

(55) Kwon, K.; Jin, S. A.; Pak, C.; Chang, H.; Joo, S. H.; Lee, H. I.; Kim J. H.; Kim, J. M. *Catal. Today* **2011**, *164*, 186.

(56) Calvillo, L.; Celorrio, V.; Moliner, R.; Lazaro, M. J. *Mater. Chem. Phys.* **2011**, *127*, 335.

(57) Calvillo, L.; Gangeri, M.; Perathoner, S.; Centi, G.; Moliner, R.; Lazaro, M. J. *Int. J. Hydrogen Energy* **2011**, *36*, 9805.

(58) Guo, Y.; He, J.; Wang, T.; Xue, H.; Hu, Y.; Li, G.; Tang, J.; Sun, X. *J. Power Sources* **2011**, *196*, 9299.

(59) Liu, S.-H.; Chen, S.-C.; Sie, W.-H. *Int. J. Hydrogen Energy* **2011**, *36*, 15060.

(60) Tintula, K. K.; Sahu, A. K.; Shahid, A.; Pitchumani, S.; Sridhar, P.; Shukla, A. K. *J. Electrochem. Soc.* **2011**, *158*, B622.

(61) Liu, S.-H.; Wu, M.-T.; Lai, Y.-H.; Chiang, C.-C.; Yu, N.; Liu, S.-B. *J. Mater. Chem.* **2011**, *21*, 12489.

(62) Wu, Z.; Lv, Y.; Xia, Y.; Webley, P. A.; Zhao, D. *J. Am. Chem. Soc.* **2012**, *134*, 2236.

(63) Sun, X.; He, J.; Tang, J.; Wang, T.; Guo, Y.; Xue, H.; Li, G.; Ma, Y. *J. Mater. Chem.* **2012**, *22*, 10900.

(64) Maiyalagan, T.; Alaje, T. O.; Scott, K. *J. Phys. Chem. C* **2012**, *116*, 2630.

(65) Wu, Z.; Li, W.; Xia, Y.; Webley, P. A.; Zhao, D. *J. Mater. Chem.* **2012**, *22*, 8835.

(66) Xiang, D.; Yin, L. *J. Mater. Chem.* **2012**, *22*, 9584.

(67) Zeng, J.; Francia, C.; Dumitrescu, M. A.; Monteverde Videla, A. H. A.; Ijeri, V. S.; Specchia, S.; Spinelli, P. *Ind. Eng. Chem. Res.* **2012**, *51*, 7500.

(68) Kwon, K.; Sa, Y. J.; Cheon, J. Y.; Joo, S. H. *Langmuir* **2012**, *28*, 991.

(69) Wang, X.; Lee, J. S.; Zhu, Q.; Liu, J.; Wang, Y.; Dai, S. *Chem. Mater.* **2010**, *22*, 2178.

(70) Liu, R.; Wu, D.; Feng, X. L.; Mullen, K. *Angew. Chem. Int. Ed.* **2010**, *49*, 2565.

(71) Borup, R.; Meyers, J.; Pivovar, B.; Kim, Y. S.; Mukundan, R.; Garland, N.; Myers, D.; Wilson, M.; Garzon, F.; Wood, D.; Zelenay, P.; More, K.; Stroh, K.; Zawodzinski, T.; Boncella, J.; McGrath, J. E.; Inaba, M.; Miyatake, K.; Hori, M. Ota, K.; Ogumi, Z.; Miyata, S.; Nishikata, A.; Siroma, Z.; Uchimoto, Y.; Yasuda, K.; Kimijima, K. I.; Iwashita, N. *Chem. Rev.* **2007**, *107*, 3904.

(72) Lei, Z.; Bai, S.; Xiao, Y.; Dang, L.; An, L.; Zhang, G.; Xu, Q. *J. Phys. Chem. C* **2008**, *112*, 722.

(73) Jun, S.; Joo, S. H.; Ryoo, R.; Kruk, M.; Jaroniec, M.; Liu, Z.; Ohsuna, T.; Terasaki, O. *J. Am. Chem. Soc.* **2000**, *122*, 10712.

(74) Zhao, D.; Sun, J. Y.; Li, Q. Z.; Stucky, G. D. *Chem. Mater.* **2000**, *12*, 275.

(75) Deck, C. P.; Vecchio, K. *Carbon* **2006**, *44*, 267.

(76) Datta, K. K. R.; Balasubramanian, V. V.; Ariga, K.; Mori,, T.; Vinu, A. *Chem-Eur. J.* **2011**, *17*, 3390.

(77) Pak, C.; Chang, H.; Yoo, D. J.; Kim, J. M. *U.S. Pat. Appl*. **2006**, 0116284 A1.

4. Intrinsic Relationship between Enhanced Oxygen Reduction Reaction Activity and Nanoscale Work Function of Doped Carbons

4.1. Introduction

The oxygen reduction reaction (ORR) is a key process in clean energy technologies, such as polymer electrolyte fuel cells (PEFCs)[1,2] and metal-air batteries.[3] The state of the art electrocatalysts used in the ORR predominantly rely on platinum-based catalysts to overcome the sluggish reaction kinetics of the ORR.[4] However, the high cost and scarcity of platinum, as well as its susceptibility to poisoning and declining activity with use, are major drawbacks for the extensive deployment of these energy conversion devices. Therefore, a great deal of research has been devoted to developing non-precious metal-based[5-7] or metal-free[8-11] catalysts as potential replacements for the Pt-based catalysts. In particular, since Dai and co-workers reported a very high ORR activity for nitrogen-doped carbon nanotubes (CNTs),[12] metal-free ORR catalysts based on heteroatom-doped carbon nanostructures have seen remarkable progress during the last few years.

Recent studies have demonstrated that the doping of heteroatoms into nanostructured carbons can give rise to an enhanced performance in the ORR in terms of both activity and reaction kinetics, when compared with their undoped analogues.[12-23] In addition, multiple-dopants-incorporated nanocarbons showed further improvement in the ORR performances.[24-30] In efforts to elucidate the promotion effects of dopants in the ORR, it was suggested that changes in the charge and spin densities of the carbon lattice are major factors for the enhanced performance observed with doped nanocarbons;[12,16,19,21,23,25,26,28,29,31] however, these suggestions are based entirely on theoretical calculations. Experimental studies that can systemically correlate the impact of heteroatom doping in nanocarbons with enhanced ORR activity are rare.

Herein, we report direct experimental evidence that the nanoscale work function of doped nanocarbons, measured by Kelvin probe force microscopy (KPFM), is strongly correlated with the ORR activity and reaction kinetics of doped nanocarbon catalysts. We prepared a set of catalysts based on ordered mesoporous carbons (OMCs), which were selectively doped with N, S, and O. The triple-doped N,S,O-OMC exhibited superior catalytic activity and reaction kinetics in the ORR in an alkaline medium, when compared with the dual-doped (N,O-OMC and S,O-OMC) and the mono-doped (O-OMC) OMC catalysts. Using surface-sensitive KPFM measurements, we demonstrate that the reactivity trend of the OMCs in the ORR can be intrinsically correlated with the work functions of the respective catalysts. Therefore, if the local work function of the OMCs can be lowered in the presence of dopants, it is possible to boost the ORR, suggesting new evidence of enhanced ORR activity associated with heteroatom doping.

4.2. Experimental Section

4.2.1. Synthesis of heteroatom-doped ordered mesoporous carbons

Synthesis of SBA-15. Pluronic® P123 (8.0 g, M_w = 5800, Aldrich), deionized (DI) water (251.4 g), and 35% HCl (48.6 g, 35 wt%, Samchun) were added to a 500 mL polypropylene bottle, and the resulting mixture was stirred at 35 °C for 1 h. After the P123 was completely dissolved, tetraethyl orthosilicate (17.0 g, 98%, Aldrich) was added and the solution was stirred for 5 min and aged at 35 °C without stirring for 24 h. The reaction mixture was transferred into a Teflon®-lined autoclave and heated at 150 °C for 24 h. The resulting precipitate was filtered, washed twice with DI water, and then dried in an oven at 60 °C for 1 d. The dried sample was calcined at 550 °C for 5 h in air.

Synthesis of OMC. A solution containing the aromatic mesophase pitch (3.02 g, Mitsubishi Gas Chemical Company) and tetrahydrofuran (80 mL, OCI) was sonicated for 1 h. SBA-15 (2.0 g) was added to the solution, and the resulting mixture was stirred at room temperature for 1 h and then dried in an oven at 60 ^{o}C overnight. The dried mixture was added to a quartz tube furnace and heated to 350 ^{o}C at a rate of 1.4 ^{o}C min^{-1}, which exceeds the softening point of the aromatic mesophase pitch (320 ^{o}C). After maintaining the mixture at 350 ^{o}C for 4 h, it was heated to 900 ^{o}C at a rate of 2.6 ^{o}C min^{-1} and kept at this temperature for 2 h. The resulting carbon–silica composite was then washed twice with 10 wt% hydrofluoric acid (J.T. Baker) at room temperature for 1 h to remove the SBA-15 template.

Synthesis of O-OMC. Sucrose (1.375 g, Samchun) and 95% H_2SO_4 (0.14 g, Samchun) were dissolved in DI water (5 g). SBA-15 (1 g) was added to the solution and the resulting mixture placed in an oven at 100 °C for 6 h. The oven temperature was increased to 160 °C and kept at 160 ^{o}C for 6 h. The silica–carbon composite was added to a solution containing sucrose (0.83 g), H_2SO_4 (0.09 g), and DI water (5 g). The reaction mixture was heated at 100 °C for 6 h and increased to 160 °C for a further 6 h. The carbonization was carried out by pyrolysis upon heating to 900 °C under a flow of nitrogen for 2 h. The silica was leached out using the same procedure as described for OMC.

Synthesis of N,O-OMC. SBA-15 (1 g) was added to a solution of glucosamine (1.54 g, Aldrich), H_2SO_4 (0.17 g), and DI water (5 g). The mixture was placed in an oven and treated at 100 °C and 160 °C using the same procedure described for O-OMC. The composite was added to a solution containing glucosamine (0.96 g), H_2SO_4 (0.11 g), and DI water (5 g) and heated at 100 °C and 160 °C as described for O-OMC. The mixture was then heated to 900 °C at a ramping rate of 2.5 °C min^{-1}, and kept at this temperature for 3 h under a flow of nitrogen. The silica was leached out using the same procedure as described for the OMC.

Synthesis of S,O-OMC. SBA-15 (1 g) was added to a solution of *p*-toluenesulfonic acid (1.85 g, Aldrich) and acetone (1.85 g, Samchun). The composite material was placed in an oven and heated at 100 ^{o}C and 160 ^{o}C using the same procedure described for O-OMC. The infiltration-drying process

was repeated using a solution containing *p*-toluenesulfonic acid (1.85 g) and acetone (1.15 g). The resulting mixture was carbonized at 900 °C under a flow of nitrogen for 3 h. S,O-OMC was obtained upon leaching the silica using the same procedure as described for the OMC.

Synthesis of N,S,O-OMC. SBA-15 (1 g) was added to a solution containing glucosamine (0.76 g), *p*-toluenesulfonic acid (0.92 g), H_2SO_4 (0.08 g), and DI water (5 g). The mixture was heated at 100 °C and 160 °C using the same procedure described for O-OMC. The infiltration-drying process was repeated using 66 w/w% of the initial reactants with the exception of DI water (5 g). The N,S,O-OMC was obtained after carbonization and acid washing using the procedure as described for the OMC.

4.2.2. Characterization methods

All characterization was carried out at the Ulsan National Institute of Science and Technology (UNIST) Central Research Facilities (UCRF) Center. X-ray photoelectron spectroscopy (XPS) was performed using a K-alpha instrument from Thermo Fisher. X-ray powder diffraction (XRPD) data was measured using a Rigaku D/MAZX 2500V/PC diffractometer at 40 kV and 200 mA equipped with a Cu Kα (λ = 1.5418 Å) source, with a step size of 0.02° in 2θ. Transmission electron microscopy (TEM) images were obtained using a JEOL JEM-2100 microscope. High-angle annular dark-field scanning transmission electron microscopy (HAADF STEM) images and the corresponding elemental mapping images were obtained using a JEOL JEM-2100F microscope. The morphologies of the samples were observed using a Hitachi S-4800 scanning electron microscope (SEM) operating at 10 kV. The nitrogen adsorption-desorption isotherms were measured at -196 °C using liquid nitrogen on a BELSORP-MAX instrument. Prior to the adsorption measurement, the samples were evacuated at 200 °C under vacuum ($p < 10^{-5}$ mbar) for 12 h. The specific surface area was determined in the relative pressure range of 0.05 - 0.3 of the Brunauer-Emmett-Teller (BET) plot and the total pore volume calculated from the amount adsorbed at a relative pressure of ~ 0.98-0.99. The pore size distribution was obtained using the Barrett-Joyner-Halenda (BJH) method. This data is summarized in Table 4.1.

4.2.3. Electrochemical measurements

Electrochemical characterization of the samples was carried out using an IviumStat electrochemical analyzer. The electrochemical experiments were performed at room temperature (25 °C) under atmospheric pressure using a three-compartment electrochemical cell. A graphite counter electrode and Hg/HgO reference electrode (XR400, Radiometer Analytical) with 1 M KOH (99.999%, Aldrich) filling solution were used. The Hg/HgO reference electrode was calibrated to the reversible hydrogen electrode (RHE) before every measurement.

For the ORR performance measurement, a rotating ring-disk electrode (RRDE) with a glassy

carbon disk (GC, 4 mm in diameter) and a Pt ring (5 mm in inner diameter and 7 mm in outer diameter) was used as the working electrode (ALS, Cat. No. 012613). The RRDE was polished with 1.0 and 0.3 μm alumina suspensions to generate a mirror finish. The catalyst ink was prepared by mixing the catalyst (7.5 mg), Nafion (75 μL), deionized water (100 μL), and ethanol (1.01 mL, >99.9%, Samchun) [for Pt/C catalyst, 5 mg of 20 wt% Pt/C (Johnson & Matthey, HiSPEC 3000), 40 μL of Nafion, and 1.15 mL of ethanol were used] using ultrasonication for at least 30 min. The resulting catalyst loading was 0.15 mg cm^{-2}, except Pt/C catalyst (0.1 mg_{cat} cm^{-2}). Prior to the electrochemical measurements, a potential cycle from 0.05 to 1.2 V was applied in a N_2-saturated solution of 0.1 M KOH for 50 cycles at a scan rate of 100 mV s^{-1} for electrochemical cleaning. The cyclic voltammogram was obtained under the same conditions used for electrochemical cleaning, except the scan rate was changed to 20 mV s^{-1} for 3 cycles. Linear sweep voltammetry (LSV) curves for the ORR were obtained using a potential cycle from 1.1 to 0.2 V (for Pt/C, LSV curve was obtained from 0.2 to 1.1 to avoid the formation of Pt-O species.) in an O_2-saturated solution of 0.1 M KOH with O_2 purging at different rotating speeds. The ORR measurement was independently repeated three times, and the averaged currents were used.

For the evaluation of four-electron selectivity, the potential of the Pt ring was fixed at 1.3 V (vs. RHE) during LSV scans for the ORR. The number of electrons transferred was calculated by

$$n = \frac{4}{1 + \frac{I_R}{N \times I_D}}$$

where: I_D, I_R, and N are the disk current, the ring current, and the collection coefficient, respectively. The value of N was determined to be 0.44 in a 1 M KNO_3 + 2 mM $K_3Fe(CN)_6$ solution at a rotating speed of 1000 rpm.

The ORR activity and four-electron selectivity of the undoped/doped OMC catalysts were also evaluated in acid using the same experimental conditions, except the use of 0.1 M $HClO_4$ electrolyte.

4.3. Results and Discussion

Heteroatom-doped OMCs with hexagonal mesostructures were prepared *via* a nanocasting method using SBA-15 mesoporous silica as a template and N-, S-, and O-containing carbon sources as precursors. Glucosamine, *p*-toluenesulfonic acid, and sucrose were used as sources of carbon as well as dopants. For the preparation of the triple-doped N,S,O-OMC, a mixture of glucosamine and *p*-toluenesulfonic acid was infiltrated into the SBA-15 template and carbonized at 900 °C under an inert atmosphere, followed by the removal of the SBA-15 template using HF. The dual-doped OMCs, N,O-OMC and S,O-OMC, were prepared from a mixture of glucosamine and sucrose and *p*-toluenesulfonic acid and sucrose, respectively. Mono-doped O-OMC was produced from sucrose

under similar conditions. It should be noted that whilst earlier literature generally neglected the role of oxygen as a dopant, there is currently an increasing notion that oxygen can modify the catalytic activity of nanocarbons.[11,18,23] For comparison, the nearly dopant-free OMC was prepared using a mesophase pitch.

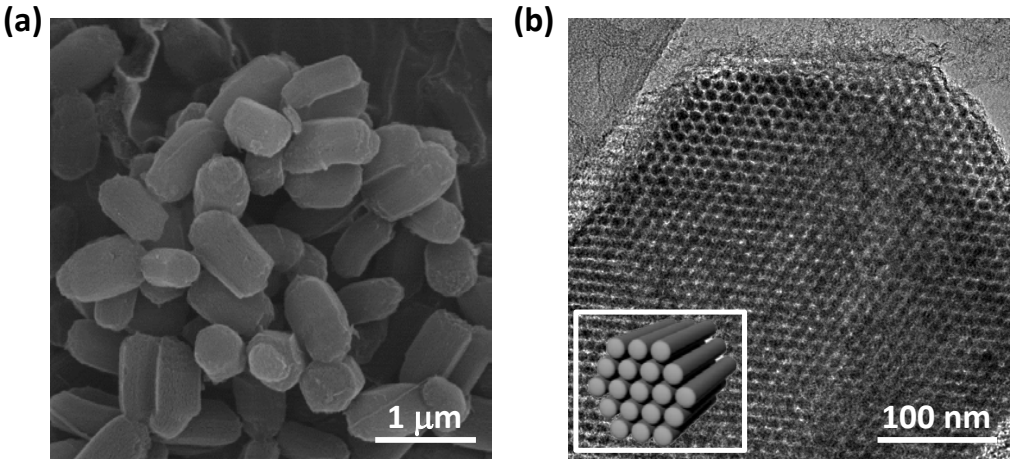

Figure 4.1. Characterization of the N,S,O-OMC. (a) SEM image, (b) TEM image taken parallel to the pore direction.

Scanning and transmission electron microscope (SEM and TEM, respectively) images revealed that the silica template, SBA-15 was successfully replicated onto the doped OMCs while preserving its morphology (Figure 4.1a, b). The well-resolved small-angle XRD peaks of the doped OMCs (Figure 4.2) indicated a CMK-3-type two dimensional, hexagonally ordered mesostructure.[32] Nitrogen physisorption analysis revealed that the N,S,O-OMC has a uniform mesopore centered at ~ 9.6 nm with a high Brunauer-Emmett-Teller (BET) surface area (1060 cm^2 g^{-1}) and total pore volume of 1.85 cm^3 g^{-1}. The other doped OMCs also showed high BET surface areas and pore volumes, similar to those found with the N,S,O-OMC (Figure 4.3 and Table 4.1).

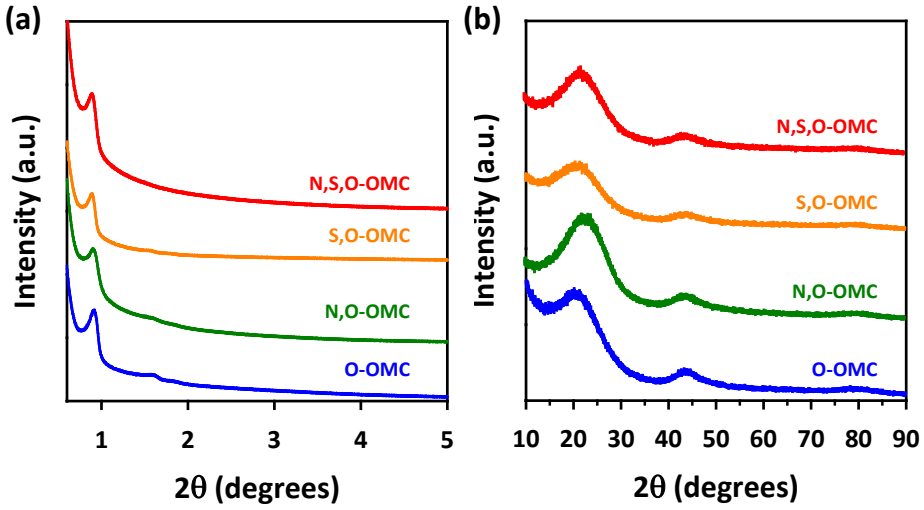

Figure 4.2. (a) Small-angle and (b) wide-angle XRD patterns of the doped OMCs.

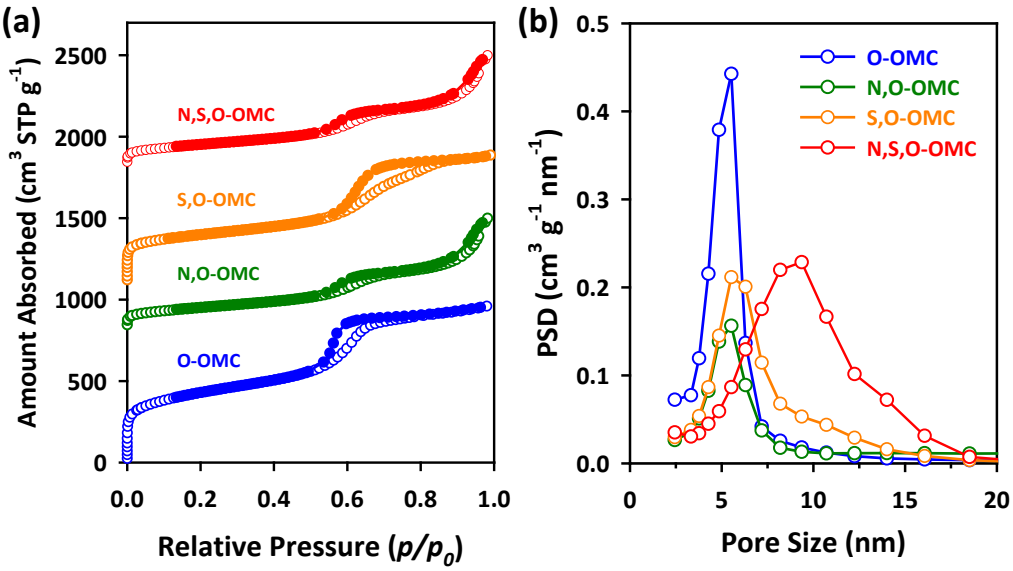

Figure 4.3. (a) N_2 adsorption-desorption isotherms of the doped OMCs and (b) their corresponding pore size distribution (PSD) curves obtained from the adsorption branches.

Table 4.1. BET surface areas, pore volumes, and pore sizes of the doped OMCs.

Sample	BET surface area (m^2 g^{-1})[a]	Pore volume (cm^3 g^{-1})[b]	Pore size (nm)[c]
O-OMC	1550	1.48	5.5
N,O-OMC	534	1.08	5.5
S,O-OMC	1080	1.22	5.5
N,S,O-OMC	1060	1.85	9.3

[a]BET surface area was calculated in the relative pressure range of 0.05-0.3.
[b]Pore volume was calculated at the relative pressure of 0.98-0.99.
[c]Pore size was calculated by the BJH method using the adsorption branches of isotherms.

The presence of dopants in the N,S,O-OMC was confirmed by using high angle annular dark field scanning TEM (HAADF STEM) image coupled with the elemental mapping image of the respective elements (Figure 4.4a). The high-resolution XPS C 1s spectrum of the N,S,O-OMC (Figure 4.4b) was highly asymmetric because of the presence of C-C and C=C bonds as well as heteroatom-containing bonding moieties. The deconvolution of the C 1s peak includes the C-S-C (284.1 eV), C-C/C=C (284.8 eV), C-O (285.6 eV), and C-N-C (286.8 eV) bonding moieties, which indicates that the N, S, and O dopants were successfully incorporated into the carbon framework of the N,S,O-OMC (Figure 4.4b).[26] The details of the chemical composition of the doped and undoped OMCs are summarized in Table 4.2. Overall, a series of five OMCs with similar textural properties bearing different types of dopant have been prepared and can be used as model catalysts for the systematic investigation of the dopant effects in the ORR.

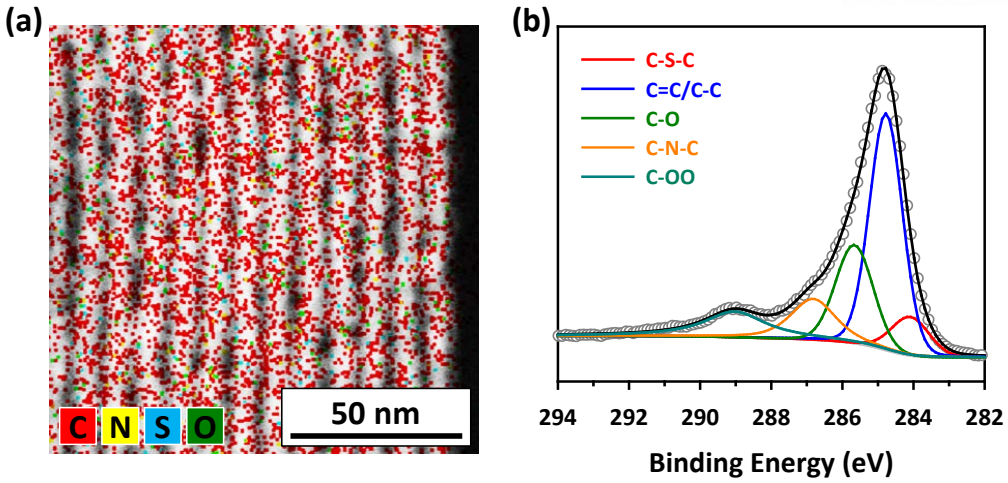

Figure 4.4. (a) HAADF-STEM image overlapped with the corresponding C, N, S, and O elemental mappings, and (b) XPS C 1s spectrum.

Table 4.2. Chemical compositions of the undoped and doped OMCs (at%).[a]

Sample	C	N	S	O
OMC	97.8	-	-	2.2
O-OMC	93.5	-	-	6.4
N,O-OMC	85.9	2.4	-	11.6
S,O-OMC	91.7	-	3.5	4.8
N,S,O-OMC	90.3	2.1	0.7	6.9

[a]Chemical compositions of the doped OMCs were obtained from XPS analysis.

To investigate the electrocatalytic activity of the heteroatom-doped OMCs in the ORR, linear sweep voltammetry (LSV) experiments were performed on a rotating ring disk electrode (RRDE) using an O_2-saturated solution of 0.1 M KOH, at a scan rate of 5 mV s^{-1} and a rotating speed of 1600 rpm (Figure 4.5a and Table 4.3). Among the investigated samples, the OMC displayed the lowest ORR activity in terms of on-set and half-wave potentials. The single-doped O-OMC showed enhanced ORR activity, when compared to the OMC, indicating the beneficial effect of oxygen atoms in the ORR. The dual doping of N and O in N,O-OMC resulted in higher ORR activity when compared to the O-OMC. However, the sulfur and oxygen dual-doped S,O-OMC exhibited a lower ORR activity than that found with O-OMC. It is known that electronegative N atoms (3.04) break the charge neutrality of C atoms (2.55) atoms in the sp^2 carbon lattice, providing adsorption sites for oxygen moelcules.[12] On the other hand, sulfur atoms (2.58) have an electronegativity similar to that of carbon atoms (2.55) and the effect of sulfur doping on the ORR is still controversial.[11,23] Similar to our results, Qiao and co-workers reported that S-doped graphene has a higher adsorption free energy of the ORR intermediate (OOH) compared to that of O-doped graphene, resulting in lower ORR

activity.[23] Finally, triple-doped N,S,O-OMC exhibited a further enhancement in ORR activity when compared to N,O-OMC, which make the N,S,O-OMC the most active catalyst amongst the doped OMCs prepared in this study. The most active N,S,O-OMC showed an on-set potential at 0.85 V and its kinetic current density at 0.75 V was 3.8 mA cm^{-2}. The enhanced ORR activity of the N,S,O-OMC catalyst is consistent with those previously reported.[26,27,30]

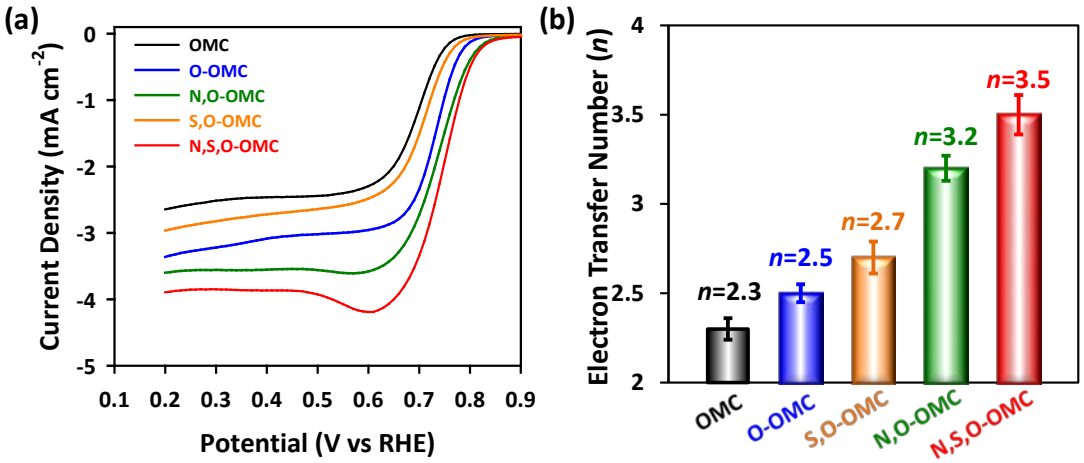

Figure 4.5. (a) LSV curves of the doped OMCs for the ORR. (b) The electron transfer numbers of the doped OMCs at 0.6 V (vs. RHE) during the ORR.

Table 4.3. ORR activity and reaction kinetics of the undoped and doped OMCs.

Sample	On-set potential (V *vs.* RHE)	Half-wave potential (V *vs.* RHE)	Kinetic current at 0.75 V vs RHE (mA cm^{-2})	Electron transfer number at 0.6 V vs RHE
OMC	0.77	0.69	0.3	2.2
O-OMC	0.80	0.71	1.2	2.5
N,O-OMC	0.84	0.74	2.5	3.2
S,O-OMC	0.79	0.70	0.5	2.7
N,S,O-OMC	0.85	0.75	3.8	3.5

To gain further insight into the role of heteroatom doping in carbon, we investigated the reaction kinetics using the RRDE method. The H_2O_2 yields (Figure 4.6) were calculated by measuring the ring current, from which the number of electrons (*n*) transferred during the ORR could be obtained (Figure 4.5b and Table 4.3). The O-OMC had an *n* value of 2.5 at 0.6 V, suggesting that its oxygen reduction proceeds via a quasi-two-electron process. Note that the participation of a surface quinone group of oxygen functionalized carbon during the reduction of O_2 often leads to the peroxide pathway.[11] On the other hand, N or S doping to nanostructured carbon was found to convert the ORR activity from a two-electron to a four-electron reduction pathway.[16,21] In addition, the enhanced four-electron selectivity was also observed in the dual doped OMC catalysts. The *n* values for the dual-doped N,O-OMC and S,O-OMC were 3.2 and 2.7, respectively. Triple-doped N,S,O-OMC displayed

an increased *n* value of 3.5, which indicated that the ORR over the N,S,O-OMC proceeded *via* a quasi-four-electron pathway. This result suggests that triple doping with N, S, and O in the OMC has a synergistic impact on the ORR activity and selectivity, giving rise to enhanced performance when compared to the dual- doped and mono-doped OMCs.

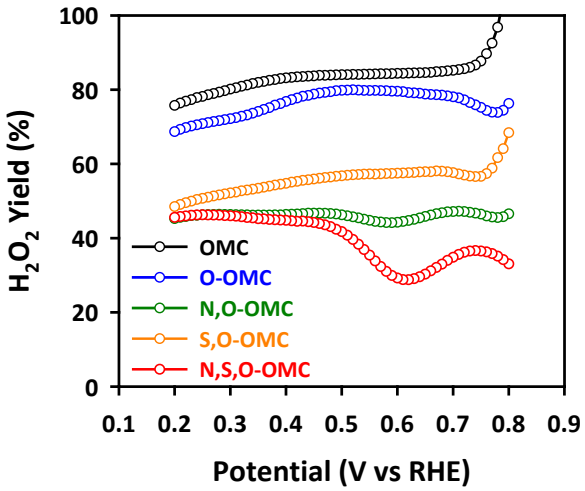

Figure 4.6. H_2O_2 yields of the undoped and doped OMCs calculated from the measurement of the ring current during the ORR.

The experimental results presented in this work as well as in previously reported studies[8-30] clearly suggest that heteroatom doping in carbon lattices can provide enhanced ORR activity and reaction kinetics. Dai and co-workers substantiated this phenomenon by density functional theory (DFT) calculations; they showed that the high electron affinity of N in N-doped carbon nanotubes can induce a positive charge density on an adjacent C atom, which can facilitate oxygen adsorption and subsequently weaken the bonding in the oxygen molecule.[12] For the dual-doped system, Qiao and co-workers suggested using DFT calculations that N and S dual-doped graphene induces an upshift of its maximum spin density, which results in a significantly enhanced ORR activity.[26] Luo et al. showed the enhanced ORR activity of N-doped graphene was associated with the reduced work function due to an increase in the density of π states near the Fermi level using ultraviolet photoemission spectroscopy.[33]

In our study, the local work function of doped OMC was characterized using KPFM to understand the correlation between ORR activity and the variation in work function, and to address the role of the dopants in the enhancement of the ORR activity. KPFM is a derivative imaging mode of scanning probe microscopy and is a versatile technique that can directly monitor the changes in local work function of solid surfaces with an energy resolution of at ~ 10 mV, together with the corresponding topography. Because KPFM measures the voltage required to nullify the work function difference between the conductive tip and the sample (φ_{tip} - φ_{sample}), the contrast in the contact potential difference (CPD) image is equivalent to the local work function variation of the sample.[34-36]

Hence, KPFM has been widely used to investigate the influence of dopants or atomic scale defects on the variation of work function.[34-36]

KPFM measurements on the OMC surfaces were carried out using an Agilent 5500 atomic force microscope (AFM) with a conductive non-contact cantilever coated with Pt/Ir and a nominal resonance frequency of 75 kHz. For the CPD measurement, samples were prepared by transferring the OMCs onto a gold-coated silicon wafer using a drop-casting method. Because the OMC partially covers the gold substrate, the measured CPD value on gold substrates can be used as the reference value. Therefore, the work function of various doped OMCs can be determined at a nanometer scale without any ambiguity.

Figure 4.7a, b shows the topographical and CPD images simultaneously taken on the O-OMC, respectively. Figure 4.7c shows the line profiles acquired along the white dashed lines of the O-OMC sample. he height of the O-OMC was typically 100-200 nm. The dark contrast observed in the CPD image indicates a high sample work function, therefore the φ of the O-OMC is higher than that of the gold plate by ~ 50 mV (Figure 4.7c). Considering that φ_{Au}, and φ_{carbon} are reported as 4.9-5 eV[37,38] and ~ 5 eV,[39,40] respectively, the measured value of the work function on the OMC is consistent with those previously reported. However, the CPD images of N,S,O-OMC clearly show a different contrast, as shown in the topographical (Figure 4.7d) and CPD images (Figure 4.7e). Figure 4.7f shows the line profile of the topographical and CPD images acquired along the white dashed lines for the N,S,O-OMC sample. As shown in Figure 4.7e, f, the triply doped N,S,O-OMC displays a bright contrast indicating a lower work function than observed with φ_{Au} of ~ 70 mV.

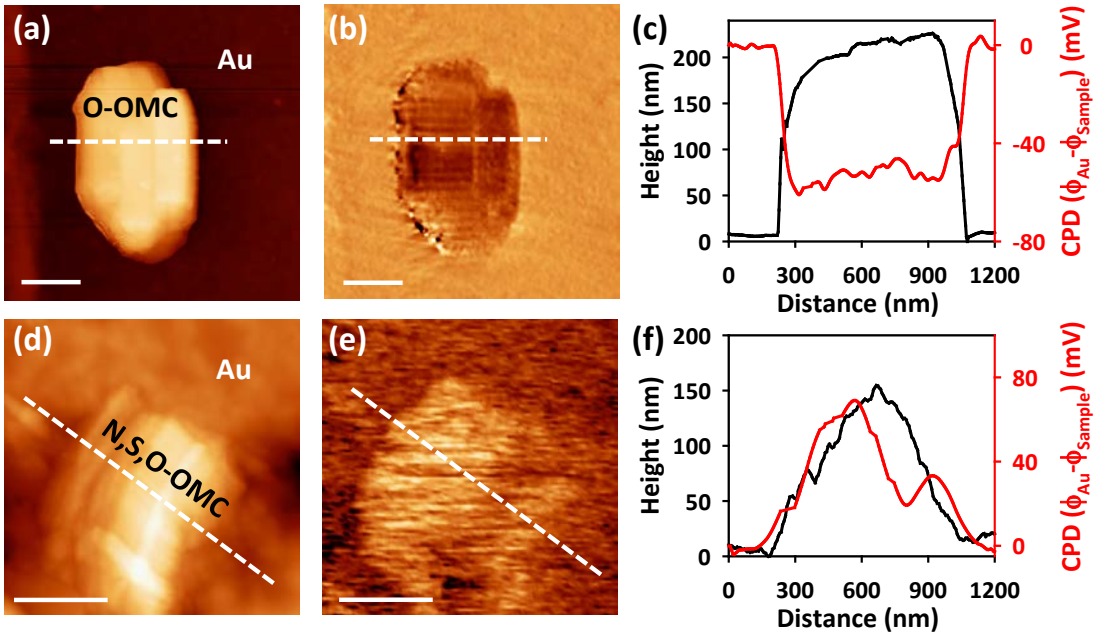

Figure 4.7. (a,d) Topography and (b,e) CPD images for the O-OMC (top) and the N,S,O-OMC (bottom). The scale bar at the bottom left of the Figures is 400 nm. For both samples, the height and CPD profiles along the white dashed lines are drawn in (c) and (f) as the black and the red lines, respectively.

To increase the reproducibility and ascertain the correlation with the ORR activity tests, CPD measurements were carried out on the multiple OMC particles placed at various locations (Figure 4.8a). The error bar in Figure 4.8a represents the standard deviation associated with the multiple measurements on 5 different samples and the insets show representative CPD maps for each sample. Figure 4.8a shows a plot of the CPD measured on OMC, O-OMC, S,O-OMC, N,O-OMC, and N,S,O-OMC, which clearly reveals a systematic variation of CPD values (and therefore their work functions) depending on the type of dopants used. The CPD images of the samples (Figure 4.8a, inset) exhibit gradual changes from the darkest contrast found in the OMC to the brightest contrast found in the N,S,O-OMC, in accordance with changes in the CPD values. This systematic change in work functions of the samples is depicted in the energy diagram of the tip-sample systems shown in Figure 4.8b.

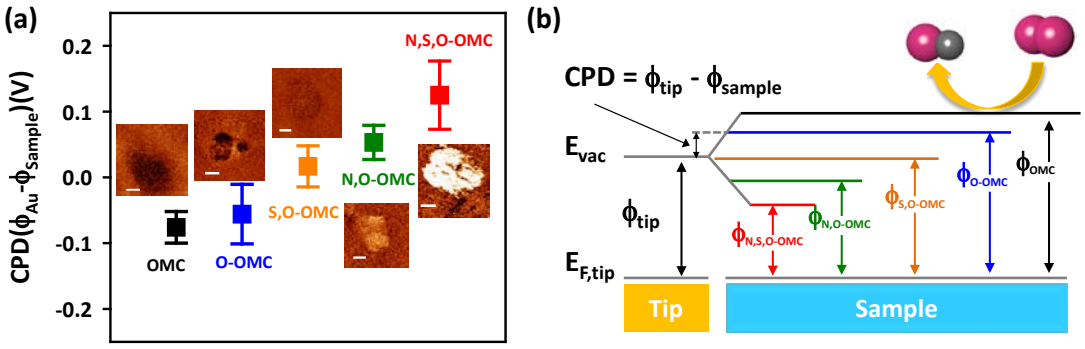

Figure 4.8. (a) The CPD variation depending on the OMC dopants. (Insets: representative CPD images for each specimen using a common CPD scale. Scale bar is 200 nm) (b) Energy diagram of the tip–sample system where oxygen reduction can be activated when an electron overcomes the potential barrier of the work function. E_{vac} implies the vacuum level. For each sample, the colors for the work function notation in Figure 4.8b match those in Figure 4.8a.

The work functions of the doped OMCs were correlated with their kinetic current densities at 0.75 V (Figure 4.9a), and with their electron transfer numbers (*n*) during the ORR (Figure 4.9b). These Figures show that these kinetic parameters are inversely proportional to the work functions of each sample. In particular, the *n* values of the doped OMCs have a strong linear relationship with their work function. This indicates that a sample with a lower work function (i.e. higher CPD value) has a lower energetic barrier for donating electrons from the surface of the catalyst to the adsorbed oxygen, thereby facilitating the formation of the OOH species, which is known to be the rate determining step in the ORR.[23] We also measured the ORR activity of the doped OMCs in an acidic medium (0.1 M $HClO_4$), and correlated the ORR reactivity with the work function values (Figure 4.10). We found that the LSV curves of the doped OMCs in acid showed the same trend as those in alkaline solutions. In addition, the correlation between the ORR activity and kinetics of the doped OMCs in acid with their work functions exhibited the same trends as those measured in alkaline solutions, confirming that the work function of a carbon-based catalyst can be used as an effective parameter for predicting the ORR activity.

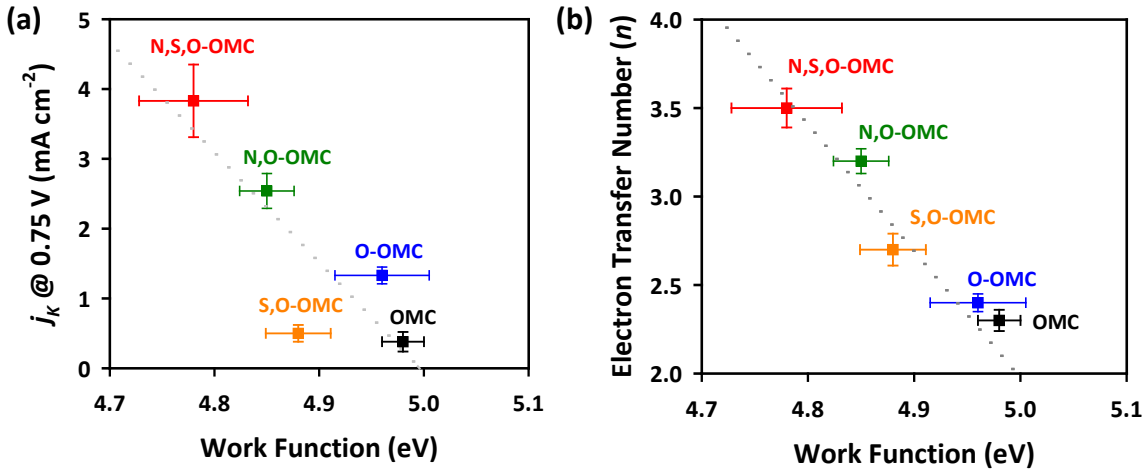

Figure 4.9. (a,b) Correlation of ORR activity (a) and four-electron selectivity (b) of the doped OMCs with their work function values.

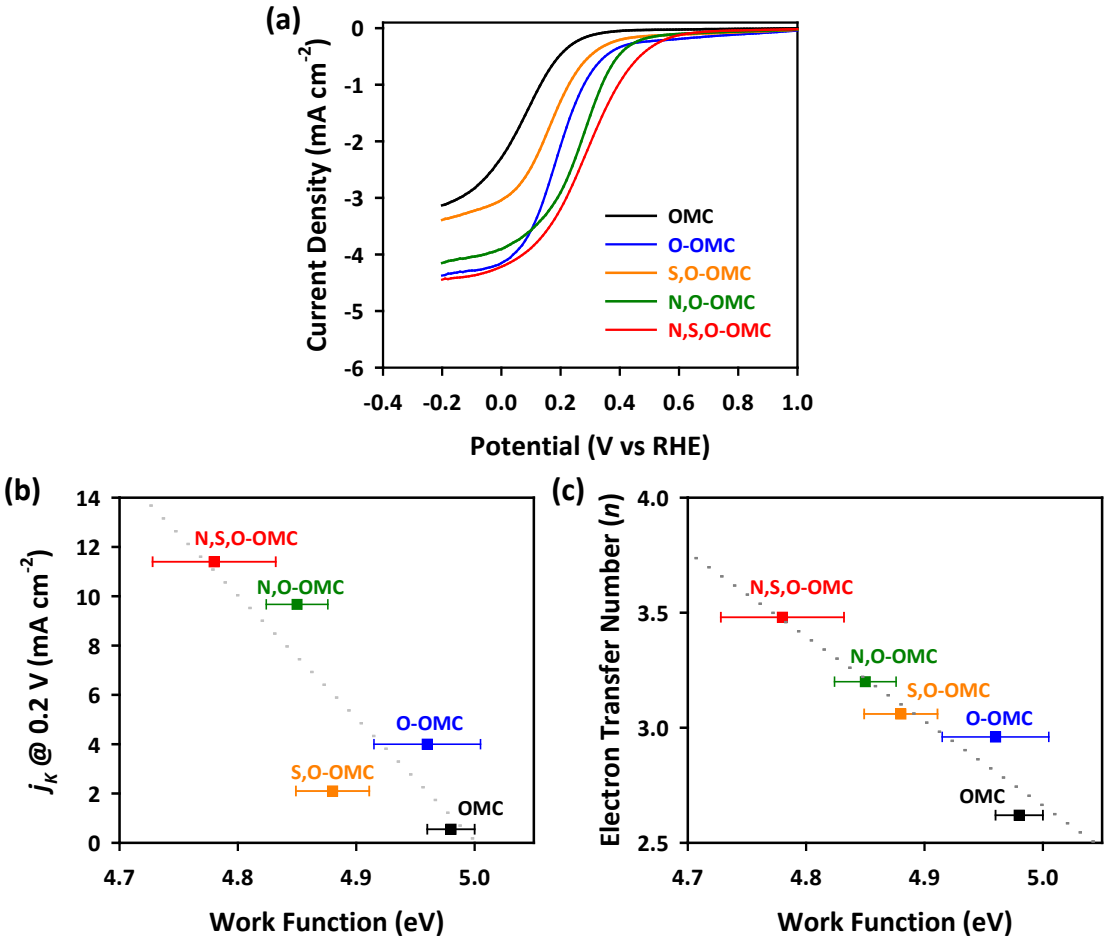

Figure 4.10. (a) LSV curves of the undoped and doped OMCs for the ORR in 0.1 M $HClO_4$. (b,c) Corresponding correlation of the ORR activity (b) and four-electron selectivity (c) with their work function values.

4.4. Conclusions

In conclusion, we have prepared a series of heteroatom-doped OMCs as metal-free electrocatalysts for a systematic study into the dopant effects in the ORR. The triple-doped N,S,O-OMC catalyst displayed the best ORR activity and four-electron selectivity, when compared to the dual-doped (N,O- and S,O-OMC) and mono-doped (O-OMC) OMC catalysts. KPFM was used to investigate the doped OMCs and their work function was found to be dependent on the type of dopant used. Significantly, we established that the nanoscale work function of the doped OMCs, measured by KPFM, could be correlated with their ORR activity and reaction kinetics. Spatial mapping of the CPD led to determination of the reference work function of the gold surface and the nanoscale work function of doped OMC without ambiguity. We envisage from this unprecedented insight that the work function of the doped nanocarbons can be generally used as an activity descriptor for the ORR as well as other catalytic reactions. In addition, this study may provide the design principle for the development of advanced electrocatalysts for other important reactions.

4.5. References

(1) Steele, B. C. H.; Heinzel, A. *Nature* **2001**, *414*, 345.

(2) Debe, M. K. *Nature* **2012**, *486*, 43.

(3) Bruce, P. G.; Freunberger, S. A.; Hardwick, L. J.; Tarascon, J. M. *Nat. Mater.* **2012**, *11*, 19.

(4) Gasteiger, H. A.; Kocha, S. S.; Sompalli, B.; Wagner, F. T. *Appl. Catal. B* **2005**, *56*, 9.

(5) Lefevre, M.; Proietti, E.; Jaouen, F.; Dodelet, J. -P. *Science* **2009**, *324*, 71.

(6) Wu, G.; More, K. L.; Johnston, C. M.; Zelenay, P. *Science* **2011**, *332*, 443.

(7) Cheon, J. Y.; Kim, T.; Choi, Y.; Jeong, H. Y.; Kim, M. G.; Sa, Y. J.; Kim, J.; Lee, Z.; Yang, T. H.; Kwon, K.; Terasaki, O.; Park, G. G.; Adzic, R. R.; Joo, S. H. *Sci. Rep.* **2013**, *3*, 2715.

(8) Zheng, Y.; Jiao, Y.; Jaroniec, M.; Jin, Y.; Qiao, S. Z. *Small* **2012**, *8*, 3550.

(9) Dai, L. *Acc. Chem. Res.* **2013**, *46*, 31.

(10) Paraknowitsch, J. P.; Thomas, A. *Energy Environ. Sci.* **2013**, *6*, 2839.

(11) Wang, D.-W.; Su, D. *Energy Environ. Sci.* **2014**, *7*, 576.

(12) Gong, K.; Du, F.; Xia, Z.; Durstock, M.; Dai, L. *Science* **2009**, *323*, 760.

(13) Liu, R.; Wu, D.; Feng, X.; Müllen, K. *Angew. Chem., Int. Ed.* **2010**, *49*, 2565.

(14) Qu, L.; Liu, Y.; Baek, J.-B.; Dai, L. *ACS Nano* **2010**, *3*, 1321.

(15) Yang, S.; Feng, X.; Wang, X.; Müllen, K. *Angew. Chem., Int. Ed.* **2011**, *50*, 5339.

(16) Zheng, Y.; Jiao, Y.; Chen, J.; Liu, J.; Liang, J.; Du, A.; Zhang, W.; Zhu, Z.; Smith, S. C.; Jaroniec, M.; Lu, G. Q.; Qiao, S. Z. *J. Am. Chem. Soc.* **2011**, *133*, 20116.

(17) Kwon, K.; Sa, Y. J.; Cheon, J. Y.; Joo, S. H. *Langmuir* **2012**, *28*, 991.

(18) Silva, R.; Voiry, D.; Chhowalla, M.; Asefa, T. *J. Am. Chem. Soc.* **2013**, *135*, 7823.

(19) Yang, L.; Jiang, S.; Zhao, Y.; Zhu, L.; Chen, S.; Wang, X.; Wu, Q.; Ma, J.; Ma, Y.; Hu, Z.

Angew. Chem., Int. Ed. **2011**, *50*, 7132.

(20) Yang, S. B.; Zhi, L. J.; Tang, K.; Feng, X.; Maier, J.; Müllen, K. *Adv. Funct. Mater.* **2012**, *22*, 3634.

(21) Jeon, I.-Y.; Zhang, S.; Zhang L.; Choi, H.-J.; Seo, J.-M.; Xia, Z.; Dai, L.; Baek, J.-B. *Adv. Mater.* **2013**, *25*, 6138.

(22) Yang, D.; Bhattacharjya, D.; Inamdar, S.; Park, J.; Yu, J. S. *J. Am. Chem. Soc.* **2012**, *134*, 16127.

(23) Jiao, Y.; Zheng, Y.; Jaroniec, M.; Qiao, S. Z. *J. Am. Chem. Soc.* **2014**, *136*, 4394.

(24) Wang, S.; Iyyamperumal, E.; Roy, A.; Xue, Y.; Yu, D.; Dai, L. *Angew. Chem., Int. Ed.* **2011**, *50*, 11756.

(25) Wang, S.; Zhang, L.; Xia, Z.; Roy, A.; Chang, D. W.; Baek, J. B.; Dai, L. *Angew. Chem., Int. Ed.* **2012**, *51*, 4209.

(26) Liang, J.; Jiao, Y.; Jaroniec, M.; Qiao, S. Z. *Angew. Chem., Int. Ed.* **2012**, *51*, 11496.

(27) Liu, X.; Antonietti, M. *Adv. Mater.* **2013**, *25*, 6284.

(28) Zheng, Y.; Jiao, Y.; Ge, L.; Jaroniec, M.; Qiao, S. Z. *Angew. Chem., Int. Ed.* **2013**, *52*, 3110.

(29) Zhao, Y.; Yang, L.; Chen, S.; Wang, X.; Ma, Y.; Wu, Q.; Jiang, Y.; Qian, W.; Hu, Z. *J. Am. Chem. Soc.* **2013**, *135*, 1201.

(30) Xu, J.; Dong, G.; Jin, C.; Huang, M.; Guan, L. *ChemSusChem* **2013**, *6*, 493.

(31) Zhang, L.; Xia, Z. *J. Phys. Chem. C* **2011**, *115*. 11170.

(32) Jun, S.; Joo, S. H.; Ryoo, R.; Kruk, M.; Jaroniec, M.; Liu, Z.; Ohsuna, T.; Terasaki, O. *J. Am. Chem. Soc.* **2000**, *122*, 10712.

(33) Luo, Z.; Lim, S.; Tian, Z.; Shang, J.; Lai, L.; MacDonald, B.; Fu, C.; Shen, Z.; Yu, T.; Lin, J. *J. Mater. Chem.* **2011**, *21*, 8038.

(34) Liscio, A.; Palermo, V.; Samori, P. *Acc. Chem. Res.* **2010**, *43*, 541.

(35) Liu, C.; Hwang, Y. J.; Jeong, H. E.; Yang, P. *Nano Lett.* **2011**, *11*, 3755.

(36) Kim, J.-H.; Hwang, J. H.; Suh, J.; Tongay, S.; Kwon, S.; Hwang, C. C.; Wu, J.; Park, J. Y. *Appl. Phys. Lett.* **2013**, *103*. 171604.

(37) de Boer, B.; Hadipour, A.; Mandoc, M. M.; van Woudenbergh, T.; Blom, P. W. M. *Adv. Mater.* **2005**, *17*, 621.

(38) Ravirajan, P.; Haque, S. A.; Durrant, J. R.; Poplavskyy, D.; Bradley, D. D. C.; Nelson, J. *J. Appl. Phys.* **2004**, *95*, 1473.

(39) de Jonge, N.; Allioux, M.; Doytcheva, M.; Kaiser, M.; Teo, K. B. K.; Lacerda, R. G.; Milne, W. I. *Appl. Phys. Lett.* **2004**, *85*, 1607.

(40) Gao, R.; Pan, Z.; Wang, Z. L. *Appl. Phys. Lett.* **2001**, *78*, 1757.

5. Ordered Mesoporous Porphyrinic Carbons with Very High Electrocatalytic Activity for the Oxygen Reduction Reaction

5.1. Introduction

Owing to their high energy conversion efficiency and environmental benignity as well as their suitability for small electronic devices, residential power generation and automobile transportation, PEFCs have long been considered promising energy conversion devices.[1-5] As electrocatalysts of PEFCs, carbon-supported platinum-based nanoparticles have been used predominantly as anode as well as cathode electrodes.[3-5] However, even Pt-based electrocatalysts exhibit sluggish kinetics for the ORR at the cathodes of PEFCs. Moreover, they tend to sinter or agglomerate into larger particles during long-term fuel cell operation, resulting in a marked loss of activity.[6] The prohibitively high cost and scarcity of Pt have also been bottlenecks that further impede the widespread use of PEFCs. Therefore, the high cost along with the low durability of Pt-based catalysts triggered the quest for low-cost, high-performance non-precious metal catalysts.

Since Jasinski reported the electrocatalytic activity of Co-phthalocyanine in ORR in an alkaline medium,[7] the class of non-precious metal catalysts has been a topic of continuous interests.[8-40] The non-precious metal catalysts for ORR consist of naturally abundant transition metals (primarily Fe or Co), nitrogen, and carbon; such catalysts are commonly prepared by mixing the sources of each component, followed by pyrolysis in inert or reactive gas environment.[8-11] Although synthetic optimization in recent years has led to improved activities and durability in non-precious metal catalysts,[12-27] particularly in alkali media,[22,23] their ORR activity are still significantly lower than Pt-based catalysts in acidic electrolytes, as manifested by their larger overpotentials (or half-wave potentials) by 45 - 400 mV. This situation has required the realistic comparison of the ORR activities of non-precious metal catalysts at 0.8 V[41] instead of 0.9 V, at which Pt-based catalysts are commonly gauzed.[3]

Here we report on a simple approach to scalable and highly reproducible synthesis of a new family of nonprecious metal catalysts - self-supported, transition metal-doped ordered mesoporous porphyrinic carbons (M-OMPCs) - which exhibit Pt-like catalytic activity for the ORR. The M-OMPC catalysts were prepared by nanocasting ordered mesoporous silica (OMS) templates with metalloporphyrin precursors, and were constructed with three-dimensional networks of porphyrinic carbon frameworks. Our synthetic strategy for the non-precious metal catalysts included a multitude of advantages that would be favorable to PEFC applications. First, our synthetic route is amenable to simple and mild experimental conditions. Previous approaches to non-precious metal-based M-N-C (M= Fe or Co) catalysts relied, in most cases, on the use of two or three separate sources for metal, nitrogen, and carbon.[8-11] Furthermore, to obtain high ORR activity, employing multiple pyrolysis steps

or toxic ammonia gas was unavoidable.[16-20] In contrast, our method could produce M-N-C catalysts from a single metalloporphyrin precursor in a single pyrolysis step under inert atmosphere without using ammonia gas. Second, the pore sizes and connectivity of the M-OMPC catalysts were readily tunable by utilizing OMS templates with different pore sizes and structures. Third, the synthesis of the M-OMPC catalysts could be readily scaled up, with the preservation of structural integrity, to a few tens of grams in a single batch. Fourth, well-developed, hierarchical micro-mesopores would be advantageous for efficient transport of fuels and by-products. Finally, the M-OMPC catalysts showed very high surface areas, which could significantly increase the density of the catalytically active sites accessible to reactants. Among the family of M-OMPC catalysts, the Fe and Co co-doped OMPC (FeCo- OMPC) showed an extremely high electrocatalytic activity for ORR in acidic media. To our knowledge, its ORR activity is one of the best among the non-precious metal catalysts reported in the literature, and even higher than the state-of-the-art Pt/C catalyst by 80 % at 0.9 V (vs. reversible hydrogen electrode, RHE). In addition, the FeCo-OMPC showed superior long-term durability and methanol-tolerance in ORR, compared to the Pt/C. Density functional theory (DFT) calculations coupled with extended X-ray absorption fine structure (EXAFS) analysis revealed a weakening of the interaction between oxygen atom and FeCo-OMPC compared to Pt/C. We attribute the high ORR activity of the FeCo-OMPC to its relatively weak interaction with oxygen as well as the high surface area design of catalyst.

5.2. Experimental Section

5.2.1. Synthesis of ordered mesoporous porphyrinic carbons

M-OMPC catalysts. M-OMPC catalysts were synthesized by a solid-state nanocasting method[42,43] that used OMS as a template and FeTMPPCl (Porphyrin Systems) and CoTMPP (TCI) as precursors. Calcined OMS (1.0 g) was mixed with the precursor (1.0 g), and the mixture was ground for 10 min in a mortar and transferred to an alumina crucible. The mixture was subsequently heated at temperatures ranging from 600 °C to 1000 °C with a ramping rate of 2.5 °C min^{-1}, and was held at a specific temperature for 3 h under nitrogen flow. The resulting carbon-silica composite was then washed twice with 10% HF (J. T. Baker) at room temperature for 1 h to remove the OMS template.

Mesoporous silica MSU-F. Large pore mesoporous silica MSU-F was synthesized following the literature method[44]. Pluronic® P123 (8.4 g) and DI water (336.8 g) were added to a 500 mL polypropylene bottle, and the mixture was stirred at 35 °C. After P123 was completely dissolved, mesitylene (4.2 g, 98%, Aldrich) was added and the solution was stirred again for 1 h at 35 °C. Sodium silicate solution (20.6 g, ~26.5% SiO_2, Aldrich) and 10% acetic acid (43.7 g, 99.7 wt%, Junsei) were sequentially added, and the solution was aged at 35 °C with stirring for 20 h. The reaction mixture was then transferred to a Teflon®-lined autoclave and heated at 100 °C for 24 h. Subsequent washing and calcination were carried out in the same manner described above for SBA-15.

Synthesis of FeCo-KB catalyst. Carbon black (Ketjenblack® 300) was mixed with a 1:1 (in mass ratio) precursor mixture of FeTMPPCl and CoTMPP, pyrolysed at 800 °C under N_2 flow, and finally washed with 0.5 M H_2SO_4 at 80 °C for 8 h. The Fe and Co loadings in the FeCo-KB catalyst were 1.7 and 1.2 %, respectively, which were similar to the metal loadings in the FeCo-OMPC catalyst.

Synthesis of FeCo-Cabosil catalyst. Fumed silica (Cab-O-sil® M-5, Fluka) was mixed with a 1:1 (in mass ratio) precursor mixture of FeTMPPCl and CoTMPP, pyrolysed at 800 °C under N_2 flow. The silica was leached out by the same procedure as described for M-OMPC catalysts.

5.2.2. Characterization methods

X-ray diffraction (XRD) patterns of the samples were measured with an X-ray diffractometer (Rigaku D/Max 2500V/PC) equipped with a Cu Kα source operating at 40 kV and 200 mA. The morphologies of the samples were observed using a scanning electron microscope (SEM) (Quanta 200, FEI) operating at 18 kV. The microstructural and elemental analyses of the catalyst powders were performed using HRTEM, HAADF-STEM [JEOL JEM 2100F with a probe forming Cs corrector at 200 kV (convergence angle: 30 mrad, semi-angles for HAADF detector: 61-163 mrad)], and EELS techniques (FEI Titan3 G2 cube 60-300 with an image forming Cs corrector equipped with a monochromator). EELS spectra were collected using a Gatan Quantum 965 spectrometer where a monochromated electron beam was excited. The porous structures of the samples were analysed by a nitrogen adsorption experiment at -196 °C using a BEL BELSORP-Max system. The surface areas of the samples were calculated using the Brunauer-Emmett-Teller (BET) equation. The mesopore and micropore size distributions of the samples were calculated using the Barrett-Joyner-Halenda (BJH) and the Horvath-Kawazoe (HK) algorithms, respectively. The surface compositions of the catalysts were measured using an X-ray photoelectron spectrometer (XPS) (K-Alpha, Thermo Scientific), equipped with a monochromatic Al K-α X-ray source (1486.6 eV). Individual chemical components of the N 1s binding energy (BE) region were fitted to the spectra by the Gaussian (Gaussian 70, Lorentzian 30)-function after a linear (Shirley)-type background subtraction. The carbon, hydrogen, and nitrogen contents in the samples were determined by Thermo Scientific Flash 2000 elemental analyzer. The metal contents in the catalysts were measured by inductively coupled plasma optical emission spectrometry (ICP-OES) using a Varian 720-ES instrument.

5.2.3. Electrochemical measurements

The electrochemical characterization of the catalysts was performed using an IviumStat electrochemical analyzer. The characterization experiments were performed at room temperature (25 °C) using a three-electrode electrochemical cell. A Pt-wire counter electrode separated by fritted glass and an Ag/AgCl reference electrode were used. All potentials in this study were reported with

respect to the RHE. A rotating ring-disk electrode (RRDE) was used as a working electrode. The RRDE was polished with a 1.0 μm alumina suspension and then with a 0.3 μm suspension to afford a mirror finish. The catalyst (30 mg) was mixed with deionized (DI) water (0.1 mL), ethanol (1.01 mL), and 5 wt% Nafion® (0.075 mL, 5 wt% in isopropanol, Aldrich). The resulting slurry was ultra-sonicated for 30 min to generate a catalyst ink. The ink (3.0 μL) was pipetted onto the 0.126 cm2 glassy carbon electrode, resulting in a catalyst loading of 596 μg cm^{-2}. Before the electrochemical measurements, the catalyst was cleaned by cycling the potential between 0 and 1.2 V at 100 mV s^{-1} for 50 cycles using a N_2-saturated 0.1 M $HClO_4$ solution as an electrolyte. Cyclic voltammetry (CV) was performed over voltages ranging from 0 to 1.2 V at a scan rate of 20 mV s^{-1} using a N_2-saturated 0.1 M $HClO_4$ electrolyte. ORR activity was recorded in O_2-saturated 0.1 M $HClO_4$ electrolyte with linear sweep voltammetry (LSV) performed for voltages ranging from 1.1 to 0.2 V at a scan rate of 5 mV s^{-1}. The disk rotation speed was 100-2500 rpm. Commercial 20 wt% platinum on Vulcan® carbon black (Pt/C, E-TEK) was measured for comparison. The catalyst ink was prepared as follows. The Pt/C catalyst (5 mg) was mixed with DI water (0.1 mL), ethanol (1.07 mL), and 5 wt% Nafion® (0.013 mL, in isopropanol, Aldrich). Other experimental conditions were the same as for the M-OMPC catalysts, except that ORR activity data were collected from anodic sweeps. The durability tests were performed on the catalysts by cycling the electrode potential between 0.6 and 1.0 V at 50 mV s^{-1} for 10,000 cycles.

5.3. Results and Discussion

5.3.1. Synthesis and structural characterization of M-OMPC catalysts.

Figure 5.1a schematically shows our synthetic strategy for the M-OMPC catalysts. We exploited a nanocasting method[45,46] for the preparation of the M-OMPC catalysts using OMSs as hard templates. As representative examples, 1 g of a metalloporphyrin precursor was mixed with 1 g of the SBA-15 template, and the mixture was pyrolyzed at 800 °C under nitrogen. The use of 5,10,15,20-tetrakis(4-methoxyphenyl)-21H,23H-porphine iron(III) chloride (FeTMPPCl), 5,10,15,20-tetrakis(4-methoxyphenyl)-21H,23H-porphine cobalt(II) (CoTMPP), or a 1:1 (mass ratio) mixture of FeTMPPCl and CoTMPP as precursors afforded Fe-OMPC, Co-OMPC, or FeCo-OMPC, respectively. The transmission electron microscopy (TEM) image of the FeCo-OMPC (Figure 5.1b) clearly showed that uniform carbon nanorods of 10 nm in diameter were arranged in a honeycomb-like hexagonal structure, with uniform mesopores being generated between the carbon nanorods. This clearly indicates that the SBA-15 silica template was faithfully replicated into a negative replica, FeCo-OMPC. The TEM images of the final FeCo-OMPC sample indicated no formation of metallic particles, although the possible existence of very small metallic particles (<1 nm) cannot be ruled out.

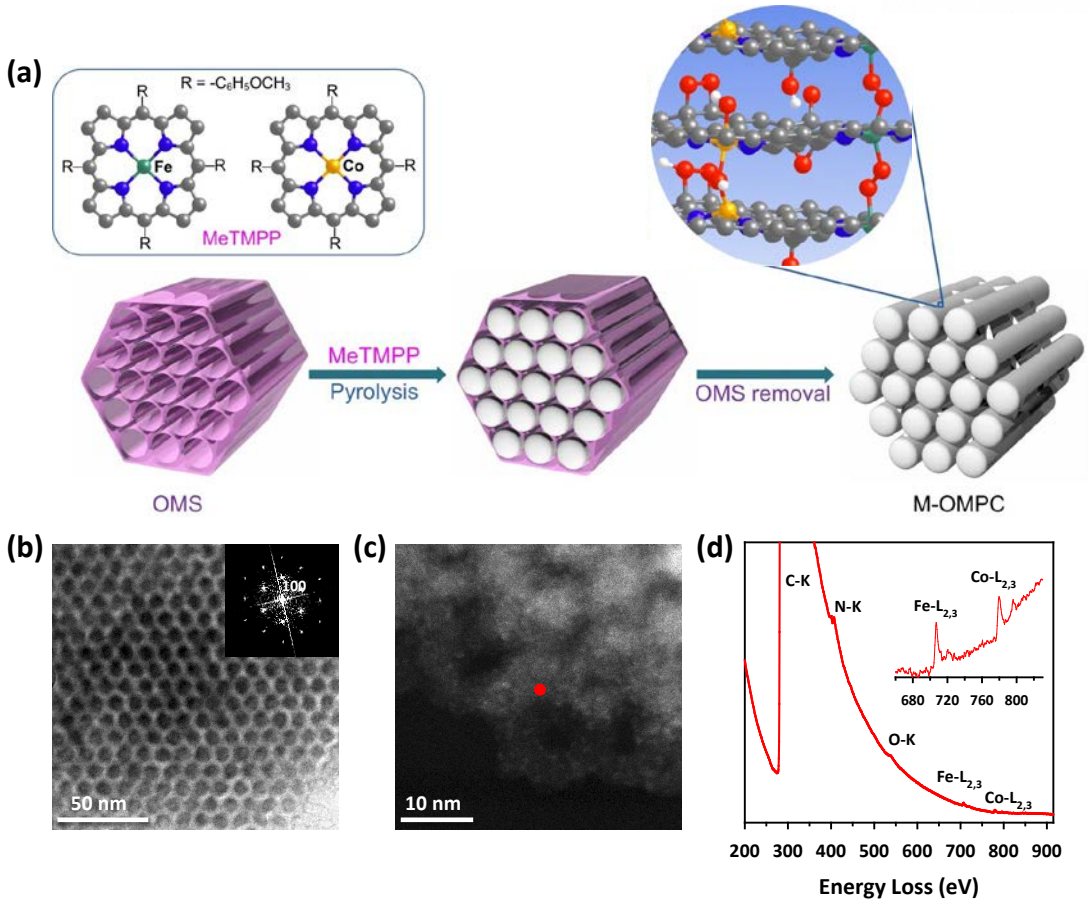

Figure 5.1. Synthetic strategy and characterization of M-OMPC catalysts. (a) Schematic synthetic strategy. The M-OMPC catalysts were synthesized via a nanocasting method that employed OMSs as templates and metalloporphyrins as the carbon source. The high temperature pyrolysis resulted in an OMS/carbon composite, after which the final M-OMPC catalysts were generated through the removal of the OMS template by HF etching. Grey, blue, green, orange, red, and white spheres represent C, N, Fe, Co, O, and H, respectively. (b) TEM image and the corresponding Fourier diffractogram (inset) of FeCo-OMPC templated from SBA-15 mesoporous silica showing hexagonal arrays of uniform carbon nanorods and mesopores generated between the nanorods. (c) HAADF STEM image of FeCo-OMPC catalyst. (d) EELS at the region of the red spot in the HAADF STEM image.

The low-angle X-ray diffraction patterns of M-OMPCs (Figure 5.2) exhibited three distinct diffraction lines corresponding to the (100), (110), and (200) planes of the hexagonal mesostructure. The nitrogen adsorption analysis of the FeCo-OMPC (Figure 5.3) revealed that the catalysts had well-developed mesoporosity and high surface areas. The pore size distribution curve (Figure 5.3, inset) of the FeCo-OMPC analyzed by the Barrett-Joyner-Halenda and the Horvath-Kawazoe methods showed peak maxima at 4.9 nm (mesopore) and 0.5 nm (micropore), respectively. The high porosity of FeCo-OMPC stemming from the hierarchical micro-mesopores provided a very high Brunauer-Emmett-Teller (BET) surface area of 1,190 m^2 g^{-1} and a total pore volume of 1.40 cm^3 g^{-1} (Table 5.1). The nanocasting employing metalloporphyrin precursors is general, and could be extended to other OMS templates; the nanocasting using MSU-F silica with large, spherical mesopores yielded large pore (ca. 20 nm) FeCo-OMPC(L) (Figure 5.4 and Table 5.1).

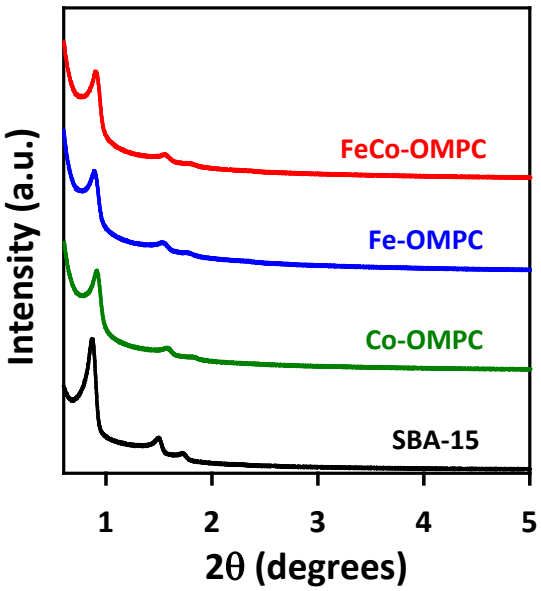

Figure 5.2. Low-angle XRD patterns of SBA-15 and M-OMPC catalysts.

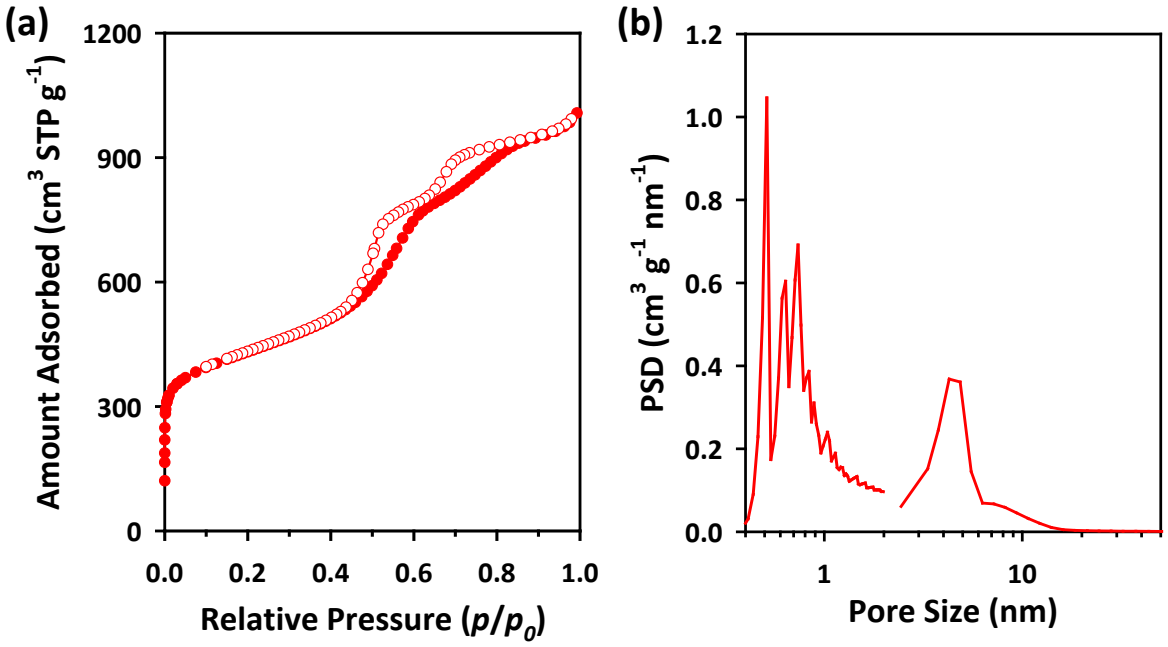

Figure 5.3. (a) N_2 adsorption isotherms of SBA-15 template and FeCo-OMPC catalyst. (b) The pore size distribution (PSD) curve of FeCo-OMPC obtained from adsorption branch of its isotherm.

Table 5.1. Structural properties of prepared catalysts.

Catalysts	S_{BET} (m^2 g^{-1})[a]	V_{tot} (cm^3 g^{-1})[b]	d_{meso} (nm)[c]
FeCo-OMPC	1190	1.40	4.85
Fe-OMPC	1168	1.49	4.27
Co-OMPC	1112	1.35	4.27
FeCo-OMPC (L)	930	1.65	18.5
OMPC	1496	1.76	4.27
FeCo-KB	105	0.79	3.33
FeCo-Cabosil	546	1.15	10.77

[a]BET specific surface areas obtained from N_2 adsorption isotherm in the range of p/p_0 = 0.05-0.2.
[b]Total pore volumes.
[c]Primary mesopore diameter calculated from BJH method.

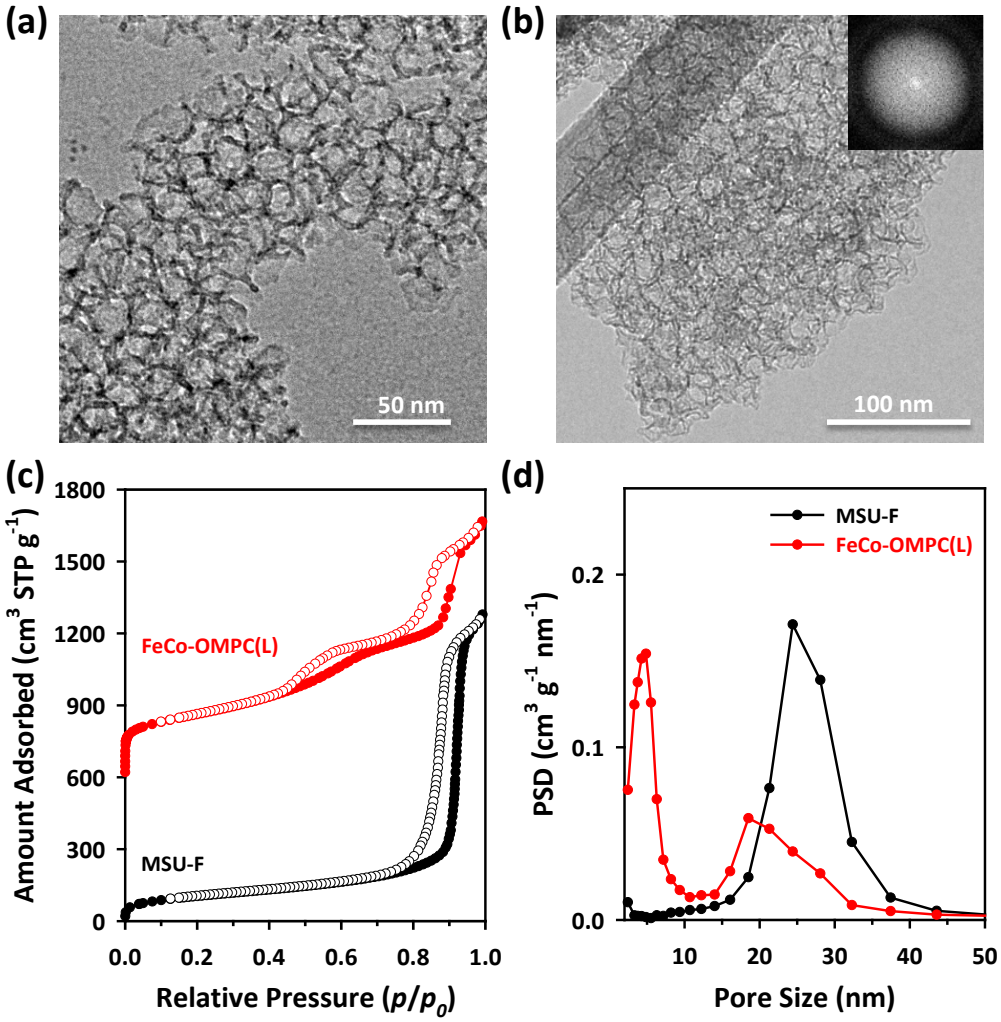

Figure 5.4. Structural characterization of MSU-F silica and FeCo-OMPC(L). (a) TEM image of large pore MSU-F mesoporous silica template. (b) TEM image and the corresponding Fourier diffractogram (inset) of large pore FeCo-OMPC(L) templated from MSU-F mesoporous silica. (c) N_2 adsorption isotherms of MSU-F mesoporous silica template and FeCo-OMPC(L) catalyst. (d) The corresponding pore size distribution (PSD) curves obtained from adsorption branches of their isotherms. The isotherm of FeCo-OMPC(L) is shifted 600 cm^3 g^{-1} upwards for clarity.

We analyzed the distribution and chemical states of the elements in the FeCo-OMPC. The high angle annular dark field scanning transmission electron microscopy (HAADF STEM) image (Figure 5.1c) showed bright dots (heavy elements, Fe and Co), which were uniformly distributed over a single particle. Furthermore, an electron energy loss spectroscopy (EELS) spectrum (Figure 5.1d) acquired at the red spot in Figure 5.1c clearly indicated the presence of C, N, O, Fe, and Co. The X-ray photoelectron spectroscopy (XPS) survey spectrum of the FeCo-OMPC (Figure 5.5a) also revealed the presence of C, N, O, Fe, and Co on the surface of the catalyst. The detailed analysis of the N 1s spectrum (Figure 5.5b) showed three peaks centered at 398.2, 399.8, and 401.8 eV, which could be associated with pyridinic, pyrrolic or metal-N, and graphitic groups, respectively. Inductively coupled plasma-optical emission spectroscopy analysis and CHNS elemental analysis indicated that the amounts of Fe, Co, and N in the FeCo-OMPC pyrolyzed at 800 °C were 2.5, 2.3, and 5.4 wt.%, respectively.

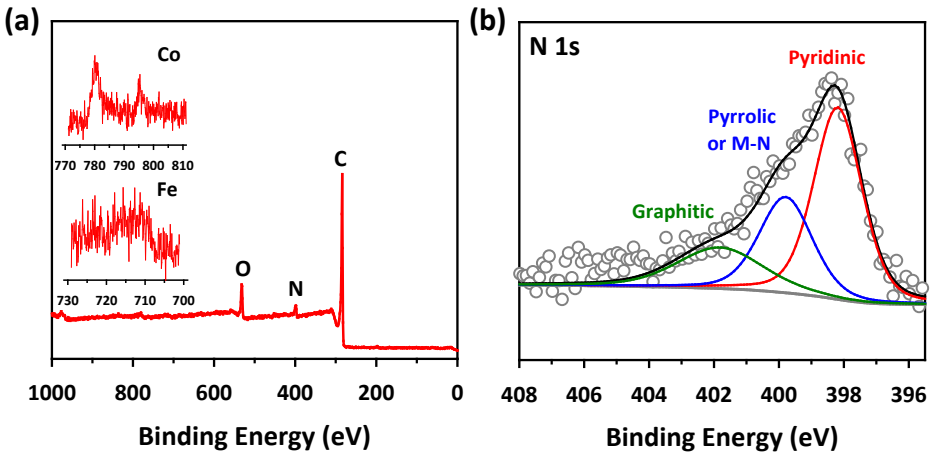

Figure 5.5. XPS survey (a) and N 1s spectra (b) of FeCo-OMPC catalyst.

5.3.2. ORR activity and durability of M-OMPC catalysts.

We next explored the electrocatalytic activity of the MOMPC catalysts along with reference catalysts using rotating ring-disk electrode (RRDE) measurements in 0.1 M $HClO_4$ solution (Figure 5.6). In general, M-OMPC catalysts showed very high ORR activity, compared to other catalysts. Of the various M-OMPC catalysts, FeCo-OMPC pyrolyzed at 800 °C under N_2 showed the highest ORR activity. FeCo-OMPC showed on-set and half-wave potentials at 1.000 V and 0.851 V, respectively (Figure 5.6a), and its kinetic current density at 0.9 V, calculated after correction for diffusion current, was 2.42 mA cm^{-2} (Figure 5.6b). The other M-OMPC catalysts also showed very high electrocatalytic activities for ORR. The large pore FeCo-OMPC(L) and monometal-doped Fe-OMPC and Co-OMPC catalysts exhibited ORR polarisation curves similar to that of FeCo-OMPC, with their half-wave potentials being shifted to lower potentials by only less than 45 mV, compared to that of the FeCo-OMPC (Figure 5.6a). We note that the synergistic effect of using two different metal centres (Fe and Co) in enhancing ORR activity was also observed in previous studies.[20,29,37]

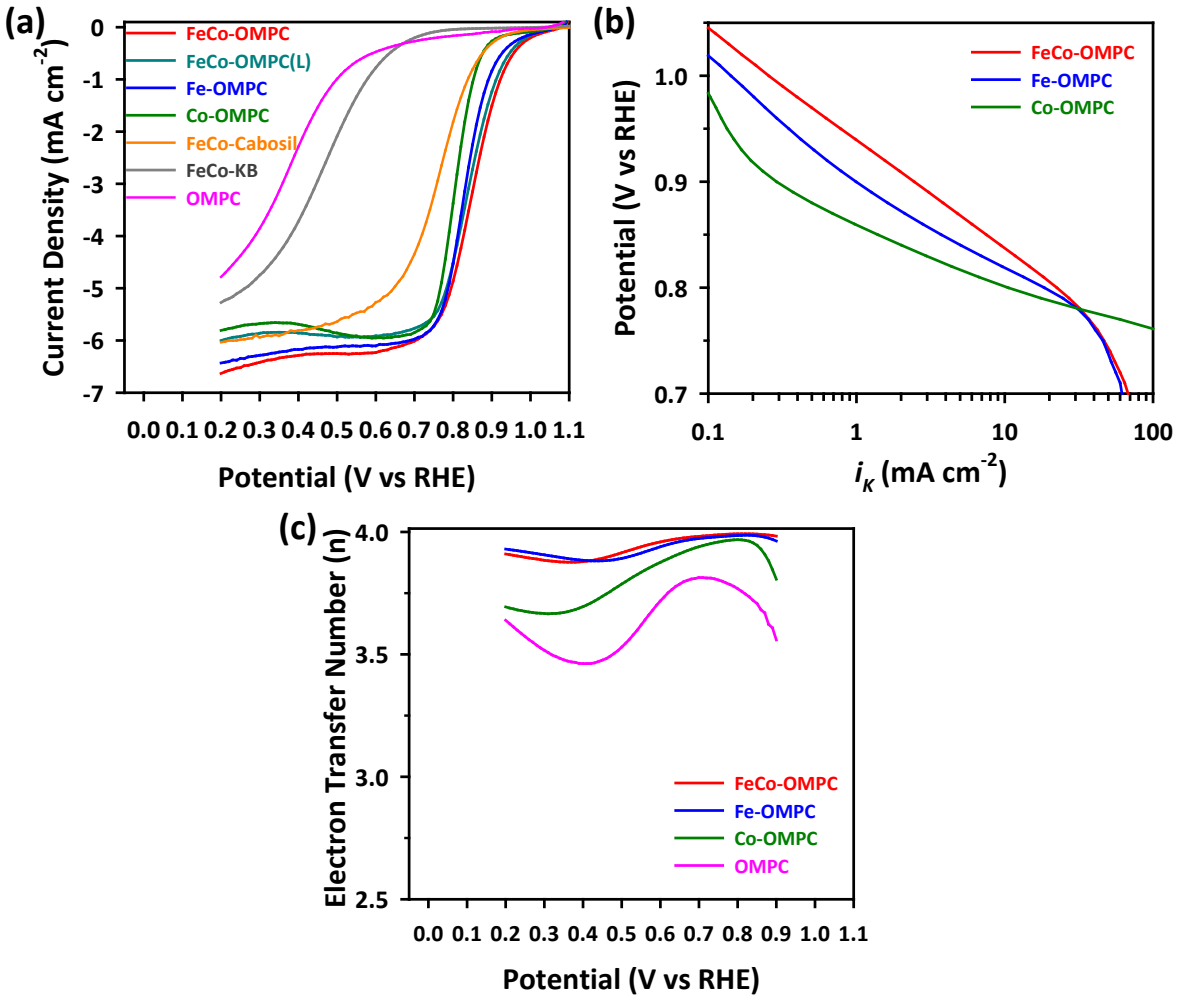

Figure 5.6. ORR activity of M-OMPC catalysts. (a) ORR polarization curves of M-OMPC (M=FeCo, Fe, Co), FeCo-OMPC(L), OMPC, and FeCo-KB catalysts in O_2-saturated 0.1 M $HClO_4$. (b) Tafel plots derived from the corresponding ORR polarization curves after mass transport correction. (c) Number of electrons transferred during ORR calculated based on ring currents. For all RRDE measurements, the catalyst loadings were 0.6 mg cm^{-2}. The electrode rotation speed was 1600 rpm and the scan rate was 5 mV s^{-1}.

The very high ORR activity of FeCo-OMPC catalyst for the ORR was remarkable, and a comparison with previously reported catalysts indicates FeCo-OMPC as one of the best non-precious metal ORR catalyst, along with the recent result from Dodelet and co-workers[18] (Table 5.2). The half-wave potential of the FeCo-OMPC was significantly shifted to positive potentials by 50 to 100 mV, compared to those of previously reported non-precious metal catalysts. Particularly, comparing the kinetic current density at 0.9 V, the FeCo-OMPC showed significant current density (2.42 mA cm^{-2}) whereas the previous catalysts exhibited only negligible currents for ORR at this potential.

Table 5.2. Comparison of half-wave potentials ($E_{1/2}$), kinetic currents (i_k) at 0.9 V and 0.8 V, and mass activity at 0.8 V of the FeCo-OMPC catalyst with previously reported catalysts.

Catalysts	$E_{1/2}$ (V vs RHE)	i_k (@ 0.9 V) (mA cm^{-2}) [a]	i_k (@ 0.8 V) (mA cm^{-2}) [b]	$i_{k,m}$ (@ 0.8 V) (A g^{-1}) [c]	Ref.
FeCo-OMPC This study	**0.851**	**2.42**	**27**	**45** [k]	**This study**
20 wt% Pt/C This study	0.865	2.08	-	-	This study
$FeCl_3$-PANI-KB [d] Wu *et al.*	0.810	-	5.8	3.5 [m]	[20]
$Fe(NO_3)_3$-NT-G [e] Li *et al.*	0.760	-	2.1	4.4 [m]	[21]
FeAc-Phen-BP [f] Meng *et al.*	0.800	-	16	20 [k]	[24]
$FeSO_4$-PANI-KB Chlistunoff	0.760	-	1.0	2.0 [m]	[25]
FeIM-ZIF-8 [g] Zhao *et al.*	0.755	-	1.0	2.6 [k]	[26]
Co-Corrole-CB [h] Huang *et al.*	0.750	-	2.6	-	[27]
FeAc-FB [i] Jaouen and Dodelet	-	-	2.5	3.1 [l]	[31]
FeTMPP-FeO^j_x-S Jaouen *et al.*	0.810	-	8.3	18 [l]	[32]
CoTMPP-FeO^j_x-S Jaouen *et al.*	0.790	-	4.6	10 [l]	[32]
FeAC-FB [i] Jaouen *et al.*	0.780	-	3.6	4.5 [l]	[32]
FeAc-PTCDA-BP [f] Jaouen *et al.*	0.760	-	2.4	3 [l]	[32]
$FeCl_3$-$Co(NO_3)_2$-HDA-KB [d] Wu *et al.*	0.780	-	5.0	8.4 [m]	[37]

All data collected from RDE measurements in acidic conditions.
[a]Mass transfer corrected kinetic current per geometric surface area of disk (kinetic current density) at 0.9 V.
[b]Kinetic current density at 0.8 V.
[c]Kinetic current per catalyst mass at 0.8 V.
[d]Ketjen Black, [e]Nanotube-graphene complex, [f]Black Pearl, [g]Fe imidazolate and zeolitic imidazolate frameworks, [h]Carbon Black, [i]Furnace black, [j]Fe oxalate, [k]0.1 M $HClO_4$, [l]pH 1 H_2SO_4, [m]0.5 M H_2SO_4.

We also compared the ORR activities of M-OMPCs with the reference catalysts. To identify the role of the metal atom (Fe or Co), we prepared a metal-free OMPC from 5,10,15,20-Tetrakis(4-methoxy-phenyl)-21H,23H porphyrin (TMPPH) precursor (Table 5.1). The metal-free OMPC showed electrocatalytic current for ORR, but its on-set and half-wave potentials were markedly shifted to lower potentials, compared to those of the M-OMPC catalysts (Figure 5.6a), suggesting a crucial role of metal atoms in catalyzing oxygen reduction. Next, we measured the ORR activity of two metalloporphyrin-driven catalysts. The first sample was prepared by impregnating a mixed precursor

of FeTMPPCl and CoTMPP onto a carbon black (Ketjenblack®, KB) support, followed by pyrolysis at 800 °C (Table 5.1).[31] The ORR activity of the resulting FeCo-KB catalyst was significantly lower than the M-OMPC catalysts, as manifested by markedly lower on-set and half-wave potentials (Figure 5.6a). The other metalloporphyrin-driven catalyst was prepared by a nanocasting method using amorphous silica particles (Cabosil) as a template and a mixture of FeTMPPCl and CoTMPP as a precursor, following the previous reports (Table 5.1).[29,33,34] Thus prepared FeCo-Cabosil catalyst showed better ORR activity than the FeCo-KB catalyst, yet its on-set and half-wave potentials were negatively shifted by 100 mV, compared to FeCo-OMPC catalyst, indicating much inferior ORR activity. The ORR activity of these reference catalysts indicates that the important role of metal in catalyzing ORR as well as high surface area and mesostructure of carbon support in enhancing ORR activity.

To assess the pathway of ORR over the M-OMPC catalysts, we measured ring currents, from which the number of electrons transferred during ORR was calculated. Figure 5.6c shows that the number of transferred electrons was above 3.9 over all potentials by the FeCo-OMPC catalyst, and the number approached 4 at a potential near 0.9 V. This clearly indicates that ORR catalyzed by the FeCo-OMPC followed a 4-electron pathway, which is typically shown by the Pt/C catalyst.[3]

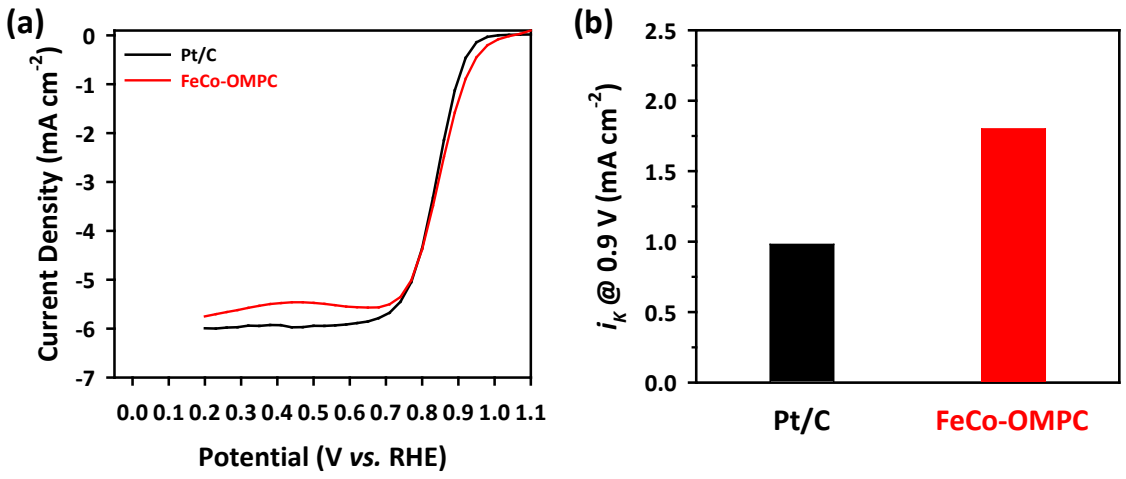

Figure 5.7. Comparison of activity and durability of Pt/C and FeCo-OMPC. (a) ORR polarization curves of Pt/C and FeCo-OMPC catalysts in O_2-saturated 0.1 M $HClO_4$ at the scan rate of 1 mV s^{-1}. (b) Corresponding kinetic currents of Pt/C and FeCo-OMPC catalysts at the scan rate of 1 mV s^{-1}.

We further compared the ORR activity of the FeCo-OMPC with the Pt/C (20 wt.% Pt supported on Vulcan carbon, E-TEK) catalyst. We found that the very high activity of the FeCo-OMPC was even better than the Pt/C catalyst (Figure 5.7a,b and Table 5.3). The ORR activity measured with a very slow scan rate of 1 mV s^{-1}, under which the contribution from the capacitive current could be virtually excluded, higher ORR activity for the FeCo-OMPC catalyst over Pt/C was clearly observed (Figure 5.7a). Importantly, the kinetic current density of the FeCo-OMPC at 0.9 V

(1.80 mA cm^{-2}) surpassed that of the Pt/C catalyst (1.00 mA cm^{-2}) by 80% (Figure 5.7b and Table 5.3). The half-wave potentials of the two catalysts were 0.845 V and 0.840 V for the FeCo-OMPC and Pt/C, respectively. The FeCo-OMPC catalyst also showed very high electrocatalytic activity in an alkaline medium. The ORR polarization curve of the FeCo-OMPC catalyst in 0.1 M KOH was nearly identical to that of the Pt/C catalyst (Figure 5.8).

Table 5.3. Half-wave potentials and kinetic current densities at 0.9 V of FeCo-OMPC and Pt/C catalysts for ORR in 0.1 M $HClO_4$ solution at a scan rate of 1 mV s^{-1}.

	Half-wave potential (V)	Kinetic current density at 0.9 V (mA cm^{-2})
FeCo-OMPC	**0.845**	**1.80**
Pt/C	0.840	1.00

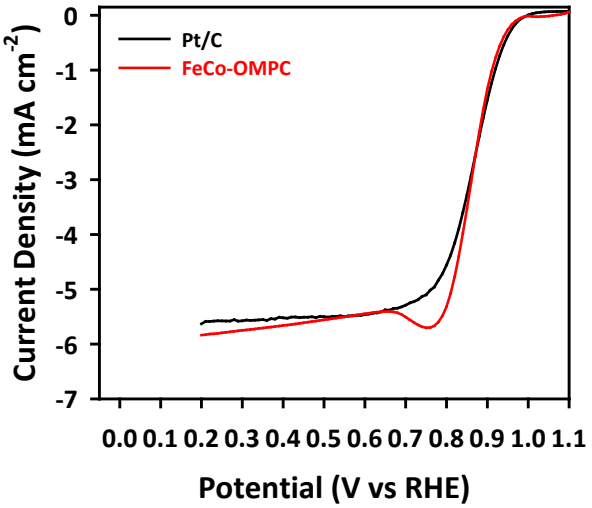

Figure 5.8. ORR polarization curves of Pt/C and FeCo-OMPC catalysts in O_2-saturated 0.1 M KOH. The catalyst loadings were 0.3 mg cm^{-2} for the FeCo-OMPC catalysts and 20 μg_{Pt} cm^{-2} for Pt/C. The electrode rotation speed was 1600 rpm and the scan rate was 5 mV s^{-1}.

For the sustainable use of fuel cell electrocatalysts, their long-term durability is critical. We explored the durability of the FeCo-OMPC catalyst by cycling the catalysts 10,000 times between 0.6 and 1.0 V (vs. RHE) at a scan rate of 50 mV s^{-1}, following the accelerated durability test protocol of the U.S. Department of Energy (DOE).[41] The changes in half-wave potentials as well as kinetic current densities between the cycling tests indicated that the FeCo-OMPC catalyst exhibited superior durability over the Pt/C catalyst. After cycling 10,000 times with O_2 bubbling the FeCo-OMPC catalyst underwent a negative shift of 30 mV in half-wave potential, whereas the Pt/C catalyst showed a negative shift of 65 mV (Figure 5.9a). Before the cycling tests, the FeCo-OMPC showed a kinetic current density of 2.44 mA cm^{-2} at 0.9 V, which was higher than the Pt/C catalyst (1.76 mA cm^{-2}) by 39% (Figure 5.9b). After cycling 10,000 times under O_2, the performance gap between the two

catalysts increased even further: FeCo-OMPC (1.31 mA cm^{-2}) exhibited an almost six-fold higher ORR activity than Pt/C (0.23 mA cm^{-2}) (Figure 5.9b). The better durability of the FeCo-OMPC catalyst may stem from its higher tolerance to the agglomeration of metallic species. We next addressed the tolerance of the FeCo-OMPC catalyst against poisoning with fuel molecules, which is directly relevant to its potential use in direct alcohol fuel cells. The ORR polarization curve of the FeCo-OMPC in the presence of 0.5 M methanol (Figure 5.10) exhibited only a small shift of half-wave potential (30 mV). In contrast, the Pt/C catalyst showed a significant negative shift (305 mV) owing to the poisoning of the surfaces of the Pt nanoparticles by CO, the decomposition product of MeOH.[21,47]

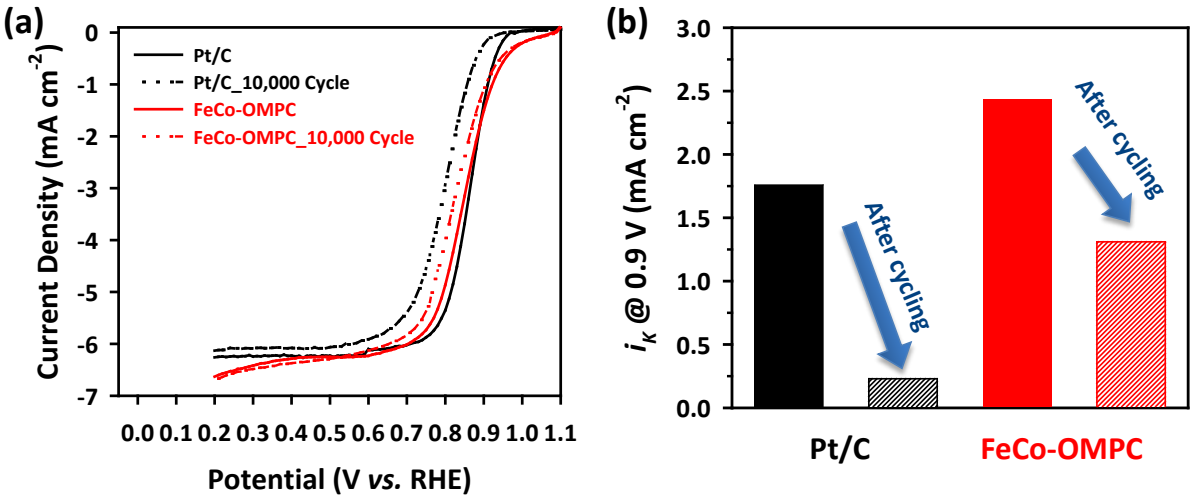

Figure 5.9. (a) ORR polarization curves of Pt/C and FeCo-OMPC catalysts before and after 10,000 potential cycles in O_2-saturated 0.1 M $HClO_4$. Potential cycling was carried out from 0.6 to 1.0 V vs. RHE at 50 mV s^{-1}. (b) Comparison of kinetic currents of Pt/C and FeCo-OMPC catalysts before and after 10,000 potential cycles.

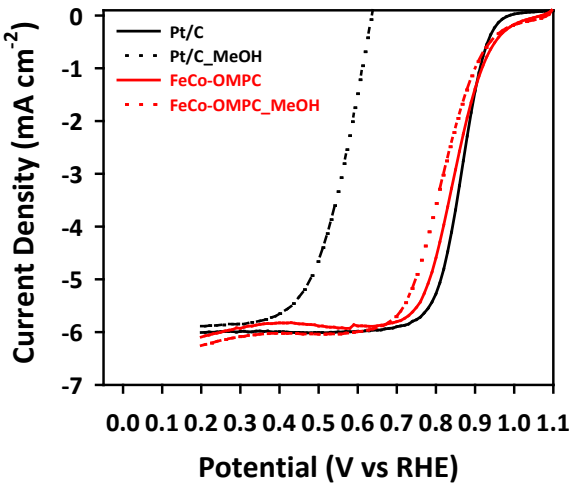

Figure 5.10. ORR polarization curves of Pt/C and FeCo-OMPC catalysts in O_2-saturated 0.1 M $HClO_4$ with or without 0.5 M methanol.

5.3.3. Active site structure identification

In order to analyze the structure of highly active catalysts for ORR, we investigated the local structure of the FeCo-OMPC catalyst with EXAFS and X-ray absorption near edge structure (XANES) analysis. The comparison of XANES spectra (Figure 5.11) revealed that the square-planar D_{4h} local symmetry shown by model compounds (Fe-phthalocyanine for Fe, and CoTMPP for Co) was broken down in the FeCo-OMPC catalyst, possibly because of the additional coordination along the axial direction. The radial distribution functions (RDFs) for the Fe (Figure 5.12a) and Co (Figure 5.12b) K-edge EXAFS spectra provided more detailed evidence for the breakdown of the square-planar symmetry in the FeCo-OMPC catalyst., with a shorter O_1 and longer O_2, respectively. On the other hand, the RDF of Co K-edge showed a single axial-coordination by the oxygen atom (OH). It is noteworthy that the distinct FT peak at around 4.3 Å at the Fe K-edge RDF corresponded to the chemical bonding interaction of Fe-(O_2)-Fe by way of the oxygen molecule as a pillaring element between the interlayers, which is similar to the structure of face-to-face porphyrin-based ORR catalyst.[48] Based on the EXAFS curve-fitting results, structural parameters around each metal, including bond distances and coordination numbers were obtained and summarized in Table 5.4.

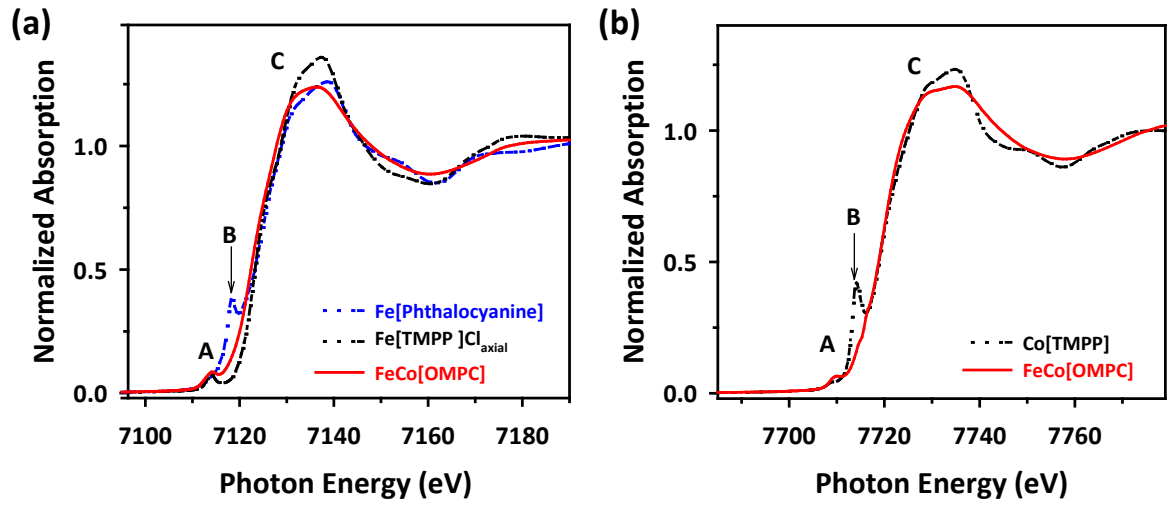

Figure 5.11. (a) Fe and (b) Co K-edge X-ray absorption near edge structures (XANES) spectra of FeCo-OMPC and model compounds.

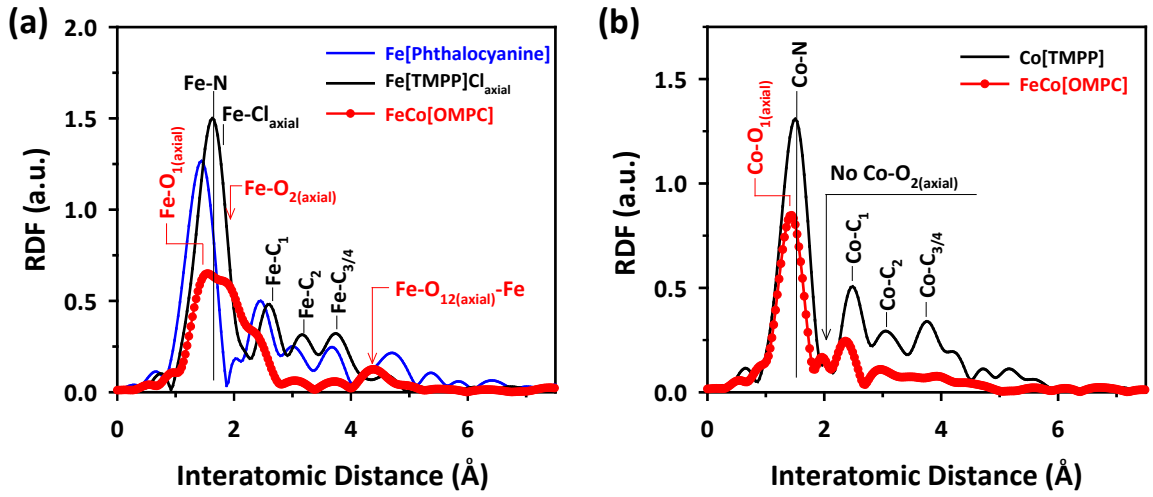

Figure 5.12. EXAFS and DFT results. (a, b) Radial distribution functions (RDF) of Fourier-transformed k^2-weighted Fe (a) and Co (b) K-edge EXAFS for FeCo-OMPC catalyst, in comparison with reference materials.

Table 5.4. The structural parameters obtained from EXAFS curve-fitting process for the Fe and Co K-edge k^2-weighted EXAFS spectra of the FeCo-OMPC catalyst.

Edge	Path	⊿E (eV)[a]	N[b]	R (Å)[c]	σ^2 (x10^{-3}Å^2)[d]
Fe K-edge	Fe – $O_{1/axial}$	-3.08	1.67	1.88	3.38
	Fe – N_{eq}	1.68	2.83	2.01	4.65
	Fe – $O_{2/axial}$	-8.35	1.96	2.43	2.93
	Fe – C1(5-membered ring)	-9.28	1.68	2.56	2.97
	Fe – C2(6-membered ring)	-6.67	3.42	2.95	7.39
	Fe – C3	3.08	2.42	3.69	5.07
	Fe – $O_{12/axial}$ – Fe	1.76	0.93	4.78	4.91
Co K-edge	Co – $O_{1/axial}$	-7.68	1.05	1.87	2.64
	Co – N_{eq}	-0.18	2.29	1.94	4.08
	Co – C1 (or C2)	-2.08	1.80	2.89	1.81
	Co – $O_{12/axial}$ – Co(1)	5.77	0.62	4.46	8.94
	Co – $O_{12/axial}$ – Co(2)	9.25	0.27	4.85	7.44

[a]Energy shift.
[b]Coordination number.
[c]Bond distance.
[d]Debye-Waller factor for each scattering path.

We then constructed several models (Figure 5.13) for DFT calculations based on the experimental findings. On the basis of the EXAFS data, DFT calculations using bilayer Model III suggested that the Co centers were connected with OH (~0.98 Å), while the Fe centers were connected with OO (~1.40 Å) (Figure 5.14). We found that the averaged M-M distance of the 2-layer model (Model III) was ~4.6 Å, which was in good agreement with the EXAFS results as well as the HRTEM observation of interlayer distances (4.8 Å) within the FeCo-OMPC frameworks (Figure 5.15). We carried out DFT calculations to elucidate the enhanced ORR activity of the FeCo-OMPC catalyst compared to those of Fe-OMPC, Co-OMPC, and Pt/C catalysts. We adopted the binding energy of atomic oxygen (BO) as a descriptor for calculating ORR activity.[49] Two oxygen atoms were placed at the active metal sites on the surface. First, we used a small bilayer (0001) surface generated from Model IV bulk structure. The change of the metal centers and bridging species from the mixed FeCo-OMPC to pure Fe- or Co-OMPC led to strengthened O-surface interactions (-3.14 eV/atom for FeCo-OMPC and -4.94 eV/atom and -4.02 eV/atom for Fe-OMPC and Co-OMPC, respectively) (Figure 5.16a and Table 5.5). Furthermore, we found that Fe more strongly binds O than Co on FeCo-OMPC (-3.52 eV versus -2.79 eV, respectively). This indicates that a proper mixing of Fe and Co decreased the binding energy of oxygen. It is well known that slight weakening of the O interaction with catalyst surfaces is a key factor in down-shifting of the d-band centers, thereby increasing the ORR activity.[50] In a further comparison with Pt(111) using a more realistic Model II surface (Figure 5.16b), the FeCo-OMPC catalyst (-3.33 eV/atom) showed a slight decrease in BO from that of Pt(111) (-3.58 eV/atom), indicating an enhanced ORR activity of the FeCo-OMPC catalyst over Pt(111).

Based on the results from various characterization methods and the DFT calculation, the very high activity of M-OMPC catalysts, particularly FeCo-OMPC, appears to originate from a combination of several factors. The nanocasting from OMS templates afforded ordered mesoporous catalysts with very high surface area, wherein the number of porphyrinic active sites could be enlarged. The direct conversion of porphyrin precursor inside the nanopores of the OMS template allowed for catalytically active M-N bondings intact in the final carbogenic structures. In addition, the combined use of two different metal centers (Fe and Co) could endow synergistic effect in FeCo-OMPC, which was manifested as weakened interaction with oxygen, compared to monometal-doped OMPCs and Pt(111) surface.

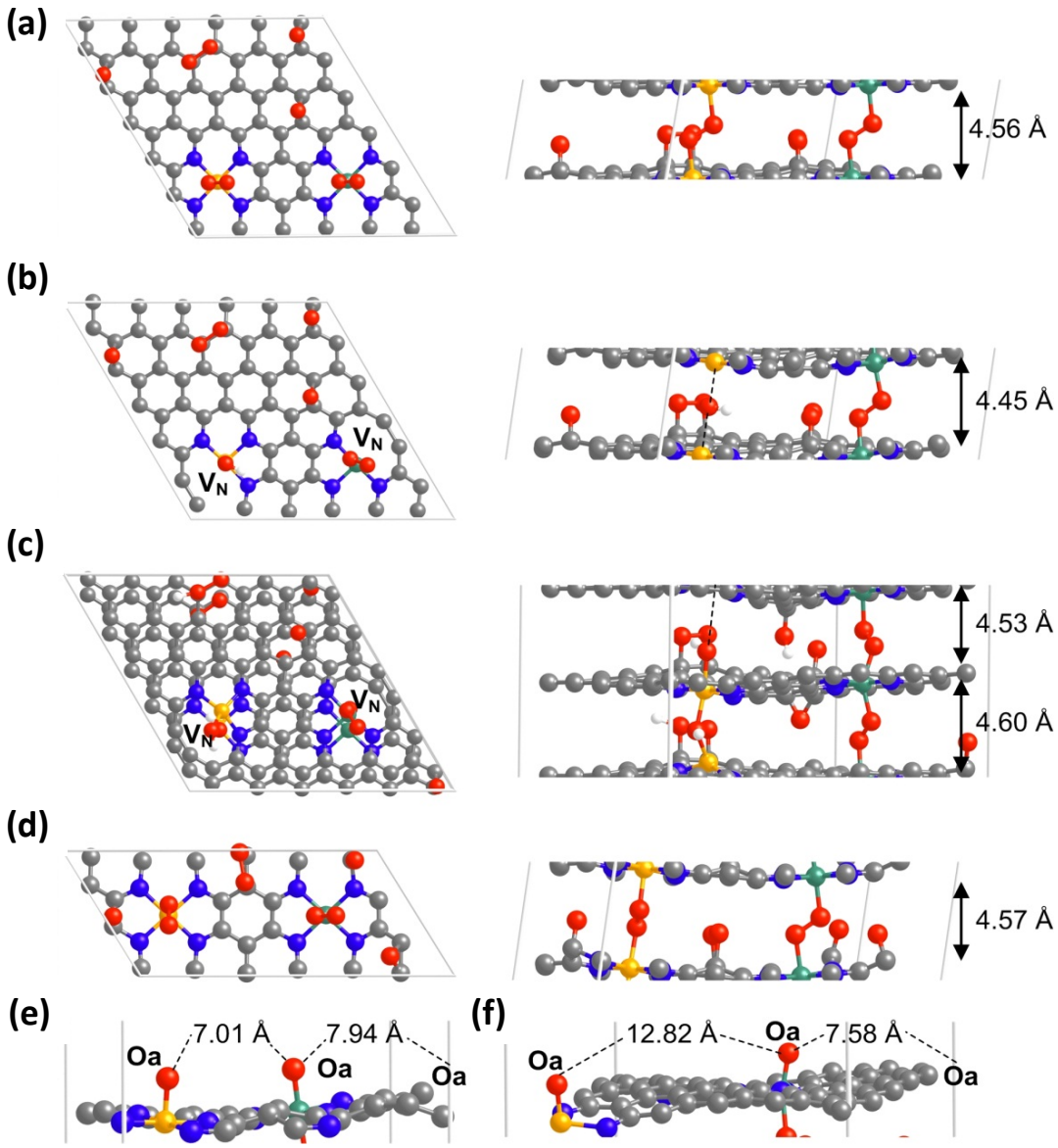

Figure 5.13. Top and side views of bulk structures (a) **Model I** (60 C, 8 N, 9 O, 1 Fe, and 1 Co atoms), (b) **Model II** (60 C, 6 N, 8 O, 1 Fe, 1 Co, and 1 H atoms), (c) **Model III** (120 C, 12 N, 14 O, 2 Fe, 2 Co, and 2 H atoms), and (d) **Model IV** (24 C, 8 N, 8 O, 1 Fe, 1 Co, and 2 H atoms). **Model I** was first built, and then, **Model II** was prepared by removing two nitrogen atoms, representing nitrogen vacancies ($\mathbf{V_N}$) and by replacing OO bridging Co-Co with OH. To generate $\mathbf{V_N}$, we fully re-optimized the structures by removing nitrogen atoms one by one. Based on **Model II**, **Model III** was constructed. To save the computational time for surface calculations, a simplified bulk structure of **Model IV** was built. **Model I**, **Model II**, and **Model IV** have one layer in the bulk structure, while **Model III** has two layers. Side views of (e) the surface from **Model IV** and (f) that from **Model II** with a vacuum space of 10 Å. For clarity, only the topmost layer was shown. **Oa** represent adsorbed oxygen species. Grey, blue, green, orange, red, and white spheres represent C, N, Fe, Co, O, and H, respectively.

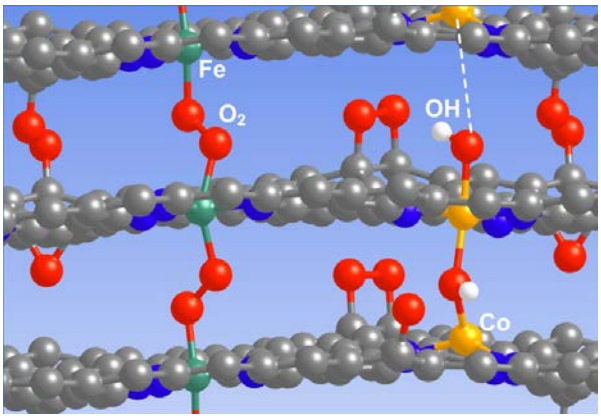

Figure 5.14. Schematic of a representative FeCo-OMPC model. Grey, blue, green, orange, red, and white spheres represent C, N, Fe, Co, O, and H, respectively.

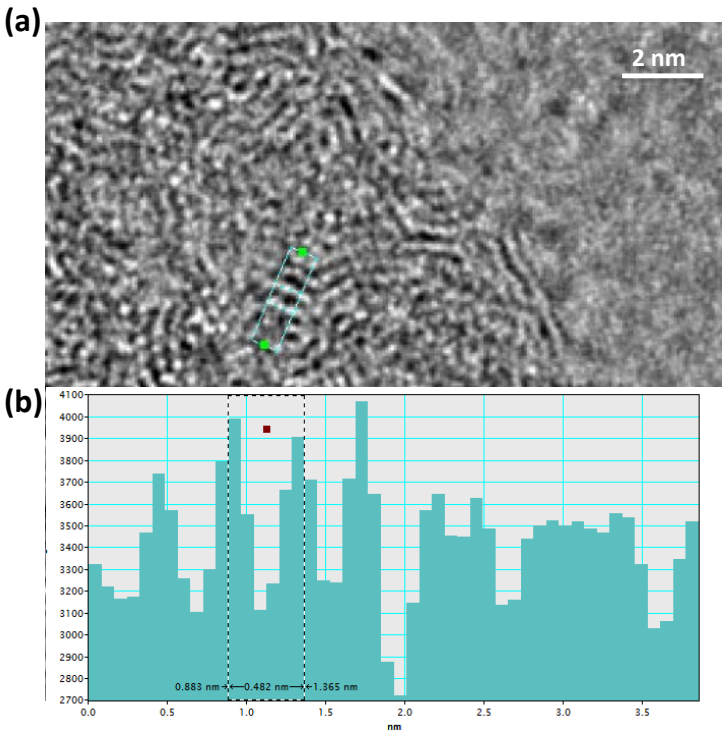

Figure 5.15. (a) HRTEM image of frameworks within FeCo-OMPC catalyst. (b) Interlayer distance between adjacent carbogenic layers. The distance is 0.48 nm.

Table 5.5. Binding of oxygen (BO) on the surfaces using the **Model IV** and **Model II** bulk structures.

Model IV[a]	Fe-OMPC	Co-OMPC	FeCo-OMPC	Pt(111)[a]
BO (eV/atom)	–4.94	–4.02	–3.14	–3.47
Model II[b]	Fe-OMPC	Co-OMPC	FeCo-OMPC	Pt(111)[c]
BO (eV/atom)	–	–	–3.33	–3.58

[a]The surfaces were fixed and only the adsorbates were fully relaxed.
[b]The bottom bilayer was fixed, and the top bilayer and the adsorbates were fully relaxed.
[c]The topmost two layers and the adsorbates were fully relaxed, while the bottom three layers were fixed.

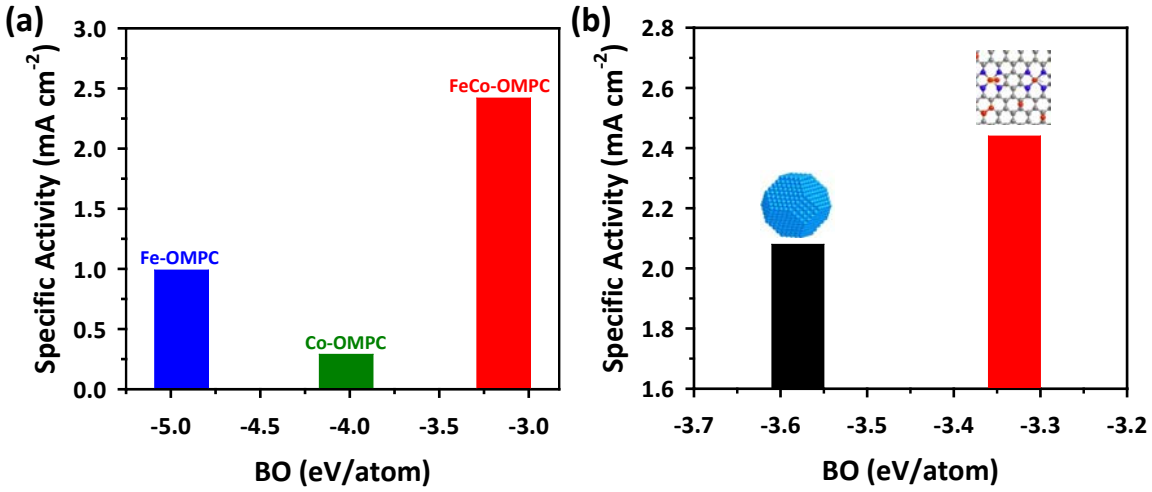

Figure 5.16. (a) Specific activity against binding energy of oxygen atom (BO) over Fe-, Co-, and FeCo-OMPC catalysts using Model IV. For these BO calculations, the surfaces were fixed, and only the adsorbed oxygen species were fully optimized. The geometrical parameters are summarized in Table 5.5. (b) Specific activity against binding energy of atomic oxygen (BO) over Pt/C and FeCo-OMPC catalysts.

5.3.4. PEFC single cell tests

We carried out preliminary single cell tests for a PEFC that employed the large pore FeCo-OMPC(L) catalyst as a cathode. The open circuit voltage of single cell was 0.98 V under pure oxygen condition. The current density and power density of the single cell at 0.6 V were 513 mA cm^{-2} and 0.308 W cm^{-2}, respectively (Figure 5.17a). The volumetric activity at 0.8 V (Figure 5.17b), obtained from the intersection of the extrapolated Tafel slope (dashed line) with the 0.8 V axis, was 131 A cm^{-3} (solid red circle), which showed a high possibility of achieving the US DOE's target of FY 2017.[41]

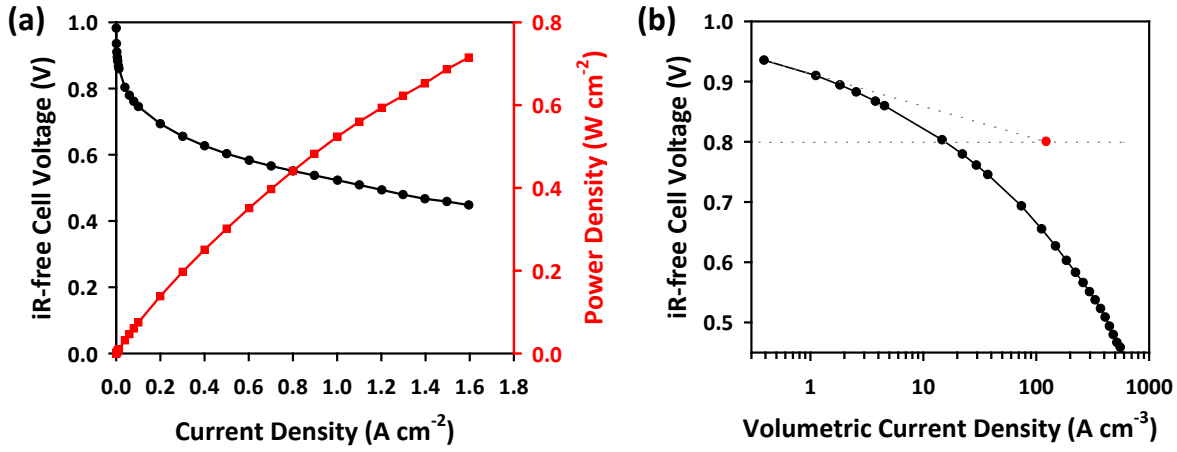

Figure 5.17. PEFC single cell performance. (a) H_2-O_2 fuel cell iR-corrected polarization plot of FeCo-OMPC(L) (the red line is the corresponding power density). (b) Volumetric current density vs. iR-free cell voltage.

We also performed long-term durability test using FeCo-OMPC(L) catalyst as a cathode (Figure 5.18). At an operating voltage of 0.5 V, the single cell showed an initial current density of 0.5 A cm^{-2}. The single cell underwent the drop in current density until 40 h under operation, yet after which it showed steady current density at 0.2 A cm^{-2}. These PEFC single cell results need improvement in terms of both activity and durability.

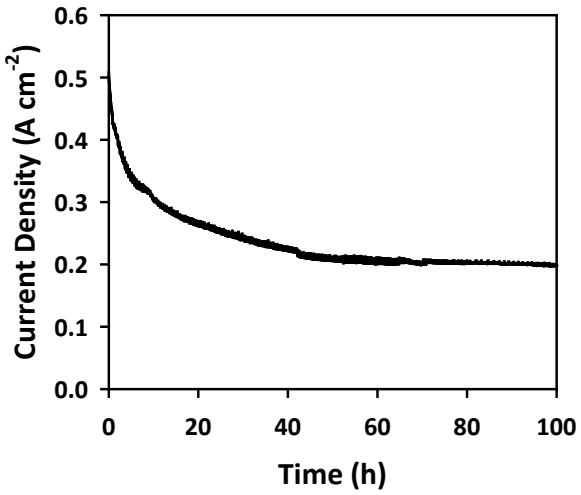

Figure 5.18. Long-term durability test for a PEFC that employed FeCo-OMPC(L) cathode at a constant voltage of 0.5 V operated with H_2-O_2.

5.4. Conclusions

We have presented a new family of electrocatalysts based on the ordered mesoporous porphyrinic architecture, which show a very high ORR activity in an acidic medium that compares favorably to Pt/C catalysts. We attribute the high activity of the FeCo-OMPC catalyst to its weak interaction with oxygen, its high surface area that can expose a high density of active sites, and the use of porphyrin precursors. The M-OMPC catalysts also showed enhanced durability and poison-tolerance, compared to the Pt/C catalysts. Significantly, we point out that the synthetic route to M-OMPC catalysts is very simple and general and is amenable to large scale synthesis. Recent years have witnessed a rapid progress in the development of electrocatalysts for ORR. For instance, nanoparticles composed of a Pt monolayer on PdAu core,[51] intermetallic Pt-Co nanoparticles,[52] and mesostructured PtNi thin films[53] have demonstrated significantly improved ORR activity and durability in acidic media. We believe that, along with these new catalysts, the M-OMPCs could emerge as highly promising catalysts for ORR. Furthermore, the design concept towards enhanced electrocatalytic performances presented in this work could be extended to other electrocatalytic reactions in energy devices, such as metal-air batteries and electrolyzers.

5.5. References

(1) Steele, B. C. H.; Heinzel, A. *Nature* **2001**, *414*, 345.

(2) Arico, A. S.; Bruce, P.; Scrosati, B.; Tarascon, J.-M.; Van Schalkwijk, W. *Nat. Mater.* **2005**, *4*, 366.

(3) Gasteiger, H. A.; Kocha, S. S.; Sompalli, B.; Wagner, F. T. *Appl. Catal. B* **2005**, *56*, 9.

(4) Debe, M. K. *Nature* **2012**, *486*, 43.

(5) Rabis, A.; Rodriguez, P.; Schmidt, T. J. *ACS Catal.* **2012**, *2*, 864.

(6) Borup, R.; Meyers, J.; Pivovar, B.; Kim, Y. S.; Mukundan, R.; Garland, N.; Myers, D.; Wilson, M.; Garzon, F.; Wood, D.; Zelenay, P.; More, K.; Stroh, K.; Zawodzinski, T.; Boncella, J.; McGrath, J. E.; Inaba, M.; Miyatake, K.; Hori, M. Ota, K.; Ogumi, Z.; Miyata, S.; Nishikata, A.; Siroma, Z.; Uchimoto, Y.; Yasuda, K.; Kimijima, K. I.; Iwashita, N. *Chem. Rev.* **2007**, *107*, 3904.

(7) Jasinski, R. *Nature* **1964**, *201*, 1212.

(8) Wang, B. *J. Power Sources* **2005**, *152*, 1.

(9) Bezerra, C. W. B.; Zhang, L.; Lee, K.; Liu, H.; Marques, A. L. B.; Marques, E. P.; Wang, H.; Zhang, J. *Electrochim. Acta* **2008**, *53*, 4937.

(10) Jaouen, F.; Proietti, E.; Lefèvre, M.; Chenitz, R.; Dodelet, J.-P.; Wu, G.; Chung, H. T.; Johnston, C. M.; Zelenay, P. *Energy Environ. Sci.* **2011**, *4*, 114.

(11) Chen, Z.; Higgins, D.; Yu, A.; Zhang, L.; Zhang, J. *Energy Environ. Sci.* **2011**, *4*, 3167.

(12) Gupta, S.; Tryk, D.; Bae, I.; Aldred, W.; Yeager, E. *J. Appl. Electrochem.* **1989**, *19*, 19.

(13) Lefèvre, M.; Dodelet, J.-P.; Bertrand, P. *J. Phys. Chem. B* **2002**, *106*, 8705.

(14) Jaouen, F.; Lefèvre, M.; Dodelet, J.-P.; Cai, M. *J. Phys. Chem. B* **2006**, *110*, 5553.

(15) Bashyam, R.; Zelenay, P. *Nature* **2006**, *443*, 63.

(16) Lefèvre, M.; Proietti, E.; Jaouen, F.; Dodelet, J.-P. *Science* **2009**, *324*, 71.

(17) Proietti, E.; Jaouen, F.; Lefèvre, M.; Larouche, N.; Tian, J.; Herranz, J.; Dodelet, J.-P. *Nat. Commun.* **2011**, *2*, 416.

(18) Jaouen, F.; Goenllner, V.; Lefèvre, M.; Herranz, J.; Proietti, E.; Dodelet, J.-P. *Electrochim. Acta* **2013**, *87*, 619.

(19) Wu, L.; Nabae, Y.; Moriya, S.; Matsubayashi, K.; Islam, N. M.; Kuroki, S.; Kakimoto, M.-A.; Ozaki, J.-I.; Miyata, S. *Chem. Commun.* **2010**, *46*, 6377.

(20) Wu, G.; More, K. L.; Johnston, C. M.; Zelenay, P. *Science* **2011**, *332*, 443.

(21) Li, Y.; Zhou, W.; Wang, H.; Xie, L.; Liang, Y.; Wei, F.; Idrobo, J.-C.; Pennycook, S. J.; Dai, H. *Nat. Nanotech.* **2012**, *7*, 394.

(22) Chung, H. T.; Won, J. H.; Zelenay, P. *Nat. Commun.* **2013**, *4*, 1922.

(23) Li, Y.; Gong, M.; Liang, Y.; Feng, J.; Kim, J.-E.; Wang, H.; Hong, G.; Zhang, B.; Dai, H. *Nat. Commun.* **2013**, *4*, 1805.

(24) Meng, H.; Jaouen, F.; Proietti, E.; Lefevre, M.; Dodelet, J.-P. *Electrochem. Commun.* **2009**, *11*, 1986.

(25) Chlistunoff, J. *J. Phys. Chem. C* **2011**, *115*, 6496.

(26) Zhao, D.; Shui, J.-L.; Chen, C.; Reprogle, B. M.; Wang, D.; Liu, D.-J. *Chem. Sci.* **2012**, *3*, 3200.

(27) Huang, H.-C.; Shown, I.; Chang, S.-T.; Hsu, H.-C.; Du, H.-Y.; Kuo, M.-C.; Wong, C.-H.; Chen, L.-C.; Chen, K.-H. *Adv. Funct. Mater.* **2012**, *22*, 3500.

(28) Koslowski, U. I.; Abs-Wurmbach, I.; Fiechter, S.; Bogdanoff, P. *J. Phys. Chem. C* **2008**, *112*, 15356.

(29) Nallathambi, V.; Lee, J.-W.; Kumaraguru, S. P.; Wu, G.; Popov, B. N. *J. Power Sources* **2008**, *183*, 34.

(30) Garsuch, A.; d'Eon, R.; Dahn, T.; Klepel, O.; Garsuch, R. R.; Dahn, J. R. *J. Electrochem. Soc.* **2008**, *155*, B236.

(31) Charreteur, F.; Jaouen, F.; Dodelet, J.-P. *Electrochim. Acta* **2009**, *54*, 6622.

(32) Jaouen, F.; Herranz, J.; Lefèvre, M.; Dodelet, J.-P.; Kramm, U. I.; Herrmann, I.; Bogdanoff, P.; Maruyama, J.; Nagaoka, T.; Garsuch, A.; Dahn, J. R.; Olson, T.; Pylypenko, S.; Atanassov, P.; Ustinov, E. A. *ACS Appl. Mater. Interfaces* **2009**, *1*, 1623.

(33) Olson, T.; Chapman, K.; Atanassov, P. *J. Power Sources* **2008**, *108*, 557.

(34) Olson, T.; Pylypenko, S.; Fulghum, J. E.; Atanassov, P. *J. Electrochem. Soc.* **2010**, *157*, B54.

(35) Choi, J.-Y.; Hsu, R. S.; Chen, Z. *J. Phys. Chem. C* **2010**, *114*, 8048.

(36) Wu, G.; Johnston, C. M.; Mack, N. H.; Artyushkova, K.; Ferrandon, M.; Nelson, M.; Lezama-Pacheco, J. S.; Conradson, S. D.; More, K. L.; Myers, D. J.; Zelenay, P. *J. Mater. Chem.* **2011**, *21*, 11392.

(37) Wu, G.; Nelson, M.; Ma, S.; Meng, H.; Cui, G.; Shen, P. K. *Carbon* **2011**, *49*, 3972.

(38) Ma, S.; Goenaga, G. A.; Call, A. V.; Liu, D.-J. *Chem-Eur. J.* **2011**, *17*, 2063.

(39) Lee, D. H.; Lee, W. J.; Lee, W. J.; Kim, S. O.; Kim, Y.-H. *Phys. Rev. Lett.* **2011**, *106*, 175502.

(40) Byon, H. R.; Suntivich, J.; Shao-Horn, Y. *Chem. Mater.* **2011**, *23*, 3421.

(41) *The US DRIVE Fuel Cell Technical Team Tecnology Roadmap (Revised August 11, 2011)* http://www.uscar.org/guest/tlc/2/Hydrogen-Fuel-Cell-TLC.

(42) Lee, K. T.; Ji, X.; Rault, M.; Nazar, L. F. *Angew. Chem. Int. Ed.* **2009**, *48*, 5661.

(43) Jo, Y.; Cheon, J. Y.; Yu, J.; Jeong, H. Y.; Han, C.-H.; Jun, Y.; Joo, S. H. *Chem. Commun.* **2012**, *48*, 8057.

(44) Kim, S.-S.; Pauly, T. R.; Pinnavaia, T. J. *Chem. Commun.* **2000**, 1661.

(45) Joo, S. H.; Choi, S. J. Oh, I.; Kwak, J.; Liu, Z.; Terasaki, O.; Ryoo, R. *Nature* **2001**, *412*, 169.

(46) Lu, A. -H.; Scuth, F. *Adv. Mater.* **2006**, *18*, 1793.

(47) Kwon, K.; Sa, Y. J.; Cheon, J. Y.; Joo, S. H. *Langmuir* **2012**, *28*, 991.

(48) Collman, J. P.; Denisevich, P.; Konai, Y.; Marrocco, M.; Koval, C.; Anson, F. C. *J. Am. Chem.*

Soc. **1980**, *102*, 6027.

(49) Greeley J.; Stephens, E. L.; Bondarenko, A. S.; Johansson, T. P.; Hansen, H. A.; Jaramillo, T. F.; Rossmeisl, J.; Chorkendorff, I.; Nørskov, J. K. *Nat. Chem.* **2009**, *1*, 552.

(50) Zhang, J.; Vukmirovic, M. B.; Xu, Y.; Mavrikakis, M.; Adzic, R. R. *Angew. Chem. Int. Ed.* **2005**, *44*, 2132.

(51) Sasaki, K.; Naohara, H.; Choi, Y.; Cai, Y.; Chen, W.-F.; Liu, P.; Adzic, R. R. *Nat. Commun.* **2012**, *3*, 1115.

(52) Wang, D.; Xin, H. L.; Hovden, R.; Wang, H.; Yu, Y.; Muller, D. A.; DiSalvo, F. J.; Abruna, H. D. *Nat. Mater.***2013**, *12*, 81.

(53) van der Vliet, D. F.; Wang, C.; Tripkovic, D.; Strmcnik, D.; Zhang, X. F.; Debe, M. K.; Atanasoski, R. T.; Markovic, N. M.; Stamenkovic, V. R. *Nat. Mater.* **2012**, *11*, 1051.

6. Graphitic Nanoshell/Mesoporous Carbon Nanohybrids as Highly Efficient and Stable Bifunctional Oxygen Electrocatalysts for Aqueous Na-Air Batteries

6.1. Introduction

Bifunctional oxygen electrocatalysis involving both oxygen evolution and reduction reactions (OER and ORR, respectively) are ubiquitous and play a pivotal role in energy conversion and storage devices, such as metal-air batteries and fuel cells.[1-4] The widespread deployment of these electrochemical systems relies predominantly on the development of highly active, stable, and abundant material-based bifunctional oxygen electrocatalysts. Both oxygen electrode reactions involve four electron transfer reactions, which are kinetically sluggish.[2-4] Hence, precious metals such as Pt, Ir, and Ru have thus far been the prevalent choice for oxygen electrocatalysts because of their high activity;[5,6] however, their high cost and scarcity has triggered a recent surge in the development of new, cost-effective bifunctional electrocatalysts. In this context, non-precious metal-based bifunctional electrocatalysts, including nanostructured carbons doped with heteroatoms (and transition metals)[7-14] and metal oxides[15-26] (including perovskites[27-31]), have been actively pursued as potential replacements for precious metal-based electrocatalysts. However, the realization of balanced, high catalytic activity for both reactions using these non-precious metal catalysts remains a challenge. For instance, heteroatom-doped carbon nanostructures have shown high ORR activity in an alkaline medium; however, their OER activities have been far less pronounced.[8,10,12] In the case of transition metal oxides, including perovskites, while they have demonstrated precious metal-like OER activity in base; however, their low electrical conductivity results in unsatisfactory ORR activity.[15,27-31]

Na-air batteries are currently of immense interests because of their high capacity and energy density, as well as the abundance of Na compared to Li. While non-aqueous Na-air batteries have thus far been prevalently investigated,[32-34] they suffer from the formation of solid discharge products such as Na_2O_2 and NaO_2 on the surface of the air electrode, which are insoluble in the non-aqueous electrolyte and eventually deteriorate its electrochemical performances by clogging air permeation electrode.[35-37] In contrast, an aqueous Na-air battery can, in principle, be free of the irreversibility problem, as its discharge product (NaOH) can be readily soluble in an aqueous solution. Despite its considerable potential, however, the aqueous Na-air battery has only been reported as a dischargeable primary battery system.[38]

Here, we report the design of highly integrated, bifunctional oxygen electrocatalysts based on graphitic nanoshell/mesoporous carbon (GNS/MC) nanohybrids, which combined multiple structural motifs responsible for both OER and ORR. The GNS/MC exhibited very high activity and durability for the OER and ORR in an alkaline medium. The oxygen electrode activity (the potential

gap between the OER potential at 10 mA cm^{-2} and the ORR potential at -3 mA cm^{-2}) of the GNS/MC was as low as 0.72 V, which is one of the best performances among non-precious metal bifunctional oxygen electrocatalysts. The GNS/MC also exhibited very high long-term durability for the OER and ORR. The high electrocatalytic performance of the GNS/MC can be ascribed to the contributions of residual transition metal (Ni and Fe) entities, nitrogen-doped defect-rich graphitic nanoshells, and the high surface area of the mesoporous structure. Significantly, in aqueous Na-air battery tests, the GNS/MC-based cell exhibited superior performance to Ir/C- and Pt/C-based cells and demonstrated the first example of rechargeable aqueous Na-air battery.

6.2. Experimental Section

6.2.1. Synthesis of graphitic nanoshell/mesoporous carbon nanohybrids

The GNS/MC catalyst was synthesized via a solid-state nanocasting method using SBA-15 silica as a template, with a 3:7 (mass ratio) mixture of NiPc (Sigma Aldrich) and FePc (TCI) as precursors, respectively. Calcined SBA-15 (1.0 g) was mixed with the precursor (1.0 g), and the mixture was ground for 10 min in a mortar and transferred to an alumina crucible. The mixture was subsequently heated at temperatures ranging from 800 to 1200 °C with a ramping rate of 2.5 °C min^{-1}, and was held at a specific temperature for 3 h under N_2 flow. The resulting carbon-silica composite was then washed twice with 10 % HF (J. T. Baker) at room temperature for 1 h to remove the SBA-15 template. Ni-MC, Fe-MC, and OMC catalysts were synthesized using the same method as employed for the GNS/MC catalyst synthesis, except NiPc, FePc, and Pc (Sigma Aldrich) were used as precursors, respectively.

6.2.2. Characterization methods

XRD patterns of the samples were obtained using an X-ray diffractometer (Rigaku D/Max 2500V/PC) equipped with a Cu Kα source operating at 40 kV and 200 mA. The morphologies of the samples were observed using SEM (Quanta 200, FEI) operating at 18 kV. The microstructural and elemental analyses of the catalyst powders were performed using HR-TEM, HAADF-STEM (JEOL, JEM 2100F) with a probe-forming Cs corrector at 200 kV and energy dispersive X-ray spectroscope (EDS). The porous structures of the samples were analyzed *via* a nitrogen adsorption experiment at -196 °C using a BEL BELSORP-Max system. The surface areas of the samples were calculated using the BET equation, while the mesopore size distributions of the samples were calculated using the Barrett-Joyner-Halenda (BJH) method. XPS measurements were performed on ESCLAB 250Xi (Thermo Scientific), equipped with a monochromatic Al K-α X-ray source (1486.6 eV). Individual chemical components of the N 1s binding energy (BE) region were fitted to the spectra using the Gaussian (Gaussian 70, Lorentzian 30)-function after a linear (Shirley)-type background subtraction. The Raman spectra were obtained using a WITec alpha300R couple with a He-Ne laser of 532 nm at

1.0 mW.

6.2.3. Electrochemical measurement

The experiments were performed at room temperature (25 °C) using a three-electrode electrochemical cell. The OER and ORR activities were measured using a rotator (Pine AFMSRCE) and bipotentiostat (CHI Instruments 760E). A graphite counter electrode and a Hg/HgO reference electrode were used. All potentials reported in this study were with respect to the RHE. A glassy carbon rotating-disk electrode was used as a working electrode. This electrode was polished with a 1.0 μm alumina suspension and then with a 0.3 μm suspension to afford a mirror finish. The catalyst (7.5 mg) was mixed with deionized (DI) water (0.1 mL), ethanol (0.86 mL), and 5 wt% Nafion® (0.038 mL, 5 wt% in isopropanol, Aldrich). The resulting slurry was ultra-sonicated for 30 min to generate a catalyst ink. The ink (10.0 μL) was pipetted onto the 0.2475 cm^2 glassy carbon electrode, resulting in a catalyst loading of 300 μg cm^{-2}. Before the electrochemical measurements, the catalyst was cleaned by cycling the potential between 0 and 1.2 V at 100 mV s^{-1} for 50 cycles using a N_2-saturated 0.1 M KOH solution as an electrolyte. CV was performed over voltages ranging from 0 to 1.2 V at a scan rate of 20 mV s^{-1} using a N_2-saturated 0.1 M KOH electrolyte. The rotating ring-disk electrode measurements were used to determine the ORR activity and four-electron selectivity of the catalysts. OER activity was obtained in a N_2-saturated 0.1 M KOH electrolyte with CV performed for voltages ranging from 1.2 to 1.8 V at a scan rate of 5 mV s^{-1}. The OER current from the cathodic sweep scan was recorded. ORR activity was recorded in O_2-saturated 0.1 M KOH electrolyte with LSV performed for voltages ranging from 1.1 to 0.2 V at a scan rate of 5 mV s^{-1}. The OER and ORR currents were recorded after *iR*-drop compensation. The disk rotation speed was 1600 rpm. 20 wt% Pt on Vulcan® carbon black (Pt/C, JM) and 20 wt% Ir on Vulcan® (Ir/C, Premetek) were measured for comparison. The catalyst ink was prepared as follows. The Pt/C (or Ir/C) catalyst (5 mg) was mixed with DI water (0.1 mL), ethanol (1.06 mL), and 5 wt% Nafion® (0.04 mL, in isopropanol, Aldrich). The resulting slurry was ultra-sonicated for 30 min to generate a catalyst ink. The ink (6.0 μL) was pipetted onto the 0.2475 cm^2 glassy carbon electrode, resulting in a catalyst loading of 20 μg_{Pt} cm^{-2}. The other experimental conditions were the same as in the case of the GNS/MC catalyst, except that ORR activity data were collected from anodic sweeps. Durability tests were performed on the catalysts by applying a constant current density of 5 mA cm^{-2} for 20 h for the OER and by cycling the electrode potential between 0.6 and 1.0 V at 50 mV s^{-1} for 30,000 cycles for the ORR. A square wave voltammetry experiment was performed in a N_2-saturated 0.1 M KOH solution with a 2 mV potential increment, 5 mV potential amplitude, and 5 Hz frequency.

6.3. Results and Discussion

6.3.1. Preparation and characterization of GNS/MC catalysts

The design of our carbon-based bifunctional electrocatalysts was based on the nanocasting method using a mesoporous silica template. Ni- and Fe-phthalocyanines (NiPc and FePc, respectively) were used as precursors (Figure 6.1a). The NiPc and FePc were chosen because: (i) they yield carbon frameworks doped with metallic (Ni and Fe) and N species, which can endow the OER and ORR with high activities; and (ii) they can generate highly graphitic structures *in situ*, which can enhance the durability for oxygen electrocatalysis. To exploit these possibilities, we extensively prepared carbon nanostructures with different mass ratios between NiPc and FePc precursors and pyrolysis temperatures. Typically, a metal-Pc precursor (1 g) was mixed with SBA-15 silica, and the mixture was pyrolyzed at 1000 ^{o}C under a N_2 flow. After etching of the silica template, a carbon-based product was obtained. The use of NiPc, FePc, or their mixture as a precursor yielded Ni-MC, Fe-MC, or Ni_xFe_y-MC nanostructures, respectively. For comparison, ordered mesoporous carbon (OMC) was also prepared using metal-free phthalocyanine (Pc) as a precursor.

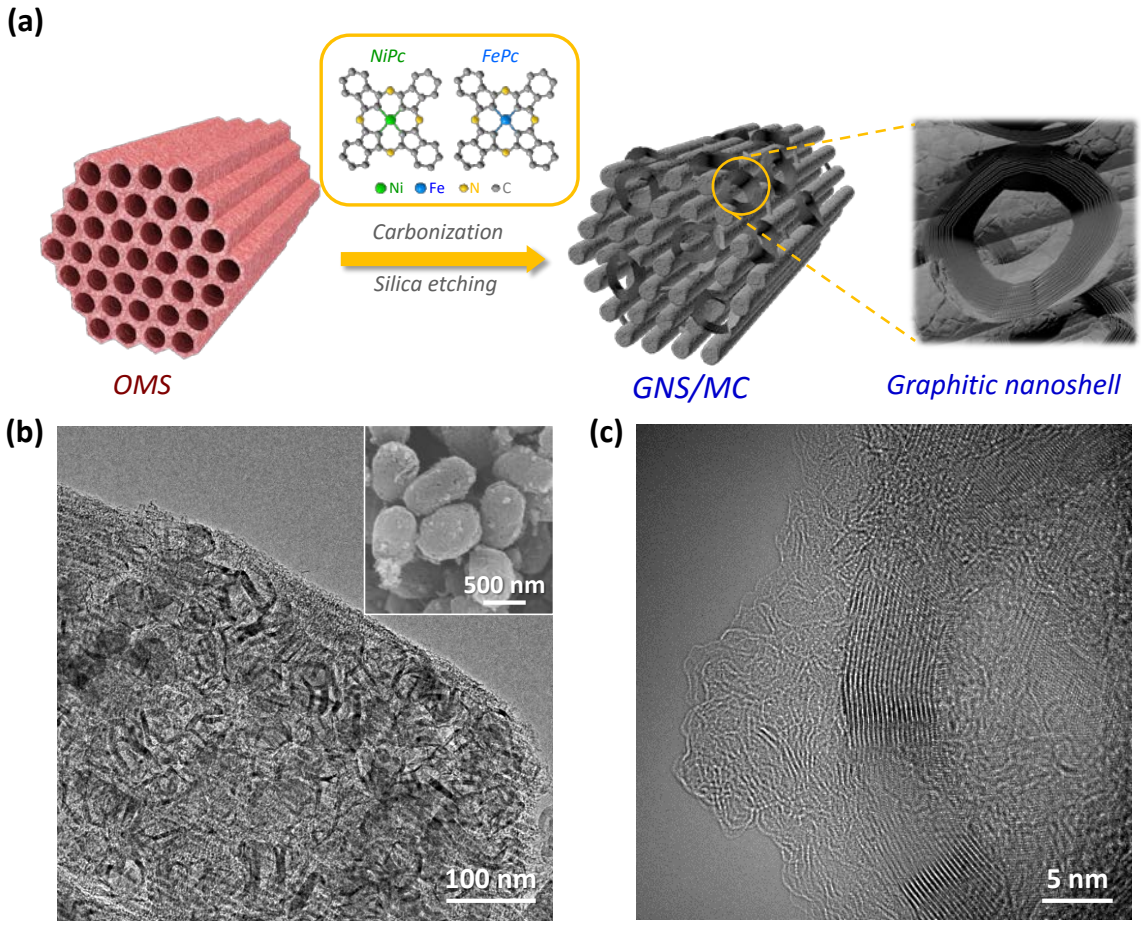

Figure 6.1. Synthetic strategy and characterization of GNS/MC nanohybrids. (a) Schematic illustration of the GNS/MC preparation: (i) NiPc and FePc carbonization in the presence of ordered mesoporous silica (OMS). (ii) OMS template etching with 10 wt% HF solution to yield the GNS/MC. (b) TEM images of the GNS/MC (inset: SEM image). (c) HR-TEM image of the GNS/MC.

We found that a sample prepared using a NiPc:FePc = 3:7 mass ratio at a pyrolysis temperature of 1000 ^{o}C (Ni_3Fe_7-MC) yielded a mesoporous carbon structure enriched with graphitic nanoshells, and exhibited the optimum bifunctional activity for the OER and ORR. Hereafter, the Ni_3Fe_7-MC material is referred to as GNS/MC, and the characterization and electrocatalytic investigation are focused on the GNS/MC, Ni-MC, and Fe-MC catalysts pyrolyzed at 1000 ^{o}C.

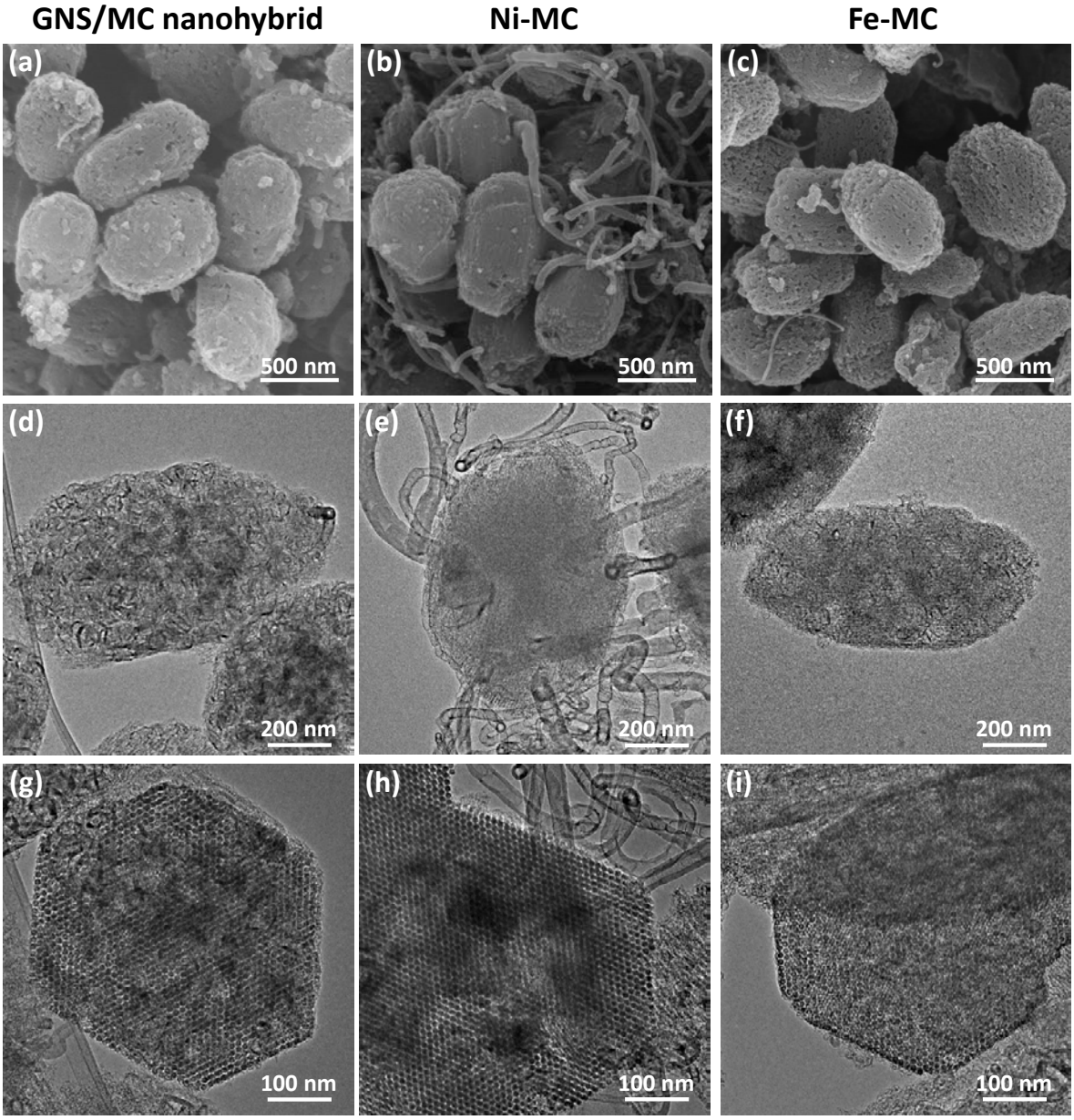

Figure 6.2. (a-c) SEM and (d-i) TEM images of (a,d,g) GNS/MC, (b,e,h) Ni-MC, and (c,f,i) Fe-MC catalysts.

The GNS/MC structure was observed using scanning electron microscopy (SEM; Figure 6.1b, inset and Figure 6.2a) and transmission electron microscopy (TEM; Figure 6.1b,c and Figure 6.2d,g), and the images revealed the formation of highly graphitic nanoshells with ca. 50 nm in hollow core size within mesoporous carbon particles. A high-resolution TEM (HR-TEM) image

(Figure 6.1c) further revealed the presence of ~8 nm thick graphitic nanoshells embedded in the mesoporous carbon structures. The Ni-MC exhibited a significantly different morphology, where carbon nanotubes were grown from the surfaces of mesoporous carbon particles (Figure 6.2b,e,h,). For the Fe-MC, a similar structure to that of the GNS/MC was observed, yet the formation of graphitic nanoshells was much less pronounced than in the case of the GNS/MC (Figure 6.2c,f,i). These results suggest that the use of both NiPc and FePc precursors is essential for the formation of highly dense, graphitic nanoshells inside the mesoporous structure.

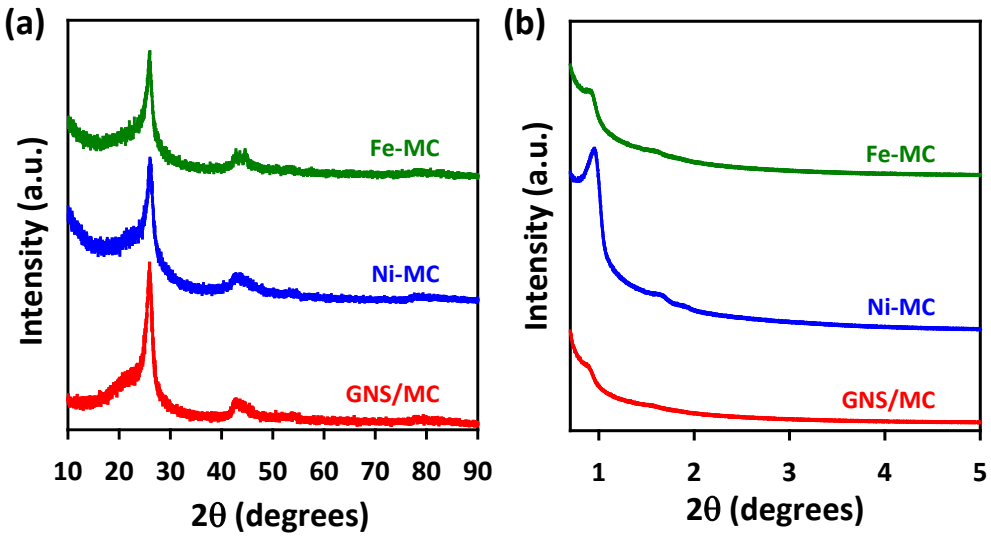

Figure 6.3. (a) Wide-angle and (b) small-angle XRD patterns of GNS/MC, Ni-MC, and Fe-MC catalysts.

The highly graphitic nature of the GNS/MC and mesostructure formation within this material were confirmed by wide- and small-angle X-ray diffraction (XRD) patterns, respectively (Figure 6.3). The GNS/MC exhibited a uniform mesopore centered at ~4.8 nm with a large Brunauer-Emmet-Teller (BET) surface area (815 m^2 g^{-1}) and a total pore volume of 1.30 cm^3 g^{-1}, as revealed by nitrogen physisorption analysis (Figure 6.4 and Table 6.1). The Ni-MC, Fe-MC, and OMC catalysts also exhibited similar textural properties to the GNS/MC. Inductively coupled plasma-optical emission spectroscopy and CHNS elemental analysis indicated that the GNS/MC predominantly consisted of carbon and nitrogen (1.9 wt%) with very small amounts of Ni (0.18 wt%) and Fe (0.21 wt%). The presence of nitrogen and metals in the GNS/MC was further confirmed *via* high-angle annular dark-field scanning TEM (HAADF STEM) coupled with the energy dispersive X-ray spectroscopy (Figure 6.5), as well as high-resolution X-ray photoelectron spectroscopy (XPS) (Figure 6.6). We note that the HR-TEM failed to identify any metallic nanoparticles in the GNS/MC. Hence, we suppose that the Ni and Fe species may exist in a molecularly dispersed form, rather than as nanoparticles.

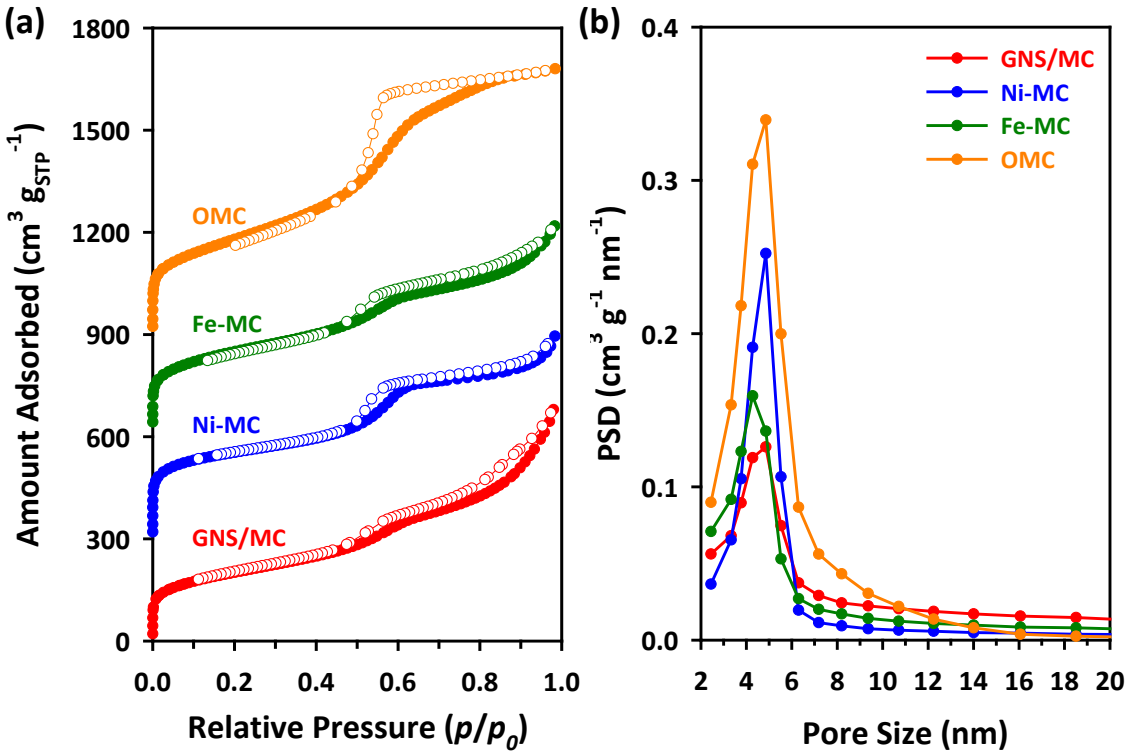

Figure 6.4. (a) N_2 adsorption isotherms of GNS/MC, Ni-MC, Fe-MC, and OMC catalysts and (b) corresponding pore size distribution (PSD) curves obtained from adsorption branches. For clarity, the N_2 isotherms of the Ni-MC, Fe-MC, and OMC are shifted upwards by 300, 600, and 900 cm^3 g^{-1}, respectively.

Table 6.1. Structural parameters and metal content of GNS/MC, Fe-MC, Ni-MC, and OMC catalysts.

Catalyst	S_{BET} (m^2 g^{-1})[a]	V_{tot} (cm^3 g^{-1})[b]	d_{meso} (nm)[c]	Metal Contents (wt%)[d]
GNS/MC	815	1.30	4.8	0.18 (Ni); 0.21 (Fe)
Ni-MC	930	0.92	4.8	1.5
Fe-MC	890	0.96	4.3	1.7
OMC	997	1.21	4.8	-

[a]BET specific surface area obtained from N_2 adsorption isotherm in the range of p/p_0 = 0.05-0.2.
[b]Total pore volume determined at p/p_0 = 0.95.
[c]Primary mesopore diameter calculated from BJH method.
[d]Determined by ICP-OES analysis.

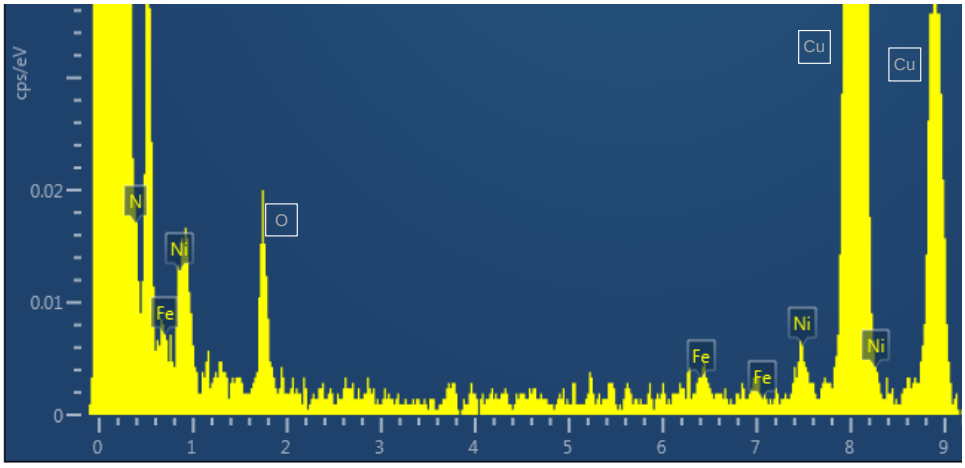

Figure 6.5. EDS spectrum of GNS/MC. The peaks corresponding to Cu originate from TEM grid.

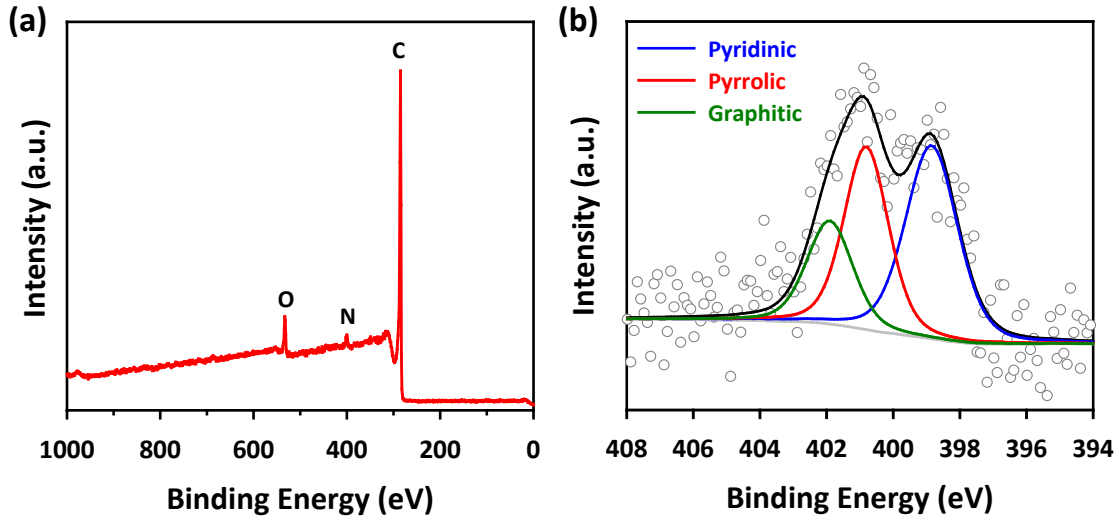

Figure 6.6. XPS spectra of GNS/MC: (a) survey and (b) N 1s spectra.

6.3.2. Bifunctional electrocatalytic activity and durability for OER and ORR

The bifunctional electrocatalytic activity of the GNS/MC, Ni-MC, and Fe-MC catalysts was evaluated using a rotating ring-disk electrode (RRDE) in an O_2-saturated 0.1 M KOH. The electrocatalytic activities of OMC, Pt/C (20 wt% Pt, Johnson Matthey), and Ir/C (20 wt% Ir, Premetek) were also measured as a benchmark. The linear sweep voltammetry (LSV) polarization curves for the OER and ORR and a bar graph comparing the oxygen electrode activity clearly revealed that the GNS/MC was the best-performing bifunctional catalyst among the compared samples (Figure 6.7a,b). For the OER, the GNS/MC exhibited an overpotential of 340 mV to yield 10 mA cm^{-2} (equivalent to 10 % solar-to-fuel conversion under one sun radiation), which was substantially lower than that of the monometal-doped Ni-MC (480 mV) and Fe-MC (500 mV). This indicates the critical importance of the presence of both Ni and Fe metals for the enhancement of OER activity. Furthermore, the GNS/MC outperformed the precious metal-based Pt/C (660 mV) and Ir/C (370 mV) catalysts. We

confirmed that the high OER activity exhibited by the GNS/MC originate from water oxidation rather than from other side reactions (Figure 6.8).[13] Regarding the ORR activity, the potential required to reach -3 mA cm^{-2} (almost equal to the half-wave potential, $E_{1/2}$) was 0.85 V (*vs.* RHE) for the GNS/MC, which was significantly higher than that of Ir/C (0.69 V) and compared favorably with Pt/C (0.88 V). Interestingly, the ORR activity of Fe-MC ($E_{1/2}$=0.85 V) was as high as that of the GNS/MC, whereas the Ni-MC ($E_{1/2}$=0.75 V) showed lower ORR activity; this suggests that the presence of Fe is important for the promotion of the ORR activity.

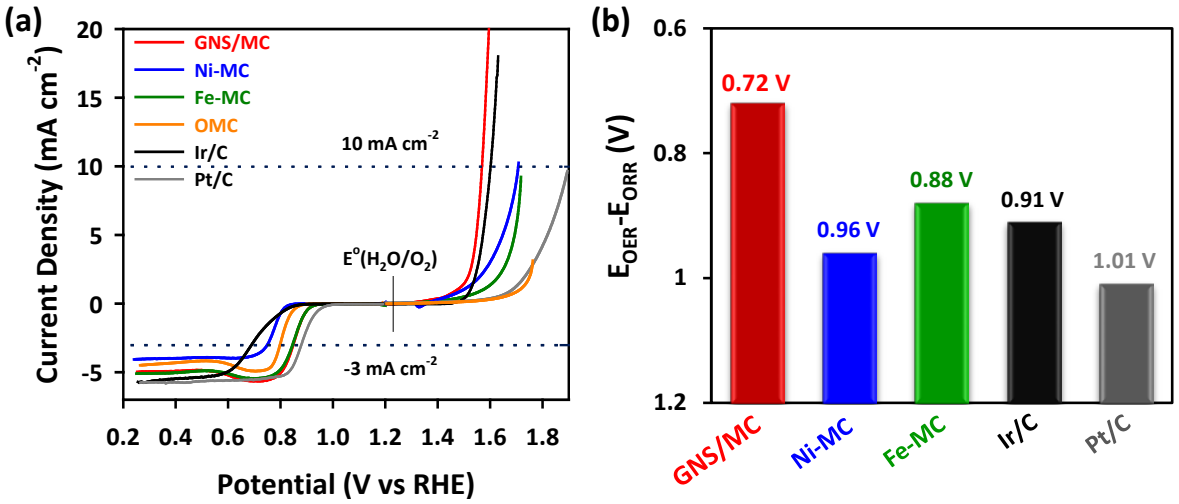

Figure 6.7. Electrocatalytic activity and durability for OER and ORR. (a) OER and ORR polarization curves of GNS/MC, Ni-MC, Fe-MC, OMC, Ir/C, and Pt/C catalysts in an O_2-saturated 0.1 M KOH at 1600 rpm rotation speeds and at 5 mV s^{-1} scan rate. (b) Comparison of oxygen electrode activity (E_{OER}-E_{ORR}) of GNS/MC, Ni-MC, Fe-MC, OMC, Ir/C, and Pt/C catalysts. Note that the y-axis (E_{OER}-E_{ORR}) values increase in a reverse manner.

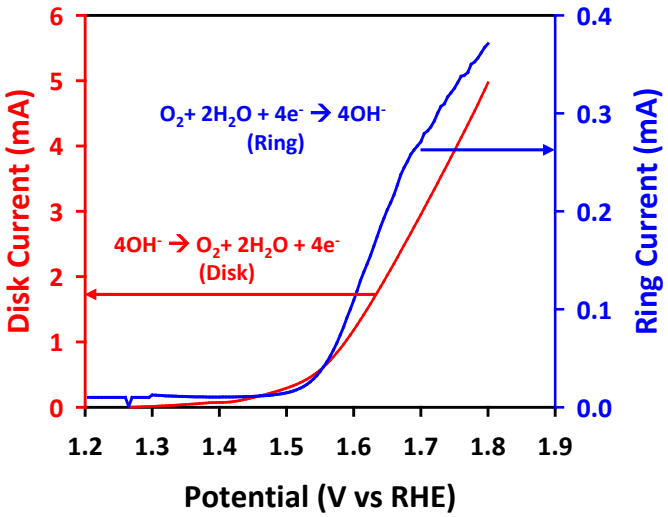

Figure 6.8. Disk and ring current during OER of GNS/MC catalyst in N_2-saturated 0.1 M KOH at 5 mV s^{-1} scan rate with 1600 rpm rotation speed. The ring potential was set to 0.4 V vs RHE.

The bar graph in Figure 6.9 compares the bifunctional oxygen electrode activities of the various catalysts; this activity is defined as the potential gap between the OER potential at 10 mA cm^{-2} and the ORR potential at -3 mA cm^{-2}. By this metric, the GNS/MC exhibited the best oxygen electrode activity (0.72 V), far exceeding that of the Ni-MC (0.96 V) and Fe-MC (0.88 V), as well as those of the precious metal-based Ir/C (0.91 V) and Pt/C (1.01 V) catalysts. The GNS/MC exhibited Tafel slopes of 80 and 50 mV/decade for the OER and ORR, respectively, which were close to those of the precious metal-based Ir/C (90 mV/decade for the OER) and Pt/C (60 mV/decade for the ORR), as shown in Figure 6.10.

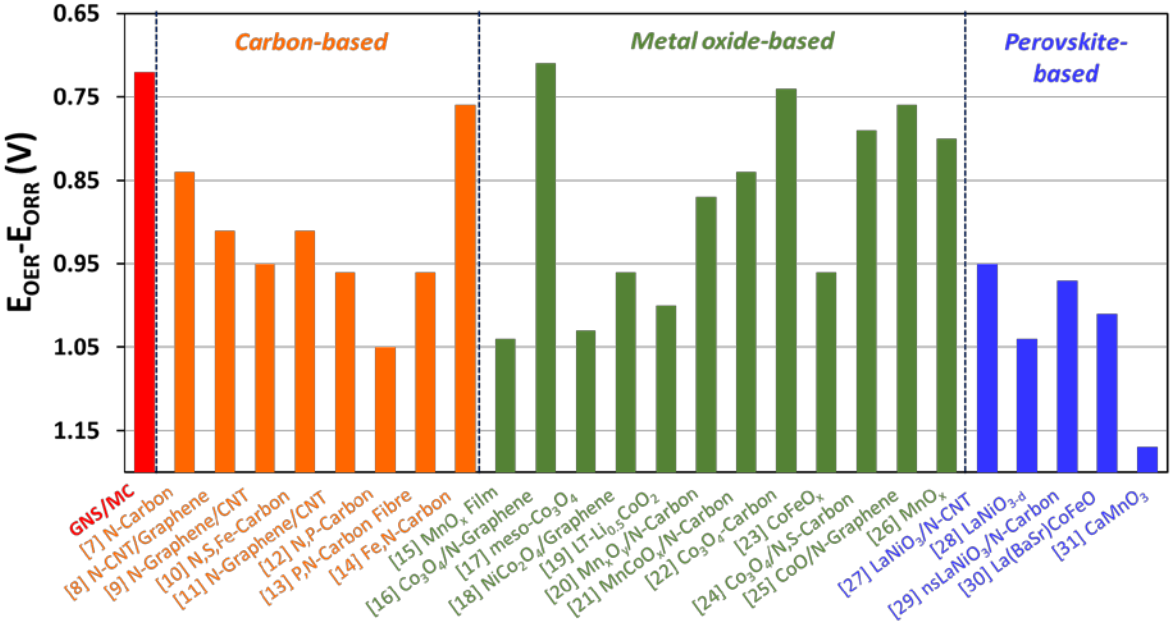

Figure 6.9. Comparison of oxygen electrode activity of GNS/MC catalyst with those of previously reported catalysts, including carbon-, metal oxide-, and perovskite-based catalysts (the numbers on the x-axis are citations).

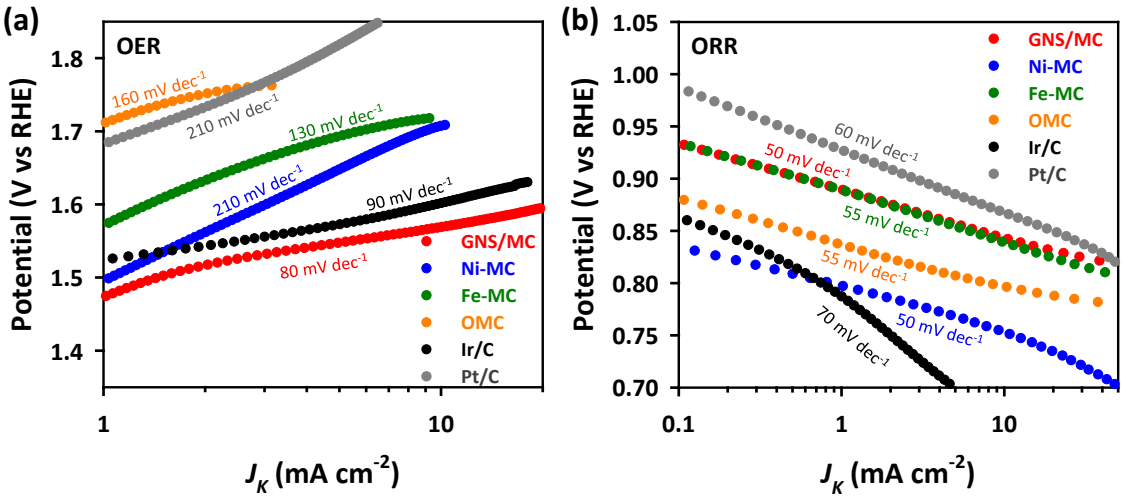

Figure 6.10. Tafel plots of GNS/MC, Ni-MC, Fe-MC, OMC, Ir/C, and Pt/C catalysts for (a) OER and (b) ORR.

An extensive comparison of the observed oxygen electrode activity with those of previously reported high-performance catalysts indicates that GNS/MC is one of the best-performing bifunctional catalysts (Figure 6.9 and Tables 6.2, 6.3). Notably, when compared to the doped carbon catalysts, the oxygen electrode activity of GNS/MC (0.72 V) is unprecedentedly high. Furthermore, the activity of GNS/MC even rivals that of the most active transition metal-based Co_3O_4/N-rmGO catalyst (0.71 V),[16] despite the very small amounts of metal (0.39 wt%) present in the former compared to that in the latter (~70 wt%).

Table 6.2. Oxygen electrode activities of GNS/MC, Ni-MC, Fe-MC, OMC, Ir/C, and Pt/C catalysts.

Catalyst	E_{OER} V@10 mA cm^{-2} (*vs.* RHE)	E_{ORR} V@-3 mA cm^{-2} (*vs.* RHE)[a]	Oxygen Electrode Activity (V *vs.* RHE)[b]
GNS/MC	1.57	0.85	0.72
Ni-MC	1.71	0.75	0.96
Fe-MC	1.73	0.85	0.88
OMC	-	0.80	-
Ir/C	1.60	0.69	0.91
Pt/C	1.89	0.88	1.01

[a]The potential at which an ORR current density of -3 mA cm^{-2} was reached at 1600 rpm.
[b]The potential gap between the E_{OER} and E_{ORR} (E_{OER}-E_{ORR}).

Table 6.3. Oxygen electrode activity of GNS/MC catalyst compared with those of previously reported catalysts, including carbon-, metal oxide-, and perovskite-based catalysts.

Catalyst	OER[a]		ORR[b]		Oxygen Electrode Activity (V *vs.* RHE)	Ref
	E_{OER} V@10 mA cm^{-2} (*vs.* RHE)	Tafel Slope (mV dec^{-1})	E_{ORR} V @ -3 mA cm^{-2} (*vs.* RHE)	Tafel Slope (mV dec^{-1})		
GNS/MC	**1.57**	**80**	**0.85**	**70**	**0.72**	**This work**
N-doped Carbon	1.61	~110	0.77	-	0.84	[7]
N-doped CNT/Graphene[c]	1.75	-	0.84	-	0.91	[8]
N-doped Graphene/CNT	1.65	-	0.64	-	0.95	[9]
N,S,Fe-doped Carbon	1.78	-	0.87	-	0.91	[10]
N-doped Graphene/CNT	1.63	83	0.67	-	0.96	[11]
N,P-doped Carbon	1.87 (@8 mA cm^{-2})	-	0.82	-	1.05	[12]
P,N-doped Carbon Fibre[d]	1.63	61.6	0.67	122	0.96	[13]
Fe,N-doped Carbon	1.59	-	0.83	-	0.76	[14]

MnO_x Film	1.77	-	0.73	-	1.04	[15]
Co_3O_4/N-Graphene	1.54	67	0.83	42	0.71	[16]
meso-Co_3O_4	1.64	100	0.61	60	1.03	[17]
$NiCo_2O_4$/Graphene[c]	1.66	164	0.70	37	0.96	[18]
LT-$Li_{0.5}CoO_2$	1.64	60	0.64	-	1.0	[19]
Mn_xO_y/N-doped Carbon	1.68	82.6	0.81	-	0.87	[20]
$MnCoO_x$/N-doped CNT	1.66	-	0.82	-	0.84	[21]
Co_3O_4-Carbon[d]	1.52	70	0.78	89	0.74	[22]
$CoFeO_x$	1.72	102	0.76	54	0.96	[23]
Co_3O_4/N,S-doped Carbon	1.61	47	0.82	-	0.79	[24]
CoO/N-doped Graphene	1.57	71	0.81	48	0.76	[25]
MnO_x on Stainless Steel mesh[e]	1.62	-	0.82		0.80	[26]
$CaMnO_3$	1.91	-	0.74	75	1.17	[27]
$LaNiO_3$/N-CNT	1.76	-	0.81	-	0.95	[28]
$LaNiO_{3-\delta}$	1.61	80	0.57	95	1.04	[29]
ns$LaNiO_3$/N-doped Carbon	1.61	51	0.64	45	0.97	[30]
La(BaSr)CoFeO	1.57	-	0.56	-	1.01	[31]

[a]Conversion of Hg/HgO electrode, Ag/AgCl electrode, and SCE were conducted by adopting the reported data. E(RHE)=E(Hg/HgO) + 0.884 V, E(Ag/AgCl) + 0.916 V, and E(SCE) + 0.985 V
[b]The potential at which an ORR current density of -3 mA cm^{-2} was reached at 1600 rpm.
[c]E_{OER} was obtained at which the measured current is equal to one-half of the diffusion-limited current value (half-wave potential, $E_{1/2}$) at 900 rpm.
[d]E_{OER} was obtained from half-wave potential measured at carbon fibre (P,N-doped Carbon Fibre) and Cu foil (Co_3O_4-Carbon) as working electrode, respectively.
[e]E_{OER} was defined at which an ORR current density of -5mA cm^{-2} was reached. Stainless steel was used as working electrode.

The GNS/MC also exhibited excellent durability for the OER and ORR. The OER durability of this material was assessed with a chronopotentiometry at 5 mA cm^{-2} (Figure 6.11a), which revealed that the OER activity was maintained up to 20 h after the initial voltage drop. This demonstrates the appreciable stability of the GNS/MC under oxidizing conditions. For the ORR durability test, the GNS/MC underwent potential cycling between 0.6 and 1.0 V for 30,000 times at 50 mV s^{-1} (Figure 6.11b and Figure 6.12). The GNS/MC exhibited remarkable durability, as revealed by an almost identical CV, a minimal negative shift of $E_{1/2}$ by 15 mV, and preserved morphology after the durability test.

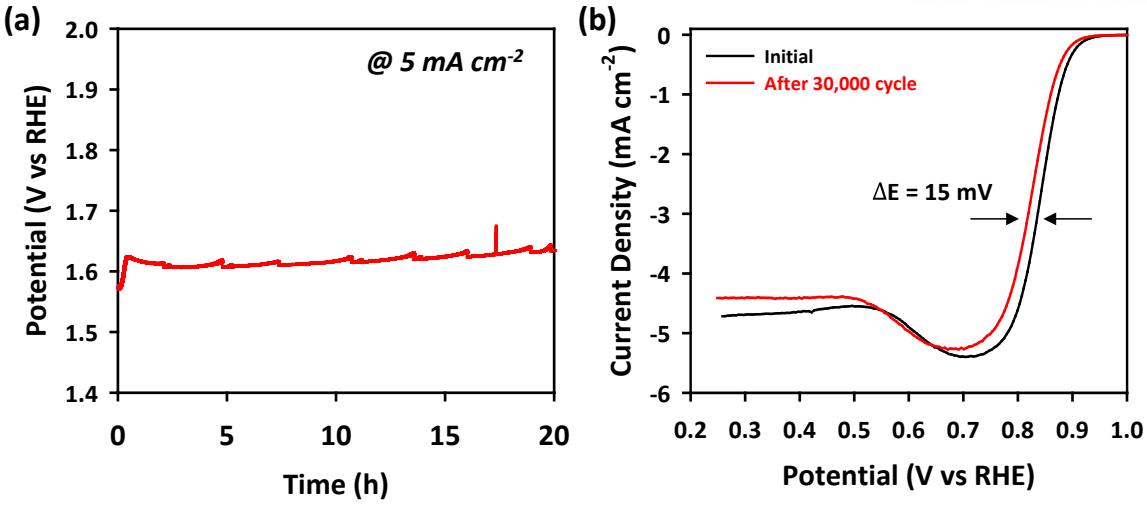

Figure 6.11. (a) OER chonoamperometric response of GNS/MC at 5 mA cm^{-2} constant current density. (b) ORR polarization curves of GNS/MC before and after 30,000 potential cycling in a N_2-saturated 0.1 M KOH. Potential cycling was conducted from 0.6 to 1.0 V vs. RHE at 50 mV s^{-1}.

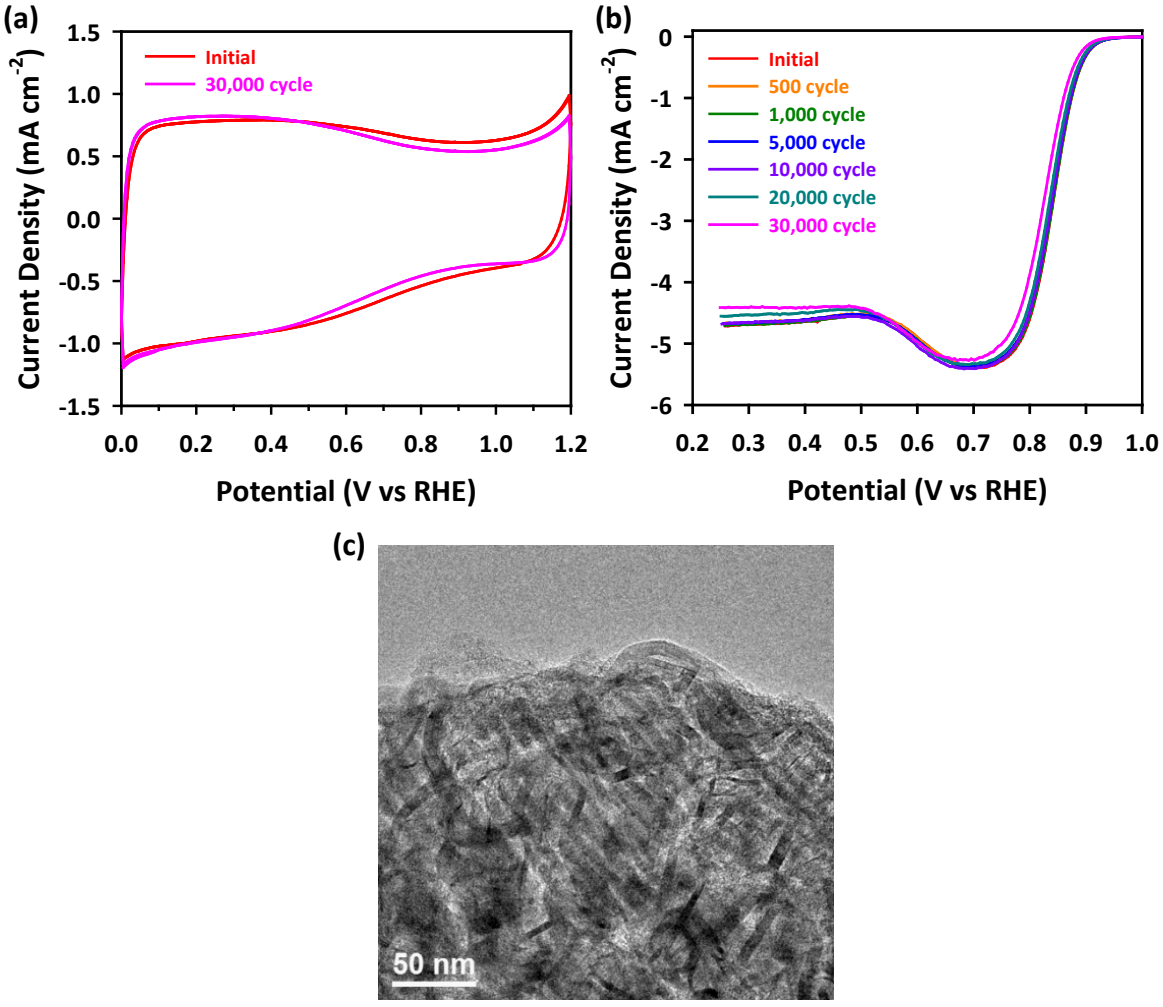

Figure 6.12. (a) Cyclic voltammogram of GNS/MC catalyst before and after 30,000 potential cycles in N_2-saturated 0.1 M KOH solution. (b) Evolution of ORR polarization curves for GNS/MC under potential cycling in N_2- saturated 0.1 M KOH solution. (c) Corresponding TEM images after potential cycling.

6.3.3. Origin of highly bifunctional catalytic activity of GNS/MC

In order to understand the origin of the high catalytic activity and durability, we further scrutinized the structural entities of the GNS/MC catalyst using X-ray absorption spectroscopy (XAS). The *in situ* Ni K-edge X-ray absorption near edge structure (XANES) spectra of the catalysts and Ni reference samples were measured in 0.1 M KOH solution (Figure 6.13). Under open circuit voltage (OCV), the GNS/MC and Ni-MC catalysts exhibited a decreased peak intensity at ~8337 eV (a fingerprint of the Ni^{2+} square planar complex[39]), compared to the NiPc precursor, along with the evolution of a new peak at ~8332 eV (Figure 6.13a). These simultaneous changes suggest the formation of axial ligand(s) (commonly bridging O and/or hydroxyl/H_2O)[40] to Ni centers in the GNS/MC and Ni-MC catalysts. When a potential of 1.8 V was applied (OER condition), the XANES spectra of the GNS/MC exhibited an increase in the white line intensity, indicating the further oxidation of the Ni centers, possibly due to the adsorption of reactive oxygenated species. The *in situ* Ni K-edge extended X-ray absorption fine structure (EXAFS) spectra of the GNS/MC (Figure 6.13b) under OCV revealed a major peak at approximately 1.5 Å, which is associated with metal-N bonding.[39] Interestingly, an increase in the intensity of this peak was observed under an oxidative potential (1.8 V), indicating the formation of oxygenated adsorbates (O-Ni-N_x). Notably, in comparing the GNS/MC and Ni-MC catalysts, the former showed higher peak intensity at 1.5 Å than the latter, which can be associated with the superior OER activity of the GNS/MC containing both Ni and Fe species. Recent literature has also identified the promoting role of Fe species for the OER.[41]

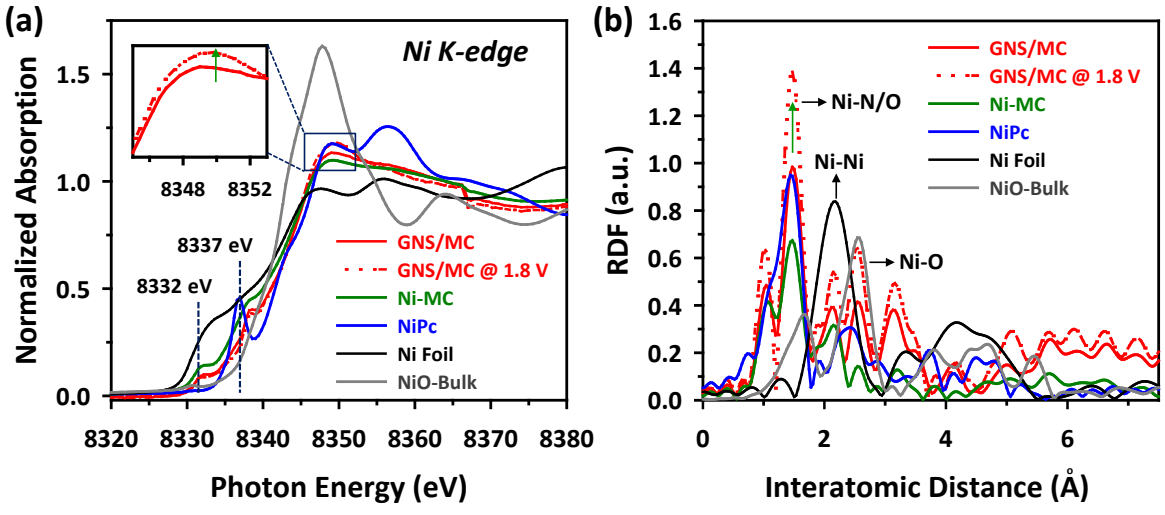

Figure 6.13. XAS characterization. (a) Ni K-edge XANES and (b) EXAFS spectra of GNS/MC, NiPc, and Ni related references. The EXAFS and XANES spectra of the GNS/MC catalyst were collected under the *in situ* electrochemical condition.

The *in situ* Fe K-edge XAS analyses of the catalysts were also performed (Figure 6.14a,b). The Fe K-edge EXAFS spectrum of the GNS/MC revealed a significant reduction in the Fe-N peak at

1.4 Å (Figure 6.14b) compared to that of the FePc precursor, along with the evolution of a new peak at ~2.2 Å. These changes suggest that, after the high-temperature pyrolysis, some portion of the Fe-N moieties were transformed into metallic, oxide, or carbide Fe phases, which are undetectable to HR-TEM and XPS analyses. We suppose that the preserved Fe-N moieties and Fe carbide phase could contribute to the high ORR activity of the GNS/MC and Fe-MC catalysts, as revealed by recent works on high-performance Fe-N/C ORR catalysts.[42-48] The XAS results imply that the OER is predominantly catalyzed by Ni species with Fe exerting a synergistic role, whereas the ORR is enhanced by the presence of Fe species.

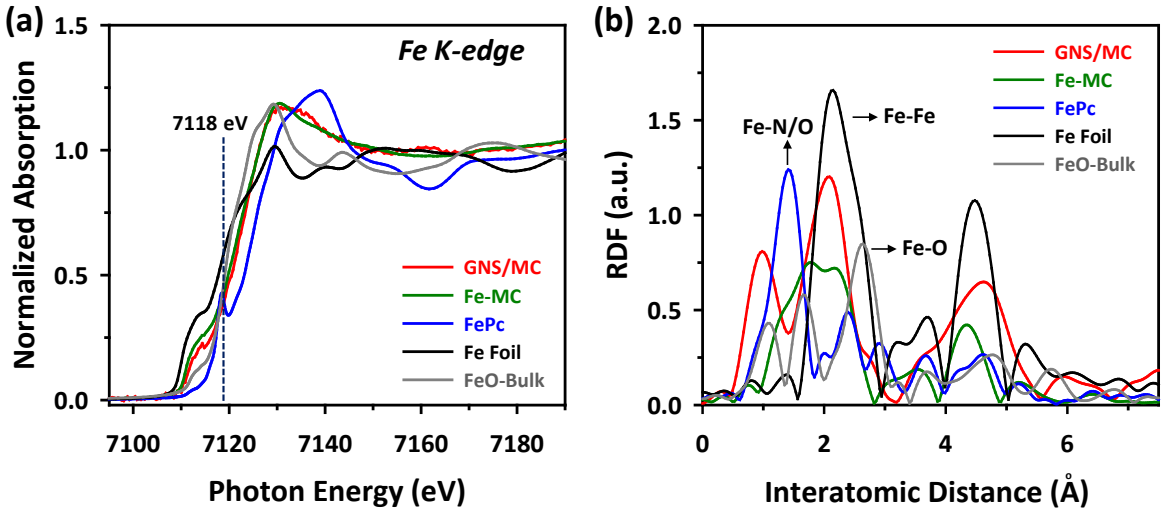

Figure 6.14. XAS characterization (a Fe K-edge XANES and (b EXAFS spectra of GNS/MC, FePc, and Fe related references. The EXAFS and XANES spectra of the GNS/MC catalyst were collected under the *in situ* electrochemical condition.

We further investigated the presence of metal-N coordination using square wave voltammetry (SWV) measurements (Figure 6.15).[49] The SWVs of the GNS/MC and the Ni-MC catalysts exhibited a small peak at above 1.4 V corresponding to the oxidation of metal-N ligand.[44] In contrast, the Fe-MC and OMC showed no oxidation peak. Interestingly, there was a positive shift in the ligand oxidation peak from the Ni-MC to the GNS/MC, which can be associated with stronger binding of the axial OH group.[50] Hence, the Ni-N coordination in the GNS/MC is more amenable to the adsorption of the OH group than the Ni-MC catalyst, providing further evidence for the enhanced OER activity of the GNS/MC catalyst. The anodic shift of the Ni redox peaks due to the incorporation of Fe has also been observed in a Fe-doped nickel oxyhydroxide ($Ni_{1-x}Fe_xOOH$) catalyst.[41]

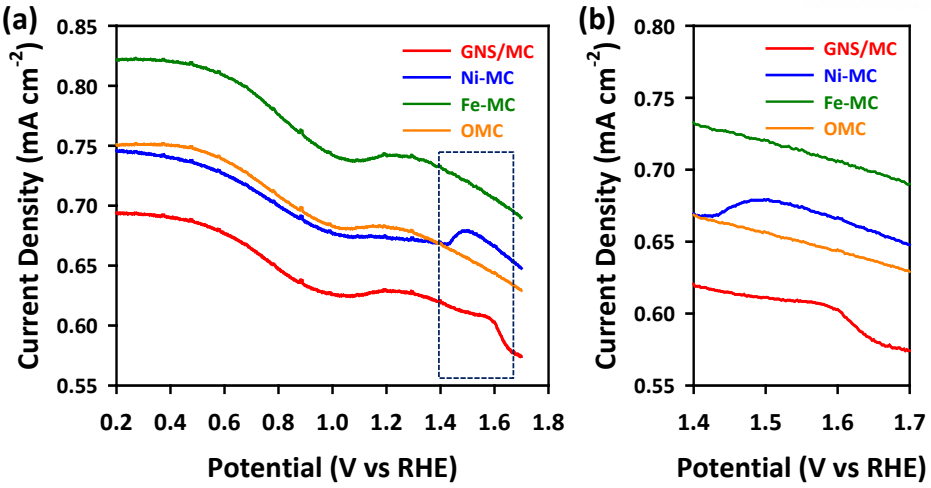

Figure 6.15. Square wave voltammetry analysis. (a) Square wave voltammetry profiles of GNS/MC, Ni-MC, Fe-MC, and OMC catalysts collected in a N_2-saturated 0.1 M KOH and (b) corresponding enlarged area profiles.

Next, the graphitic nature of the catalysts was assessed suing Raman spectroscopy (Figure 6.16). The Raman spectra of all catalysts showed two major peaks, corresponding to the D (disordered, ~1350 cm^{-1}) and G (graphitic nature, ~1580 cm^{-1}) bands.[51] The intensity ratios between the D and G (I_D/I_G) peaks revealed that the GNS/MC had the lowest I_D/I_G value (0.51), followed by the Fe-MC (0.86), Ni-MC (0.98), and OMC (0.99), indicating the very high graphitic character of the graphitic shell in the GNS/MC. We note that the GNS/MC exhibited more pronounced Raman peaks above ~2250 cm^{-1}; this indicates the high defect nature of the graphitic shell in the GNS/MC.[51] Furthermore, a downshift in the G peak was observed for the GNS/MC compared to those of other catalysts (Figure 6.16b); it has been suggested that this is a feature of strained or curved graphitic planes.[52] Note that previous works indicated that the presence of N atoms at graphitic carbon defects can lead to enhanced carbon-based catalyst OER activity.[7] Furthermore, the highly graphitic structure of the GNS/MC should be responsible for its excellent durability.

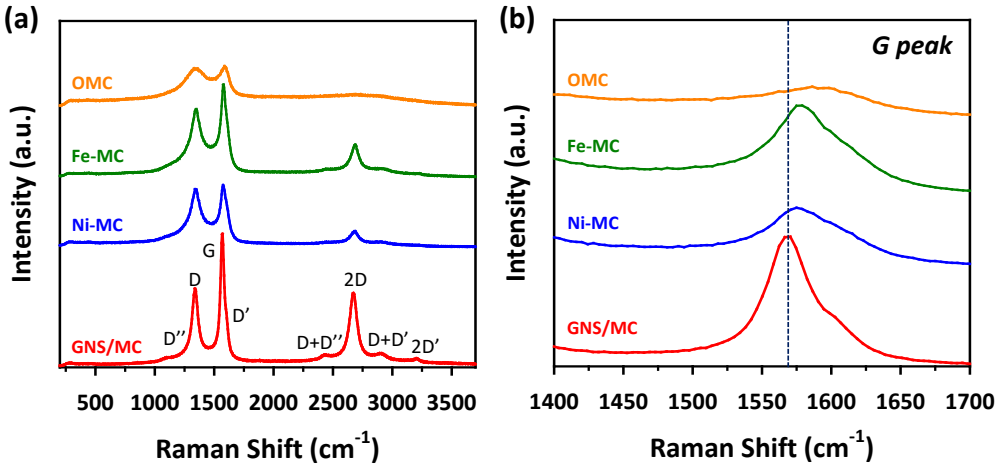

Figure 6.16. Raman spectroscopy characterization. (a) Raman spectra of GNS/MC, Ni-MC, Fe-MC, and OMC catalysts and (b) enlarged area spectra of G peak.

Based on the above discussion, the synergistic role of Ni and Fe species as well as the presence of graphitic nanoshell structure could contribute to the very high catalytic activity and durability of GNS/MC catalyst.

6.3.4. Aqueous Na-air battery performance

We next exploited our GNS/MC as an air cathode for application in an aqueous Na-air battery. Figure 6.17a,b shows a schematic illustration and digital picture of the rechargeable aqueous Na-air battery, which is composed of Na metal and catalyst-coated carbon paper as an anode and cathode, respectively. $NaCF_3SO_3$/TEGDME (non-aqueous electrolyte) and 0.1 M NaOH aqueous solution were used as an anolyte and catholyte, respectively. The NASICON solid electrolyte was employed to selectively exchange the sodium ions from catholyte to anode and vice-versa as well as it is used to separate anolyte and catholyte to avoid the mixing of both electrolytes. In Figure 6.14a, during discharging of the cell, Na metal is oxidized to Na ions (eq.1) that transfer to the cathode side through the NASICON solid electrolyte. In the cathode side, oxygen diffused from the cathode is reduced and form OH^- (ORR, oxygen reduction reaction) by reaction with H_2O (eq. 2). During charging of the cell, the above reactions occur in the opposite direction; Na-ions are reduced to Na in the anode side (eq. 1), and oxygen evolution reaction (OER) occurs at the cathode side (eq. 2). The electrochemical reactions during charging and discharging at the anode and cathode sides can be described as follows:

Anode: $Na \leftrightarrow Na^+ + e-$	E° =+2.71 V	(1)
Cathode: $O_2 + 2H_2O + 4e- \leftrightarrow 4OH^-$	E° = +0.40 V	(2)
Overall: $4Na + O_2 + 2H_2O \leftrightarrow 4NaOH$	E = 3.11 V	(3)

The charge-discharge curves of aqueous Na-air batteries based on the different cathodes are shown in Figure 6.18a, where ΔV denotes the voltage difference between the charge and discharge voltages. It is clear that the GNS/MC-based battery exhibited the best performance, having the lowest ΔV of 115 mV; this was followed by the Pt/C (179 mV), Ir/C (364 mV), and carbon paper with no catalyst (698 mV). These charge/discharge experiments clearly verified the superiority of GNS/MC among the prepared catalysts in the full-cell configuration, which was also demonstrated in the half-cell tests using the RRDE method, although the voltage difference order (GNS/MC>Pt/C>Ir/C) observed in the aqueous Na-air battery test results is partially inconsistent with oxygen electrode activity order (GNS/MC>Ir/C>Pt/C) measured with the RRDE method. The round-trip efficiency (the charge-to-discharge voltage ratio) was also the highest for the GNS/MC-based battery, at 96.28 % (Table 6.4). In a cell configuration, an aqueous Na-air battery comprising GNS/MC achieved a maximum power density of 78.2 mW g^{-1} at a current density of 60 mA g^{-1} (Figure 6.18b).

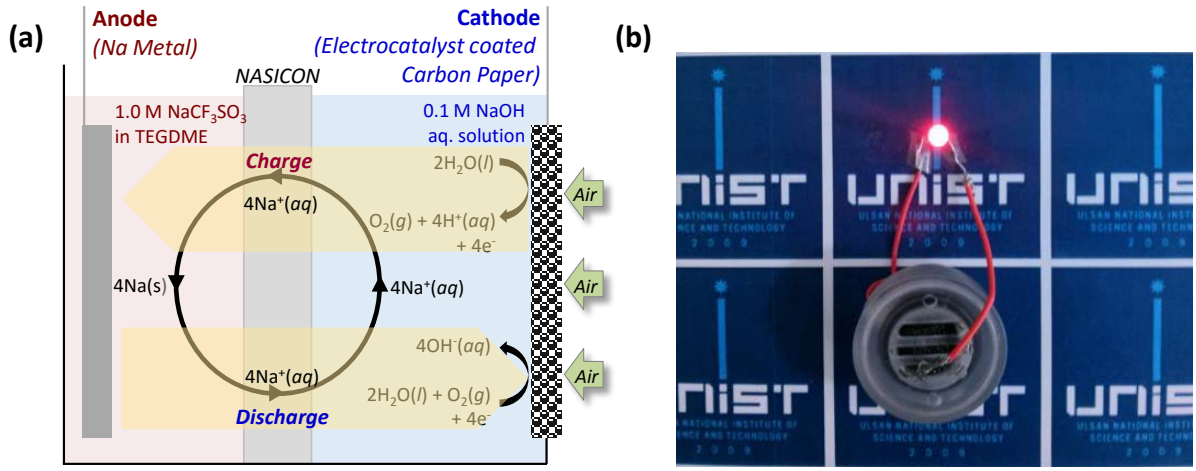

Figure 6.17. Aqueous Na-air battery performance. (a) Schematic illustration of rechargeable aqueous Na-air battery and reactions during charge/discharge process. 1.0 M $NaCF_3SO_3$/tetraethylene glycol dimethyl ether (TEGDME) (non-aqueous electrolyte) and 0.1 M NaOH aqueous solution were used as an anolyte and a catholyte, respectively. Na super ionic conducting (NASICON) solid electrolyte was employed to selectively exchange the Na ions from the catholyte to anode and *vice versa* as well, and to separate the anolyte and the catholyte to prevent the mixing of both electrolytes. As illustrated in Figure 6.17a, upon charging, the Na ions diffuse from the catholyte to the anode through the NASICON solid electrolyte. Simultaneously, OER occurs at the cathode. Similarly, upon discharging, the Na ions back-diffuse from the anode to the catholyte through the NASICON solid electrolyte while the ORR occurs at the cathode. (b) Digital picture of aqueous Na-air battery using GNS/MC coated carbon paper.

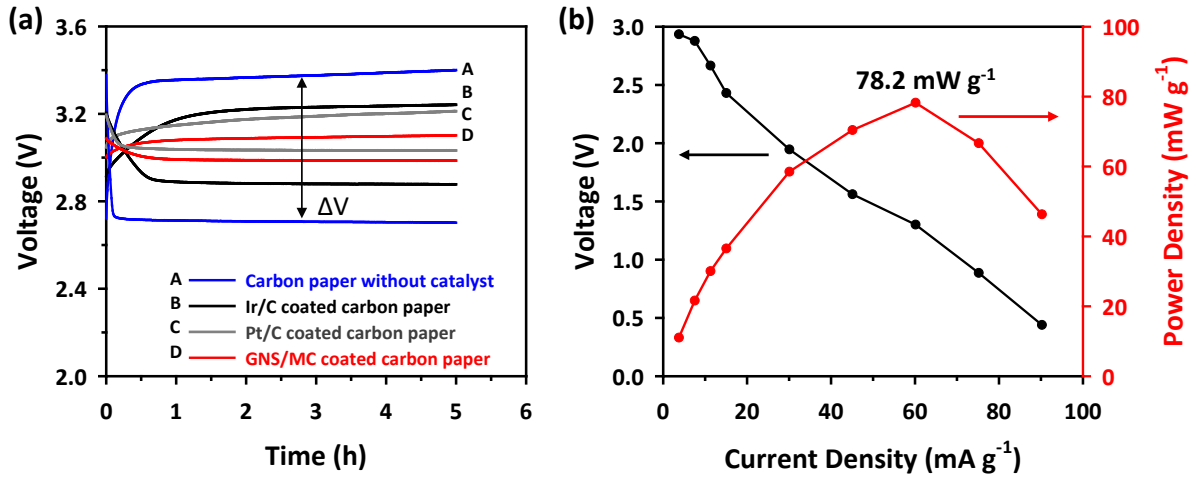

Figure 6.18. (a) Comparison of voltage difference between charge and discharge voltage plateaus of aqueous Na-air batteries using various electrocatalysts-coated carbon papers. (b) Power density curve of aqueous Na-air battery using GNS/MC catalyst-coated carbon paper at 3-90 mA g^{-1} current density.

Table 6.4. Comparison of voltage difference and round trip efficiencies of aqueous Na-air batteries using different cathode materials: GNS/MC, Pt/C, Ir/C, and carbon paper without catalyst.

Catalyst	Charge Voltage Plateau (V)	Discharge Voltage Plateau (V)	Voltage Gap (V)	Round Trip Efficiency (%)
GNS/MC	3.1015	2.9862	0.1153	96.28
Pt/C	3.2119	3.0324	0.1795	94.41
Ir/C	3.2416	2.8777	0.3639	88.77
Carbon-paper w/o catalyst	3.4003	2.7022	0.6981	79.47

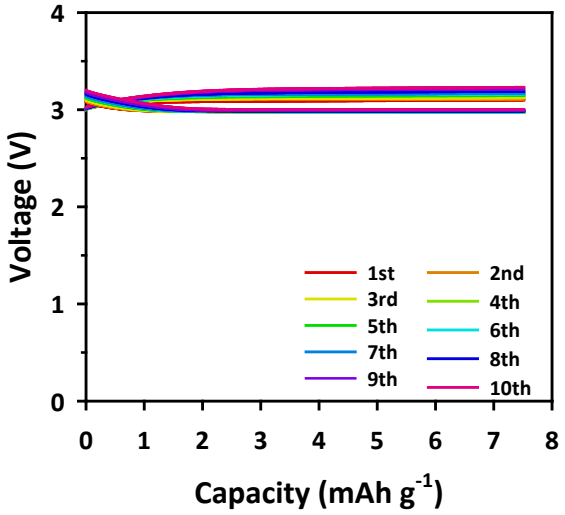

Figure 6.19. Charge/discharge curves of aqueous Na-air battery using GNS/MC coated carbon paper for 10 cycles.

Figure 6.19 shows the charge-discharge curves of the aqueous Na-air battery with the GNS/MC electrocatalyst coated carbon paper, which clearly indicated that the cell could be reversibly charged or discharged. The discharge potential of the cell was almost completely preserved for 10 cycles, reflecting the excellent ORR stability of the GNS/MC. The charge potential has increased with increasing cycles (from 3.102 V to 3.240 V). The GNS/MC catalyst preserved its original morphology after 10 cycles of aqueous Na-air battery test, as revealed by the TEM images (Figure 6.20). To the best of our knowledge, this is the first example of rechargeable aqueous Na-air battery to date. With the above results, we confirmed that the GNS/MC is a highly promising electrocatalyst for the aqueous Na-air battery with its low voltage difference, higher round-trip efficiency, high power density, and excellent charge-discharge stability.

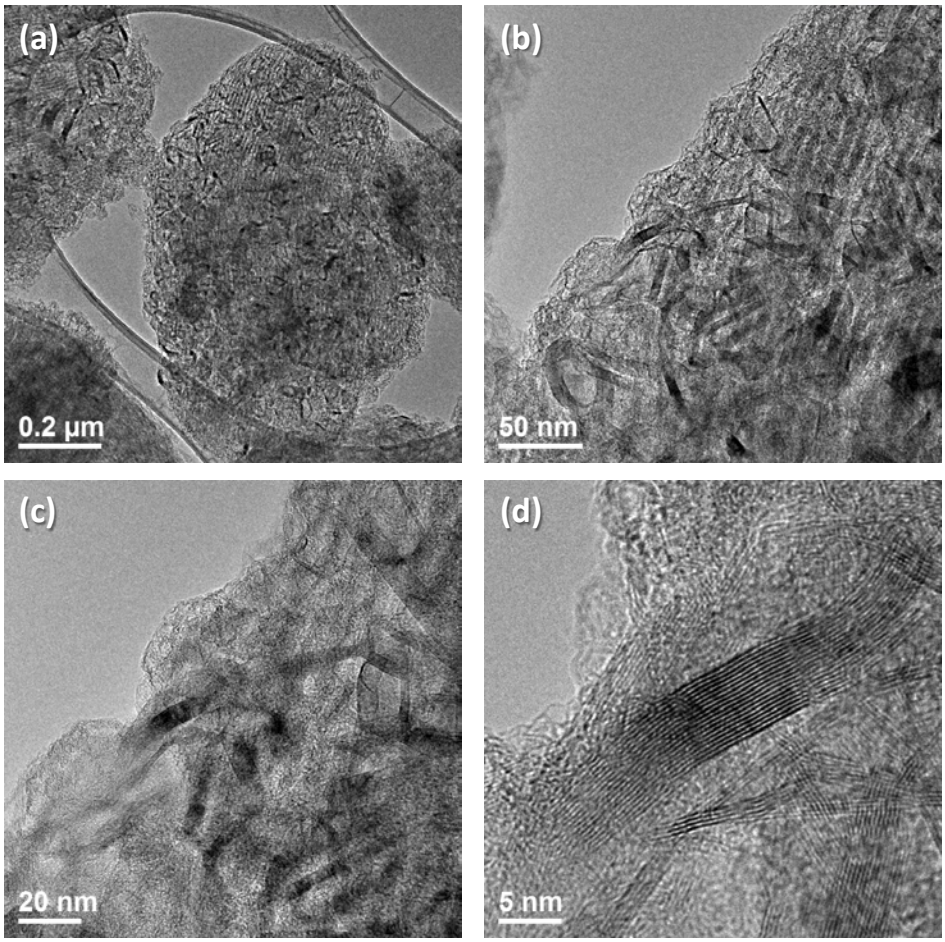

Figure 6.20. TEM image of the GNS/MC catalyst after 10 cycles of the aqueous Na-air battery cell test.

6.4. Conclusions

We have demonstrated a highly active and robust bifunctional oxygen electrocatalyst based on GNS/MC nanohybrids, which integrate multiple structural motifs that are responsible for the two oxygen electrode reactions (OER and ORR). The GNS/MC, which contains highly graphitic, defect-rich nanoshells contents and small amounts of Ni and Fe entities, exhibits very high OER and ORR activities and an oxygen electrode activity value of 0.72 V. This is one of the highest performances among carbon-based catalysts and surpasses that of precious metal-based Ir/C and Pt/C catalysts. *In situ* XAS and Raman spectroscopy data have provided critical insights into the structure of catalytic entities in the GNS/MC catalyst for the OER and ORR. Significantly, the first example of rechargeable aqueous Na-air battery has been demonstrated using the GNS/MC as an air cathode. We believe that the integrated design concept demonstrated using the GNS/MC can be further extended to other carbon-based electrocatalysts, for application in advanced energy-conversion and storage systems.[53]

6.5. References

(1) Bruce, P. G.; Freunberger, S. A.; Hardwick, L. J.; Tarascon, J.-M. *Nat. Mater.* **2012**, *11*, 19.

(2) Park, S.; Shao, Y.; Liu, J.; Wang, Y. *Energy Environ. Sci.* **2012**, *5*, 9331.

(3) Katsounaros, I.; Cherevko, S.; Zeradjanin, A. R.; Mayrhofer, K. J. J. *Angew. Chem. Int. Ed.* **2014**, *53*, 102.

(4) Jiao, Y.; Zheng, Y.; Jaroniec, M. Qiao, S. Z. *Chem. Soc. Rev.* **2015**, *44*, 2060.

(5) McCrory, C. C. L.; Jung, S.; Ferrer, M. I.; Chatman, S. M.; Peters, J. C.; Jaramillo, T. F. *J. Am. Chem. Soc.* **2015**, *137*, 4347.

(6) Debe, M. K. *Nature* **2012**, *486*, 43.

(7) Zhao, Y.; Nakamura, R.; Kamiya, K.; Nakanishi, S.; Hashimoto, K. *Nat. Commun.* **2013**, *4*, 2390.

(8) Park, H. W.; Lee, D. U.; Liu, Y.; Wu, J.; Nazar, L. F.; Chen, Z. *J. Electrochem. Soc.* **2013**, *160*, A2244.

(9) Wen, Z.; Ci, S.; Hou, Y.; Chen, J. *Angew. Chem. Int. Ed.* **2014**, *53*, 6496.

(10) Sahraie, N. R.; Paraknowitsch, J. P.; Gobel, C.; Thomas, A. Strasser, P. *J. Am. Chem. Soc.* **2014**, *136*, 14486.

(11) Tian, G.-L.; Zhao, M.-Q.; Yu, D.; Kong, X.-Y.; Huang, J.-Q.; Zhang, Q. Wei, F. *Small* **2014**, *10*, 2251.

(12) Zhang, J.; Zhao, Z.; Xia, Z.; Dai, L. *Nat. Nanotech.* **2015**, *10*, 444.

(13) Ma, T. Y.; Ran, J.; Dai, S. Jaroniec, M.; Qiao, S. Z. *Angew. Chem. Int. Ed.* **2015**, *54*, 4646.

(14) Zhao, Y.; Kamiya, K.; Hashimoto, K.; Nakanishi, S. *J. Phys. Chem. C* **2015**, *119*, 2583.

(15) Gorlin, Y.; Jaramillo, T. F. *J. Am. Chem. Soc.* **2010**, *132*, 13612.

(16) Liang, Y.; Li, Y.; Wang, H.; Zhou, J.; Wang, J.; Regier, T.; Dai, H. *Nat. Mater.* **2011**, *10*, 780.

(17) Sa, Y. J.; Kwon, K.; Cheon, J. Y.; Kleitz, F.; Joo, S. H. *J. Mater. Chem. A* **2013**, *1*, 9992.

(18) Lee, D. U.; Kim, B. J.; Chen, Z. *J. Mater. Chem. A* **2013**, *1*, 4754.

(19) Maiyalagan, T.; Jarvis, K. A.; Therese, S.; Ferreira, P. J.; Manthiram, A. *Nat. Commun.* **2014**, *5*, 3949.

(20) Masa, J.; Xia, W.; Sinev, I.; Zhao, A.; Sun, Z.; Grützke, S.; Weide, P.; Muhler, M.; Schuhmann, W. *Angew. Chem. Int. Ed.* **2014**, *53*, 8508.

(21) Zhao, A.; Masa, J.; Xia, W.; Maljusch, A.; Willinger, M.-G.; Clavel, G.; Xie, K.; Schlögl, R.; Schuhmann, W.; Muhler, M. *J. Am. Chem. Soc.* **2014**, *136*, 7551.

(22) Ma, T.; Dai, S.; Jaroniec, M.; Qiao, S. Z. *J. Am. Chem. Soc.* **2014**, *136*, 13925.

(23) Indra, A.; Menezes, P. W.; Sahraie, N. R.; Bergmann, A.; Das, C.; Tallarida, M.; Schmeiber, D.; Strasser, P.; Driess, M. *J. Am. Chem. Soc.* **2014**, *136*, 17530.

(24) Zhang, C.; Antonietti, M.; Fellinger, T. P. *Adv. Funct. Mater.* **2014**, *24*, 7655.

(25) Mao, S.; Wen, Z.; Huang, T.; Hou, Y.; Chen, J. *Energy Environ. Sci.* **2014**, *7*, 609.

(26) Ng, J. W. D.; Tang, M.; Jaramillo, T. F. *Energy Environ. Sci.* **2014**, *7*, 2017.

(27) Chen, Z.; Yu, A.; Higgins, D.; Li, H.; Wang, H.; Chen, Z. *Nano Lett.* **2012**, *12*, 1946.

(28) Zhou, W.; Sunarso, J. *J. Phys. Chem. Lett.* **2013**, *4*, 2982.

(29) Hardin, W. G.; Slanac, D. A.; Wang, X.; Dai, S.; Johnston, K. P.; Stevenson, K. J. *J. Phys. Chem. Lett.* **2013**, *4*, 1254.

(30) Jung, J. I.; Jeong, H. Y.; Lee, J. S.; Kim, M. G.; Cho, J. *Angew. Chem. Int. Ed.* **2014**, *53*, 4582.

(31) Han, X.; Cheng, F.; Zhang, T.; Yang, J.; Hu, Y.; Chen, J. *Adv. Mater.* **2014**, *26*, 2047.

(32) Hartmann, P.; Bender, C. L.; Vračar, M.; Dürr, A. K.; Garsuch, A.; Janek, J.; Adelhelm, P. *Nat. Mater.* **2013**, *12*, 228.

(33) Das, S. K.; Lau, S.; Archer, L. A. *J. Mater. Chem. A.* **2014**, *2*, 12623.

(34) Araujo, R. B.; Chakraborty, S.; Ahuja, R. *Phys. Chem. Chem. Phys.* **2015**, *17*, 8203.

(35) Yadegari, H.; Li, Y.; Banis, M. N.; Li, X.; Wang, B.; Sun, Q.; Li, R.; Sham, T.-K.; Cui, X.; Sun, X. *Energy Environ. Sci.* **2014**, *7*, 3747.

(36) Kwak, W.-J.; Chen, Z.; Yoon, C. S.; Lee, J.-K.; Amine, K.; Sun, Y.-K. *Nano Energy* **2015**, *12*, 123.

(37) Hartmann, P.; Bender, C. L.; Sann, J.; Durr, A. K.; Jansen, M.; Janek, J.; Adelhelm, P. *Phys. Chem. Chem. Phys.* **2013**, *15*, 11661.

(38) Hayashi, K.; Shima, K.; Sugiyama, F. *J. Electrochem. Soc.* **2013**, *160*, A1467.

(39) Avakyan, L. A.; Manukyan, A. S.; Mirzakhanyan, A. A.; Sharoyan, E. G.; Zubavichus, Y. V.; Trigub, A. L.; Kopacheva, N. A.; Bugaev, L. A. *Opt. Spectrosc.* **2013**, *114*, 347.

(40) Colpas, G. J.; Maroney, M. J.; Bagyinka, C.; Kumar, M.; Willis, W. Sl.; Suib, S. L.; Baidya, N.; Mascharak, P. K. *Inorg. Chem.* **1991**, *30*, 920.

(41) Trotochaud, L.; Young, S. L.; Ranney, J. K.; Boettcher, S. W. *J. Am. Chem. Soc.* **2014**, *136*, 6744.

(42) Lefèvre, M.; Proietti, E.; Jaouen, F.; Dodelet, J.-P. *Science* **2009**, *324*, 71.

(43) Wu, G.; More, K. L.; Johnston, C. M.; Zelenay, P. *Science* **2011**, *332*, 443.

(44) Li, Y.; Zhou, W.; Wang, H.; Xie, L.; Liang, Y.; Wei, F.; Idrobo, J.-C.; Pennycook, S. J.; Dai, H. *Nat. Nanotech.* **2012**, *7*, 394.

(45) Cheon, J. Y.; Kim, T.; Choi, Y.; Jeong, H. Y.; Kim, M. G.; Sa, Y. J.; Kim, J.; Lee, Z.; Yang, T.-H.; Kwon, K.; Terasaki, O. Park, G.-G.; Adzic, R. R.; Joo, S. H. *Sci. Rep.* **2013**, *3*, 2715.

(46) Hu, Y.; Jensen, J. O.; Zhang, W.; Cleemann, L. N.; Xing, W.; Bjerrum, N. J.; Li, Q. *Angew. Chem. Int. Ed.* **2014**, *53*, 3675.

(47) Wu, Z.-Y.; Xu, X.-X.; Hu, B.-C.; Liang, H.-W.; Lin, Y.; Chen, L.-F.; Yu, S.-H. *Angew. Chem. Int. Ed.* **2015**, *54*, 8179.

(48) Strickland, K.; Miner, E.; Jia, Q.; Tylus, U.; Ramaswamy, N.; Liang, W.; Sougrati, M.-T.; Jaouen, F.; Mukerjee, S. *Nat. Commun.* **2015**, *6*, 7343.

(49) Rama, N.; Mukerjee, S. *Adv. Chem. Phys.* **2012**, *2012*, 491604.

(50) Kadish, K. M.; van Caemelbecke, E.; Royal, R. Electrochemistry of metalloporphyrins in nonaqueous media in *The Porphyrin Handbook*, **2000**, *vol. 8*, chapter 55, 1–97, Academic Press, San Diego, Calif, USA.

(51) Ferrari, A. C.; Basko, D. M. *Nat. Nanotech.* **2013**, *8*, 235.

(52) Obraztsova, E. D.; Fujii, M.; Hayashi, S.; Kuznetsov, V. L.; Butenko, Yu. V.; Chuvilin, A. L. *Carbon* **1998**, *36*, 821.

(53) Raccichini, R.; Varzi, A.; Passerini, S.; Scrosati, B. *Nat. Mater.* **2015**, *14*, 271.